In-situ Transmission Electron Microscopy of Crystal Growth under MOVPE Conditions

Dissertation

zur
Erlangung des Doktorgrades
der Naturwissenschaften
(Dr. rer. nat.)

dem

Fachbereich Physik
der Philipps-Universität Marburg

vorgelegt von

Maximilian Widemann

aus

Marburg

Marburg, 2023

Vom Fachbereich Physik
der Philipps-Universität Marburg
als Dissertation angenommen am: 11.04.2023
Erstgutachter: Prof. Dr. Kerstin Volz
Zweitgutachter: Prof. Dr. Marina Gerhard
Tag der mündlichen Prüfung: 25.04.2023
Hochschulkennziffer: 1180

Sieht aus wie ein Sargdeckel, könnte aber auch ein Sprungbrett sein.
Bernd Stromberg

Contents

CHAPTER 1

Introduction

Modern society is extensively dependent on technologies based on semiconducting materials. Everyday life is barely conceivable without using cell phones, the internet, or computers. Despite the technological progress of the last decades, major challenges still have to be overcome. As one of the most important examples, climate change requires more efficient and sustainable energy usage, production and storage to reduce greenhouse gas emissions. Advancements in semiconductor technology could significantly contribute to this goal by developing more energy-efficient devices or technologies for renewable energy generation. For example, today, light emitting diodes (LEDs) are widely established as light sources and replaced more energy-consuming lighting systems reducing the energy demand [1]. A further example, which is currently subject of research, is the development of more efficient laser light sources emitting wavelengths with low dispersion or at the absorption minimum of glass fibers of 1.3 µm and 1.55 µm, respectively. Since optical communication applied for the continuously increasing amount of data transferred via the internet has become one of the biggest consumers of energy [2] and is based on lasers with high energy demand for cooling and poor energy efficiency, such devices would be capable of saving large amounts of energy [3–8]. An additional exemplary technology are solar cells, which are already established. However, their potential still needs to be fully exploited. Besides improving their efficiency, solar cells are currently being investigated for their potential in hydrogen generation by direct photoelectrochemical water splitting [9]. By this, solar energy would not only be converted into electrical power but also stored in chemical form. Hydrogen provides the advantage of portability and can fuel, for example, the energy-intensive steel industry. These are just a few possible examples of how semiconductor research has shaped our world and will continue to do so.

The material system investigated in this thesis is the III/V semiconductor compound gallium phosphide (GaP) in the form of nanowires. Besides conventional layered and processed bulk materials, nanowire structures are promising candidates for the technological demands mentioned above. Laser diodes operating at room temperature with wavelengths tunable in the telecommunication band of 1.2 µm to 1.6 µm can be produced using InP/InAs heterostructure nanowires [10]. Because of their strong ability of defect-free relaxation [11] nanowire heterostructures can have much higher lattice mismatches of around 10 % [12] compared to their bulk material counterparts. Furthermore, nanowires could be integrated on silicon substrates and be implemented on silicon-based solar cells to augment their efficiency [13]. GaP nanowires offer a direct band gap energy of 2.1 eV capable of photoelectrochemical hydrogen generation from solar energy and water [14–16].
The prevalent fabrication process of semiconducting materials is that of metal organic vapor phase epitaxy (MOVPE) since it has been shown to be scalable for commercial production and the most versatile fabrication method capable of producing even metastable materials [17]. Furthermore, it is not only capable of producing bulk, layered, two-dimensional, or quantum dot structures, but it is also compatible with the fabrication of nanowire structures. Research in MOVPE has been ongoing for over five decades. However, fundamental research is still required for a more complete understanding of this process, often referred to as black box.
This work is meant to introduce a new experimental method to investigate MOVPE, aiming to provide new insights into the growth process and deepen its understanding. The method combines the growth of semiconductor materials with structural analysis and live recording at the atomic scale by *in-situ* transmission electron microscopy (TEM). To this end, a closed gas cell and heating holder setup is modified to safely conduct toxic and pyrophoric metal organic precursor gases to a sample located on a heated substrate [18]. Thus, it acts as an MOVPE reactor at a micrometer scale inside a transmission electron microscope. The live imaging during the growth under MOVPE conditions cannot be realized in conventional reactor designs. However, they are compatible with *in-situ* techniques like reflection anisotropy spectroscopy (RAS) for surface structure investigations [19], optical reflectometry for growth rate determination [20–22] or mass spectrometry providing insights in chemical and thermodynamic processes during growth [23]. Other *in-situ* TEM setups based on environmental TEM (ETEM) [24], which are already commonly used and provided impressive results, for example, in nanowire growth at atomic resolution [25] are limited in gas phase pressure [26–28]. Precursor gases are directly injected into the vacuum of the microscope. Therefore, their conditions are closer to those present

in molecular beam epitaxy (MBE) rather than MOVPE [29]. The here presented setup is capable of a much wider range of growth conditions in terms of temperature, partial pressures, and gas flow comparable to MOVPE.
As the applied method is new in this field of research, a proof of concept is needed. An important question tackled in this thesis is about the comparability of the micrometer-scaled setup with actual MOVPE reactors. To clarify this question, the crucial process of the thermal decomposition of metal organic precursors in MOVPE is investigated by mass spectrometry and compared to findings in MOVPE setups. Furthermore, it will be shown that nanowire growth can be performed in the *in-situ* TEM holder via the vapor liquid solid (VLS) mechanism as it is also performed in conventional reactor designs. The live observation of this process delivers new insights into the fundamentals of this process, which are connected to the structure's geometry that are not accessible in post-growth studies or other techniques than *in-situ* electron microscopy. Nevertheless, post-growth investigations deliver indispensable complementary information on the grown structures. In this thesis, high-resolution TEM (HRTEM) and scanning precession electron diffraction (SPED) are utilized for structural analysis. Thereby, information on planar defects in the form of twin boundaries could be obtained, which are also relevant for the growth process. This thesis is organized in the following way. Chapter 2 describes the required physical background, including the description of crystal structures and their symmetry, the reaction kinetics of molecules during decomposition, ionization of molecules and their mass separation, as well as TEM relevant principles of the interaction between electrons and matter. The subsequent chapter 3 gives explanations of the applied experimental methods. The crystal growth by MOVPE is treated with a particular focus on the growth of nanowires via the VLS mechanism. Afterwards, the fundamentals of TEM-relevant imaging techniques and analytic methods are presented. The chapter closes with a description of the utilized *in-situ* TEM setup and its applications. Results of this thesis are provided in chapter 4. It starts with the findings on the thermal decomposition of metal organic precursors in the *in-situ* holder. Afterwards, results of the live observation of GaP nanowire VLS growth are shown, followed by structural investigations in post-growth studies. The chapter ends with the description of a substrate preparation technique and the first results on epitaxial growth on a Si(111) surface. Finally, the most important outcomes of the thesis are summarized in chapter 5.

CHAPTER 2

Physical Background

This thesis addresses the implementation of *in-situ* transmission electron microscopy (TEM) as an experimental method for the investigation of the dynamic processes taking place in semiconductor crystal growth. In this chapter, the theoretical background of the involved physics will be described, beginning with the description of the relevant crystal structures. Subsequently, the theory of reaction kinetics relevant to molecule decomposition is discussed. Furthermore, the physics behind quadrupole mass spectrometry (QMS) utilized in this work for residual gas analysis is explained. Finally, the chapter is finished by explaining the electron matter interaction and the arising phenomena, which is essential for all electron microscopy techniques.

2.1 Description of Crystal Structures

In the scope of this work, group IV and group III/V semiconductor materials are investigated. One of their significant properties is their crystalline structure, meaning their atoms are periodically ordered in all dimensions. Assuming a perfect crystal, every atom's surroundings are the same over the whole crystal lattice. Thus, the structure is unchanged by a translation T from one lattice point $\vec{r}$ to another, which is described by the equation

$$T(\vec{r}) = T\left(\vec{r} + \vec{R}\right) \tag{2.1}$$

where $\vec{R}$ is a lattice vector consisting of a linear combination

$$\vec{R} = u\vec{a_1} + v\vec{a_2} + w\vec{a_3} \qquad u,v,w \in \mathbb{Z} \tag{2.2}$$

of the fundamental translation vectors $\vec{a_1}$, $\vec{a_2}$ and $\vec{a_3}$, which are also called basis vectors [30]. The unit cell is the volume created by these basis vectors, which is repeated indefinitely in their directions. The atoms located in the unit cell form the basis of the crystal lattice. The shape of the unit cell and the position of basis atoms within define the crystal structure. The crystal's periodic properties lead to symmetries, described by the symmetry operators of the structure. Each symmetry operator and their linear combinations map the crystal structure onto itself. This means it is a transformation of three-dimensional space that preserves distances and angles and that leaves the crystal structure as a whole unchanged. Mathematically the set of symmetry operators form an algebraic group together with the multiplication operation [31]. The symmetry operations may include mirroring, glide reflections, rotations, screw rotations, inversion, or combinations of these [32]. In total, 230 space groups exhibiting unique symmetry can be defined, which are ordered and numbered by the International Union of Crystallography and can be found, for example, in reference [33].

2.1.1 Semiconductor Crystals

Relevant to this work are crystal structures of the semiconductor materials silicon and gallium phosphide. Silicon is an element of group IV of the periodic table. An atom obtains four valence electrons that form an sp^3 orbital hybridization in a crystal. They build four covalent bonds to neighboring silicon atoms creating a tetrahedral bonding structure with bonds angled at 109.47° to each other. This results in the diamond crystal structure (space group No. 227), which is shown in figure 2.1 a). It consists of two face

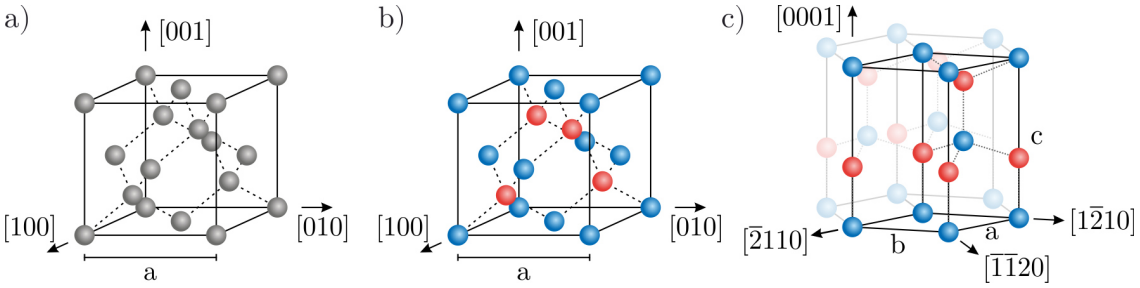

Figure 2.1: a) unit cell of the cubic diamond structure of silicon consisting of two shifted fcc lattices. b) cubic zinc blende unit cell of III/V semiconductors. Each of the two fcc lattices is either occupied with atoms of group III (blue) or group V (red) c) unit cell of the hexagonal wurtzite structure. The hexagonal symmetry becomes clearer together with two more unit cells that are indicated faded.

centered cubic (fcc) sublattices shifted by 1/4 of the unit cell's space diagonal to each other. Gallium phosphide bulk material crystallizes in a similar structure, but in contrast to silicon, it contains two elemental species. Each of them occupies one of the fcc sublattices. The result is the zinc blende structure (space group No. 216) [34], displayed in figure 2.1 b). In principle, gallium phosphide can also crystallize in the wurtzite structure (space group No. 186). However, this phase is not stable for bulk material at ambient conditions due to its higher volume energy compared to zinc blende [35]. But since its surface energy is in general lower than the one of zinc blende [36], it may become more favorable for structures with a very high surface-to-volume ratio like it is the case for nanowires [36–38]. The wurtzite structure has a hexagonal symmetry rather than a cubic one, as can be seen in figure 2.1 c). Often it is beneficial to describe the lattice with its reciprocal lattice in momentum space. Its reciprocal basis vectors $\vec{b_1}$, $\vec{b_2}$ and $\vec{b_3}$ can be derived by the real space lattice vectors

$$\vec{b_i} = 2\pi\epsilon_{ijk}\frac{\vec{a_j} \times \vec{a_k}}{\vec{a_i}\,(\vec{a_j} \times \vec{a_k})} \qquad i,j,k = 1,2,3 \tag{2.3}$$

with ϵ_{ijk} being the Levi-Cevita symbol [39]. From this follows the relation

$$\vec{a_i} \cdot \vec{b_j} = 2\pi\delta_{ij} \qquad i,j,k, = 1,2,3 \tag{2.4}$$

where δ_{ij} describes the Kronecker symbol. Analogue to the real lattice vector $\vec{R}$, a reciprocal lattice vector $\vec{G}$ is defined in momentum space as

$$\vec{G} = h\vec{b_1} + k\vec{b_2} + l\vec{b_3} \qquad h,k,l \in \mathbb{Z} \tag{2.5}$$

pointing from one reciprocal lattice point to another. Simultaneously, h, k and l define a family of parallel and equidistant planes in real space, which are orthogonal to the corresponding vector $\vec{G}$. Consequently, each reciprocal lattice point represents a periodicity in the real lattice along the direction of $\vec{G}\,(h,k,l)$. h, k and l are called Miller indices [40]. In practice, they are used to define the orientation of a single plane (hkl) illustrated in figure 2.2 a) - d) or a family of planes $\{hkl\}$ in the crystal lattice. The Miller indices can also be derived directly from real space by determining the intersections of the plane with the coordinate axes. The smallest integer multiple of the reciprocal distances of these intersections determines the indices. If a plane is parallel to an axis, meaning the intersection is at infinity, the corresponding index becomes zero. Negative indices are

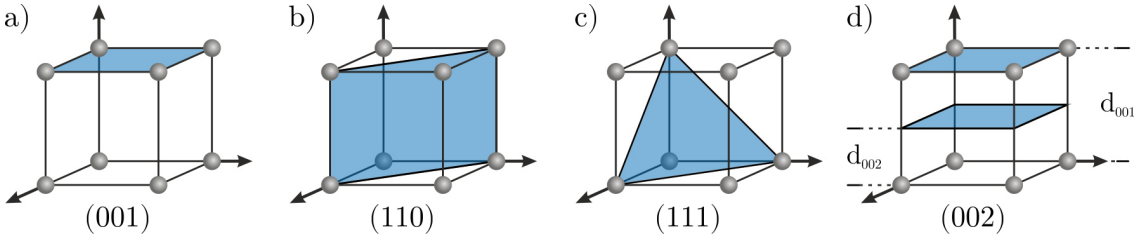

Figure 2.2: Planes of different orientations (blue) and their Miller indices. a) (001), b) (110), c) (111), d) (002)

denoted by a bar over their number. Real structures, however, are not perfect crystals due to impurities, structural imperfections and their finite extent.

2.1.2 Nanowire Crystals

Nanowires are structures with a large aspect ratio, with length and width in the order of 10^4 nm and 10^1 nm, respectively. Due to their narrow extension in two dimensions, they are often referred to as one-dimensional structures. This fact leads to different properties of nanowires compared to their bulk material counterparts. The Gibbs free energy of a material is given by the Gibbs free energy of the volume G_V and its surface contribution [41]

$$G = G_V + \sigma^s A, \tag{2.6}$$

with σ^s and A being the surface tension and surface respectively. The surface contribution can be neglected for bulk materials with a vanishing surface-to-volume ratio. However, for nanowire structures, it can have a huge influence. III/V semiconductor bulk materials usually crystallize in zinc blende structure since its energy is lower than that of wurtzite [35]. The latter forms surface facets with lower surface energies than those of zinc blende [36]. For structures with large surface-to-volume ratios, such as nanowires, this can lead to crystallization in wurtzite structure [36–38]. Furthermore, it is possible to change between these two structures within a single nanowire by tweaking the growth conditions [29].
In heterostructures, the strain at the interfaces can be relaxed via the nanowire surfaces [11]. This enables defect-free heterostructures with much higher lattice mismatches than planar growth in bulk structures. This property is promising for integration of III/V compounds on substrates with a high mismatch, such as silicon of up to 11.5 % [12], as well as nanowire heterostructures having a lattice mismatch of 7 % [42, 43].

On the one hand, they differ in structural properties, which leads to physical differences on the other hand. For example, band gap energies are different for ZB and WZ [34, 44, 45] and may also change from indirect to direct, as is the case for gallium phosphide [46].

2.2 Reaction Kinetics

A kinetic description of reactions that take place during crystal growth helps to understand phenomena like mass transport, growth rate limitations, surface reactions, or reactions proceeding in the gas phase [47]. This chapter emphasizes gas phase reactions, as these are capable of describing the thermal decomposition of molecules. They are called homogeneous reactions due to the fact that they happen in a singular phase. In contrast, reactions proceeding in multiple phases, like gas and solid phases at the surface, are called heterogeneous. Furthermore, if only one molecule is involved, they are classified as a unimolecular reaction of the form $AB \rightarrow A + B$. Reactions between two molecules are called bimolecular reactions of the form $A + B \rightarrow C + D$.

2.2.1 Reaction Rates

The theory of reaction rates postulates that reactants proceed to products via the formation of an activated intermediate state [47]. The energy diagram for a unimolecular decomposition can be seen in figure 2.3. If a molecule AB receives the activation energy ΔE_1^*, it is capable of overcoming the energy barrier to form the intermediate state AB^* in a first step and decomposes into the products A and B in a second step releasing the energy ΔE_{-1}^*. The resulting energy difference is given by the reaction enthalpy $\Delta H = \Delta E_1^* - \Delta E_{-1}^*$. For the case illustrated by the black curve, with $\Delta E_1^* < \Delta E_{-1}^*$, the reaction is exothermic and releases energy. If $\Delta E_1^* > \Delta E_{-1}^*$ applies as depicted in blue, the reaction is endothermic and requires additional energy to take place. In a catalyzed reaction, the energy barrier ΔE_1 is reduced, and a lower activation energy is required, as indicated by the red curve. In the simple case of a unimolecular reaction serving as an example, the rate of the reactions is equal to the product of concentration and reaction constant k_1. The latter is described by the Arrhenius equation

$$k_1 = A_1 \exp\left(-\frac{\Delta E_1^*}{k_B T}\right) \tag{2.7}$$

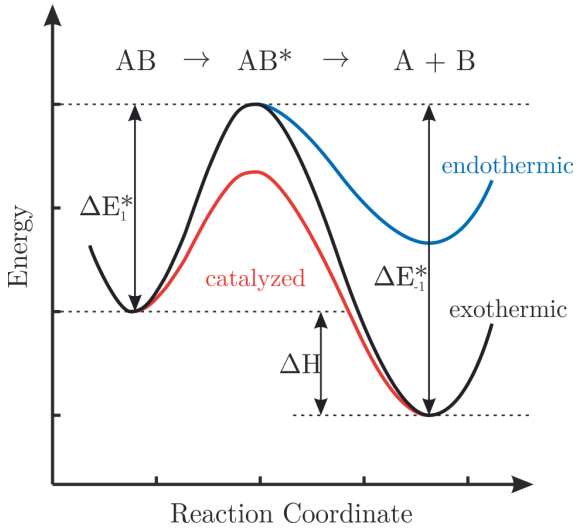

Figure 2.3: Schematic diagram of energy versus reaction coordinate illustrating the activation energy and enthalpy of precursor decomposition. Exothermic reaction in black, endothermic reaction in blue and catalyzed exothermic reaction in red (adapted from [47, 48])

with Boltzmann constant k_B and temperature T [49]. The preexponential frequency factor A_1 is determined by the change in entropy ΔS with

$$A_1 = \frac{k_B T}{h} \cdot \exp\left(\frac{\Delta S}{k_B}\right) \tag{2.8}$$

whereas h describes the Planck constant. A_1 ranges from $10^{13.08}\mathrm{s}^{-1}$ to $10^{13.35}\mathrm{s}^{-1}$ in the temperature regime from 300 °C to 800 °C for vanishing entropy ($\Delta S = 0$) [47]. The value of A_1 will differ from this frequency drastically if the entropy changes.

2.2.2 Homogeneous Reaction Mechanisms

Usually, several reactions are involved in the unimolecular homogeneous thermal decomposition of metal organic precursors. This section describes the most prominent reactions for the investigated molecules.

The most common pyrolysis reaction is a simple homolytic fission [47]. It describes the cleavage of a bond so that both molecular fragments between which the bond is broken retain a bonding electron. For an even number of paired electrons, this results in the formation of two radicals [50]. The bond between the alkyl group R and the group III or V atom M is cleaved preferentially for metal organic precursors. This produces a radical

M-species and a radical alkyl group, as seen in the exemplary reaction scheme in figure 2.4.

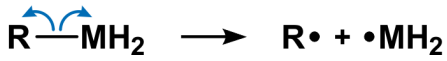

Figure 2.4: Homolytic fission reaction. The blue arrows indicate positive charge transfer (adapted from [50]).

The covalent bond may also break with an unequal distribution of the involved bonding electrons. In this reaction, referred to as heterolytic fission, both electrons remain with a single molecular fragment. The result is two oppositely charged reaction products. The charge distribution is determined by the electronegativity of the involved species [50]. In figure 2.5 the heterolytic fission is illustrated exemplarily again with a breaking bond between an alkyl group R and atom M. The group III or V atom remains positively

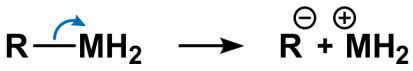

Figure 2.5: Heterolytic fission reaction. The blue arrow indicates positive charge transfer (adapted from [50]).

charged, whereas the alkyl group is negatively charged.
For molecules with larger alkyl groups, intramolecular coupling may occur. This reaction describes a molecule rearrangement in the pyrolysis transition state where two atomic species interact with each other, forming a bond at the cost of their previous ones. For example, in $PH_2(C_4H_9)$ (tertiary butyl phosphine), the central C atom interacts with an H atom bound to the P. As a result, the P-H and P-C bonds break, and the H binds to the central C atom resulting in the two molecular species PH and C_4H_{10}. This reaction is shown in the scheme of figure 2.6. A further decomposition reaction for molecules

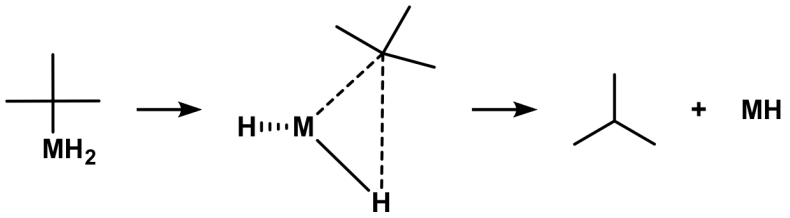

Figure 2.6: Intramolecular coupling reaction on the example of $PH_2(C_4H_9)$ (M=P).

with larger alkyl groups is given by β-hydrogen elimination. In the case of group V precursors with atomic species M, the filled p-orbital interacts with an H atom bound to a neighboring C atom in the β position. This leads to wider bonding distances and

redistribution of electrons in the transition state. As a result, the C_α-M bond breaks, and charge is transferred towards the M atom. Further, the M atom binds to the transition hydrogen atom (H_{tr}), the H_{tr}-C_β bond is cleaved, and a C=C double bond is formed between C_α and C_β. This process is sketched in figure 2.7 on the example of a hydride bond to a tertiary butyl group, again the example of $PH_2(C_4H_9)$ applies. In this scheme,

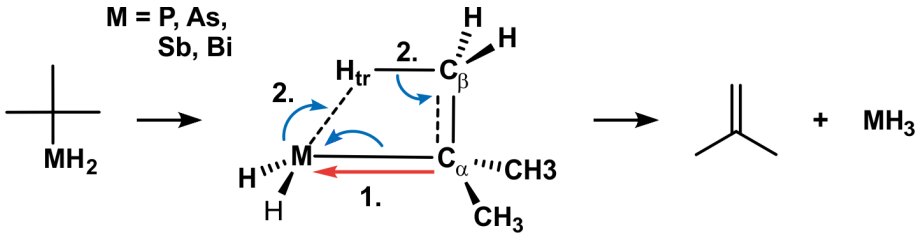

Figure 2.7: β-hydrogen elimination reaction. The blue and red arrows indicate charge transfer and the largest bond elongation respectively (adapted from [51]).

the donation of an H atom from the tertiary butyl group to the M atom forms C_4H_8 (isobutene) and MH_3 (e.g., phosphine with M=P). For molecules containing larger alkyl groups, β-hydrogen elimination typically possesses lower activation energies than homolysis [47, 51].

As an example of a bimolecular reaction, the alkyl exchange is illustrated in figure 2.8. In

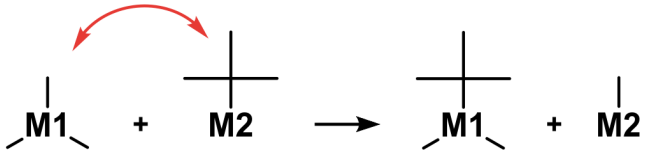

Figure 2.8: Illustration of an alkyl exchange reaction. The example shows the exchange of a methyl group and a tertiary butyl group.

this reaction, two molecules that contain alkyl groups exchange them. In the illustration, a molecule with atomic species M1 has three methyl groups, whereas the M2 containing molecule has a tertiary butyl group. One of the methyl groups is exchanged with the tertiary butyl group, and two new molecules are produced.

Radicals formed in unimolecular reactions, such as hydrogen or methyl radicals, are also significant for pyrolysis via bimolecular reactions. They are capable of initiating pyrolysis of other molecular species by attacking [52]. Hydrogen radicals, for example, can form in a specific homolysis reaction, where a single or a pair of hydrogen atoms dissociate from the molecule prior to the removal of an alkyl group [53]. Other radical species that can initiate decomposition reactions are the formed alkyl radicals [54].

Besides the mentioned reactions, which are the most relevant ones for the molecules investigated in this work, there exist a multitude of other decomposition pathways which can occur, especially for molecular species with different structures as the presented examples. For more detailed information on reaction mechanisms, the reader is referred to the literature of, e.g., Stringfellow [47].

2.3 Quadrupole Mass Spectrometry

Mass spectrometry is applied as an analytic technique in several areas, such as biology, medicine, pharmacy, chemistry, physics and many more. It can determine an unknown analyte's molecular stoichiometry, composition, molecular weight, structure, or isotopic abundance. This opens a vast and interdisciplinary field of operation in natural and life sciences.

The principle behind mass spectrometry is to ionize an analyte and separate its ions with respect to their mass over charge ratio (m/Z). In general, it is required to transfer the analyte to the gas phase to ionize the particles before they are separated and afterwards detected. The ionization can occur through various mechanisms such as electron ionization, thermal ionization, chemical ionization, electrospray ionization, field ionization, fast atom bombardment, or laser desorption ionization. Here the electron ionization (EI) process will be described in further detail as it is used in this work.

In EI, electrons are accelerated, impinge the analyte, and may transfer a fraction of their energy to a neutral particle M, bringing it to an excited state where the particle stays neutral or may be ionized. In the latter case, the most desirable process is the loss of electrons resulting in a positive radical ion $M^{+\bullet}$

$$M + e^- \longrightarrow M^{+\bullet} + 2e^- \tag{2.9}$$

If more than one electron is ejected, the resulting ion is doubly ($M^{2+\bullet}$) or even triply ($M^{3+\bullet}$) charged. The minimal energy needed to bring a specific molecule to an ionized state is called its ionization energy (IE) and is dependent on the neutral species. It is in the range from 7 eV to 15 eV, excluding some noble gases having an IE of up to 24.6 eV in the case of helium [55]. Figure 2.9 a) demonstrates the transition to ionic states. Here the energy of a diatomic molecule is plotted in the ground state (M) and excited state ($M^{+\bullet}$) versus the reaction coordinate r, which describes the internuclear atomic spacing. The time it takes an electron to travel the distance through a molecule is in the order of 10^{-15} s,

whereas the molecule itself moves less than 1 pm in this time. Also, vibrational motions are slower by over two orders of magnitude. Hence, the molecule can be considered at rest during ionization [56]. The Born-Oppenheimer approximation states that electronic motions can be separated from nuclear motions because of their significant difference in mass [57]. Additionally, the Franck-Condon principle says that electronic transitions occur much faster than the nucleus moves to its new equilibrium position [58, 59]. This means that the transition from ground to an excited state appears as a vertical transition in the energy versus reaction coordinate diagram. Besides the loss of electrons, various other

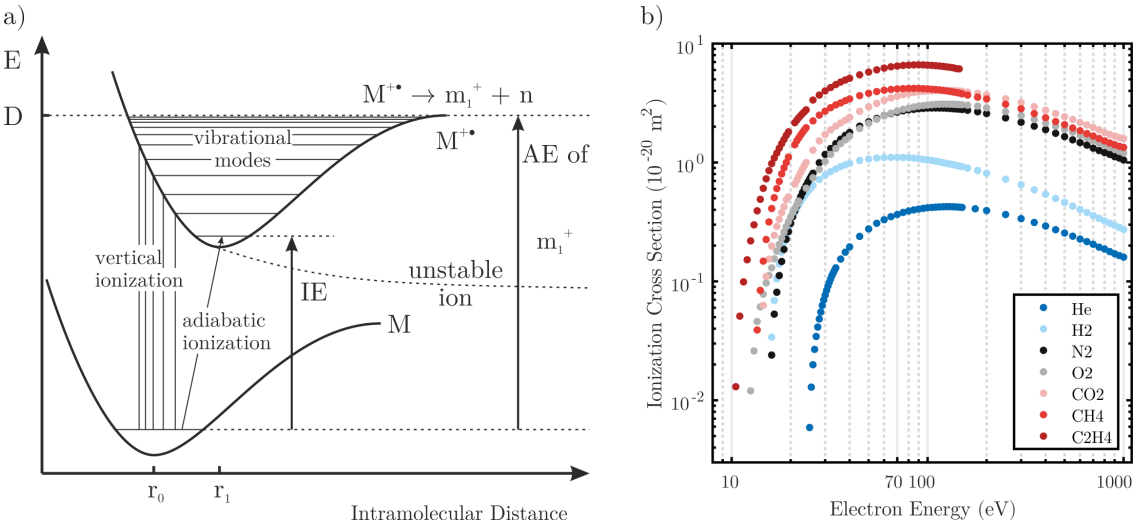

Figure 2.9: a) Transition to an ionic state for a diatomic molecule. Electron ionization is displayed as a vertical transition to a vibrational mode. In contrast, the transition into the vibrational ground state appears as a diagonal line called adiabatic ionization. Exceeding the dissociation energy (D) leads to fragmentation. Unstable molecules do not possess vibrational modes with energy minimums and dissociate by ionization (adapted from [56]). b) Ionization cross sections for various molecular species. All of them show a plateau around 70 eV and IE below 25 eV (data taken from [60]).

ionization processes may occur. If the transferred energy is high enough, the molecule can dissociate. Figure 2.9 a) depicts this as the dissociation energy D. Transferring an energy to the molecule that its energy exceeds the dissociation energy, leads to fragmentation of $(M^{+\bullet})$ creating an ionic (m^+) and neutral (n) particle

$$M^{+\bullet} \longrightarrow m^+ + n \tag{2.10}$$

The energy difference between the molecule's ground state and dissociation energy required for arising of m^+ is called the appearance energy (AE) of the fragment m^+. Depending on

the molecule's structure, a multitude of fragments, which themselves can dissociate, can be formed, each with its own probability to occur. By this, each molecular species obtains a characteristic fragmentation pattern with a distinct distribution of mass over charge ratios and relative peak intensities. Nevertheless, its appearance depends also on the ionization conditions, like electron energy, since the ionization cross-section, describing the ionization efficiency, depends on energy. Additionally, relative abundances in fragmentation patterns vary with ionization energy [61, 62]. It is obvious that if the exciting electron carries the IE, it is, in principle, capable of transferring it completely to the neutral particle to excite an ionic state, but the probability of this event is close to zero, as is the ionization efficiency. An energy increase leads to a steady increase up to a certain energy where a plateau in ionization cross section is reached, as can be seen in 2.9 b) by the example of several particle species. Even though the ionization cross-section depends on the neutral species, all species possess their plateau at an energy of around 70 eV. Operating an ionizer at this energy leads to a maximum yield for most ions, and small deviations in energy do not affect their ionization cross-section by much. Furthermore, all particles can be ionized efficiently. Due to these facts, conventionally 70 eV is the utilized energy to record mass spectra allowing for quantification and enabling comparability between different setups and facilitating the creation of mass spectra databases like that of the National Institute of Standards and Technology (NIST) [63].

One can make use of several different filter techniques and applications. Time of flight analyzers, for example, divide the ions by accelerating an ion pulse with a voltage up to specific kinetic energy and measuring their time dispersion. Since their velocity depends on the ion mass, the ions of unequal mass reach the detector at different times [64]. Magnetic sector instruments split the ions concerning their momentum in a magnetic field by deflecting them via the Lorentz force. Ions of different masses will hit the detector at different positions, providing information on their mass-over-charge ratio. Orbitrap devices measure the oscillations of trapped ions. A Fourier transformation of their induced mirror current to an electrode reveals their oscillation frequencies, which depend on the ion mass [23, 65]. In practice, plenty of couplings between ionizers and filters are present, each with its advantages and disadvantages. This work focuses on quadrupole mass filters (QMF), the principle of which is explained in the following.

The utilization of QMF's was performed independently by Paul and Steinwedel [66] and Post [67] in 1953 after the discovery of the strong focusing effect in 1950 [68, 69], which was used to compensate diverging effects in particle accelerators. Further developments led Wolfgang Paul and Hans G. Dehmelt to be awarded the Nobel Prize in Physics in 1989

for the development of the ion trap technique. The theory of the QMF is summed up, for example, by Campana [70]. A more detailed description can be found in Dawson's book [71].
Filtering in a QMF proceeds by an electromagnetic quadrupole field. In an ideal field, the potential $\Phi(\vec{r})$ at any coordinate $\vec{r}$ can be expressed as the sum of perpendicular potentials in $\vec{x}$, $\vec{y}$ and $\vec{z}$

$$\Phi\left(\vec{r}\right) = \Phi\left(\vec{x},\vec{y},\vec{z}\right) = \Phi\left(\vec{x}\right) + \Phi\left(\vec{y}\right) + \Phi\left(\vec{z}\right) \tag{2.11}$$

The strong focusing effect relies on a force acting on the particles, which is proportional to the distance from the origin [69].
The force is given by

$$\vec{F_x} = e\vec{E_x} = -e\frac{\partial\Phi\left(\vec{x}\right)}{\partial\vec{x}} \propto x \tag{2.12}$$

with the elemental charge e and the electric field in x-direction $\vec{E_x}$. From equation (2.12), it can be concluded that the force at the origin vanishes, as does the potential $\Phi(\vec{x}=0)$. Consequently, such a potential needs to be of the form

$$\Phi\left(\vec{x}\right) = a\vec{x}^2 \tag{2.13}$$

with a constant a. The same considerations can be made for the y- and z-directions with the respective constants b and c. Since there is no field in z-direction, one can set $c = 0$ leading to the total potential, which is only dependent on $\vec{x}$ and $\vec{y}$

$$\Phi\left(\vec{x},\vec{y}\right) = a\vec{x}^2 + b\vec{y}^2 + c\vec{z}^2 = a\vec{x}^2 + b\vec{y}^2. \tag{2.14}$$

From Laplace's equation

$$\nabla^2\Phi\left(\vec{x},\vec{y}\right) = 2a + 2b = 0 \tag{2.15}$$

it can be concluded that $a = -b$. At the field boundaries $(x,y) = (r_0,0)$ the potential needs to equal the applied electrode potential Φ_0.

$$\Phi\left(r_0,0\right) = \Phi_0 = ar_o^2 \qquad \Rightarrow \qquad a = \frac{\Phi_0}{r_o^2} \tag{2.16}$$

From Laplace's equation (2.15) it follows analogous

$$b = -\frac{\Phi_0}{r_o^2}. \tag{2.17}$$

Equation (2.14) then results in the potential

$$\Phi(\vec{x},\vec{y}) = \Phi_0 \frac{\vec{x}^2 - \vec{y}^2}{r_o^2}. \tag{2.18}$$

The equipotentials created by a hyperbolic quadrupole geometry, utilized in mass filters, are shown in figure 2.10 a). The applied potential Φ_0 consists of a direct current voltage

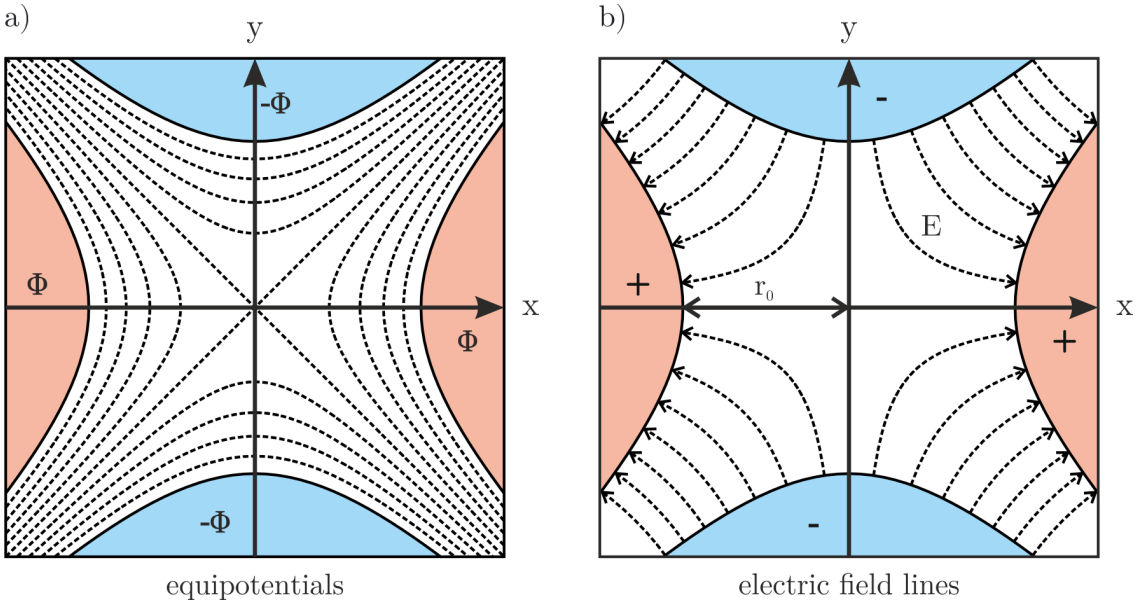

Figure 2.10: a) Equipotentials of the quadrupole field. Red electrodes are on a positive and blue on a negative potential. b) Resulting electric field lines.

U and an alternating voltage V oscillating with an angular frequency ω. With t being the time, it can be written as

$$\Phi_0 = U + V \cos(\omega t). \tag{2.19}$$

Inserting this potential into equation (2.14) gives the field potential

$$\Phi(\vec{x},\vec{y}) = (U + V \cos(\omega t)) \frac{\vec{x}^2 - \vec{y}^2}{r_o^2}. \tag{2.20}$$

From this, the electric fields in x, y and z direction can be derived as

$$E_x = -\frac{\partial \Phi\left(\vec{x},\vec{y}\right)}{\partial \vec{x}} = -\frac{2}{r_0^2}\left(U + V\,\cos\left(\omega t\right)\right)x \tag{2.21}$$

$$E_y = -\frac{\partial \Phi\left(\vec{x},\vec{y}\right)}{\partial \vec{y}} = \frac{2}{r_0^2}\left(U + V\,\cos\left(\omega t\right)\right)y \tag{2.22}$$

$$E_z = -\frac{\partial \Phi\left(\vec{x},\vec{y}\right)}{\partial \vec{z}} = 0 \tag{2.23}$$

The electric field lines are displayed in figure 2.10 b) for the respective geometry. The equations of motion for a particle with mass m experiencing an acceleration $\vec{a}$ in the quadrupole field follow from $\vec{F} = e\vec{E} = m\vec{a}$

$$\frac{d^2x}{dt^2} + \frac{2e}{mr_0^2}\left(U + V\,\cos\left(\omega t\right)\right)x = 0 \tag{2.24}$$

$$\frac{d^2y}{dt^2} - \frac{2e}{mr_0^2}\left(U + V\,\cos\left(\omega t\right)\right)y = 0 \tag{2.25}$$

$$\frac{d^2z}{dt^2} = 0 \tag{2.26}$$

From these equations, it can be concluded that the motion in x-, y- and z-direction of particles are independent of each other and that the velocity in z-direction is unchanged. With the introduction of dimensionless variables

$$\xi = \frac{\omega t}{2}, \qquad a_\mu = \frac{8eU}{m\omega^2}\gamma, \qquad q_\mu = \frac{4eV}{m\omega^2}\gamma \tag{2.27}$$

where μ equals either x or y and γ replaces $\frac{1}{r_0^2}$ or $-\frac{1}{r_0^2}$ respectively, the equations of motion in x and y can be combined to

$$\frac{d^2\mu}{d\xi^2} + \left(a_\mu + 2q_\mu\,\cos\left(2\xi\right)\right)\mu = 0 \tag{2.28}$$

This equation is known as the Mathieu equation. It was first studied in 1868 by Émile Mathieu, who used it to describe the vibrational modes of a stretched membrane with elliptical boundary [72]. Solutions of this linear second-order differential equation are tabled in literature [73] and can be found, for example, in the work of McLachlan [74]. Stable solutions of the equation follow the form [71]

$$\begin{aligned}\mu(\xi) = A(\mu,\xi) \sum_{n=-\infty}^{\infty} C_{2n}(a_\mu,q_\mu) \cos(2n + \beta(a_\mu,q_\mu)) \\ + B(\mu,\xi) \sum_{n=-\infty}^{\infty} C_{2n}(a_\mu,q_\mu) \sin(2n + \beta(a_\mu,q_\mu))\end{aligned} \tag{2.29}$$

Here A and B are functions of the initial conditions μ and $\frac{d\mu}{d\xi}$, C_{2n} and β are functions of a_μ and q_μ [70]. For distinct values of a_μ and q_μ, the ion trajectory is stable following a superposition of sine waves. These stable solutions are independent of the initial conditions and result in limited values of ξ [75]. Unstable trajectories have too high of amplitude or diverge from the z-axis, resulting in practice hitting the electrodes or leaving the filter to the side. In figure 2.11 the a_μ, q_μ space is plotted. The first three stability regions can be seen marked in yellow and labeled as I to III. The relevant stability region I, which is utilized in QMF, is bound by a_0, which defines the x-stability (red)

$$|a_\mu| < a_0 = -\frac{1}{2}q_\mu^2 + \frac{7}{128}q_\mu^4 - \frac{29}{2304}q_\mu^6 + \frac{68687}{18874368}q_\mu^8 + \mathcal{O}(10) \tag{2.30}$$

and b_1 defining the y-stability (blue)

$$\begin{aligned}|a_\mu| < b_1 = 1 - q_\mu - \frac{1}{8}q_\mu^2 + \frac{1}{64}q_\mu^3 + \frac{1}{1536}q_\mu^4 + \frac{11}{36864}q_\mu^5 + \frac{49}{589824}q_\mu^6 \\ - \frac{55}{9437184}q_\mu^7 - \frac{265}{113246208}q_\mu^8 + \mathcal{O}(9).\end{aligned} \tag{2.31}$$

Technical details on the design and realization of a QMF are described in chapter 3.4.2.

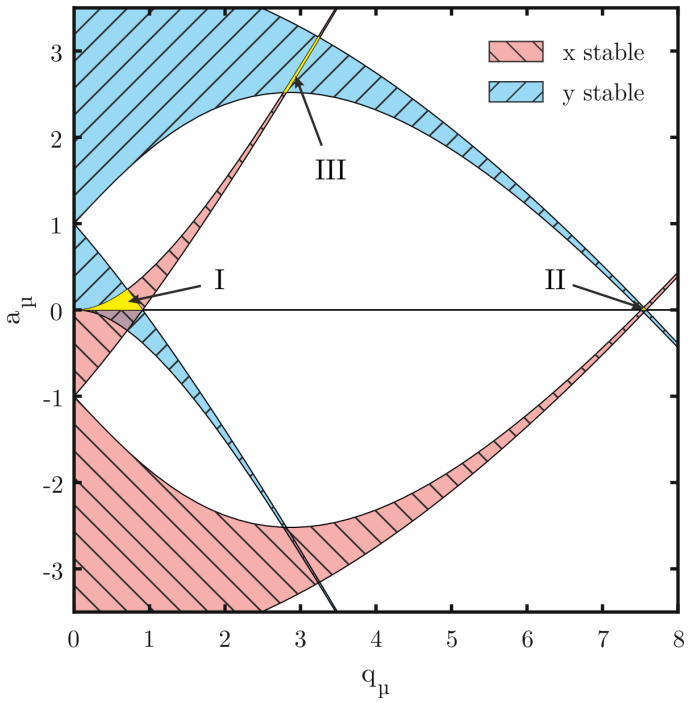

Figure 2.11: a_μ, q_μ space illustrating stable regions in x (red) and y (blue). Stability regions I to III, where both x and y are stable, are marked in yellow. The QMF relevant region I is bound by a_0 and b_1.

2.4 Electron Matter Interaction

Electron microscopy is based on the interaction of electrons with the investigated specimen. The interaction leads to multiple processes, which can be utilized, for example, to generate images, analyze its structure or determine its chemical composition. These processes can be divided into elastic and inelastic as well as coherent and incoherent interactions. An overview of signals emanating from the sample can be seen in figure 2.12 a). If the energy of the impinging electron is maintained during the interaction, the process is called elastic. Accordingly, a process called inelastic occurs when energy is transferred during the interaction. A process is coherent if the electron wave phase relations are persistent. Otherwise, it is called incoherent.

This chapter will treat the relevant phenomena for contrast generation in TEM. In the case of conventional TEM, the image formation is a consequence of the diffraction of electrons in the sample. The investigated III/V semiconductors are typically crystalline. The coherent elastic scattering at the screened Coulomb potential of these periodic structures is typically

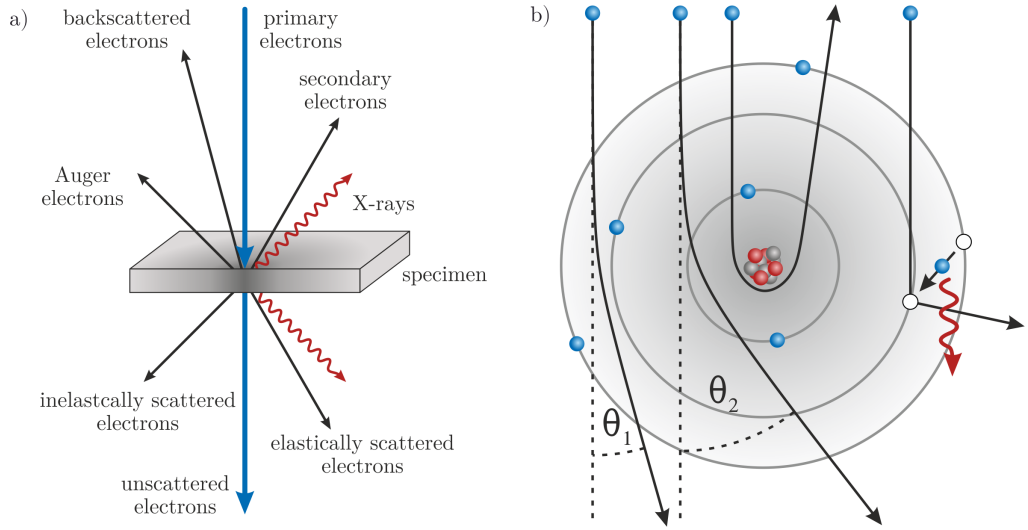

Figure 2.12: a) Overview of interaction processes caused by high-energy electrons and matter. b) illustration of elastic scattering due to the Coulomb potential of the atom core. On the right side, the emission of a secondary electron and a characteristic X-ray is indicated (adapted from [76]).

referred to as diffraction. Scattering angles are narrow in this case, as sketched in figure 2.12 b).

Another imaging technique is high-angle annular dark field (HAADF) imaging, commonly used in scanning transmission electron microscopy (STEM). The contrast arises from electrons scattered to higher angles, mainly through thermal diffuse scattering (TDS), where thermally displaced atoms in the specimen scatter the electrons. The phase relationship of the electrons gets lost during this, rendering it incoherent. This scattering happens due to the deflection at the nuclei, where the surrounding electrons play only a minor role, as illustrated in figure 2.12 b).

For chemical analysis of a TEM sample, inter alia inelastic processes are exploited. Among these, the energy transfer can lead to the knockout of an electron from the sample. An electron from a higher state can emit the energy difference as a characteristic X-ray photon during its transition by occupying this vacant state. In energy-dispersive X-ray spectroscopy (EDX), these photons are analyzed. Complementary, the energy loss of incident electrons mirroring the atomic energy levels is analyzed in electron energy loss spectroscopy (EELS). Other processes exist, like the emission of Auger electrons and photon emission by cathodoluminescence, which are not covered in this section.

2.4.1 Electron Diffraction

Electron diffraction is one of the fundamental mechanisms for image generation in conventional transmission electron microscopy. Understanding the physics behind this mechanism enables various experimental applications in materials science. The kinematic approximation is used to simplify the complex nature of electron diffraction. However, this approximation comes to its limits easily, for example, in the description of thicker TEM samples. In the following, the details of kinematic theory will be explained.
The fundamental assumption of kinematic approximation is that an electron undergoes just a single interaction with the atom's Coulomb potentials without losing energy. Consequently, all processes are assumed to be elastic, and multiple scattering events are not considered. Hence, the electron's momentum and energy are conserved. The approximation of single scattering becomes invalid for a thicker specimen. Due to the significant mass difference between electrons and atoms, energy transfer can be neglected. Thus, the assumption of an elastic scattering process represents a good approximation.
Considering the interaction of an electron wave with a single atom, the electrons wave function $\Psi(\vec{r})$ has to fulfill the stationary Schrödinger equation

$$\nabla^2\Psi(\vec{r}) + \frac{8\pi^2 me}{h^2}E\Psi(\vec{r}) = \frac{8\pi^2 me}{h^2}\Phi(\vec{r})\,\Psi(\vec{r}) \tag{2.32}$$

where m is the relativistic electron mass, e is the elementary charge, h is the Planck's constant, E is the kinetic energy of the electron and $\Phi(\vec{r})$ is the Coulomb potential of the atom [77]. This inhomogeneous differential equation can be solved by the addition of its general homogeneous solution $\Psi_0(\vec{r})$ ($\Phi(\vec{r}) = 0$) and a special inhomogeneous solution $\Psi_S(\vec{r})$. The homogeneous differential equation is solved by a plain incidence electron wave described by

$$\Psi_0(\vec{r}) = \exp\left(-2\pi i\vec{k_0}\vec{r}\right) \tag{2.33}$$

with $\vec{k_0}$ being the wave vector of the incident wave [77]. With the abbreviation $k' = \frac{\sqrt{2meE}}{h}$ and the help of a Green's function

$$G(\vec{r} - \vec{r}') = \frac{1}{4\pi}\frac{\exp(-2\pi i k'|\vec{r} - \vec{r}'|)}{|\vec{r} - \vec{r}'|} \tag{2.34}$$

a special solution of the inhomogeneous differential equation is given by

$$\Psi_S(\vec{r}) = \int_{\Omega} \frac{8\pi^2 me}{h^2} G(\vec{r}-\vec{r}\,')\,\Phi(\vec{r}\,')\,\Psi(\vec{r}\,')\,d^3\vec{r}\,' \tag{2.35}$$

where Ω is the scattering volume [77]. Inserting equation (2.34) gives the special solution as

$$\Psi_S(\vec{r}) = \frac{2\pi me}{h^2} \int_{\Omega} \frac{\exp(-2\pi i k'|\vec{r}-\vec{r}\,'|)}{|\vec{r}-\vec{r}\,'|} \Phi(\vec{r}\,')\,\Psi(\vec{r}\,')\,d^3\vec{r}\,'. \tag{2.36}$$

According to the assumption of single scattering the wave function $\Psi(\vec{r}\,')$ can be replaced by the initial incident plain wave function $\Psi_0(\vec{r}\,')$. In the following, we consider that $|\vec{r}\,'| \lll |\vec{r}|$, meaning the observation point is very far away from the scattering atom so that $\vec{r}-\vec{r}\,'$, $\vec{k}\,'$ and $\vec{r}$ are parallel (see figure 2.13). In this case

$$|\vec{r}-\vec{r}\,'| = r - \frac{\vec{r}\,'\cdot\vec{k}\,'}{k'} \tag{2.37}$$

is a valid approximation, which leads to

$$\Psi_S(\vec{r}) = \frac{\exp(-2\pi i k' r)}{r} \cdot \frac{2\pi me}{h^2} \int_{\Omega} \exp\left(-2\pi i\left(\vec{k_0}-\vec{k}\,'\right)\vec{r}\,'\right) \Phi(\vec{r}\,')\,d^3\vec{r}\,'. \tag{2.38}$$

The term $\vec{k_0}-\vec{k}\,'$ is defined as scattering vector $\vec{K}$, which is related to the scattering angle θ by $K = \frac{2}{\lambda}\sin\left(\frac{\theta}{2}\right)$ with the relativistic de Broglie wavelength λ. Additionally, the term

$$\frac{2\pi me}{h^2} \int_{\Omega} \exp\left(-2\pi i \vec{K}\vec{r}\,'\right) \Phi(\vec{r}\,')\,d^3\vec{r}\,' = f\left(\vec{K}\right) \tag{2.39}$$

is defined as the atomic scattering factor. Equation (2.39) reveals, that $f\left(\vec{K}\right)$ is proportional to the Fourier transform of the Coulomb potential $\Phi(\vec{r})$ and therefore a measure for the scattering amplitude. Furthermore, $f\left(\vec{K}\right)$ strongly depends on the scattering atom species since it depends on the atom's Coulomb potential. Values for the atomic scattering factors are provided by Doyle and Turner [78]. They parameterized $f\left(\vec{K}\right)$ as a linear combination of Gaussians, which fits very well for small scattering angles. Weickenmeier and Kohl provided values for higher scattering angles [79]. A parameterized description by a linear combination of Gaussians and Lorenzians can be found in Kirkland's book

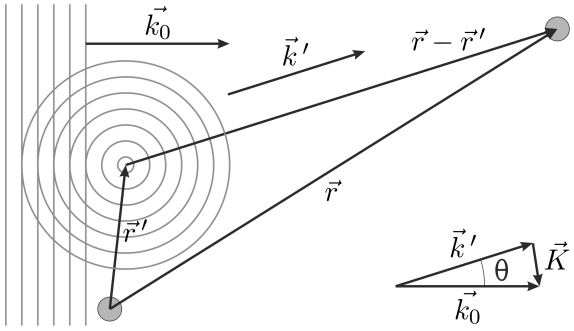

Figure 2.13: Incident plane wave scattered by a single scatter center acting as a spherical wavelet source.

[80]. Lorenzians describe the behavior correctly at high scattering angles, whereas the Gaussians empirically fit the behavior at low angles. Finally, the solution of equation (2.32) is given by the overall wave function

$$\Psi\left(\vec{r},\vec{K}\right) = \exp\left(-2\pi i\vec{k_0}\vec{r}\right) + \frac{\exp\left(-2\pi k\,'r\right)}{r} f\left(\vec{K}\right) \tag{2.40}$$

which is a superposition of the incident plane wave and a spherical wave with amplitude $f\left(\vec{K}\right)$ as illustrated in figure 2.13. This model can be extended from a single atom as a scattering center to a periodic lattice of unit cells. The position of the jth base atom in a unit cell can be described by the vector $\vec{r_j}$. The position of the kth unit cell is indicated by the lattice vector $\vec{R_k}$ (see equation 2.2). By use of these vectors, every atom in the lattice can be described. Summing over all unit cells and base atoms generates the whole lattice, and its potential distribution can be described. This is illustrated in figure 2.14. Each base

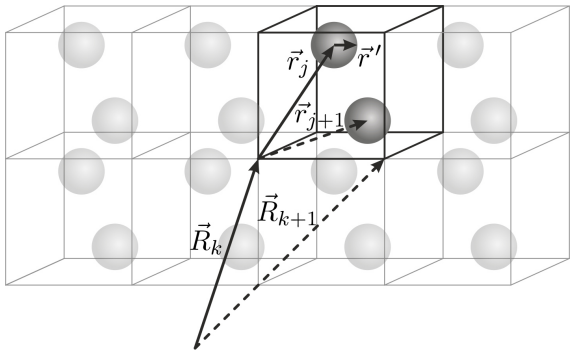

Figure 2.14: Coordinates of unit cells and their atoms. The kth unit cell is highlighted

atom has its atomic scattering factor $f_j\left(\vec{K}\right)$ based on the atomic number. Substituting the single atom in equation (2.38) by the sum over all atoms in the lattice leads to the superposition of all scattered waves at the atom positions

$$\begin{aligned}\Psi_S\left(\vec{r},\vec{K}\right) =& \frac{\exp\left(-2\pi i k' r\right)}{r} \cdot \frac{2\pi m e}{h^2} \\ & \cdot \sum_k \sum_j \int_\Omega \exp\left(-2\pi i \vec{K}\left(\vec{r}\,' + \vec{r_j} + \vec{R_k}\right)\right) \Phi\left(\vec{r}\,'\right) d^3 r\,'.\end{aligned} \tag{2.41}$$

This equation can be written as

$$\Psi_S\left(\vec{r},\vec{K}\right) = \frac{\exp\left(-2\pi i k' r\right)}{r} \cdot F_S\left(\vec{K}\right) \cdot G\left(\vec{K}\right) \tag{2.42}$$

with the structure amplitude (or structure factor)

$$F_S\left(\vec{K}\right) = \sum_j f_j\left(\vec{K}\right) \exp\left(-2\pi i \vec{K} \vec{r_j}\right) \tag{2.43}$$

and the lattice amplitude (or shape factor)

$$G\left(\vec{K}\right) = \sum_k \exp\left(-2\pi i \vec{K} \vec{R_k}\right). \tag{2.44}$$

The structure amplitude $F_S\left(\vec{K}\right)$ can again be regarded as the Fourier transform of all scattering factor distributions $f_j\left(\vec{K}\right)$. Since TEM samples have a finite thickness, it is necessary to include the spatial extent of the sample in the scattered wave function. Waves that originate from different points of the sample have different path lengths and therefore different phases when they meet at the observation point. This can be taken into account by Fresnel's zone construction method [81]. For a thin foil specimen of thickness t, one obtains

$$\Psi_S\left(\vec{K}\right) = i\lambda t \frac{F_S\left(\vec{K}\right) G\left(\vec{K}\right)}{V_{unit\,cell}} \exp\left(-2\pi i \vec{k_0} \vec{d}\right), \tag{2.45}$$

where $V_{unit\,cell}$ is the unit cell volume and $\vec{d}$ is the vector normal to the specimen surface, whose length corresponds to the distance between the specimen surface and the observation point.

The diffraction pattern originates from the interference of the diffracted waves emanating

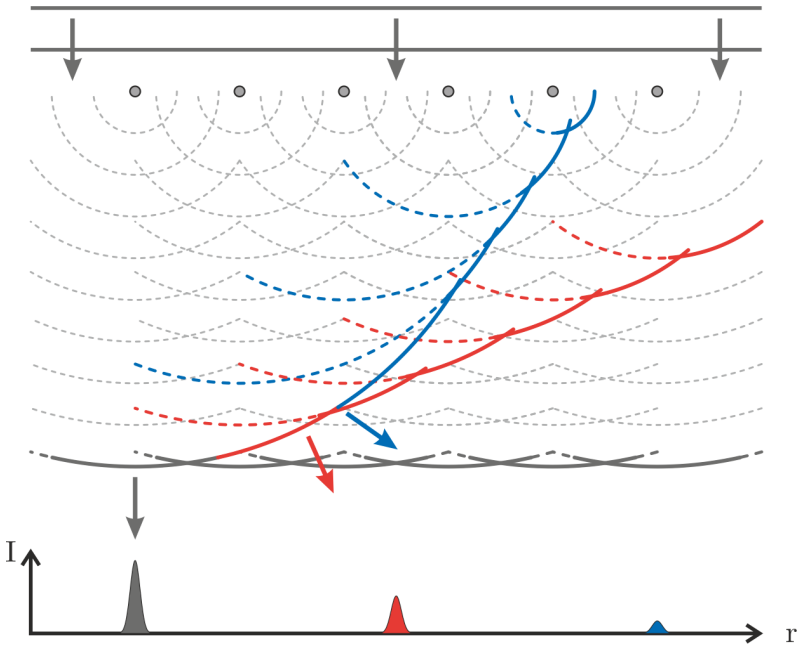

Figure 2.15: Diffracted waves interfering with each other and form diffraction peaks of different orders in the diffraction pattern. The incident and undiffracted beams are shown in gray. The first and second order are shown in red and blue, respectively (adapted from [76]).

from the periodically arranged unit cells, shown schematically in figure 2.15. The lattice amplitude $G\left(\vec{K}\right)$ from equation (2.44) becomes a sum of delta functions at positions satisfying

$$\vec{K} \cdot \vec{R} = n \qquad n \in \mathbb{N}, \tag{2.46}$$

where $\vec{K}$ is a reciprocal lattice vector $\vec{g}_{hkl}$ (see equation (2.5)) with Miller indices h, k and l. This relation is called the Laue condition for constructive interference. Vector $\vec{R}$ is a lattice vector (equation 2.2) and together with the relation from equation (2.3)

$$\left(h\vec{b_1} + k\vec{b_2} + l\vec{b_3}\right) \cdot \left(u\vec{a_1} + v\vec{a_2} + w\vec{a_3}\right) = uh + vk + wl, \tag{2.47}$$

is obtained, which proves that equation (2.46) is fulfilled for $\vec{K} = \vec{g}_{hkl}$. Thus, only distinct scattering vectors will result in diffraction spots. This can be illustrated by the construction of the so-called Ewald sphere [82] depicted in figure 2.16. The incident wave vector $\vec{k_0}$ points from P towards the origin of the reciprocal lattice O. All possible diffracted wave

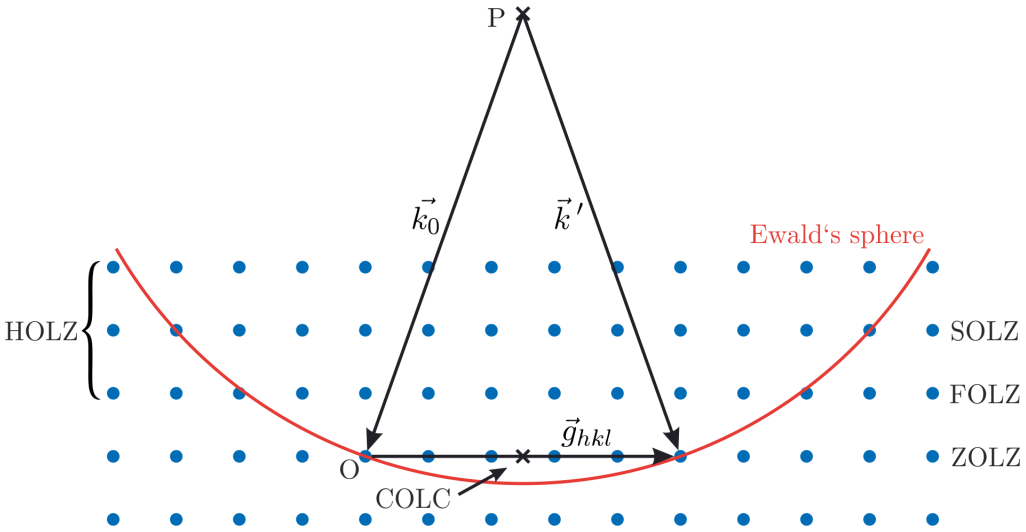

Figure 2.16: Ewald's sphere construction illustrating the constructive interference condition. The blue dots indicate the reciprocal lattice. The surface of all possible scattering directions of $\vec{k}'$ builds Ewald's sphere marked in red.

vectors $\vec{k}'$ create a sphere with radius $\left|\vec{k_0}\right| = \left|\vec{k}'\right| = 1/\lambda$ and center point P. Reciprocal lattice points intersecting the sphere fulfill the condition for constructive interference (equation (2.46)). The reciprocal lattice plane of the origin is called the zero-order Laue zone (ZOLZ), and the two above are called the first and second-order Laue zone (FOLZ and SOLZ). All orders of Laue zones above the zero order are referred to as higher-order Laue zones (HOLZ). The intersections of Ewald's sphere with every Laue zone result in ring-like diffraction patterns called Laue circles. These share a central point called the center of Laue circles (COLC), which is a measure of the incident angle of the electron beam relative to the lattice planes. The observed intensity I of the peaks with Miller indices hkl correspond to the absolute square of the wave function Ψ_S, which is proportional to the absolute square of the structure amplitude and depends therefore on the scattering vector

$$I\left(\vec{g}_{hkl}\right) = \left|\Psi_S\left(\vec{g}_{hkl}\right)\right|^2 \propto \left|F_S\left(\vec{g}_{hkl}\right)\right|^2 . \tag{2.48}$$

So far, a lattice of infinite extent has been considered. In reality, the observed specimen has a finite size and is especially thin in one dimension to enable electrons to transmit. This affects the reciprocal lattice by elongating the lattice points in that dimension forming

reciprocal lattice rods (relrods). This weakens the Laue condition, which is not only fulfilled for $\vec{K} = \vec{g}_{hkl}$ anymore, but

$$\vec{K} = \vec{g}_{hkl} + \vec{s}, \tag{2.49}$$

where $\vec{s}$ describes the excitation error from Laue conditions. Inserting this equation into equation (2.43) yields

$$F_S\left(\vec{g}_{hkl} + \vec{s}\right) = F_S\left(\vec{g}_{hkl}\right) \sum_u \sum_v \sum_w \exp\left(-2\pi i \left(u a_1 s_1 + v a_2 s_2 + w a_3 s_3\right)\right). \tag{2.50}$$

The sums can be replaced by an integration over the crystal volume $V_{crystal}$ deriving

$$F_S\left(\vec{g}_{hkl} + \vec{s}\right) = \frac{F_S\left(\vec{g}_{hkl}\right)}{V_{unit\,cell}} \int\limits_{V_{crystal}} \exp\left(-2\pi i \vec{s}\vec{r}\right) d^3r. \tag{2.51}$$

For an cuboid shaped sample with side lengths L_1, L_2 and L_3 the equation

$$\begin{aligned} F_S\left(\vec{g}_{hkl} + \vec{s}\right) &= \frac{F_S\left(\vec{g}_{hkl}\right)}{a_1 a_2 a_3} \int_0^{L_1} \int_0^{L_2} \int_0^{L_3} \exp\left(-2\pi i \left(r_1 s_1 + r_2 s_2 + r_3 s_3\right)\right) d^3r \\ &= \prod_{j=1}^{3} \exp\left(-\pi i s_j L_j\right) \frac{\sin\left(\pi s_j L_j\right)}{\pi s_j a_j} \end{aligned} \tag{2.52}$$

is obtained. Considering again a thin foil specimen, where one dimension of the sample is very narrow, which allows the approximation of length $L_1, L_2 \to \infty$ and $L_3 \to 0$, leading to

$$F_S\left(\vec{g}_{hkl} + \vec{s}\right) = L_1 L_2 \delta\left(s_1\right) \delta\left(s_2\right) \exp\left(-2\pi i s_3 t\right) \frac{\sin\left(\pi s_3 t\right)}{\pi s_3}. \tag{2.53}$$

The intensity of a peak with Miller indices hkl follows from equations (2.45), (2.48) and (2.53) as

$$I_{\vec{g}_{hkl}}\left(s_3\right) = I_0 \left(\frac{\lambda F\left(\vec{g}_{hkl}\right)}{\pi V_{unit\,cell}}\right)^2 \frac{\sin^2\left(\pi s_3 t\right)}{s_3^2} = I_0 \frac{\sin^2\left(\pi s_3 t\right)}{\xi_{\vec{g}_{hkl}}^2 s_3^2}. \tag{2.54}$$

Whereat I_0 is the initial intensity and

$$\xi_{\vec{g}_{hkl}} = \frac{\pi V_{unit\,cell}}{\lambda F\left(\vec{g}_{hkl}\right)} \tag{2.55}$$

the extinction distance. This means that the intensity of the diffracted beam varies sinusoidally with sample thickness t.

2.4.2 Image Formation and Phase Contrast

Up to this point, the influence of our specimen on the incident electron wave function was described, which got modulated by the Coulomb potential. To understand the image formation in TEM, the wave function emanating from the object's exit surface will be followed until it forms the image.
The sample is located at a distance matching the focal length f of the objective lens. The exit electron wave function $\Psi\left(\vec{r}\right)$ propagates towards the objective lens. The spatial vector $\vec{r}$ is now assumed to be two-dimensional and perpendicular to the electron beam direction (or optical axis). The objective lens generates the diffraction pattern in the back focal plane, which can be described by the Fourier transform of the electron wave $\mathcal{F}\left[\Psi\left(\vec{r}\right)\right]$. Further propagation from the back focal plane to the image plane corresponds to an inverse Fourier transform. For an ideal microscope, which does not possess any aberrations or imperfections, the image intensity is given by the intensity of the wave function at the object exit surface $\left|\mathcal{F}^{-1}\{\mathcal{F}\left[\Psi\left(\vec{r}\right)\right]\}\right|^2 = \left|\Psi\left(\vec{r}\right)\right|^2$ [77]. In reality, every lens induces distortions in the electron wave, which further compounds in the microscopes following lenses. The induced error strongly decreases with reducing the angle of incidence, which is inversely proportional to the magnification. Therefore the angle is reduced after every magnification step, and so is the induced imaging error. Due to this, it is sufficient to consider the aberrations of the objective lens only. These are characterized by an error function $C\left(\vec{k}\right)$ describing the distortion of the wave function, which is mainly caused by spherical aberration and defocus. The observed image intensity $I\left(\vec{r}\right)$ is then given by [77]

$$I\left(\vec{r}\right) = \mathcal{F}^{-1}\{C\left(\vec{k}\right)\mathcal{F}\left[\Psi\left(\vec{r}\right)\right]\}. \tag{2.56}$$

The way this intensity can be interpreted and which parameters will influence it depends on the imaging mode and imaging conditions and will be discussed in chapter 3.2.
In the low-angle regime, where the Bragg scattering dominates, the exit electron wave functions are scattered coherently at the crystal lattice. These waves interfere with each

other, resulting in an intensity modulation. The resulting contrast is called phase contrast. This phenomenon can be explained by describing the diffracted beams as plane waves. For simplicity, only two beams are considered to form the image for now, the direct beam ($\vec{g} = \vec{0}$) and a diffracted beam ($\vec{g} \neq \vec{0}$), in the two beam approximation. Then, the electron wave function is the superposition of these two plain waves

$$\psi(\vec{r}) = I_{\vec{0}} \exp\left(2\pi i \left(\vec{k_0}\vec{r}\right)\right) + I_{\vec{g}} \exp\left(2\pi i \left(\vec{k}'\vec{r}\right)\right). \tag{2.57}$$

$I_{\vec{0}}$ and $I_{\vec{g}}$ are the intensities for a diffracted beam according to equation (2.54), depending on s_3. We can substitute $\vec{k}' = \vec{k_0} + \vec{g} + \vec{s}$ (equation (2.49)) and simplify the equation according to the Howie-Whelan equations [76] by writing A for $I_{\vec{0}}$ and express $I_{\vec{g}}$ as

$$I_{\vec{g}} = B \exp(i\delta), \tag{2.58}$$

where

$$B = \frac{\pi}{\xi_{\vec{g}}} \frac{\sin(\pi t s)}{\pi s} \qquad \text{and} \qquad \delta = \frac{\pi}{2} - \pi t s \tag{2.59}$$

while again approximating the sample to be very thin and deriving the wave function

$$\Psi(\vec{r}) = \exp\left(2\pi i \left(\vec{k_0}\vec{r}\right)\right) \left[A + B \exp\left(2\pi i \left(\vec{g} + \vec{s}\right)\vec{r} + i\delta\right)\right]. \tag{2.60}$$

The intensity can be expressed as the absolute square of the wave function

$$\begin{aligned} I(\vec{r}) &= |\Psi(\vec{r})|^2 \\ &= A^2 + B^2 + AB\left[\exp\left(2\pi i \left(\vec{g} + \vec{s}\right)\vec{r} + i\delta\right) + \exp\left(-2\pi i \left(\vec{g} + \vec{s}\right) - i\delta\right)\right] \\ &= A^2 + B^2 + 2AB\cos\left(2\pi \vec{g}'\vec{r} + \delta\right) \end{aligned} \tag{2.61}$$

with use of $\vec{g}' = \vec{g} + \vec{s}$. This vector is effectively perpendicular to the beam and defined to be parallel to the x-direction. With substitution of δ following equation (2.59) we get

$$I(\vec{r}) = A^2 + B^2 - 2AB\sin\left(2\pi g' x - \pi s t\right). \tag{2.62}$$

The interference of the two beams leads to sinusoidal intensity oscillations along the corresponding vector $\vec{g}'$ and a phase shift depending on s and t. The resulting fringes can, with care, be related to the lattice spacing of the lattice planes corresponding to $\vec{g}'$. The

phase dependency on s and t leads to a delocalization of the lattice planes. So the real planes do not necessarily have the same positions as the lattice fringes. However, they do have the same orientation and spacing. Including more beams in this description will lead to more lattice fringes with other directions, which results in the generation of the crystal lattice in the image, if enough beams are included [76].

2.4.3 Rutherford Scattering

Contrast in HAADF images is not related to electron diffraction or phase relationships of the electrons. Here high scattering angles starting at around 50 mrad (≈3°) are considered. Scattering takes place predominantly through thermal diffuse scattering (TDS) [83] at the Coulomb potential of the nuclei, which does not maintain the electrons phase. To describe this phenomenon, the electrons are considered as charged particles rather than waves. For this description, one can apply Rutherford's scattering equation, which he derived by observing α-particles scattering at a thin gold foil [84]. However, this is only an approximation, but it allows a qualitative understanding of the scattering process. Rutherford calculated the scattering cross section $\frac{d\sigma_R(\theta)}{d\Omega}$ for charged particles at a thin foil

$$\frac{d\sigma_R(\theta)}{d\Omega} = \frac{e^4 Z^2}{16\left(4\pi\varepsilon_0 E_{kin}\right)^2} \frac{1}{\sin^4\left(\frac{\theta}{2}\right)}, \tag{2.63}$$

where e is the elementary charge, Z the atomic number of the target atom, ε_0 the dielectric constant and E_{kin} the particles kinetic energy [85]. The scattering cross-section describes the probability that a particle is deflected by an angle θ into the solid angle element $d\Omega$. It is related to the atomic scattering factors $f\left(\vec{K}\right)$ (equation (2.39)) through the relation [86]

$$\frac{d\sigma_R(\theta)}{d\Omega} \propto f\left(\vec{K}\right)^2. \tag{2.64}$$

To apply equation (2.63) to electron scattering, considerations of screening and relativistic effects are necessary. The screening potential is considered by a screening function $q(\theta)$ [87]

$$\frac{d\sigma_R(\theta)}{d\Omega} q(\theta) = \frac{d\sigma_R(\theta)}{d\Omega} \frac{\sin^4\left(\frac{\theta}{2}\right)}{\left(\sin^2\left(\frac{\theta}{2}\right) + \frac{\theta_0^2}{4}\right)^2}, \tag{2.65}$$

with the Born screening angle [88]

$$\theta_0 = \frac{1.13 Z^{\frac{1}{3}}}{137\beta}. \tag{2.66}$$

Here, β is the fraction of the electron velocity and the speed of light. Together with the relativistic description of the electron wavelength, the scattering cross-section results in

$$\frac{d\sigma_R(\theta)}{d\Omega} = \frac{Z^2\lambda^4}{64\pi^4 a_0^2} \frac{1}{\left(\sin^2\left(\frac{\theta}{2}\right) + \frac{\theta_0^2}{4}\right)^2}, \tag{2.67}$$

where λ represents the relativistic electron wavelength and a_0 the Bohr radius. This scattering equation fits qualitatively well with experimental data. It explains the contrast in HAADF images, which scales roughly with the square of the atomic number Z^2 (see chapter 3.2.4 for more detail). Therefore, HAADF images obtain a Z-contrast and thus, carry chemical information about the sample. However, empirically adjusted scattering factors are used for quantitative evaluations, which can be found in literature [78–80].

2.4.4 Inelastic Scattering

Contrary to the previously mentioned processes, inelastic interaction, where incident electrons transfer energy to the matter, also takes place. These processes give rise to signals, which can be utilized to get information on the specimen. These signals especially carry chemical information.

Energy may be transferred to an electron of an atom of the sample. Electrons have discrete energy levels in an atom characteristic for each element, mirrored in the energy loss of the incident electrons. Electron energy loss spectroscopy analyzes these energies appearing as edges or peaks in recorded energy spectra, revealing, for example, the sample's chemical

composition or bonding configurations.
Inelastic processes also induce the emission of other signals (see figure 2.12). Electrons of an inner atomic shell can get ejected and escape the attractive field of the nucleus. From isolated atoms or atoms close to the surface, they can leave the sample as secondary electrons. In solids, they may escape into an unfilled state above the Fermi level. A vacancy is formed in an inner shell, and the atom remains in an excited ionized state. The atom can return to a state closer to its ground state by an electron transition from a higher energy level into the vacancy. The energy difference between the two energy states will be emitted as an X-ray photon. This energy depends on the energy level of the vacancy and the relaxing electron. Both are characteristic of an element. For hydrogen-like atoms with a single valence electron, the energy of a state E_n with principal quantum number n is given by

$$E_n = -hc_0 R_\infty \frac{Z^2}{n^2}, \tag{2.68}$$

where h is the Planck constant, c_0 is the speed of light, R_∞ is the Rydberg constant and Z is the atomic number. However, this equation fails for non-hydrogen-like atoms where electron-electron interactions raise the energy levels, and the outer electrons experience a shielded nucleus potential. Additionally, relativistic effects and spin-orbit interaction become relevant. To take this into account, an effective atomic number for each electron $Z_{eff} = Z - S(n,l)$ is introduced, with a shielding parameter $S(n,l)$ depending on the principal quantum number n and azimuthal quantum number l [89]. Values for S can be found, for example, in references [90] and [91]. The energy difference ΔE for a given transition $1 \rightarrow 2$ can be derived by

$$\Delta E = -hc_0 R_\infty \left(\frac{Z_{eff,1}^2}{n_1^2} - \frac{Z_{eff,2}^2}{n_2^2} \right). \tag{2.69}$$

There exist several possible energy differences since there may be multiple higher shells, which themselves contain different subshells.
The electron interaction with the sample's Coulomb potential also modifies the electron's velocity and momentum. Since accelerated charges emit radiation, a continuous spectrum called bremsstrahlung is generated with energies up to the X-ray regime. It overlaps with the characteristic X-rays, but due to the conservation of momentum, it is mainly emitted in the forward direction.
The electron transition to fill a vacancy can additionally lead to the escape of electrons if

the energy is transferred to an outer shell electron and its energy exceeds the binding energy. Electrons emitted this way are called Auger electrons. Similarly to the characteristic X-rays, they are unique for every element.

CHAPTER 3

Methods

This chapter introduces the experimental methods that are applied in this work. In the beginning, processes capable of crystal growth are explained, namely the metal organic vapor phase epitaxy (MOVPE) and the vapor liquid solid (VLS) growth mechanism. MOVPE represents the method of particular interest in this work since *in-situ* TEM is getting implemented to generate new insights into this field by live observation of crystal growth. It is followed by transmission electron microscopy (TEM), widely used in this thesis for characterization and observation. The construction, operating modes, and different analytical methods of a microscope are described. These sections are followed by a description of scanning electron microscopy (SEM) and focused ion beam (FIB) used for structural analysis and sample preparation. Finally, a report on *in-situ* TEM is given. The utilized closed gas cell setup is characterized, and its experimental scope and handling are discussed.

3.1 Crystal Growth

There are various methods capable of crystal growth. The one treated in the following section is MOVPE. It represents a special case of metal organic chemical vapor deposition (MOCVD), where a gaseous precursor is used to deposit layers on a substrate. In MOVPE, this deposition proceeds with an epitaxial relationship. Epitaxial means that the deposited layers continue the crystalline structure of the substrate. It stems from the ancient Greek words *ἐπί* (*epi*) "above" and *τάξις* (*taxis*) "an ordered manner". Additionally, a special growth method in MOVPE is discussed, which is the VLS growth. It uses metal catalyst

particles to spatially control the deposition and restrict them to the catalyst position, resulting in crystalline wire's growth.

3.1.1 Metal Organic Vapor Phase Epitaxy

The MOVPE is the most commonly utilized growth technique in fabricating high-quality semiconductor materials in the industry. This is due to its high versatility, upscaling capability and throughput, which is not given for molecular beam epitaxy (MBE), for example, [47]. The technique was first introduced in the late 1960s by Manasevit and Simpson [92]. They sought a way to deposit optoelectronic semiconductor materials on various non-lattice-matched substrates, such as GaAs on sapphire. Further developments in the following decades enabled high-performance materials with very low defect densities making MOVPE competitive with other epitaxial techniques. Even though it is widely used with great success nowadays, due to its complexity, it is still an object of research with many questions still needing to be answered.
The usually liquid precursors containing the atomic species used in the growth are stored in so-called bubblers. These are stainless steel containers through which the carrier gas, commonly hydrogen or nitrogen, is conducted and supersaturated with the precursor molecules. It is further conducted in the reactor, where the precursor gases get mixed at a defined partial pressure and form a laminar gas flow across the heated substrate. Due to a concentration gradient between the gas phase and solid, the precursor molecules diffuse towards the substrate. The interaction with the substrate surface decreases their velocity at the surface. In the boundary layer between the gas phase and substrate, the molecules can thermally decompose, diffuse and adsorb on available surface sites. The desired atom diffuses across the surface and incorporates into the crystal at an energetically favorable lattice site. The organic residuals of the molecules desorb and are carried away by the gas flow. The individual decomposition pathways are still under discussion, even for the intensively studied precursor molecules. The temperature, flow rate and partial pressures of the single vapor species are controlled as crucial parameters determining the crystal growth. A scheme of the fundamental reaction steps during the MOVPE process can be seen in figure 3.1.
The favored lattice site is dependent on the surface energies of the substrate σ_0, epitaxial layer σ^s and their interface σ^{int}. They are determined by the material properties and growth conditions. The system strives to minimize the total surface energy, which can lead to three different growth modes illustrated in figure 3.2 [93]. The crystal will grow layer

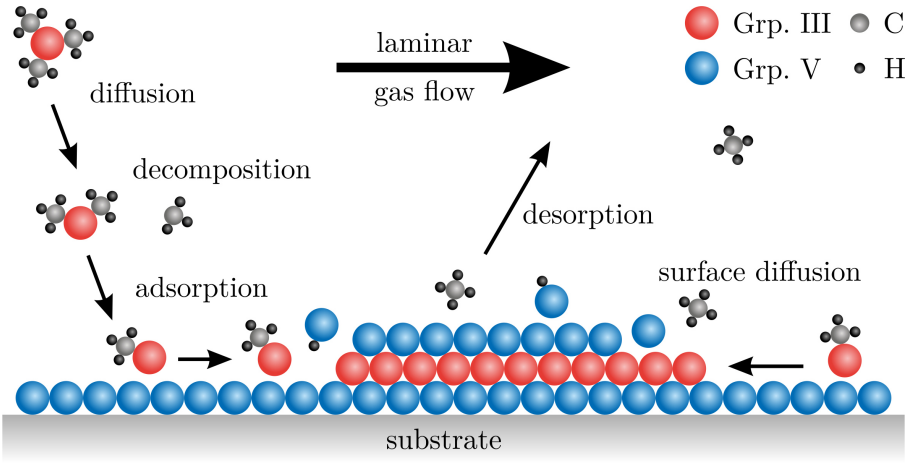

Figure 3.1: Sketch of relevant processes in MOVPE. Precursor molecules diffuse towards the surface, decompose and atoms of the carried growth species adsorb. By surface diffusion, they take a favored lattice site. Organic rest groups desorb from the surface.

by layer if the surface energy of the substrate is higher than the ones of the epitaxial layer and the interface ($\sigma_0 \geq \sigma^s + \sigma^{int}$). The atoms will first adsorb at the substrate forming a closed monolayer, followed by the next layers. This is called the Frank-van-der-Merwe growth (figure 3.2 a)) [94–96]. If, in contrast, the substrate's surface energy is lower ($\sigma_0 \leq \sigma^s + \sigma^{int}$), the atoms will first nucleate at the substrate. The nucleated surface is more favorable for adsorption than the uncovered substrate. Hence, islands will form, separated by the uncovered substrate. This mode is known as Volmer-Weber growth (figure 3.2 b)) [97]. A combination of these two modes is described by the Stranski-Krastanov growth. In this case, the surface energy of the substrate is similar to the ones of the epilayer and interface ($\sigma_0 \approx \sigma^s + \sigma^{int}$). Initially, the conditions are comparable to the Frank-van-der-Merwe growth leading to complete layers covering the substrate. At a critical layer thickness, the nucleation of islands comparable to the Volmer-Weber growth is favored. In the end, islands are formed on top of a closed layer covering the substrate (figure 3.2 c))

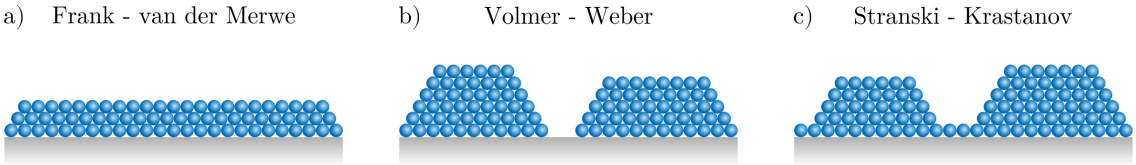

Figure 3.2: Schematic illustration of a) Franck - van der Merwe, b) Volmer - Weber and c) Stranski - Krastanov growth mode (adapted from [98]).

[99]. In general, III/V semiconductors' growth process occurs at elevated temperatures in a non-equilibrium growth regime. The partial pressures in the gas phase are higher than the corresponding equilibrium partial pressures. Furthermore, the vapor pressure of the group V compound is higher than that of the group III compound. This leads to incongruent evaporation of group V atoms. An excess of group V precursor molecules is provided to compensate for this effect to enable the adsorption rate to exceed the desorption rate. The group III flux under these conditions determines the overall growth rate. Different temperature regimes exist, where individual reaction steps limit the growth rate [100]. The regimes are depicted in figure 3.3, where the growth rate is plotted versus the reciprocal substrate temperature. It becomes clear that substrate temperature is an

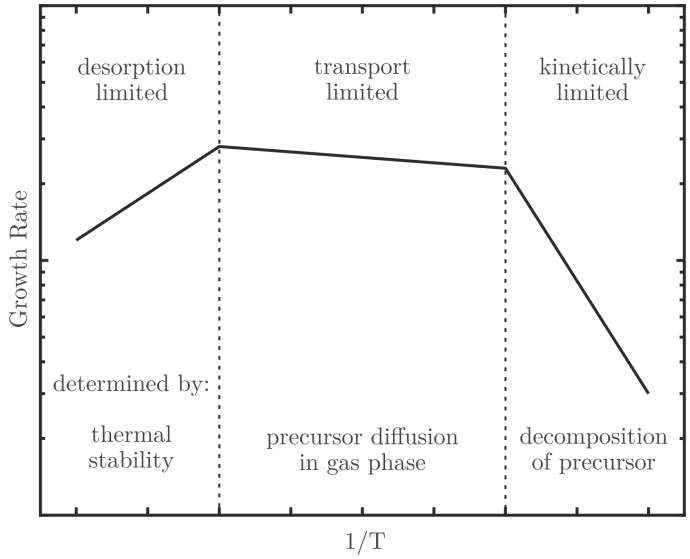

Figure 3.3: Growth rate vs. reciprocal temperature. Different regimes separated by dashed lines (adapted from [101])

essential parameter for the growth process. At low temperatures, the growth is kinetically limited, which means, that the precursor molecules are not efficiently decomposed. As a result, they cannot adsorb at the substrate surface. When the temperature exceeds the precursor's decomposition temperature, the growth rate is nearly independent of the temperature. Partially decomposed molecules adsorb on the substrate, and the growth rate is limited by the diffusion towards the surface, which is referred to as mass transport limited regime. A further temperature increase will, at some point, lead to an exponential decrease in growth rate caused by the material's thermal instability. The high thermal

energy increases the vapor pressure of the material, which increases the desorption rate. Thus, the growth is desorption limited.

3.1.2 Precursor Sources

Several precursors are available for the growth of the investigated material system of gallium phosphide. The ones used in the presented work are trimethyl gallium (TMGa) and tertiary butyl phosphine (TBP), which will be characterized in the following section. The choice of a precursor molecule is determined by its physical properties, especially in terms of its vapor pressure, decomposition temperature and stability [52]. The vapor pressure in MOVPE machines can be controlled to some extent by the bubbler's temperature and need to be considered for the adjustment of the desired partial pressure. Already small vapor pressures in the range of 1 hPa are suitable since the precursor molecules saturate the carrier gas already within the bubbler. In the setup used in this work, the carrier gas can not be conducted into the bubbler. Instead, the vapor phase above the liquid acts as the source of precursor molecules. Because of this, precursors with an appropriate vapor pressure well above 10^2 hPa are beneficial for usage. Moreover, it is not possible to heat the bubblers, so this vapor pressure needs to be available at room temperature. According to the Clausius-Clapeyron equation, the temperature dependence of the static vapor pressure p_v can be described by an exponential relationship

$$p_v = \exp\left(-\frac{\Delta G}{RT}\right) \tag{3.1}$$

with the change in Gibbs free energy on evaporation ΔG, the gas constant R and temperature T [101]. Via the heat of evaporation ΔH and the entropy for evaporation ΔS, the Gibbs free energy can be expressed as $\Delta G = \Delta H - T\Delta S$. This leads to the equation

$$\log\left(p_v\right) = A - \frac{B}{T} \tag{3.2}$$

where the constants are given by $A = \frac{\Delta S}{R}$ and $B = \frac{\Delta H}{R}$. Values for A and B can be found for numerous precursor molecules, for example, in reference [47]. The temperature dependence of static vapor pressure is plotted in figure 3.4 for gallium precursors on the left-hand side and phosphorus precursors on the right-hand side. The room temperature regime is highlighted in gray. As a general rule of thumb, the vapor pressure is higher for lighter molecules. In the case of gallium precursors, triethylgallium (TEGa) and TMGa

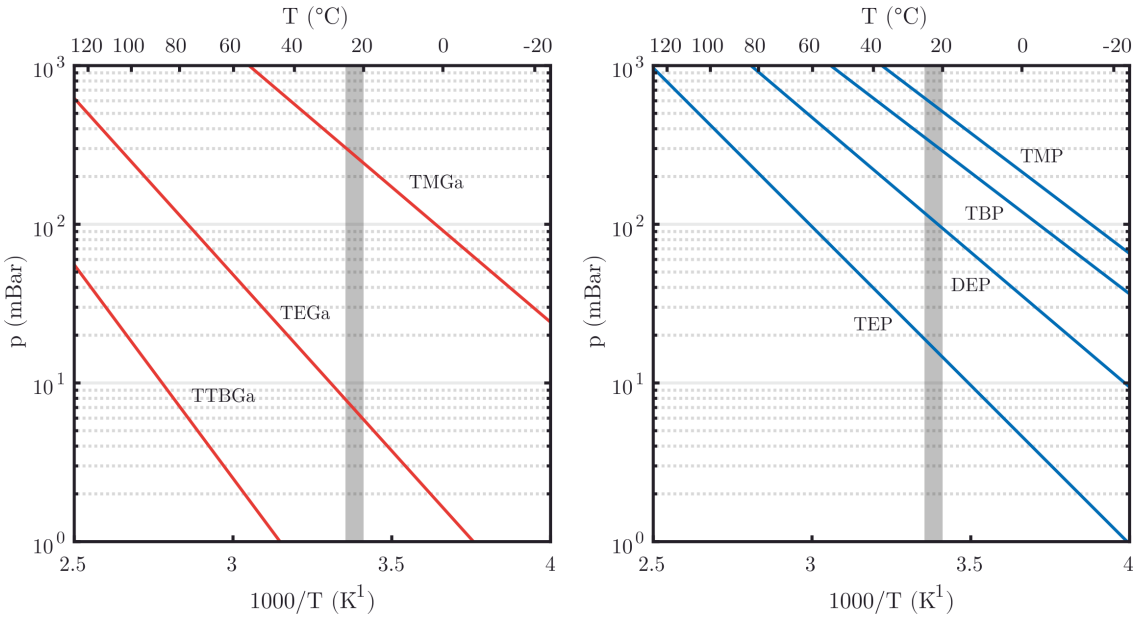

Figure 3.4: Left: Gallium precursor vapor pressures versus reciprocal temperature. Right: Phosphorus precursor vapor pressures versus reciprocal temperature. The room temperature (20 K to 25 K) is highlighted in gray (values for constants A and B taken from [47]).

have been established with great success [102]. The advantage in the use of TMGa is its higher vapor pressure of 266 hPa in comparison to 6.6 hPa for TEGa at a temperature of 22 °C (compare figure 3.4). Additionally, it exhibits a comparatively low pyrolysis temperature, defined as the temperature where 50 % of the molecule is pyrolyzed, of 430 °C in H_2 and 520 °C in N_2 [103, 104]. Furthermore, it shows excellent stability enabling storage over indefinite periods. As a group III element, Gallium has two s and one p valence electrons. In the TMGa molecule, it forms three covalent bonds with the three methyl groups with a sp^2 hybridized bonding configuration. This leads to a planar molecule with methyl ligands separated by an angle of 120° as illustrated in figure 3.5.

The phosphorus source used for the growth of gallium phosphide is TBP, whose structure is illustrated in figure 3.5. It has a vapor pressure of 314 hPa at 22 °C. In figure 3.4 can be seen that there are additional precursors like diethyl phosphine (DEP) or trimethyl phosphine (TMP) with reasonable vapor pressures at room temperature available. However, methyl and ethyl phosphorus sources are uninteresting for MOVPE since they pyrolyze slowly, and no phosphorus incorporation occurs at ordinary growth temperatures [47]. Also, phosphine (PH_3) can be used as a phosphorus source, which is gaseous under ambient conditions. It is the common phosphorus source implemented in industry. By breaking the

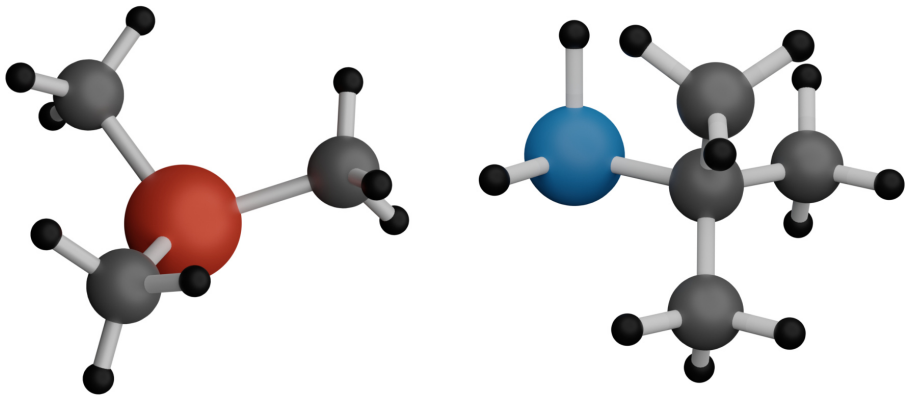

Figure 3.5: Rendering of TMGa (left) and TBP molecules (right). Gallium, phosphorus, carbon and hydrogen are illustrated in red, blue, gray and black, respectively.

phosphorus-hydrogen bonds, radicals are formed, which can adsorb at the growth surface. However, PH_3 has a very high pyrolysis temperature of around 850 °C [105], whereas the one of TBP is only 450 °C [106]. By pyrolysis, TBP tends to lose the tert-butyl group and form phosphine radicals at much lower temperatures than PH_3. As a group V element, the phosphorus atom has two s and three p valance electrons. It forms three covalent bonds in an sp^3 hybridized bonding configuration with the tert-butyl group and two hydrogen atoms. The excess lone pair electron completes the tetragonal geometry around the phosphorus atom with the inclining angle of around 109°.

3.1.3 Vapor Liquid Solid Growth

A frequently employed growth mechanism for nanowire structures is the vapor liquid solid (VLS) growth, as it is compatible with the common vapor-based growth techniques such as MBE, MOCVD and MOVPE [107]. It enables control over nanowire diameter, length, composition as well as crystal structure.
The VLS mechanism was first proposed by Wagner and Ellis in 1964 [108], who investigated the growth of silicon whiskers, nowadays called nanowires, using a gold "impurity" particle. They suggested a catalytic activity of the gold particle leading to a preferential deposition of silicon into the gold, which gets supersaturated. In 1995 Hiruma applied this method to the MOVPE process and produced GaAs and InAs nanowires [109]. Today the VLS mechanism is utilized to grow nanowires of a wide range of group IV and III/V semiconductor materials [110] for many different applications [13, 111–114]. Subsequently, a brief introduction to the VLS mechanism is given. For a more in-depth description, the reader is referred to

literature, for example, to the references [110, 115–117].
In general, particles of any metal can act as catalysts for VLS growth, each providing its advantages and disadvantages [118]. Factors influencing the choice of catalyst material are the solubility of the growth material, the phase diagram of its eutectic, incorporation of the catalyst into the nanowire, and possibilities for preparation and patterning of the material. Gold is a suitable catalyst material since it is easy to deposit, inert and shows good solubility of group IV and group III species. However, it is incorporated into the crystal in small amounts [115]. Independent of the catalyst choice, the material is liquefied by heating and acts catalytically on the decomposition of the vaporous precursor molecules [119]. The growth species diffuse into the particle, which results in a eutectic liquid nanowire seed particle. The solubility and phase of the eutectic are displayed in the eutectic phase diagram. In the more complex case of a three-species eutectic, like in the case of III/V nanowire growth (metal, group III and group V species), it was shown that a quasi binary phase diagram (metal and III/V compound) could be applied [120]. However, the literature still needs to include a quasi-binary phase diagram for gold and the investigated material gallium phosphide. At a certain point, the ongoing diffusion of growth material into the eutectic supersaturates the liquid. This leads to the growth species precipitating as a crystalline nucleus at the liquid-solid interface. By changing the precursor molecule and supplying another atomic species during the process also nanowire heterostructures can be produced [10, 121]. In figure 3.6, a sketch of the VLS process is shown.
Another important factor for nanowire growth is the substrate. The choice of crystalline surface can be used to determine the orientation of the growing nanowires. In this case, the

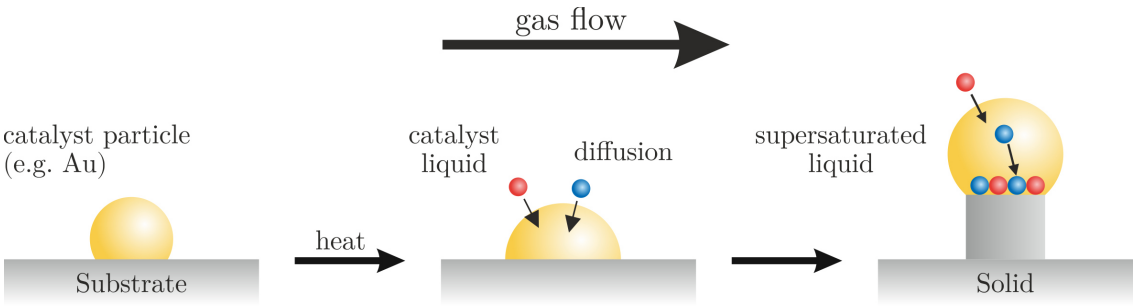

Figure 3.6: Fundamentals of the VLS mechanism. The solid particle is heated and exposed to the precursor vapor. Material diffusion from the vapor into the particle form a eutectic liquid. Once supersaturation is reached, nucleation starts at the liquid-solid interface.

nucleation at the interface is expected to be epitaxial. If the substrate does not determine the crystalline orientation, as it is, for example, in the case of amorphous surfaces, the nanowire will start to grow in a random direction [115]. The diameter of wires is largely determined by the size of their seed particle [122]. Larger particles result in an increased liquid-solid interface and, by this, in larger diameters. The growth species diffusion into the particle and towards the growth interface persists as long as the temperature and precursor supply is maintained. The nanowire continues to grow layer by layer and pushes the catalyst droplet ahead. The contact angle γ of the droplet depends on the interfacial tensions between vapor and liquid σ^{vl} and liquid and solid σ^{ls} and can be estimated by Young's equation [123, 124]:

$$\cos(\gamma) = -\frac{\sigma^{ls}}{\sigma^{vl}}. \tag{3.3}$$

The VLS growth can be divided into three main steps, illustrated in figure 3.7 a). First, the incorporation of the growth species from the vapor phase into the liquid. Second, the diffusion through the liquid towards the growth interface. And third, the crystallization of the nanowire crystal. The driving force behind these processes is the difference in the

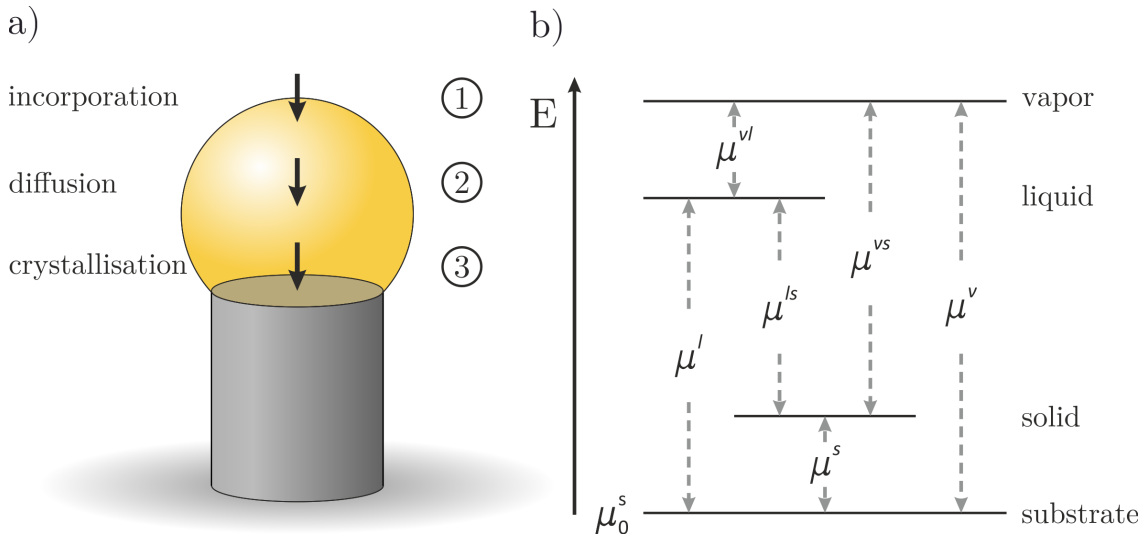

Figure 3.7: a) Growth rate-limiting steps in the VLS mechanism. b) Scheme of the chemical potentials of involved phases (adapted from [125]).

chemical potentials $\mu^{AB} = \mu^A - \mu^B$ of the participating phases A and B [126]. The Gibbs free energy of a system is defined by

$$G = U - TS - \sum_j q_j F_j \tag{3.4}$$

with internal energy U, temperature T, entropy S, generalized coordinates q_j and the corresponding force component F_j [127]. The total differential can be written as

$$dG = dU - TdS - SdT - \sum_j \left(q_j dF_j + F_j dq_j\right). \tag{3.5}$$

Replacing the total differential of internal energy [127]

$$dU = TdS + \sum_j F_j dq_j + \sum_i \mu_i dN_i \tag{3.6}$$

where μ_i denotes the chemical potential and N_i the number of particles of phase i, yields

$$dG = -SdT - \sum_j q_j dF_j + \sum_i \mu_i dN_i. \tag{3.7}$$

Thus, the chemical potential μ_i describes the change in Gibbs free energy by changing the number of particles in a particular phase

$$\mu_i = \left(\frac{\partial G}{\partial N_i}\right)_{T,F,N_{j\neq i}}. \tag{3.8}$$

Particles tend to change from higher to lower chemical potentials to minimize their energy. Each phase participating in the VLS process can be assigned a chemical potential. The corresponding energy diagram, with the potential differences, is depicted in figure 3.7 b). The reference is defined as the substrate's chemical potential μ_0^s. Each step proceeds at its own rate, depending on the growth parameters and the materials used. μ^{vl} and μ^{ls} are the driving forces for the incorporation step from vapor to liquid phase and the crystallization step from liquid to solid phase, respectively. The resulting growth rate is dependent on the respective limiting rate, which depends on the experimental conditions.
The rate of incorporation (step 1) is determined by its driving force μ^{vl} which increases the probability that a particle is incorporated, as well as the precursor partial pressure p [125]. The pressure dependence is a result of an increased amount of molecules impinging

the liquid surface at higher pressures. In literature, it is also assumed to scale with the droplet surface associated with the squared wire radius r^2 [128]. The r^2 proportionality only holds for fixed droplet geometries with constant contact angles γ, since the droplet surface is determined by r and γ.
Diffusion (step 2) through the liquid phase proceeds sufficiently fast and supports growth rates of up to $10^7\,\mathrm{nm\,s^{-1}}$ [126], which is several orders of magnitude higher than typical growth rates of up to $10^4\,\mathrm{nm\,s^{-1}}$. Hence, diffusion would only become relevant for extremely explosive growth rates.
The rate of crystallization (step 3) depends on the supersaturation of the liquid particle, which can be described with the chemical potential difference between liquid and nanowire μ^{ls} [125]. Beside these three main steps considering only the migration from the vapor phase through the droplet towards the growth front, there are other influencing factors. Growth material can also be provided by surface diffusion towards the triple phase line at the wire tip. On the one hand, this happens by direct impingement on the nanowire sidewall and, on the other hand, on the substrate. In the first case, the diffusion rate again depends on the precursor partial pressure p and on the diffusion length λ_s of the growth material on the sidewalls. The contribution to the overall growth rate is furthermore radius dependent. The diffusion on the sidewall scales with r and the growth rate with $1/r^2$ assuming a constant crystallization rate. In total, this effect is expected to scale with $1/r$. In the latter case of surface diffusion, an additional dependence on the wire length L appears because if L rises compared to the diffusion length, fewer adsorbed particles reach the growth interface [129, 130]. In addition, the nanowire density may play a crucial role in the surface diffusion rate. If the spacing between the nanowires is small compared to the surface diffusion length, the wires compete with each other, leading to a reduced effective diffusion length [131]. For larger wire spacing, this effect can be neglected.
For small radii in the range below 100 nm the Gibbs-Thomson effect [125, 128, 132–135] begins to play a role, which describes the growing contribution of surface energy to Gibbs free energy G. The supersaturation μ^{ls} can be described by

$$\mu^{ls} = \mu^l - \mu^s = \mu^l - \frac{2\Omega^s\sigma^s}{r} \tag{3.9}$$

with Ω^s and σ^s being the molar volume and surface tension of the solid, respectively [125, 126]. Equation (3.9) shows that μ^{ls} decreases with decreasing radius since the chemical potential of the nanowire μ^s rises. The lower supersaturation results in a slower growth rate. Under a certain critical radius, the chemical potentials of the nanowire μ^s and

liquid μ^l are equal. Hence, the supersaturation becomes zero, and the nanowire growth terminates [136]. The Gibbs-Thomson effect becomes negligible at larger radii since the radial dependence of μ^s vanishes. This behavior of competitively influencing the growth rate and their dependence on growth parameters and wire geometry is complex, especially when the factors contribute roughly equally strong [128, 137–139].
Other VLS-based growth mechanisms also exist, like laser-assisted catalytic growth (LCG), which combines laser ablation to form defined catalyst clusters and the VLS process [140]. Growth can also be performed by using solid rather than liquid catalyst particles, called vapor solid solid (VSS) growth [141, 142]. A further approach replaces the vapor phase with a liquid phase. In this so-called solution liquid solid (SLS) or solution solid solid (SSS) growth, a solution is heated and pressurized above its critical point, becoming supercritical [143, 144] and supplies the growth material to the catalyst particles [145, 146].

3.1.4 GaP Nanowire Growth

This work presents the growth of gallium phosphide nanowires via the VLS mechanism. The growth process was inter alia live observed in a transmission electron microscope (TEM) using an *in-situ* gas and heating setup (see section 3.4.1). The catalysts used as seed particles are colloidal gold particles with a diameter of $(19.5 \pm 9.7)\,\mathrm{nm}$. They were prepared by STREM Chemicals Inc. via laser ablation in isopropanol [147]. The resulting suspension of gold and isopropanol is drop-cast on the MEMS chip to prepare the sample. Subsequently, isopropanol evaporates, and the nanoparticles remain on the MEMS surface. TBP and TMGa are the precursor molecules acting as sources of phosphorus and gallium, respectively. Figure 3.8 shows the binary phase diagram of Au and Ga. This diagram delivers a rough estimate of the catalyst particles phase. It is considered here due to the need for literature's ternary Au-Ga-P or quasi binary Au-GaP phase diagrams. However, this estimate is reasonable since P, as a group V element, has very low solubility in Au [151].
It has been shown that the melting point for Au nanoparticles is reduced for small diameters [152–154]. This is due to the Gibbs-Thomson effect. The melting temperature for Au particles with the given size is lowered from 1063 °C, for bulk Au, to approximately 980 °C. Thus it is expected that phase boundaries in the bulk phase diagram are shifted to lower temperatures in dependence on the particle size. In the case of bulk gold, up to 12.4 % of gallium is soluble in gold at a temperature of 415 °C [149]. Phosphorus is not

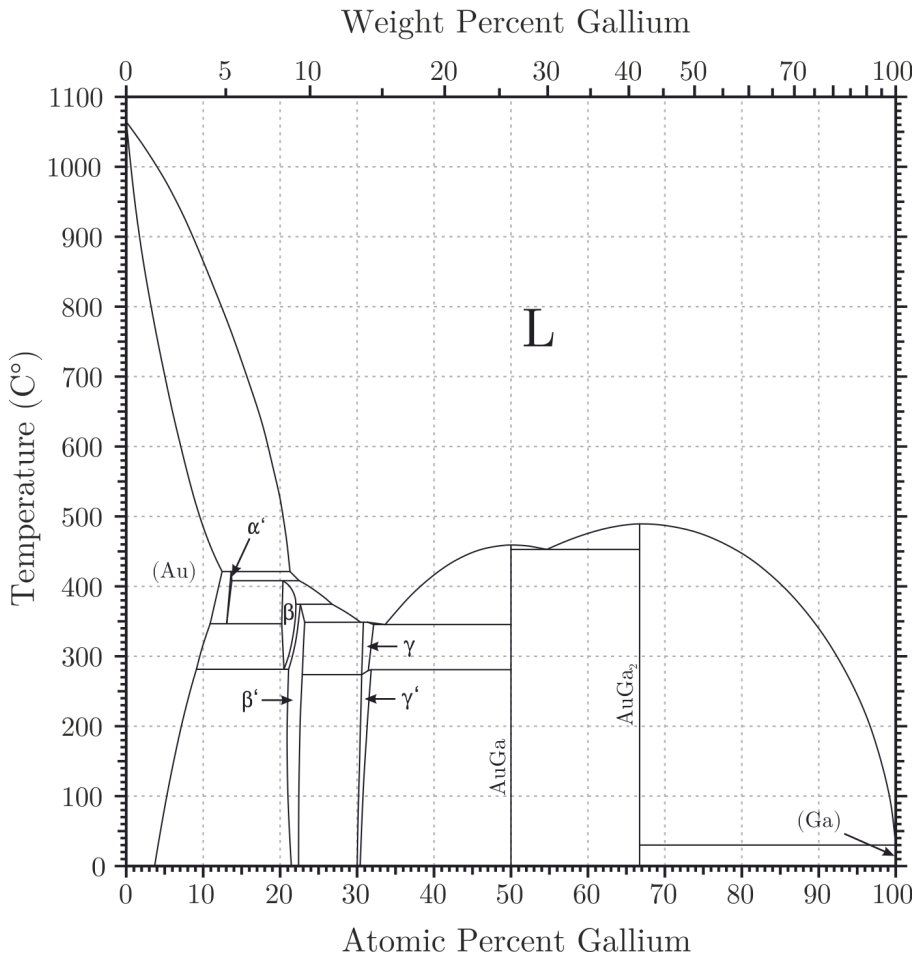

Figure 3.8: Phase diagram of the Au-Ga system (reconstructed from [148–150])

soluble in solid gold at all [151]. Therefore, it does not influence the melting temperature. Contrariwise, already a few percent of Ga incorporated into the gold drastically reduces the melting temperature. However, the solubility of Ga is reduced in small gold particles compared to bulk material [110]. Hence the phase boundaries of the (Au) phase are expected to be shifted towards lower percentages of gallium. Nevertheless, it can be concluded that the Au particles can be melted at temperatures around 400 °C due to the presence of gallium in the vapor phase diffusing into the gold. By this, a liquid gold-gallium eutectic is formed. The phosphorus concentration in the eutectic is assumed to be very small due to the low solubility, even with a surplus of phosphorus precursor in the gas phase. Furthermore, this leads to the assumption that phosphorus is mainly

present at the particle's surface, diffusing to the triple phase line. Consequently, growth limited by phosphorus or, in general, by the group V species can be performed, which is usually not the case in MOVPE. Growth is performed with a surplus of TBP in the gas phase, necessary to compensate for the incongruent evaporation of the group V species at elevated temperatures. High V/III ratios in the gas phase cause the growth to be group III limited. The transition between the limiting species depends on the used growth conditions, catalyst and precursor sources. It has been shown that nanometer-scaled structures can also be thermally stabilized in the used setup [155].

3.2 Transmission Electron Microscopy

Transmission electron microscopy (TEM) has evolved to be a powerful tool in material characterization in the past century. Today, it can provide real-space images of materials at atomic resolution, enabling observation of, for example, structural irregularities or defects at the atomic level. For this, a resolution in the sub-nanometer regime is required. In 1873 Ernst Abbe related the resolution limit of a microscope to the wavelength λ of the imaging system [156] and described its limitation by

$$d = \frac{\lambda}{n \sin(\alpha)} \tag{3.10}$$

with d being the minimal distinguishable distance, refractive index n and half angular aperture α. This criterion limits the resolution to the order of magnitude of λ making sub-nanometer resolution inaccessible with visible light. In 1924 Louis de Broglie claimed that all matter has wave-like nature and linked its wavelength and momentum p with Planck's constant h [157]

$$\lambda = \frac{h}{p}. \tag{3.11}$$

He was awarded the Nobel Prize in Physics for the formulation of this hypothesis in 1929. As a consequence, all particles can be assigned a wavelength. The relativistic wavelength of an electron utilized in TEM with acceleration voltage U is given by

$$\lambda = \frac{h}{\sqrt{2m_0 eU\left(1 + \frac{eU}{2m_0 c_0^2}\right)}} \tag{3.12}$$

where m_0 is the electron rest mass, e the elementary charge and c_0 the velocity of light. For acceleration voltages of 200 kV and 300 kV the electrons obtain a wavelength of 2.51 pm and 1.97 pm respectively. In principle, a resolution far below the sub-nanometer regime could be achieved with these wavelengths. In 1932 Max Knoll and Ernst Ruska [158–160] started on the instrumentation of electron optics. Later, in 1986, Ernst Ruska was granted the Nobel Prize in Physics for his fundamental work in electron optics and the design of the first electron microscope. Electron microscopes matched the resolution power of optical microscopes in 1934 [161] and it took until 1972 for a direct correspondence between the projected crystal structure and the imaged lattice [162].
In this chapter, the construction of a TEM as well as its imaging mechanisms are treated, with a focus on the fundamental image generation, high-resolution TEM (HRTEM) and scanning TEM (STEM), followed by utilized analytic techniques accessible in TEM, namely energy dispersive X-ray spectroscopy (EDX) and precession electron diffraction (PED).

3.2.1 Transmission Electron Microscope Construction

In this section, the setup of a TEM is described from top to bottom in the example of the JEOL JEM-3010. The additional and differing components of the also utilized JEOL JEM-2200FS are described afterwards.
In the JEOL JEM-3010, the electron beam is generated by a thermal LaB_6 electron source heated up to 1700 K. By this, the electron can overcome the work function and is emitted to the vacuum. A Wehnelt cylinder collimates the emitted electrons, forming a cross-over determining the divergence angle, passing them to the accelerating tube where they get accelerated by a voltage of 300 keV. The energy width of the resulting beam is around 1.5 eV. The first lens system consists of the condenser lenses, which form the illuminating electron beam. The beam diameter and aperture angle are adjusted by an aperture, which cuts off beams far away from the optical axis. Furthermore, the condenser lenses determine whether the specimen is illuminated with a parallel or a convergent electron beam. The beam transmits through the specimen located in a goniometer enabling movements in all spatial directions and rotation around the holder axis. The sample is located in the pole piece gap of the objective lens system. These lenses essentially perform the magnification of the sample. Due to this, they are the most important lenses in the TEM, and their aberrations are the most limiting ones for the image resolution. The diffraction pattern is formed in the back focal plane, where the objective aperture is located to select or block specific beams. The selected area aperture, located in the image plane, is used to

only gather information from distinct selected areas of the sample. The next lens system consists of the intermediate lenses. They either pass on the image in the image plane, or by reducing the focal strength, they pass on the diffraction pattern to be imaged. The following projector lenses further magnify the image (either the real image or the diffraction pattern) and project it onto a fluorescent screen or camera. The JEOL JEM-2200FS can be operated in TEM (section 3.2.2) or STEM (section 3.2.4) mode. The electron beam is generated by a ZrO/W(100) Schottky field emission gun (FEG) [163]. It consists of a tungsten tip coated with zirconium oxide acting as a cathode to lower the work function of the tungsten (100) surface. The cathode is heated up to 1800 K, and an anode applies a strong electric field that lowers the potential barrier for the electrons, allowing them to leave the cathode. An anode accelerates the emitted electrons to the desired energy of up to 200 keV. Thermionic emitted electrons are suppressed by a negative potential applied by suppressor electrodes. FEGs possess a high intensity and a relatively narrow energy width below 1 eV. The microscope is equipped with two C_S-correctors for operation in TEM and STEM mode, respectively. They reduce spherical aberration induced by the condenser lenses, reducing the electron wave's phase shift. This increases the achievable resolution (compare section 3.2.3), and a sharper probe can be formed in STEM operation. Electrons scattered to high angles can be detected with ring-shaped annular darkfield (ADF) detectors. Two of them are mounted in the microscope, above and below the intermediate lens, to cover different angular regimes. The JEOL JEM-2200FS is equipped with an omega energy filter between the intermediate and projector lens. This component spatially separates electrons of different energies, which can be utilized to perform EELS. Furthermore, with a slit aperture, a specific energy range can be selected, which can be used to reduce the chromatic aberration efficiently (see section 3.2.2), enhancing the image contrast.

3.2.2 Image Formation in Transmission Electron Microscopy

In chapter 2.4, the interaction of electrons with matter and the fundamentals of image formation were described. In the following, the formulation of Kirkland in reference [164] is followed for a more practical description of image formation. The formation process of an image can be divided into three steps. First, the electrons scatter in the specimen. Second, a diffraction pattern is formed in the back focal plane of the objective lens. And third, the image is formed in the image plane. It can be shown mathematically that these steps are related to each other by Fourier transform operations [163] (compare equation

(2.56)). However, due to imperfections in the objective lens and limited coherence, this idealized description fails in reality without consideration of aberrations. Lens aberrations disturb the spherical electron wavefront in the diffraction plane and thus reduce the sharpness of an image point. A wave aberration function $W(\omega)$ is defined, which depends on the complex position variable $\omega = u + iv$ in the diffraction plane (u,v). A third order Taylor expansion of $W(\omega)$ in polar notation with $\omega = \vec{k}\exp(i\phi)$, $A_n = |A_n|\exp(i\alpha_n)$ and $B_n = |B_n|\exp(i\beta_n)$ gives the aberration function as

$$\begin{aligned} W\left(\vec{k},\phi\right) = \frac{2\pi}{\lambda}\Big\{ & |A_0|\lambda k\cos(\phi-\alpha_0) \\ & +\frac{1}{2}|A_1|\lambda^2k^2\cos 2(\phi-\alpha_1)+\frac{1}{2}C_1\lambda^2k^2 \\ & +\frac{1}{3}|A_2|\lambda^3k^3\cos 3(\phi-\alpha_2)+\frac{1}{3}|B_2|\lambda^3k^3\cos(\phi-\beta_2) \\ & +\frac{1}{4}|A_3|\lambda^4k^4\cos 4(\phi-\alpha_3)+\frac{1}{4}|S_3|\lambda^4k^4\cos 2(\phi-\sigma_3) \\ & +\frac{1}{4}C_3\lambda^4k^4+\ldots\Big\} \end{aligned} \tag{3.13}$$

where ϕ describes the azimuthal and k the radial dependence of the aberration. Higher-order aberrations exist as well. However, their importance diminishes with increasing order. The aberration function describes a phase plane of the imaging system, which causes a phase shift of the ideal spherical wavefront. The aberration coefficients are correlated to different types of aberrations with different symmetries in ϕ. In the following, the most relevant are characterized briefly. C_1 and C_3 (often called C_S) describing the defocus and spherical aberration, respectively, show no dependence on ϕ. Defocus is mainly determined by the height (z-direction) of the sample in the TEM and describes the deviation from the Gaussian focal point. The spherical aberration causes rays impinging the lens further from the optical axis to be over-focused. The focal point is smeared out to a disc. The optimal focal length is reduced to the point where the disk has its least diameter. The aberration coefficient A_1 describes two-fold astigmatism. It occurs when a lens has unequal focal points for different planes across the lens, causing an elliptical beam distortion. It can be corrected by a set of quadrupole deflectors. The aberration coefficient B_2 quantifies the axial coma. It describes aberrations caused by illumination not parallel to the optical axis. Its consequence is a distortion of a point to a patch not symmetrical about a point exhibiting a resemblance to a comet having its tail. A further aberration, which is not covered by the aberration coefficients above, is chromatic aberration. It originates from

the energy dependency of the focusing strength of electrons determined by the Lorentz force. Since the beam is not perfectly monochromatic, it causes electron waves of different wavelengths to have different focal points.
For thin specimens, absorption can be neglected, and the sample only changes the phase of the electron wave. In this phase object approximation (POA), with neglecting the aberration function, the exit wave function can be written as

$$\Psi(\vec{r}) = \exp\left(-i\sigma\phi\left(\vec{r}\right)\right) \tag{3.14}$$

with the interaction constant

$$\sigma = \frac{2\pi me\lambda}{h^2} \tag{3.15}$$

where m is the electron mass, λ the wavelength and h the Planck constant. $\phi\left(\vec{r}\right)$ describes the projected Coulomb potential of the specimen along the beam direction. Equation (3.14) describes a phase shift in $\Psi(\vec{r})$ by $\sigma\phi\left(\vec{r}\right)$. As mentioned previously, the amplitude in the back focal plane of the objective lens is given by a Fourier transformation. If only a small defocus C_1 is allowed it can be written as

$$\begin{aligned}\psi_d\left(\vec{k}\right) &= \mathcal{F}\left\{\exp\left[-i\sigma\phi\left(\vec{r}\right)\right]\right\}\exp\left[i\pi C_1\lambda\left|\vec{k}\right|^2\right] \\ &\approx \Phi\left(\vec{k}\right)\left[1+i\pi C_1\lambda\left|\vec{k}\right|^2\right]\end{aligned} \tag{3.16}$$

where $\Phi\left(\vec{k}\right)$ represents the Fourier transform of $\exp\left[-i\sigma\phi\left(\vec{r}\right)\right]$. Thus the image amplitude is given by the inverse Fourier transform

$$\psi_i\left(\vec{k}\right) = \exp\left[-i\sigma\phi\left(\vec{r}\right)\right] + i\pi C_1\lambda\mathcal{F}^{-1}\left\{\left|\vec{k}\right|^2\Phi\left(\vec{k}\right)\right\} \tag{3.17}$$

With use of the Fourier theorem, stating that if $f\left(\vec{r}\right)$ and $\Phi\left(\vec{k}\right)$ are a Fourier transform pair, then

$$\mathcal{F}^{-1}\left\{\left|\vec{k}\right|^2\Phi\left(\vec{k}\right)\right\} = -\frac{1}{4}\pi^2\left[\nabla^2 f\left(\vec{r}\right)\right] \tag{3.18}$$

and Poisson's equation, the image intensity can be approximated in first order as

$$I\left(\vec{r}\right) \approx 1 + \left(\frac{C_1\lambda\sigma}{2\pi\varepsilon_0\varepsilon}\right)\rho\left(\vec{r}\right). \tag{3.19}$$

$\rho(\vec{r})$ represents the projected total charge density of the specimen, which includes the distribution of nuclei. The result of the projected charge density (PCD) approximation relates the image intensity to the atom positions in the specimen. Since it neglects the effect of spherical aberration, which is the dominant aberration in conventional TEM imaging, the PCD approximation is restricted to relatively low-resolution imaging or aberration-corrected imaging.

3.2.3 High Resolution Transmission Electron Microscopy

The phase contrast can be described in the scope of linear transfer theory [165]. In equation (3.13) $W\left(\vec{k}\right)$ describes the phase shift of the wave front. The resulting contrast variations with further consideration of the spherical aberration C_3 and neglecting higher order aberrations are described by the phase contrast transfer function (PCTF), which is given by [164]

$$\sin W(k) = \sin\left(\pi C_1 \lambda k^2 + \frac{\pi}{2} C_3 \lambda^3 k^4\right). \tag{3.20}$$

The sinusoidal character of the PCTF causes the contrast to oscillate around zero and gives rise to contrast inversions due to zero transitions. The first band of frequencies in the PCTF without zero crossing defines the point resolution d_1. Scherzer [166] derived a defocus setting that offsets the phase shift due to spherical aberration. With a choice of defocus according to

$$C_{1,Scherzer} = 1.2\sqrt{C_3 \lambda} \tag{3.21}$$

the zero crossings of the PCTF are shifted to frequencies above $k_{max} = 1.6\left(C_3\lambda^3\right)^{-\frac{1}{4}}$. The inverse of this frequency gives the point resolution of

$$d_1 = 0.625\left(C_3\lambda^3\right)^{\frac{1}{4}}. \tag{3.22}$$

The highest spatial frequency transferred from the specimen exit wave function to the image intensity is defined as the information limit. It is determined by spatial and temporal coherence effects in the illumination and by mechanical instabilities like acoustic noise.

These dampen the transfer of higher spatial frequencies. An envelope function can describe the effects

$$E(k) = \exp\left[-\frac{1}{2}\pi^2\Delta^2\left(\lambda k^2\right)^2\right] \tag{3.23}$$

with the focal spread Δ. In figure 3.9 the involved functions are plotted for the defocus

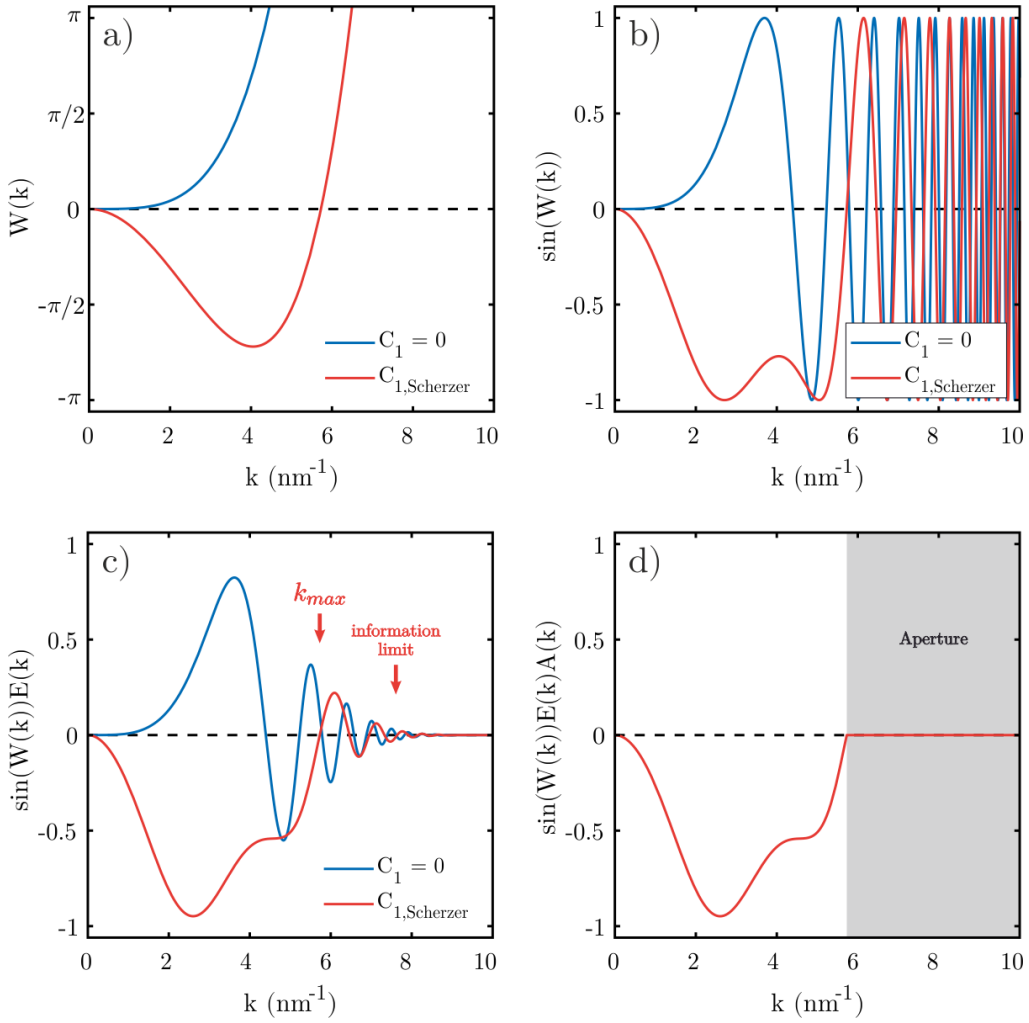

Figure 3.9: a) The phase shift of the wavefront in dependence on k. b) Contrast modulation caused by the phase shift. c) Phase contrast transfer ($U = 300\,\text{kV}$, $C_3 = 0.7\,\text{mm}$ and $\Delta = 7.5\,\text{nm}$) by consideration of the envelope. The highest interpretable spatial frequency is marked for Scherzer defocus as k_{max}. d) Effect of the aperture on the phase contrast transfer. Frequencies above k_{max} are blocked. Blue curves represent zero defocus $C_1 = 0$ and red curves Scherzer defocus.

values $C_1 = 0$ (blue) and $C_{1,Scherzer}$ (red). In plot a), the phase shift in dependence on the spatial frequency can be seen. The Scherzer defocus increases the interval where the phase shift does not flip the sign of the sine function. This consequently enlarges the interval without zero crossing, as shown in plot b). The effect of the envelope function is visible in plot c). The frequency for which the contrast transfer vanishes marks the information limit. In HRTEM, spatial frequencies above k_{max} lead to a phase contrast in the image, which cannot be interpreted. This is due to a positive and negative contrast overlap in the image. To restore the interpretability, spatial frequencies above k_{max} are absorbed by the objective lens's objective aperture in the back focal plane, described by an aperture function

$$A(k) = \theta(k_{max} - k) \tag{3.24}$$

with the Heaviside step function $\theta(k)$. Figure 3.9 d) shows the resulting phase contrast transfer function. The ray path diagram in HRTEM can be seen in the sketch of figure 3.10. Dashed lines depict beams scattered to higher spatial frequencies by the specimen. They

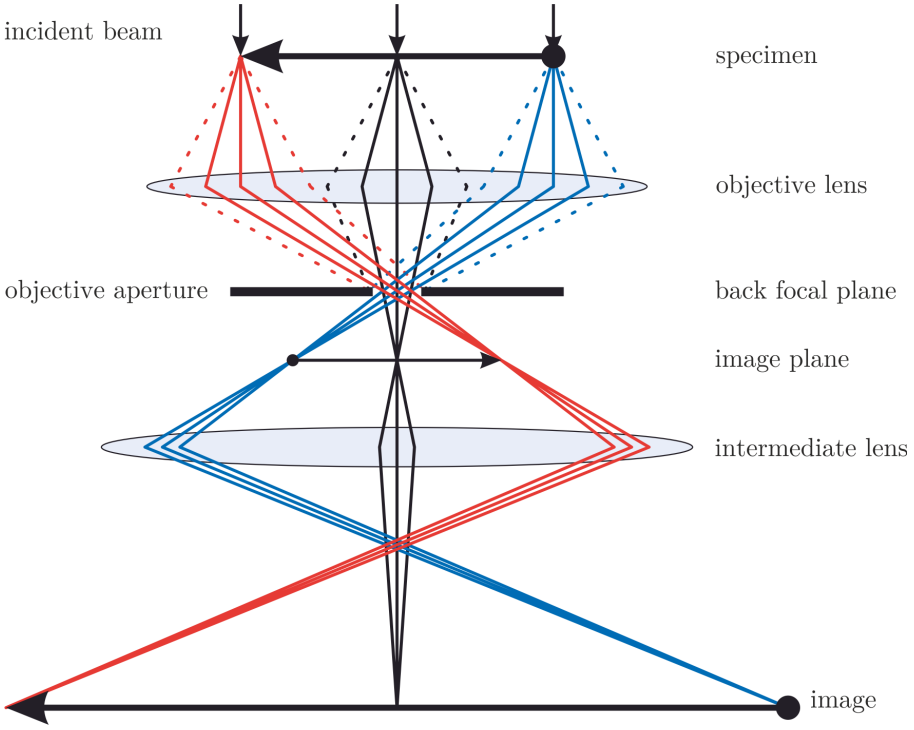

Figure 3.10: Beam path during HRTEM imaging. Beams scattered to higher frequencies, indicated by dashed lines, are blocked by the objective aperture in the back focal plane.

hit the aperture in the back focal plane. Only beams scattered to spatial frequencies within the aperture contribute to the image. With a reasonable aperture diameter, an image with interpretable contrast is generated. For the utilized JEOL JEM-3010 using electrons with an energy of 300 keV, spherical aberration $C_3 = 0.7$ mm and Scherzer defocus of $C_{1,Scherzer} = -45$ nm the resulting resolution is $d_1 = 169$ pm. This resolution is reasonable to resolve, for example, the {220} lattice planes of GaP in [001]-projection with a spacing of 193 pm [34].

3.2.4 High Angle Annular Darkfield Imaging

Image formation in STEM proceeds in a fundamentally different way than in TEM. In contrast to utilizing the coherently scattered electrons, in STEM, the incoherently scattered electrons predominantly form the image. It has been an established nano-scale analysis technique for several decades, with even sub-nanometer and atomic resolution [167–169]. A sharp convergent electron beam, the spot or probe, impinges the specimen and is scanned across the field of view by deflection coils. Scattering occurs at the atom's coulomb potential, and various signals arise as described in section 2.4. The specific signal, for example, the scattered electrons or emitted X-rays, is detected and its intensity can be plotted as a function of beam position to generate an image. The spatial resolution of the STEM is mainly determined by the size of the probe [170]. Therefore the important imaging optics are the ones above the sample that form the probe. In the JEOL JEM-2200FS, these are the condenser and objective lenses. In order to create a small probe, the image of the electron gun needs to be demagnified. Hence a small and bright electron source is beneficial. Probe sizes below interatomic spacing can be achieved.
As described in the previous section, in the example of HRTEM, the objective lens aberrations are the crucial ones determining the resolution limit of the STEM. The derivations of this section apply to STEM as well. In particular, the spherical aberration increases the width of the probe leading to more diffuse illumination. Due to this over-focusing effect, a slight under-focus again reduces the probe size in the specimen plane (see Scherzer defocus in section 3.2.3). With the use of a corrector, the spherical aberration can be compensated for low-angle beams up to approximately 70 mrad. Further, an aperture is used to exclude higher-angle aberrated beams.
In high-angle annular darkfield (HAADF) imaging, electrons scattered to high angles above approximately 50 mrad are detected and counted, which is performed by a ring-shaped yttrium aluminum perovskite detector [171]. Impinging electrons induce a scintillation

signal in the detector guided to a photomultiplier that produces an electrical current. Electrons scattered to lower angles than the inner radius of the detector can pass through its hole and can be detected afterwards by a camera. The interpretation of contrast in HAADF images is more straightforward than in HRTEM since scattering is Rutherford-like. It is also called Z-contrast imaging since the scattering intensity scales with the atomic number Z. Rutherford's scattering equation predicts a dependency on Z^2 (see equation 2.63). However, due to the screening effects of the electrons, the exponent is decreased to values between 1.6 and 1.9 depending on the inner and outer detector angles [172]. The detected angular regime can be changed by varying the effective camera length. However, Z-contrast in HAADF images enables distinguishing between elemental species directly in the image [173, 174]. Figure 3.11 illustrates the general setup and beam path in STEM.

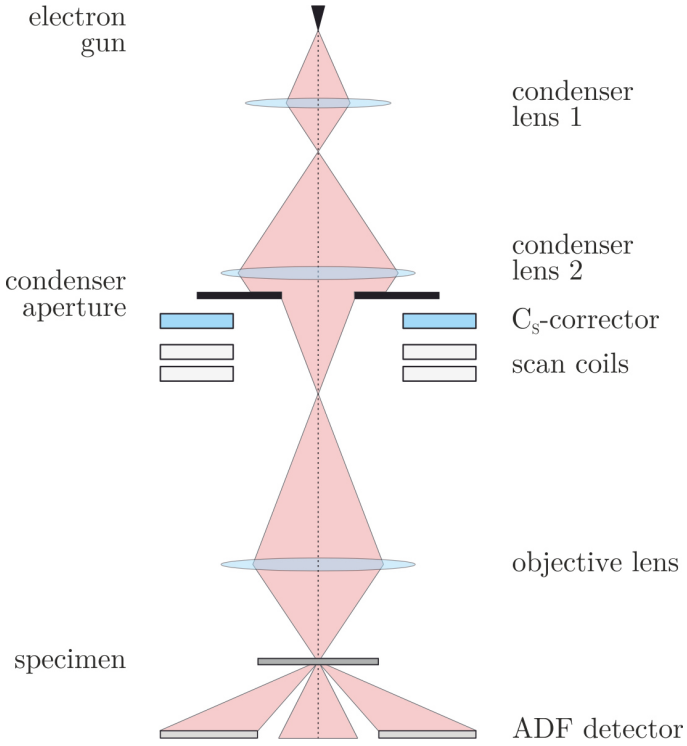

Figure 3.11: Schematic drawing of beam path in STEM.

3.2.5 Energy Dispersive X-ray Spectroscopy

Chemical analysis of the sample in the TEM can be done by Energy Dispersive X-ray Spectroscopy (EDX). In chapter 2.4.4, the electron-matter interaction with respect to inelastic scattering effects was discussed, and the generation of characteristic X-rays in the sample was explained. In the interaction volume of the electron beam with the specimen, X-ray photons are emitted. By detecting the photons of various X-ray energies, an energy dispersive spectrum is acquired.
The detector is located above the sample and mounted to the TEM column's side. X-ray detection from above the specimen reduces the overlaying bremsstrahlung signal since this is emitted primarily in the direction of the electron beam. The detector is a Bruker XFlash 5060 silicon drift detector (SDD). It consists of a high-resistivity silicon volume, which an electric field completely depletes from charge carriers. The working principle is as follows: X-ray photons entering the detector generate clouds of electron-hole pairs. The electric field separates the electrons and holes from each other. The electrons drift towards the anode, and the induced current is measured. The measured current can be translated to the energy of the photons [175].
The characteristic X-ray photons can be correlated to a specific element (compare chapter 2.4.4). The corresponding transitions are named concerning the filled electron vacancies atomic shell, for example, the innermost K-shell. To distinguish between the higher filling shells, one counts in Greek letters from the filled shell to the filling one. If, for example, an electron from the M-shell fills the L-shell vacancy, the transition is called L_α. To further distinguish between the different L- and M-subshells depending on the azimuthal quantum number l, one counts with a Roman number index in the L-shell ($L_{\text{I-III}}$) and with an Arabic number index behind the Greek index ($L_{\alpha_{1-2}}$). This leads to an explicit notation for a transition (e.g., $L_{I\alpha_2}$). However, with an energy resolution of around 129 eV, it is not possible to distinguish between the subshells and the notation L_α for the $L_{I\alpha_2}$ transition is sufficient. In practice, tabulated values for characteristic X-ray energies from empirical measurements are used and can be found, for example, in reference [176]. The electronic transitions of a specific element occur with a given probability. Some transitions are more likely than others and thereby more often detected. Consequently, the peak intensities caused by the characteristic X-rays of the element show a fixed ratio. In the case of pure materials and transitions of non-bonding shells, where chemical shifts do not have a significant impact, this fact can be utilized to separate between overlapping peaks even in the low energy regime, where the resolution would be insufficient for quantification.

EDX is compatible with TEM as well as STEM. In the first case, a spectrum is generated, collecting the emitted X-rays from the exposed sample area. In the latter case, spectra with spatial resolution can be generated due to the scanning probe. At each scan point, a complete energy spectrum is acquired. By this, the elemental distribution of the sample can be visualized and a spatial composition determination is possible. Furthermore, any number of scans across the field of view can be integrated to reduce the signal-to-noise ratio.

3.2.6 Precession Electron Diffraction

The kinematic approximation was introduced in chapter 2.4.1, assuming only elastic scattering and neglecting multiple scattering. Especially for thick samples, this approximation does not withstand and a dynamic description is required. In dynamical scattering, a diffracted beam can be treated as a new incident beam that can undergo a further scattering process into the initial direct beam or other diffracted beams. This more complex behavior makes the description of diffraction pattern intensities with the use of the structure factor invalid. Precession electron diffraction (PED) is a technique that reduces the dynamic effects and produces quasi-kinematic diffraction patterns [177]. A NanoMegas ASTAR system [178], installed at a JEOL JEM-3010, was utilized to record scanning PED (SPED) four-dimensional data sets. A precessing nanobeam is scanned over the sample, and a diffraction pattern of every scan point is acquired an evaluated by the ASTAR software package [179]. By this, spatially resolved crystal orientation maps can be obtained [180]. An optical CCD camera is used to record diffraction patterns on the fluorescence screen of the TEM with up to 180 frames per second.
In PED, the incident beam is tilted off the optical axis at a precession angle φ of up to 50 mrad ($\approx 3°$) and precessed forming a conical surface as illustrated in figure 3.12. The Ewald's sphere construction of two different incident beams with wave vector $\vec{k_0}$ is illustrated in red and blue, respectively. One precession period describes a complete rotation of 360° at a frequency of 100 Hz. Two-stage deflection coils tilt the beam above the sample and tilt it back underneath, termed descanning. It is necessary to create a spot-like diffraction pattern again, which would contain rings instead of spots without descanning due to the precessing beam [182]. Because of the off-axis beam inclinations, just a few reflections intersect with Ewald's sphere and are simultaneously excited. Since dynamic scattering occurs mainly between the few excited reflexes and the direct beam, it is strongly reduced by the missing excitation common in conventional zone axis orientation.

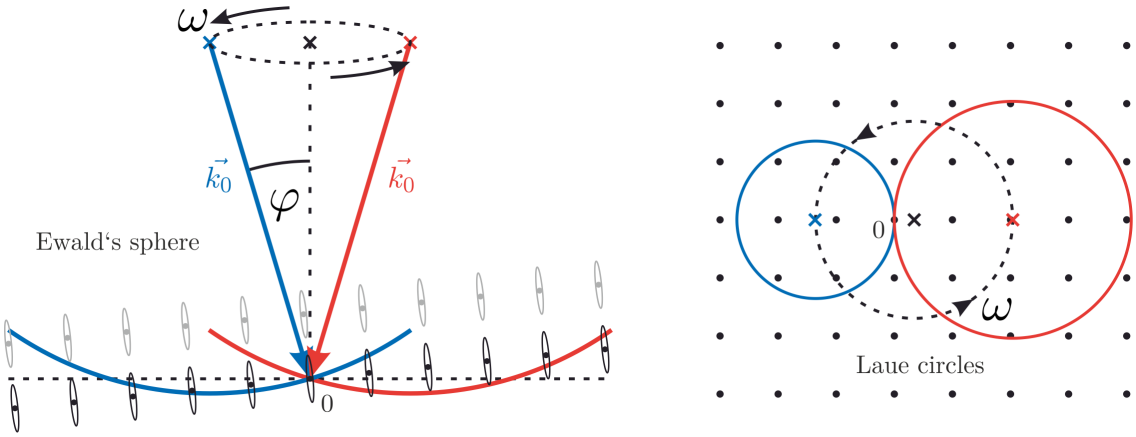

Figure 3.12: Left: vertical cross-section of reciprocal space with Ewald's sphere. Right: horizontal cross-section of reciprocal space with Laue circles (adapted from [181]).

Double diffraction, systematic intensity variation of a specific $\vec{g}_{hkl}$, and the background intensity are therefore strongly reduced [181]. The total recorded diffraction pattern is the integration over all diffraction patterns during one or multiple precession periods. Consequently, the dynamic effects between the diffracted beams are substantially reduced, leading to a quasi-kinematic appearance of the recorded diffraction pattern. PED was used for crystal phase and orientation mapping for the presented work. The key benefit of PED for this application is the elimination of the extinction error [182]. Due to the movement of Ewald's sphere through the reciprocal lattice, all reflections close to the direct beam get excited multiple times and are visible in the diffraction pattern improving their quality [183]. In addition, it is not required to perfectly align the sample in the zone axis. For high precession angles of up to 50 mrad HOLZ reflections also contribute to the diffraction, which provides the visibility of all symmetry elements for determination of space and point group [183]. For orientation determination of known crystal structures, smaller precession angles of around 10 mrad are feasible and allow for smaller probe sizes of 6 nm to 12 nm for improved lateral resolution. Euler angles can unambiguously define an absolute crystallographic orientation. These are a set of three angles describing a sequence of rotations around a given coordinate axis. The order of the rotation axes is defined by the used convention (e.g., z-x-z). Additionally, the chained rotation can either be intrinsic or extrinsic. Intrinsic rotations describe rotations of the coordinate system,

whereas extrinsic rotations describe rotations while the coordinate system's orientation is maintained. The misorientation of two sets of Euler angles $\vec{\alpha}$ and $\vec{\beta}$ is given by

$$\varphi = \cos^{-1}\left(\frac{\mathrm{Tr}\left(R_{\vec{\alpha}}^{T} R_{\vec{\beta}}\right) - 1}{2}\right) \tag{3.25}$$

which is the angle of rotation between the two respective orientations. $R_{\vec{\alpha}}$ and $R_{\vec{\beta}}$ are the rotation matrices defined by the Euler angles $\vec{\alpha}$ and $\vec{\beta}$. In highly symmetric crystals, there are indistinguishable orientations, hence leading to orientation ambiguities. This problem is solved by symmetrization, which compares the crystal's misorientations of all equivalent orientations according to its symmetry operators (see space groups in chapter 2.1). The symmetrized misorientation is defined as the smallest among these. This reduces the space of possible Euler angles by removing equivalent orientations. To determine the orientation of a specimen with a known structure, the diffraction pattern is compared to a database. The database contains simulated spot patterns for sets of Euler angles covering the Euler space defined by the crystal symmetry. Every pattern is compared to the measured one by cross-correlation template matching. A correlation index Q is defined as

$$Q(i) = \frac{\sum_{j=1}^{m} P(\vec{r_j})\, T_i(\vec{r_j})}{\sqrt{\sum_{j=1}^{m} P^2(\vec{r_j})}\sqrt{\sum_{j=1}^{m} T_i^2(\vec{r_j})}} \tag{3.26}$$

where the diffraction pattern is described by the intensity function $P(\vec{r})$ and the template i is given by $T_i(\vec{r})$. The highest value of $Q(i)$ is assigned to the specimen orientation matching the orientation of template i [184]. In principle, multiple orientations may obtain a high correlation index. In this case, the assignment is insecure since several orientations match similarly well with the diffraction pattern. Because of this, a reliability index R is defined by the correlation indices for the two highest distinct maxima in the Euler space Q_1 and Q_2 [184].

$$R = 100\left(1 - \frac{Q_2}{Q_1}\right) \qquad Q_1 > Q_2 \tag{3.27}$$

A value of $R = 100$ describes a perfectly secure matching since no other template matches the orientation. According to this, values close to zero are, on the other hand, very insecure.

3.3 Scanning Electron Microscopy and Focused Ion Beam

Scanning Electron Microscopy (SEM) allows structural analysis in the micrometer down to the nanometer scale. Additionally, a Focused Ion Beam (FIB) can be used for structural modification and imaging. Modern instrumentation combines these two techniques in Dual-Beam-Systems, like the JEOL JIB-4601F, used in this work's scope. In the following, the electron optical system of the SEM, followed by the ion optical system of the FIB, as well as their mode of operation will be described.

In SEM, a convergent electron beam is scanned across the sample. The emitted secondary electrons are counted at each beam position and correlated to the image pixel intensity. A schematic drawing of the fundamental optical parts of the Dual-Beam-System can be seen in figure 3.13. The electrons are emitted by a ZrO/W(100) Schottky FEG (compare section 3.2.1) and accelerated up to 30 keV. The gun cross-over is demagnified by the condenser lenses, which form a focused probe. The cross-over can be controlled with the aperture angle control lens to modify the beam current. Increasing the cross-over leads to more electrons being blocked by the objective aperture later. The beam is moved across the sample by deflection through the scan coils. The objective lens focuses the probe onto the sample surface. Detection of secondary electrons is performed by an Everhart-Thornley detector [185]. It consists of a scintillator inside of a Faraday cage with a small attractive potential to only catch low energetic (< 50 eV) secondary electrons. Induced scintillation signals are guided to a photomultiplier and detected as an electrical current. The SEM is capable for a spatial resolution of 1.2 nm (operated at 30 kV) and magnifications of up to 10^6.

Imaging with the FIB follows the same principle as SEM. A focused probe of ions is scanned over the sample while the secondary electron yield is measured. The optical axis of the FIB has an angle of 53° to the SEM optical axis, as indicated in the schematic of figure 3.13. A liquid metal ion source (LMIS) uses gallium to create the ion beam. The gallium is heated to form a melt and positively charged ions are extracted by electrostatic lenses. The ions are accelerated by a voltage of up to 30 kV. The lenses form a sharp probe that is focused onto the sample. Scan coils are utilized to move the probe over the sample surface. An aperture is used to control the ion current and probe diameter. A resolution of 5 nm can be reached by FIB imaging at 30 kV acceleration voltage. The gallium ions are massive compared to electrons. Consequently, the momentum transfer to the specimen is tremendously increased. The ion beam is inherently destructive and will sputter atoms from the surface. This effect is used for structural modifications of the

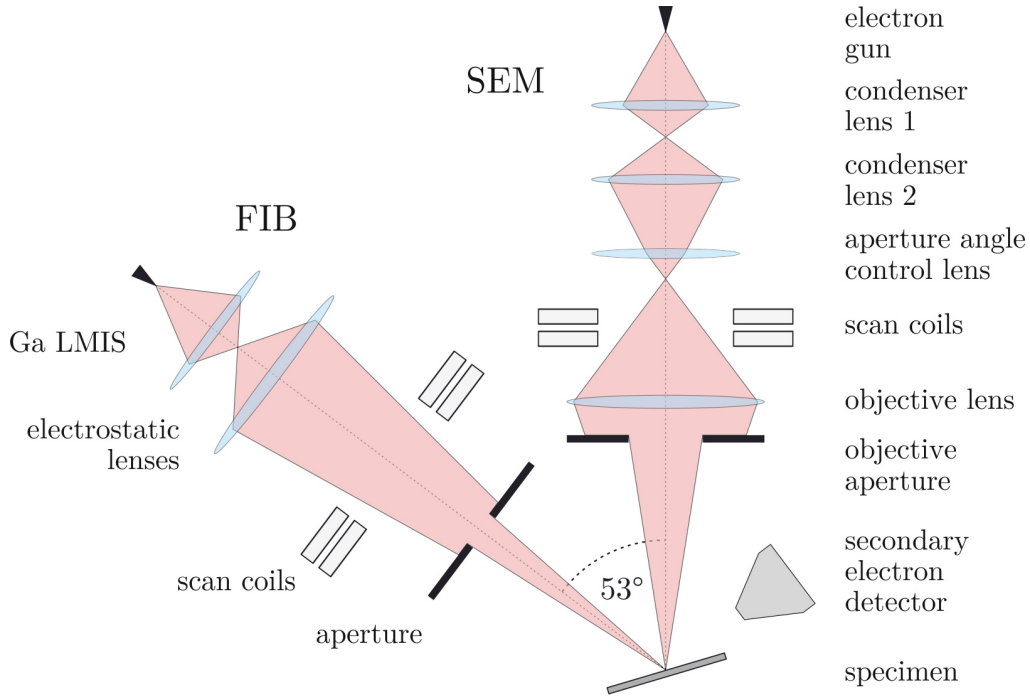

Figure 3.13: Schematic drawing of the components and beam path in the electron optical system of the SEM and ion optical system of the FIB.

sample and can even be used for TEM sample preparation, where typically thicknesses below a few hundred nanometers are needed. The drawbacks of ion beam preparations are that gallium is implanted in the sample surface as well as the creation of structurally and chemically damaged surface layers [186].

Furthermore, the Dual-Beam-System is equipped with an XFlash 5010 SDD EDX detector for chemical analysis (compare section 3.2.5) and an IB-22020GIS gas injection systems (GIS). The GIS consists of a heated tube containing typically metal organic precursor molecules that are evaporated onto the sample surface. The secondary electrons caused by the SEM or FIB lead to a chemical decomposition of these precursor gases, which leads to the deposition of material covering specific areas of the specimen. In practice, this is used to deposit surface protective layers for sample preparation, attach objects to a movable manipulator needle or support grids, or transfer TEM specimens onto the MEMS chips described in section 3.4.1. With tungsten and carbon, two different materials for deposition are available.

3.4 *In-situ* Transmission Electron Microscopy

The experimental scope of TEM is not restricted to observations of static conditions assuming that the sample remains unchanged during the experiment. Furthermore, it allows for studying dynamic processes since sequences of images are acquired in TEM, which can track potential changes in the specimen. The class of experiments where a specimen is changed or acted on while it remains under observation is referred to as *in-situ* experiments [187]. In this sense, every TEM experiment could be denoted as an *in-situ* observation, since the influence of the electron beam is tracked, but more appropriately, the term *in-situ* is used when deliberately modifying the specimen's environment. This is done with the aim to mimic the "real world", which means the real conditions prevailing out of the laboratory as closely as possible. This requires precise control and tracking of the experimental conditions the specimen is exposed to. A multitude of manipulations in the specimen's environment can be performed in TEM experiments, ranging from heating, cooling, straining, application of voltage, electric currents, or magnetic fields and the exposure of reactive gases or liquids. With this broad experimental scope, investigations on phase transformations, crystal growth, and electrical, as well as mechanical or thermal properties can be performed.

The versatile applications of *in-situ* TEM come hand in hand with increased experimental effort and complexity. Furthermore, there is no single setup enabling the whole scope of observations, but every type of experiment generally requires its own setup. One common approach is to modify the microscope itself to enable the required experimental conditions. Another is to use a special setup or sample holder with a conventional TEM. Both approaches come with their benefits and limitations. In the example of experiments performed in a gaseous environment, a microscope could be used, which allows the injection of gases into the vacuum. Such an environmental TEM (ETEM) is equipped with differential pumping stages to focus the injected reactant gases to the sample region and protect the vacuum in the rest of the column [188–190]. In principle, this maintains the imaging quality of the TEM [191] but is limited in the pressure of the gas phase at the sample of around 10^3 Pa [26]. The other option is to use a closed gas cell holder, which creates a sealed volume around the sample, which can be filled with the reactant gases. Here the drawback consists of the necessity of viewing windows inside the gas cell. The solid window interacts with the electron beam at the cost of spatial resolution, coherence and noise. But on the other hand, it enables exposing the sample to very high pressures up to 10^5 Pa [192–194], which usually matches much more with the "real world" conditions.

Furthermore, the gas volume the electron beam needs to pass is reduced and concentrated around the sample without a pressure gradient.
There are a variety of special holders available. Heating holders are equipped with a membrane at the sample region, which can be resistively heated. Cryogenic holders carry a dewar with liquid nitrogen cooling the sample. Holders based on microelectromechanical system (MEMS) chips enable the sample to be contacted electrically. Closed cell holders, also based on MEMS, allow the injection of gases or even liquids. Furthermore, they offer the possibility to combine the injection of gases or liquids with electrical biasing or heating.
The comparability to the investigated phenomenons in nature needs to be considered in all *in-situ* studies. This begins with the restrictions of TEM sample geometry. The necessity of electron transparency requires sample thicknesses below approximately 200 nm, which may strongly affect the properties of the sample compared to the bulk material. Another consideration is how closely the experimental condition in the laboratory mirror reality. The exposure to the electron beam during the TEM observation is exemplary. To estimate its influence, comparisons to unexposed sample regions can be made, as well as experiments with varying intensities or electron energies [195]. By this, it may be shown whether the beam significantly influences the specimen. However, it is beneficial to keep the electron dose as small as possible. The signal-to-noise ratio would increase by reducing the electron dose, affecting the spatial precision. To compensate for this, the exposure time could be increased, reducing the temporal resolution since it equals the exposure time. Thus a trade-off between electron dose, spatial precision and temporal resolution has to be found. For this, every experiment has its own requirements. The spatial precision σ is determined by the exposure time t and the electron dose ϱ. It follows the relation [196]

$$\sigma \propto \frac{1}{\sqrt{t \cdot \varrho}} \tag{3.28}$$

This relation is depicted in figure 3.14. The camera's sensitivity to detecting the electrons influences the limitation in electron dose. For increased sensitivity, the electron dose can be reduced accordingly without affecting spacial precision and temporal resolution. In the following, a detailed description of the modified Atmosphere gas environment setup is given, which was used in the presented work and enabled the safe handling of toxic and pyrophoric metal organic precursor gases.

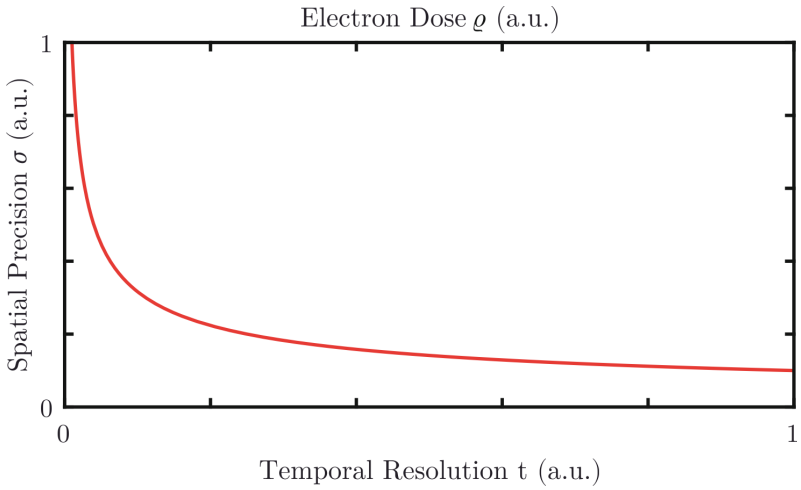

Figure 3.14: Spatial precision versus temporal resolution and electron dose (adapted from [196])

3.4.1 The Atmosphere Setup

The experimental setup needs to fulfill high safety requirements in order to perform growth experiments of III/V semiconductor materials in a safe manner. First, every gas-carrying component must be completely helium leak-tight to prevent the release of any harmful gases, which need to be disposed of after use. Moreover, the TEM laboratory needs to be equipped with a gas warning system sensitive to the precursor gases, which also need to be stored in safety containers. To comply with these safety measures, a commercially available Atmosphere system produced and designed by Protochips [197] was modified and extended [18, 198], which will be described in the following.

A piping and instrumentation diagram of the experimental setup can be seen in figure 3.15. All lines consist of non-corrosive stainless steel. On the left-hand side, the in house made gas storage locker assembly is sketched. The locker should not be placed in the same room as the TEM to enable an independent operation of the microscope and the vacuum pump, which is part of the locker assembly. Instead, it is located in a neighboring room. In the locker, the safety containers filled with the precursor gases, as well as compressed gas cylinders containing other experimental gases are stored. The locker itself fulfills the requirements of EN 14470 for fire safety and compressed gas cylinder storage. This means that it is fire safe and that all openings close automatically in case of a fire. Furthermore, an external ventilation system is attached to the locker preventing the accumulation of dangerous gases inside the locker. The liquid precursors are stored in stainless steel

bubblers with blind flanged dip tubes. In contrast to MOVPE systems, the setup operates with pure precursor gases at their respective vapor pressure. Consequently, no carrier gas is conducted into the bubbler through the dip tube. All lines can be evacuated by an Ebara EV-PA50 dry vacuum pump. The pumped gases get disposed of via a CS Cleaning Solutions AG Miniabsorber scrubbing system. An inert gas source is available with a high purity (9.0) nitrogen line with a pressure of 1 bar. The gas storage locker is connected via stainless steel lines to the manifold sketched on the right-hand side of figure 3.15. Group III and V precursors are connected to different source lines to avoid cross-contamination. The components in the manifold, located next to the microscope, are software controlled.

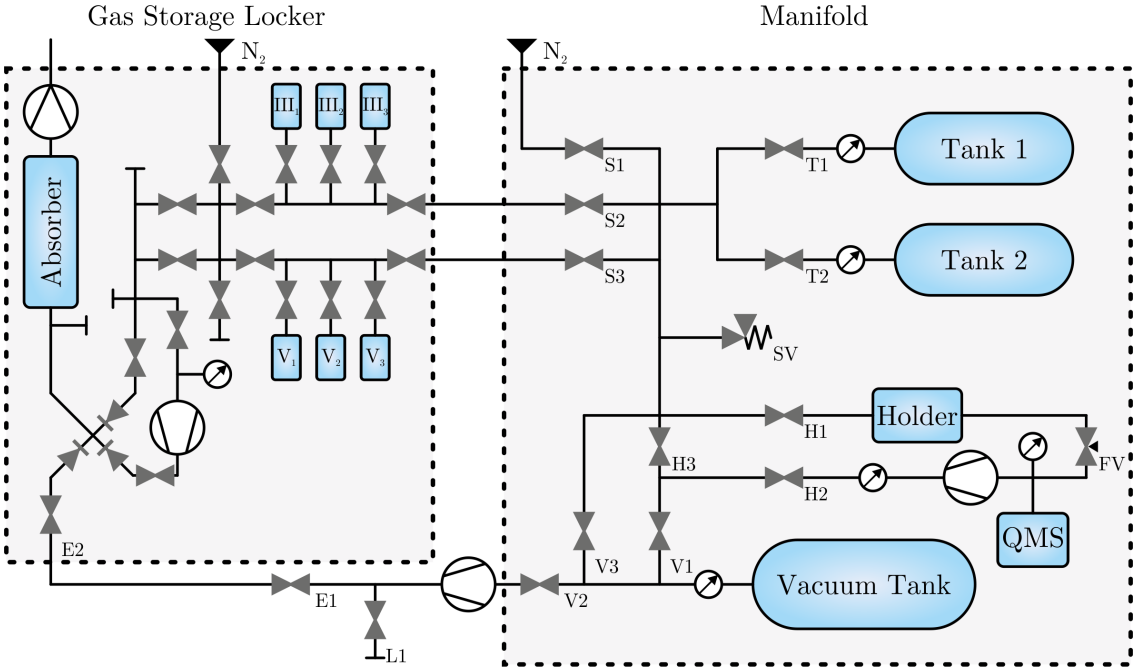

Figure 3.15: Piping and instrumentation diagram of the Atmosphere setup. The left part shows the home-built gas storage locker. On the right-hand side, the gas mixing manifold is depicted. (S1-S3: Source valves, T1-T2: Experimental tank valves, H1-H3: Holder valves, V1-V3: Vacuum tank valves, FV: Flow valve, SV: Overpressure security valve, E1-E2: Exhaust valves, L1: Leak test valve)

All valves are pneumatically switched. The experimental tanks 1 and 2, with a volume of 0.75 L each, act as a gas reservoir during an experiment. A defined gas mixture can be created in either one of the tanks by opening the sources via valves S1, S2, or S3 after one another. The pressure increase in the evacuated tank is measured, and the partial pressures of every gas species are controlled automatically by the software. The evacuated vacuum

tank with a volume of 2 L creates a pressure gradient with respect to the experimental tanks. The experimental gases are sucked through the TEM holder towards the vacuum tank without a vacuum pump causing vibrational imaging noise during an experiment. The gas flow is adjusted by a flow valve (FV) at the output line of the TEM holder. The valve manipulates the gas flow by changing its area of flow. Furthermore, it acts as an inlet valve for the ionizer chamber of the mass spectrometer, which is pumped by an Agilent TwisTorr 84 turbo molecular pump. A description of the QMS follows in section 3.4.2. The manifold can be evacuated by an Edwards XDS10 dry scroll vacuum pump, which conducts all gases towards the scrubbing system in the gas storage locker. The gas-conducting components are wrapped in heating wires that can be used to bake out the manifold at up to 75 °C for desorption of contamination from the inner surfaces. Both the locker and the manifold are modified by the addition of a leak test port enabling the attachment of a helium leak tester to check the gas tightness of the setup.
The Atmosphere *in-situ* gas cell and heating TEM holder is the core component of the setup. A cross-section is sketched in figure 3.16. The closed cell is built up by two MEMS chips, consisting of 300 µm thick silicon. They lie on top of each other on O-ring seals. The

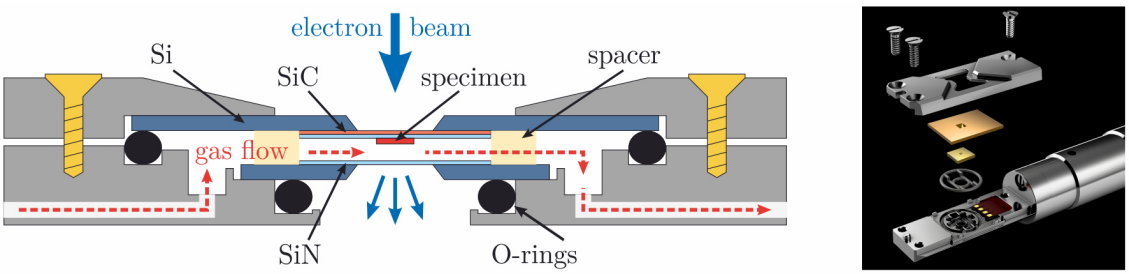

Figure 3.16: Left: Cross section of Atmosphere TEM holder tip. Right: Explosion render of the holder tip

holder lid, fixed by brass screws, presses the chips onto the O-rings and seals the volume. The smaller MEMS chip carries a 5 µm thick gold or SU-8 polymer spacer that defines the gas volume height and prevents the chips from touching each other. To form a viewing window into the cell, holes are etched into the silicon covered by a silicon nitride (SiN) membrane. One of the chips carries the sample and is equipped with a silicon carbide (SiC) heating membrane of 120 nm thickness beneath the 30 nm SiN membrane. This chip is called a thermal chip, whereas the one without a SiC membrane is called a window chip. Its SiN window thickness is 50 nm. A cross-section of the thermal chip can be seen in figure 3.17. The SiC membrane is a negative temperature coefficient (NTC) thermistor. It can

be heated by an electrical current. Its resistance is negatively correlated to its temperature [199, 200]. Hence, the membrane's temperature can be determined by measuring the resistance and comparing it to a resistance-temperature calibration curve. This is done by a closed control feedback loop. Gold traces at the MEMS chip surface electrically connect the heating membrane via the connections at the holder tip with the manifold. In the center of the membrane, six circular holes with a diameter of 9 µm and a spacing of 20 µm are etched into the SiC. They are covered by the SiN to seal the gas cell and determine the regions where the sample can be observed. Despite its thickness, the SiC is electron transparent. However, a significant fraction of the electron beam is scattered inelastically or absorbed, impeding good contrast imaging. Between the O-ring seals, there are gas

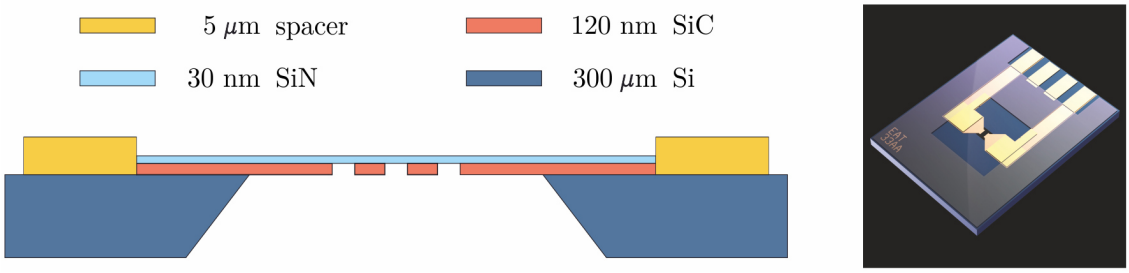

Figure 3.17: Left: Cross section of the thermal MEMS chip (adapted from [197]). Right: Rendering of the thermal chip.

inlet and outlet lines connected to the manifold to conduct the experimental gases through the holder tip across the sample. The total pressure at the sample is determined by the pressure in the experimental tank, and the leak valve at the holder's outlet line controls the gas flow rate. The gas cell is capable of total pressures of 10^5 Pa, and temperatures up to 1000 °C can be applied to the sample by the SiC heating membrane.

The thermal chip can be chosen to be the larger one, located at the top of the cell, or the smaller one, at the bottom. The first case is called a STEM-optimized geometry since less interaction of the electron beam with the membranes and gas volume takes place before it impinges the sample. Additionally, due to less screening of the MEMS chip and holder, the position at the top is beneficial for EDX, which is usually performed in STEM mode. The latter cell geometry, with the sample on the small MEMS chip at the bottom, is called a TEM-optimized geometry. Here the electron beam interacts less after it has transmitted the sample and its coherence is less affected. This assembly is advantageous for observations in TEM mode. Both configurations are capable of atomic resolution imaging under atmospheric pressure and elevated temperatures [201].

The back-streaming residual gases can be analyzed by a residual gas analyzer located at the outlet line of the holder. This is described in detail in the next section.

3.4.2 Residual Gas Analysis via Quadrupole Mass Spectrometry

In the following, the working principle of quadrupole mass spectrometry (QMS) is described. It builds on the physics of ionization and quadrupole mass filtering explained in chapter 2.3. The *in-situ* setup is equipped with an SRS RGA200 residual gas analyzer (RGA). It analyzes residual gases by ionizing some gas molecules to positive ions, separating them according to their respective masses, and measuring the ion currents at each mass. The device consists of three main parts: the ionizer, the quadrupole mass filter (QMF) and the ion detector. All these parts are in a vacuum, pumped by a turbo molecular pump. A pressure of 10^{-3} Pa or less is required for proper operation. The following descriptions and specifications are taken from reference [202].
The ionizer is of an open wire mesh design with cylindrical symmetry mounted co-axially with the filter assembly. A sketch can be seen in figure 3.18. Injection of the gas analyte

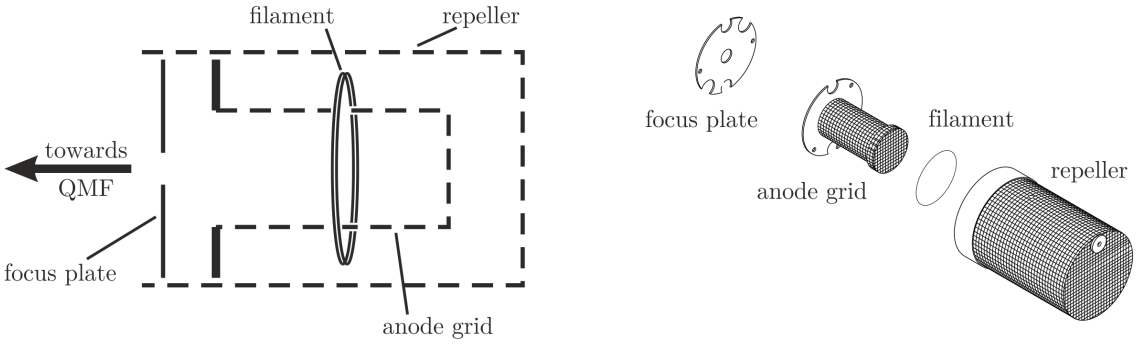

Figure 3.18: Cross section sketch of the cylindrical ionizer and explosion drawing [202].

takes place perpendicular to the cylinder axis. A 1 mA electron current is emitted thermally by a resistively heated dual thoria-coated iridium (ThO_2/Ir) wire filament, which is on a negative potential. The positively charged anode grid accelerates the electrons to an energy of 70 eV for electron impact ionization (EI). Most pass the open mesh grid and may interact with the analyte in the center of the ionizer. Electrons that did not interact or did not hit the grid enter the space between the anode grid and repeller and get re-accelerated towards the center until they ionize a molecule or are captured by the grid. The repeller is on a negative potential preventing the loss of electrons. Due to the increased electron density in the center of the anode grid volume, created ions get attracted to the center

and tend to stay within the anode. They are extracted from the ionizer by the electric field produced by a 12 V difference in voltage between the anode grid and focus plate, which is on a negative potential and collimate the ions into the filter section.
A quadrupole with cylindrical electrode rods is utilized as a mass filter. In practice, hyperbolic rods, as they were introduced in chapter 2.3, are very challenging to fabricate. It was shown that it is also possible to use cylindrical electrodes, which are easy to manufacture, if their radius is $r = 1.1486 \cdot r_0$ with r_0 being the distance of the electrodes to the center axis [203]. Figure 3.19 a) shows the ideal hyperbolic arrangement. The used filter consists of two pairs of cylindrical electrodes with length L arranged in a quadrupole geometry. The pair of electrodes in x-direction is on the potential $-\Phi_0$, whereas the ones in y-direction are on the potential $+\Phi_0$, as it is shown in figure 3.19 b). The rods have a length of 11.43 cm, a radius of $r = 0.318$ cm and a spacing of $2r_0 = 2 \cdot 0.277$ cm resulting in the ratio $\frac{r}{r_0} = 1.148$ to minimize deviations from the quadrupole field of hyperbolic rods [203]. For this geometry, the resulting field can be approximated with the ideal quadrupole field in the case of hyperbolic electrodes. As it was derived in chapter 2.3, stable trajectories depend on a_μ and q_μ, which themselves depend on the experimental parameters. Namely, the applied electrode voltages U and V, as well as the voltage's

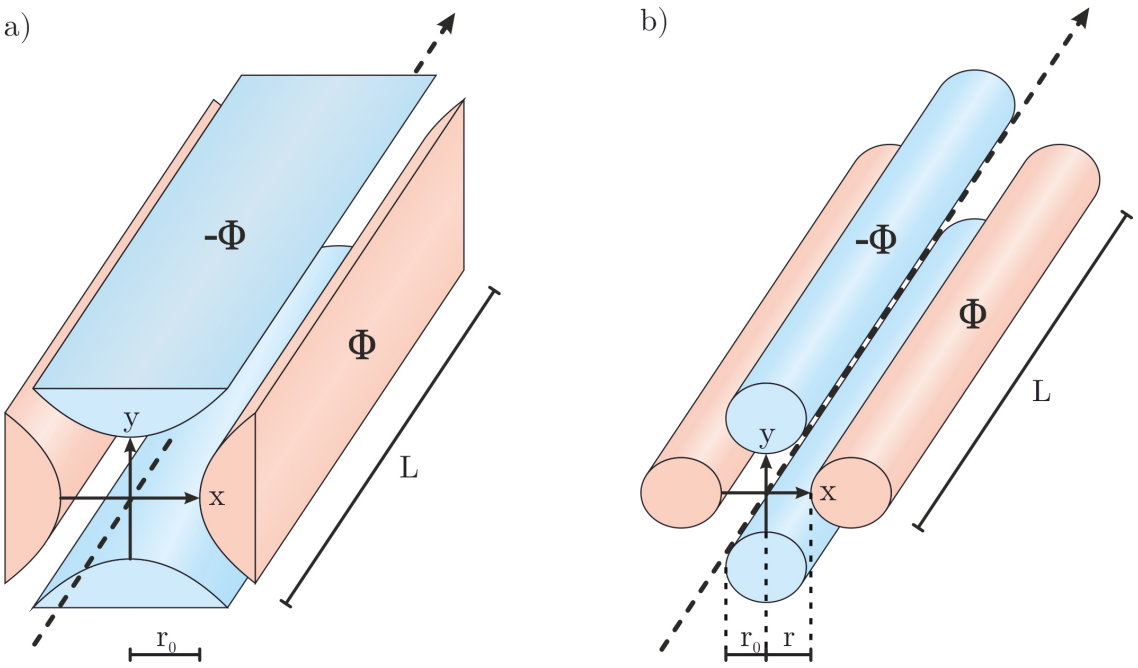

Figure 3.19: Filter geometry with a) hyperbolic electrodes and b) round electrodes

angular frequency ω, as can be seen in the equations (2.27). Thus, whether a trajectory is stable can be controlled by adjusting the voltages and the angular frequency to end up in the stability region for a given ion mass. Usually, ω is held constant, while U and V are controlled since it is easier to tune the voltages than the angular frequency precisely. The angular frequency of operation is fixed at approximately 17.4 MHz. Equation (2.27) furthermore shows, that a_μ and q_μ linearly depend on U and V respectively and inversely on the ion mass m. Operating the QMF at a fixed voltage ratio of

$$\frac{a_\mu}{q_\mu} = \frac{2U}{V} = const. \tag{3.29}$$

results in a straight line through the first stability region (I) (compare figure 2.11) in the a_μ-q_μ-space with the ratio being its slope. Stability region I is plotted in more detail in figure 3.20. The trajectories stable in x are bound by a_0 and those stable in y by b_1, highlighted in red and blue, respectively. The yellow region marks the stability region, with stable trajectories in both x and y. The position of an ion mass m on that line is defined by the absolute values of U and V. Higher masses are located closer to the origin. Increasing the voltages shifts the mass to higher values of a_μ and q_μ and vice versa. By this, a specific mass can be shifted into the stability region, enabling it to pass the QMF. If this line, called the mass scan line, intersects the stability region directly beneath its apex, only a single ion mass can pass the filter. This can be realized by adjusting the slope close to $\frac{2U}{V} \approx 0.3358$. In other words, the x-z-plane of the QMF acts as a high-pass filter transmitting higher masses, whereas the y-z-plane acts as a low-pass filter transmitting lower masses. They are controlled in a way that the overlap contains only a single stable mass. The QMF acts as a band-pass filter. To record a mass spectrum, the voltages are increased linearly, which leads to a linear increase of the stable mass intersecting the stability region. In this way, the mass is scanned across the spectrum in a range between 1 u and 200 u, and the amount of passing ions is measured. The mass scan line crosses the stability region between the intersections with a_0 at (a_1,q_1) and b_1 at (a_2,q_2). With this, the mass resolution R is defined as

$$R = \frac{a}{\Delta a_\mu} = \frac{q}{\Delta q_\mu} = \frac{m}{\Delta m} \tag{3.30}$$

with $\Delta a_\mu = a_2 - a_1$, $\Delta q_\mu = q_2 - q_1$, Δm being the range of stable masses and a, q and m being the mean of a_μ, q_μ and m at the two intersects respectively.
For small applied potentials at the beginning of a scan, ions entering the filter may be

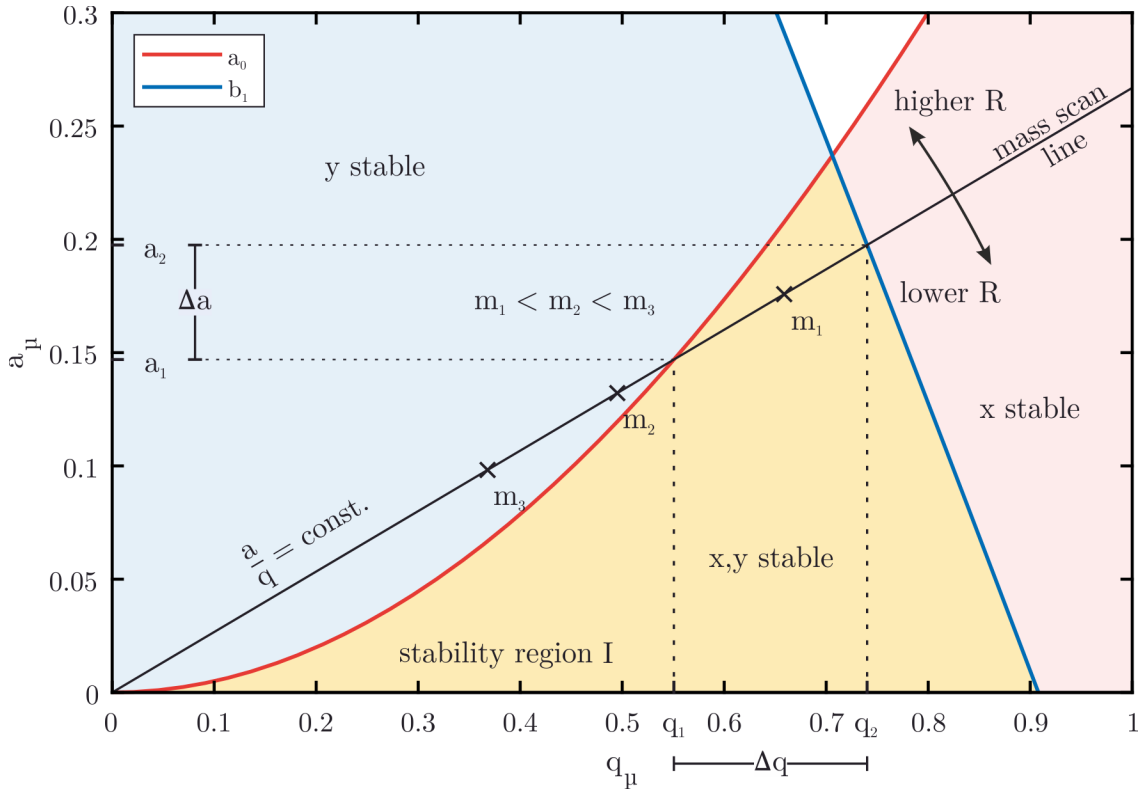

Figure 3.20: Operating principle in first stability region.

transmitted even though their trajectories are mathematically unstable. This is called zero blast and affects masses below approximately 1.5 u. Due to this, measurements are unreliable for hydrogen gas having a fragmentation pattern located at 1 u and 2 u.
The stability diagram depicts an ideal QMF. In reality, imperfections appear due to the finite radius and length of the field, the presence of fringing fields at the entrance as well as at the exit of the quadrupole, and deviations from the perfect quadrupole field [204].
The transmitted ions can either be detected with a Faraday cup (FC) or a macro multi-channel continuous dynode electron multiplier (CDEM). A sketch of the detector components and geometry is depicted in figure 3.21. The FC is a small metal bucket located on-axis behind the filter, shielded from the quadrupole field by a grounded plate at the QMF exit and a cylindrical tube. Positive ions hit the grounded detector and are neutralized by electron transfer from the metal to the ion. The extracted electrons create an electrical current, which can be measured. It corresponds to the incident ion current and is independent of the ion mass. With the FC, partial pressures down to approximately

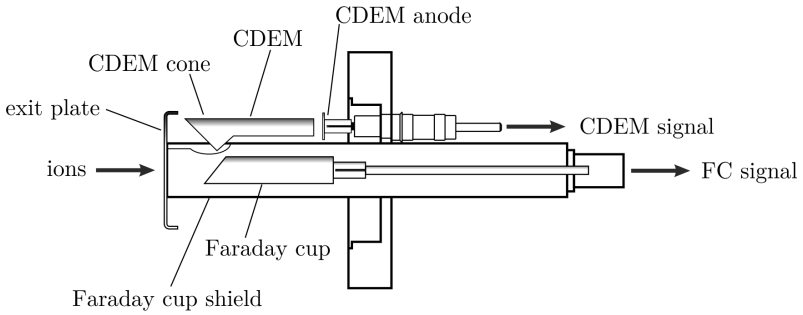

Figure 3.21: Components of the ion detector [202].

10^{-8} Pa can be detected. However, it is more beneficial to use the CDEM to detect partial pressures below 10^{-7} Pa, which has a higher sensitivity leading to an increased signal-to-noise ratio enabling faster scan rates. The CDEM consists of a straight channel tube made of resistive glass for high secondary electron yield. It is mounted off-axis up right next to the FC (see figure 3.21). A cone of the same material is attached to the front end, which is biased negatively relative to the back end. By this, the positively charged ions are efficiently attracted to the cone with high velocities and produce secondary electrons. These are subsequently accelerated down the channeled tube and produce more and more secondary electrons. A single ion can result in up to 10^7 secondary electrons impinging the anode at the end of the tube. The gain of secondary electrons is a function of the bias voltage. The total gain varies as a function of the mass of incident ions and decreases with increasing mass. This is caused by the dependence of ion-electron conversion efficiencies on the velocities of the ions. High gains result in a high sensitivity but a reduced dynamic range. With the parameters used in this work, partial pressures down to 10^{-12} Pa can be measured. However, the detector saturates at higher partial pressures than 10^{-6} Pa. To detect such pressures operation of the FC is suggested.
The total intensity H_M at a mass over charge ratio M, which is measured as an overlap of all fragmentation patterns h_{M_g} of molecular species g present in the analyte gas [205]. It can be described as

$$H_M = \sum_g h_{M_g}. \tag{3.31}$$

h_{M_g} depends on the fragmentation factor α_{M_g}, which describes the ratio of the intensity at mass over charge ratio M to the base peak intensity, the mass spectrometers sensitivity factor S_g and partial pressure p_g for the gas species g.

$$h_{M_g} = \alpha_{M_g} S_g p_g = \mu_{M_g} p_g \tag{3.32}$$

The fragmentation factor α_{M_g} and sensitivity factor S_g, combined to the spectrometer-specific fragmentation pattern $\mu_{M_g} = \alpha_{M_g} S_g$ are specific for each mass spectrometer and may vary for different setups. α_{M_g} is mainly determined by the ionization conditions like electron energy, electron current and ionizer type. S_g is defined by the ratio of the change ΔH in principal mass peak height to the corresponding change Δp in total pressure due to a change in partial pressure of the particular gas species g [206].

$$S_g = \frac{\Delta H}{\Delta p} \tag{3.33}$$

The setup is capable of *in-situ* residual gas analysis while observing the specimen in the TEM. This is used to investigate the thermal decomposition of metal organic precursor gases in the TEM holder. However, the temporal resolution of the mass spectrometry data is significantly reduced in this setup. This is due to the length of the outlet line between the holder and RGA of 1.35 m. The gas streaming back from the holder tip is pent up in that line by the leak valve. The time Δt it takes to reach the spectrometer depends on the volume flow rate Q, which depends on the mass flow rate q and the total pressure p. The equation $Q = \frac{q}{p} kT$ applies with Boltzmann constant k and temperature T. Δt can be estimated by

$$\Delta t = \frac{L}{v} = \frac{L \cdot A}{Q\,(q,p)} \tag{3.34}$$

with length L, gas velocity v and line cross sectional area A. For a pressure $p = 100\,\mathrm{hPa}$ and mass flow rate $q = 0.01\,\mathrm{sccm}$, which are the parameters used in the decomposition experiments, as well as a cross-section of $A = 0.8\,\mathrm{mm}^2$ the expected delay is $\Delta t \approx 11\,\mathrm{min}$. Furthermore, this implies that radicals that might be formed in the holder tip will react with other particles before they reach the RGA and won't be detected directly. Only their reaction products permit conclusions about their formation.

3.4.3 Pre Experimental Procedure

Experiments performed with the Atmosphere *in-situ* setup suffer from increased contamination issues compared to conventional TEM observations performed in the high vacuum conditions of the microscope column. Consequently, an increased amount of electron beam-induced depositions is observed during imaging. The specimen's environment is coupled to a system of gas volumes. Keeping the amount of contamination in any gas or vacuum system sufficiently low is challenging. Especially getting rid of water and oxygen, which react heavily with TMGa and TBP, is difficult and can only be achieved partially. This behavior leads to an increased amount of beam-induced contamination during TEM observations. Nevertheless, there exist measures to minimize this issue. First, it is crucial to keep the contamination in the system as low as possible. For this reason a bake-out of the manifold is performed after every experiment to desorb impurities from the inner surfaces. During the bake-out, the whole volume is heated to 75 °C and continuously evacuated. Beside the bake-out procedure, the entire system, including the gas storage locker, undergoes pump and purge cycles whenever the system is not in use, and no measurements are taking place at the microscope. In these cycles, the volume is repeatedly evacuated to a pressure of 0.1 hPa and filled again with ultra-pure nitrogen (9.0) up to a pressure of 1000 hPa. By this, impurities are rinsed off the surfaces and get diluted out of the system. Together this builds an efficient procedure to reduce contamination. A further source of contamination is impurities introduced by the specimen and its preparation process. In conventional TEM, this issue is tackled by plasma cleaning the specimen in the holder tip, effectively reducing impurity issues. During this process holder and sample are stored for a few minutes in a low-pressure argon-oxygen mixture [207]. A high-frequency voltage ignites an argon-oxygen plasma. Due to knock-on damage, argon ions break bonds of organic molecules at the sample surface. Then, the oxygen ions bind to these fragmented molecules forming gaseous species, which can be pumped out of the volume. This procedure is impossible with the assembled Atmosphere holder since it creates an isolated volume around the specimen. However, the individual parts, namely the two MEMS chips, including the specimen and the open holder tip can be plasma cleaned independently before the holder tip is assembled. This procedure is less effective compared to conventional holder designs since the holder and the specimen are again exposed to impurities during the assembly. However, it reduces the amount of contamination. A decontamination process of the specimen in the closed holder cell is given by heating the sample with the use of the SiC membrane and applying nitrogen pump and purge cycles to

the holder volume. By heating to elevated temperatures of several hundred degrees Celsius, impurities desorb from the hot surface and can be carried away by the streaming nitrogen. The heating temperature is mainly limited by the thermal stability of the specimen. This procedure can also be applied during an experiment and can effectively reduce electron beam-induced depositions.

CHAPTER 4

Results

In the following chapter, the central results are presented. First, findings on the thermal decomposition of metal organic precursors investigated by mass spectrometry are discussed in section 4.1. These experiments deal with the comparability between the micrometer scaled *in-situ* TEM reactor and ordinary MOVPE machines by comparing the temperature-induced gas phase reactions. Subsequently, in section 4.2, the results of the live observation of GaP nanowire growth are discussed, which have been performed by *in-situ* STEM. The real-time monitoring of the growth process enables insights concealed in post-growth studies. For example, it was found that the nanowires growth rate strongly depends on the liquid droplet geometry. However, post-growth investigations deliver indispensable complementary information. Some of these are presented in section 4.3. There, SPED was used to investigate the crystal structure and defect in the grown wires. Thereby, mechanisms of kink formation were revealed. Finally, in section 4.4, the chapter is closed with the results on substrate preparation for *in-situ* TEM experiments on VLS growth, which will enable atomically resolved imaging of the growth process by controlling the crystal orientation and bringing it into zone axis.

4.1 Thermal Precursor Decomposition

It is not apparent from the start if obtained results in the microreactor of the TEM holder tip are meaningful for processes proceeding in large industrial reactor designs. To tackle the question of given comparability, experiments can be performed in which the outcome in conventional reactors is known. Reproducibility of these results hints that obtained results in the *in-situ* TEM setup also apply to the real-world conditions. This will be done

by the observation of thermal precursor decomposition, which is a substantial process in MOCVD and MOVPE. The reaction temperatures and pathways are essential parameters that strongly determine the growth process (see chapter 3.1.1).
The decomposition is investigated by mass spectrometry of the residual gas streaming back from the heated holder volume. Temperature-induced changes in the recorded mass spectra reveal insights into the proceeding reactions and can be compared to the literature. Thermal decomposition experiments were performed with a N_2 carrier gas with a partial pressure of 100 hPa. Flow rates were kept constant at 0.01 sccm to ensure a constant pressure in the spectrometer of 9×10^{-6} hPa and thereby constant signal intensities, which are proportional to the pressure. First mass spectra were recorded of pure N_2 in all experiments. This allows measuring the background and carrier gas signal at the specific spectrometer pressure, which is described in the next section in more detail. The precursor partial pressures were adjusted to 1 hPa. This rather huge amount of precursor in the analyte is chosen to increase the measured precursor signal. By use of partial pressures present during growth processes in the range of 10^{-3} hPa, most of the peaks would either be unable to separate from overlapping peaks or vanish in noise.
However, the exact gas phase temperature is still unknown in the utilized setup. Furthermore, the surface of the heated area is in the order of only 0.01 mm^2. The surrounding region obtains a negative temperature gradient with increasing distance to the center. The investigation of a thermal MEMS chip used in a TMGa decomposition experiment with a step-wise temperature increase of 50 °C shows ring-like carbon depositions around the membrane center. These can be seen in the SEM image in figure 4.1. The center of the SiC heating membrane is the sample region possessing the highest temperature, which is given by the nominal membrane temperature. The observed rings are highlighted by white lines in the upper left part of the image. The embedded $C_{K\alpha}$ EDX map colored red shows an accumulation of carbon in the rings. It will be shown in section 4.1.3 that TMGa forms methane and methyl radicals by decomposition, which act as a carbon precursor [52, 104, 208]. Other elemental accumulations are not observed in the rings. The carbon rings enable an estimation of the temperature distribution. The step-wise temperature increase by 50 °C leads to pyrolysis and by this to deposition at higher distances to the membrane center where the required temperature is reached. The outermost deposition ring is produced with the highest applied temperature of 950 °C. The innermost ring, which is the first ring deposited during the experiment, is therefore built up by a membrane temperature of 600 °C. Since all rings emerge at the same temperature, it can be concluded that the temperature difference between the ring positions is approximately 50 °C and that

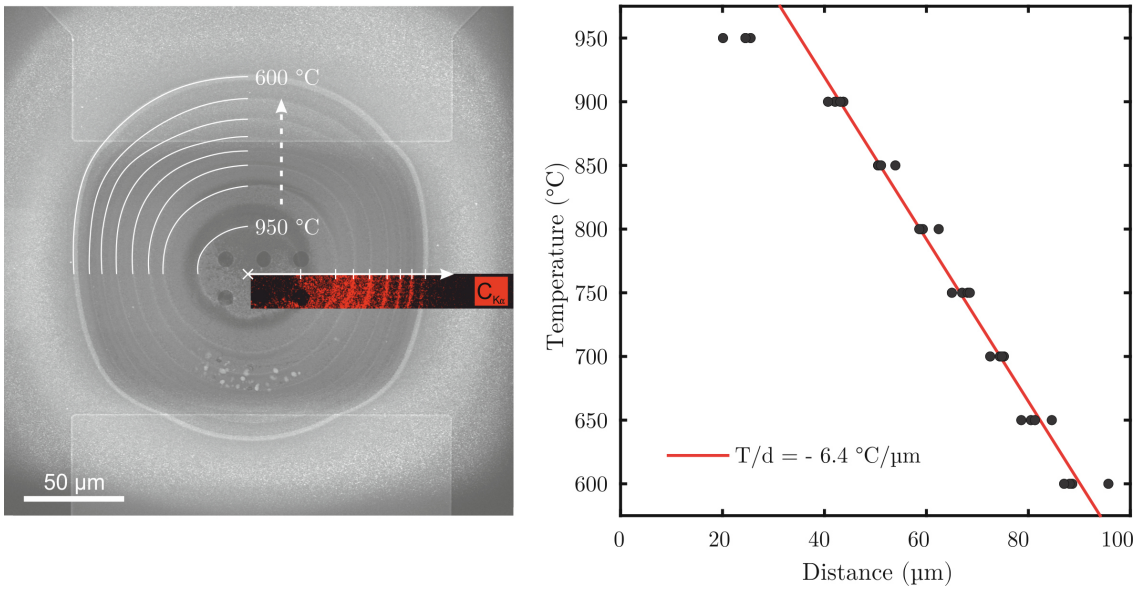

Figure 4.1: Left: SEM image of SiC membrane after TMGa decomposition experiment with 50 °C temperature steps. The formed rings are indicated with their corresponding temperature at a nominal membrane temperature of 950 °C. The inset shows an EDX elemental map of the carbon K_α line. Right: Distances of the rings from the membrane center marked by the white cross correlated to their temperature at nominal membrane temperature of 950 °C.

the outer ring is also formed at 600 °C while the highest nominal membrane temperature of 950 °C was applied. This leads to the radial temperature distribution shown in the right plot of figure 4.1. Excluding the innermost ring, the spacing between the carbon depositions is approximately constant. Distances are determined from the membrane center, marked with the white cross, in vertical and horizontal radial directions, as indicated for one direction by the white arrow. The temperature gradient at distances above 40 µm from the center is determined to $(-6.4 \pm 0.2)\,°\mathrm{C\,\mu m^{-1}}$ by a linear fit. This gradient is expected to vanish close to the membrane center since the temperature is constant in the area of SiN windows. Consequently, the gas is exposed to all temperatures between room temperature and the nominal membrane temperature. Mass spectrometry measurements on the thermal precursor deposition represent an overlap of these temperatures. Derived mass spectra intensity values are not calibrated with respect to the ionization cross section of specific molecular species and their spectrometer sensitivity since they are unknown for the used spectrometer setup. Determinations of exact partial pressures are therefore inac-

cessible without calibration measurements of the gas species with known partial pressure. Nevertheless, relative intensity changes are capable of revealing gas phase reactions.

4.1.1 Mass Spectrum Data Analysis

During *in-situ* experiments, experimental parameters and measured quantities are tracked continuously for temporal information. In mass spectrometry measurements, this results in several hundreds of single mass spectra, each containing up to hundred peaks. To evaluate this data and reveal its temporal evolution in a reasonable time, software-based evaluation is required. For this reason, a MATLAB-based program was written that evaluates the recorded spectra [209].

Peaks in an ideal mass spectrum are expected at integer values as sharp delta-like spikes. However, in reality, they obtain a broadened distribution that might not be centered around the expected position. The delocalization of peaks in a recorded mass spectrum versus the corresponding integer mass over charge value is plotted in figure 4.2 a) with black dots. It can be seen that for values above 50 u, the delocalization of the peak might become greater than 0.5 u, leading to a wrong peak position assignment. In a first step, the peak positions are determined in an interval between 5 u and 80 u, where they

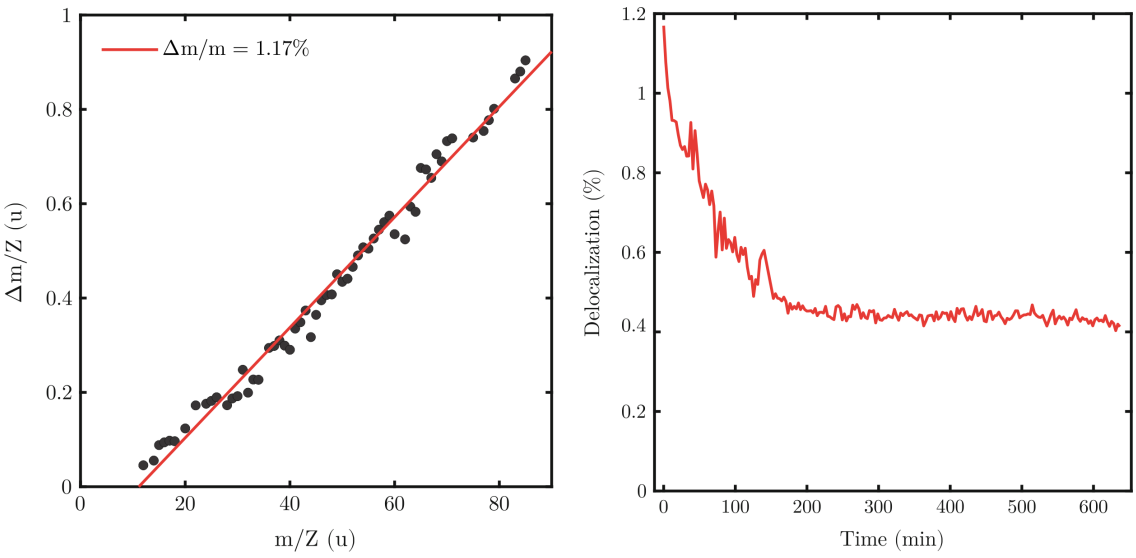

Figure 4.2: a) Measured m/Z values of a mass spectrum versus the expected ones (black dots) at $t = 0$ min. Higher values are increasingly displaced to higher masses. A linear fit (red) determines the factor of displacement Δm/m. b) Temporal evolution of the displacement factor in successively recorded mass spectra.

can be assigned correctly with knowledge about the delocalization. This is done by the Richardson-Lucy deconvolution algorithm [210, 211] with a Gaussian-shaped point spread function. The algorithm's output is delta peaks at mass over charge ratios possessing a peak in the spectrum. With a linear fit, the mass over charge axis of the mass spectrum can be scaled to the correct values. The fit is displayed in red in figure 4.2 a). This procedure has to be applied to every spectrum independently since the scaling of the m/Z-axis changes with time. In figure 4.2 b), the temporal evolution of the slope a of the linear fit can be seen. Especially during the first 200 min the deviation decreases from $a > 1\,\%$ and approaches to an plateau of $a \approx 0.4\,\%$.
Once the peak positions are known and correctly assigned to the mass over charge value, the peak intensity is determined. The most accurate way is to find a distribution function that describes the peak shape and fits it to the detected peaks. Then, the integral of the fitted distribution function determines the peak intensity. Convolutions of Gauss, Lorentz and Boltzmann distributions with a box profile were tested. Thereby, the distribution functions model the point spread function of the spectrometer, whereas the box profile represents the bandpass filter nature of the QMF. However, none of these functions is able to model the peak shape satisfactorily. This is due to unsymmetrical peak tails and peak apexes caused by the finite length of the cylindrical QMF electrodes, their imperfect quadrupole field, including fringing fields at the entrance and exit of the filter, and intrinsic oscillations of the transmitted ions itself [212, 213]. Therefore, peak intensities are determined by the sum of measured intensity values within a peak. An intensity of a peak at mass over charge ratio M determined in this way is represented by the quantity H_M.
As described in chapter 3.4.2, recorded mass spectra contain signals of every gas species g present in the analyte mixture. These individual signals possess a characteristic fragmentation pattern on the m/Z-axis overlapping each other. Thus, a real mass spectrum might contain at a single m/Z value intensity contributions from multiple gas species that need to be separated from each other. The total intensity H_M in a mass spectrum at mass M is the linear combination of the fragmentation patterns h_{M_g} of gas species g at this mass (equations (3.31)). The individual contribution to H_M depends on the partial pressure of the species and the spectrometer specific fragmentation pattern (equation (3.32)). For precursor decomposition measurements, the signal can be divided into the contribution of background gas species (BG), nitrogen (N), undecomposed precursor

(p) and the precursor's decomposition products (d). The measured signal H_M can be described by

$$H_M = h_{M_{BG}} + h_{M_N} + h_{M_p} + h_{M_d}. \tag{4.1}$$

To separate these contributions from each other, $H_M^{(1)} = h_{M_{BG}} + h_{M_N}$ is derived in a measurement of pure nitrogen as analyte. By adding the precursor gas at a specific partial pressure to the mixture, $H_M^{(2)} = h_{M_{BG}} + h_{M_N} + h_{M_p}^{(2)}$ is measured. Its fragmentation pattern overlaps with the previously measured one, and the precursor's peak intensity distribution $h_{M_p}^{(2)}$ can be obtained with

$$h_{M_p}^{(2)} = H_M^{(2)} - H_M^{(1)}. \tag{4.2}$$

Decomposition of the precursor is initiated by increasing the heating membrane's temperature. Additional decomposition species arise in the analyte gas mixture. The measurable quantity is $H_M^{(3)} = h_{M_{BG}} + h_{M_N} + h_{M_p}^{(3)} + h_{M_d}$, describing the superposition of background intensities, nitrogen, gaseous precursor and decomposition products. If the precursor gas decomposes, its partial pressure will decrease ($p_p^{(3)} < p_p^{(2)}$). Since $h_{M_g} \propto p_g$ (equation 3.32) one can derive

$$h_{M_p}^{(3)} = \frac{h_{M_p}^{(2)}}{p_p^{(2)}} p_p^{(3)} \tag{4.3}$$

Background intensities, as well as the nitrogen pattern are not affected and do not change compared to $H_M^{(2)}$. In case the fragmentation pattern of the precursor h_{M_p} contains an interference-free peak at a mass m^*, meaning no other gas species contain a peak at this mass, this peak intensity can be correlated to the precursor's partial pressure. During decomposition, it can be determined by

$$p_p^{(3)} = \frac{H_{m^*}^{(3)}}{H_{m^*}^{(2)}} p_p^{(2)}. \tag{4.4}$$

The partial pressure is decreased by the ratio of the interference-free peak intensities after ($H^{(3)}_{m^*}$) and before ($H^{(2)}_{m^*}$) decomposition. Finally, the decomposition product's peak intensity distribution can be determined with the use of equations (4.3) and (4.4) by

$$h_{M_d} = H^{(3)}_M - H^{(1)}_M - \left(H^{(2)}_M - H^{(1)}_M\right) \frac{H^{(3)}_{m^*}}{H^{(2)}_{m^*}}. \tag{4.5}$$

If no independent peak is present, only the superposition of $h^{(3)}_{M_p}$ and h_{M_d} can be derived

$$h^{(3)}_{M_p} + h_{M_d} = H^{(3)}_M - H^{(1)}_M \tag{4.6}$$

and compared to $h^{(2)}_{M_p}$.
The same procedure can be applied for mixtures of precursor gases, which may behave differently in the bimolecular case in terms of the decomposition temperature and fragmentation pattern compared to unimolecular reactions. The gas phase can be again divided into background gas species (BG), nitrogen (N), undecomposed precursors (p_1 and p_2) and their decomposition products (d). The measurable signal is described by $H^{(4)}_M = h_{M_{BG}} + h_{M_N} + h^{(4)}_{M_{p1}} + h^{(4)}_{M_{p2}} + h_{M_d}$. For both precursors the unimolecular undecomposed case $H^{(2)}_{M_{p_1}}$ and $H^{(2)}_{M_{p_2}}$ need to be known. Additionally, independent peaks in both fragmentation patterns at masses m^*_1 and m^*_2 are required. Then, the bimolecular decomposition fragmentation pattern can be derived by

$$h_{M_d} = H^{(4)}_M - H^{(1)}_M - \left(H^{(2)}_{M_{p_1}} - H^{(1)}_M\right) \frac{H^{(4)}_{m^*_1}}{H^{(2)}_{m^*_1}} - \left(H^{(2)}_{M_{p_2}} - H^{(1)}_M\right) \frac{H^{(4)}_{m^*_2}}{H^{(2)}_{m^*_2}}. \tag{4.7}$$

If for m^*_1 or m^*_2 are no independent peaks available, the decomposition product peak intensity cannot be separated from the respective precursor peak intensities just like in the unimolecular case. Nevertheless, relative changes in the overlapping peak intensities can enable qualitative conclusions on the proceeding reaction pathways.

4.1.2 Thermal Decomposition of TBP

TBP is an established metal organic source molecule for phosphorus that has been studied with respect to its decomposition behavior [208, 214–217]. In section 4.1.1, the necessity of knowing the precursor's fragmentation pattern h_m for determining the fragmentation products was explained. It was measured with the use of an analyte mixture of 100 hPa

nitrogen and 1 hPa TBP at a constant flow of 0.01 sccm. The fragmentation pattern can be derived according to equation (4.2) by subtracting the background and nitrogen contribution from the recorded mass spectrum. The relative abundances of the major peaks in the TBP mass spectrum are listed in table 4.1 and correlated to the ionic fragmentation species formed in the mass spectrometer ionizer. Intensities below 3 % of the base peak intensity are not tabulated. The tabulated values represent the characteristic pattern of

m/Z (u)	h_m (%)	Ionic species	m/Z (u)	h_m (%)	Ionic species
12	(4.1 ± 0.3)	C^+	42	(5.4 ± 0.1)	$C_3H_6{}^+$
15	(45.1 ± 0.4)	$CH_3{}^+$	43	(3.1 ± 0.1)	$C_3H_7{}^+$
16	(40.3 ± 0.3)	$CH_4{}^+$	45	(8.9 ± 0.2)	$CPH_2{}^+$
17	(23.3 ± 0.5)	$NH_3{}^+$ / OH^+	47	(5.8 ± 0.1)	$CH_2PH_2{}^+$
26	(19.7 ± 0.5)	$C_2H_2{}^+$	55	(6.4 ± 0.1)	$C_4H_7{}^+$
31	(3.5 ± 0.1)	P^+	56	(10.5 ± 0.2)	$C_4H_8{}^+$
38	(5.6 ± 0.1)	$C_3H_2{}^+$	57	(59.9 ± 1.0)	$C_4H_9{}^+$
39	(38.4 ± 0.4)	$C_3H_3{}^+$	58	(3.2 ± 0.1)	$C_4H_{10}{}^+$
40	(9.4 ± 0.2)	$C_3H_4{}^+$	75	(4.6 ± 0.1)	$C_3H_6PH_2{}^+$
41	(100.0 ± 1.3)	$C_3H_5{}^+$	90	(4.2 ± 0.1)	$C_4H_9PH_2{}^+$

Table 4.1: Relative intensities in the mass spectrum of TBP assigned to the molecular species. Fragmentation is due to 70 eV electron ionization.

TBP for the applied setup, which might vary for other ones. The base peak occurs at 41 u corresponding to $C_3H_5{}^+$. The tertiary butyl group ion abundance appears as the second highest peak in the spectrum, with a relative intensity of (59.9 ± 1.0) %. The formation of this ionic species is expected with a high abundance since TBP is designed to break at the P-C bond, as well as molecules, in general, tend to lose their largest alkyl group by fragmentation due to electron ionization [56]. This is explained by the stabilizing effect of hyperconjugation compensating a missing charge via charge redistribution [218]. The phosphine radical counterpart PH_2 with a mass of 33 u is detected with a relative abundance of (2.0 ± 0.1) %, indicating that it remains preferentially as a neutral particle after dissociation. Neither a radical nor a molecular phosphine species occurs with significant intensity in the range from 32 u to 34 u. The molecule peak of TBP at 90 u is also detected with a relative intensity of (4.2 ± 0.1) %. With this peak, an interference-free peak is available for the decomposition measurements since every formed decomposition species possess a smaller mass over charge ratio, as will be seen in the following. Methane ($CH_4{}^+$) and methyl groups ($CH_3{}^+$) are visible at mass over charge ratios of 16 u and 15 u respectively with intensities of (40.3 ± 0.3) % and (45.1 ± 0.4) %. Ethyl species are

expected as well in the mass spectrum at 27 u and 29 u. However, these are not able to be detected in this measurement due to the overlap with the peak at 28 u caused by N_2^+. Since this species make up 99 % of the analyte, its peak is so intense that the tails of this peak strongly overlap the neighboring peaks. Due to this, the peaks of ethyl groups cannot be separated from the nitrogen peak. The high abundance of (23.3 ± 0.5) % at 17 u is unexpected. Possible ions can either be NH_3^+ or OH^+. Both are not expected to be formed in this experiment. Heavier isotopes contained in methane of carbon ^{13}C or hydrogen ^2H (deuterium) are also not feasible of causing this peak since ^{13}C has a natural abundance of 1.1 % [219] and ^2H of only 0.016 % [220]. The causing molecular species could not be identified.

Mass spectrum literature values from Li et al. are tabulated in table 4.2. They measured the TBP mass spectrum in an atmospheric pressure flow tube reactor using a time of flight mass spectrometer and 70 eV EI. The analyte consisted of 5 % TBP in a deuterium (D_2) atmosphere. In figure 4.3, the mass spectra are plotted for visual comparison. Even

m/Z (u)	h_m (%)	Ionic species	m/Z (u)	h_m (%)	Ionic species
27	13.4	$C_2H_3^+$	55	6.3	$C_4H_7^+$
29	47.8	$C_2H_5^+$	57	100.0	$C_4H_9^+$
39	16.9	$C_3H_3^+$	58	6.5	$C_4H_{10}^+$
41	54.8	$C_3H_5^+$	75	13.9	$C_3H_6PH_2^+$
45	6.9	CH_2P^+	88	3.0	$C_4H_9P^+$
47	6.3	$CH_2PH_2^+$	90	20.2	$C_4H_9PH_2^+$

Table 4.2: Values of relative intensities in the mass spectrum of 5 % TBP in atmospheric pressure D_2 environment assigned to the molecular species. Values taken from Li et al. (1989) [214].

though the significant peaks are comparable, some deviations from the here presented values can be seen. The base peak appears at 57 u caused by the tertiary butyl group. However, the second highest peak is at 41 u, which is the base peak reported in this study. Furthermore, the relative intensities of the propane species $C_3H_3^+$ at 39 u and $C_3H_5^+$ at 41 u are comparable to each other. The more intense peak of $C_3H_6PH_2^+$ at 75 u as well as the molecule peak at 90 u in literature, are most probably explained by differences in the spectrometer setups and sensitivities. Ethyl groups were detected at 27 u and 29 u, however, the detection of methyl species is not reported.

The pyrolysis of TBP is initiated by increasing the heating membrane temperature to exceed the decomposition temperature of 450 °C [106]. However, gas phase temperatures are lower than the nominal membrane temperature, as is the case for susceptor tempera-

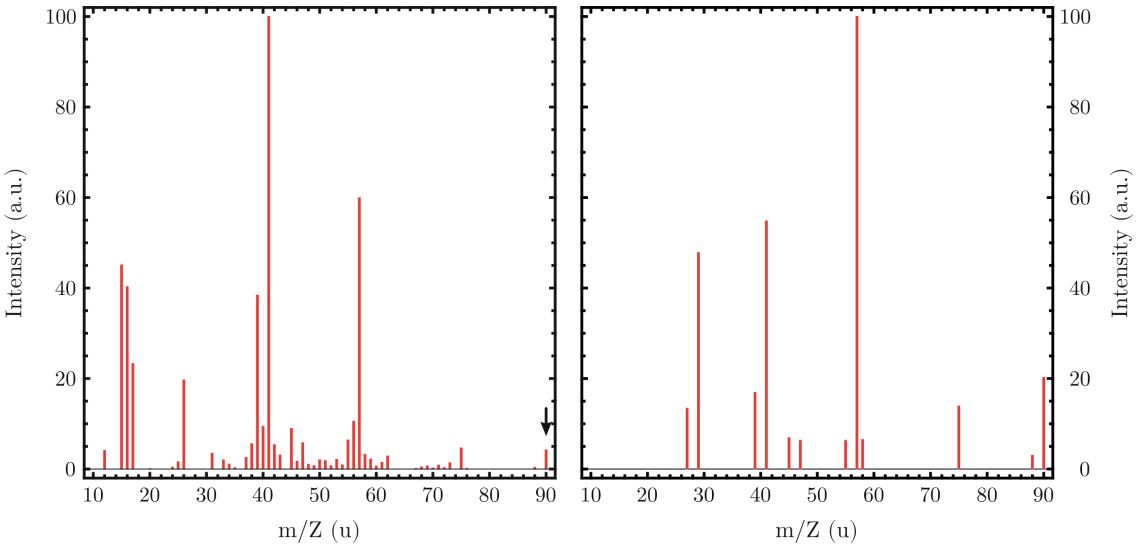

Figure 4.3: Left. Background corrected mass spectrum of TBP determined in the experiment. The independent peak at 90 u is marked by the black arrow. Right: Mess spectrum of TBP taken from literature [214] for comparison.

tures in ordinary reactor designs. The separation of decomposition products and TBP fragmentation pattern is performed according to equation (4.5), with the independent molecule peak at $m^* = 90\,\mathrm{u}$. It is important to keep in mind that the investigated gas volume is separated spatially from the one in the TEM holders reaction volume. Thus, a temporal delay between decomposition and detection, as well as gas phase reactions of formed products, arise. Furthermore, chemical active radicals might adsorb on the inner line surfaces, hindering them from reaching the spectrometer. The temperature was increased in steps of 50 °C and sustained for 50 min to compensate for the signal delay of over 10 min and to stabilize the measured intensities. Found decomposition species are methane (CH_4), phosphine (PH_3), isobutane (C_4H_{10}) and isobutene (C_4H_8). Reference spectra of phosphine, isobutane and isobutene are plotted in figure 4.4 in black, red and blue, respectively. Each molecular species provides an abundant independent peak, which allows quantifying its formation. They are marked by black arrows in the spectra. For methane, phosphine and isobutane, it is given by the base peaks at 16 u, 34 u and 43 u respectively. In the case of isobutene, the peak at 56 u can be seized as independent with an intensity of 44.5 % of the base peak. Intensities of the independent peaks of the major decomposition products can be seen in figure 4.5 plotted versus membrane temperature. With increasing temperature, all intensities rise, which seems to conflict with

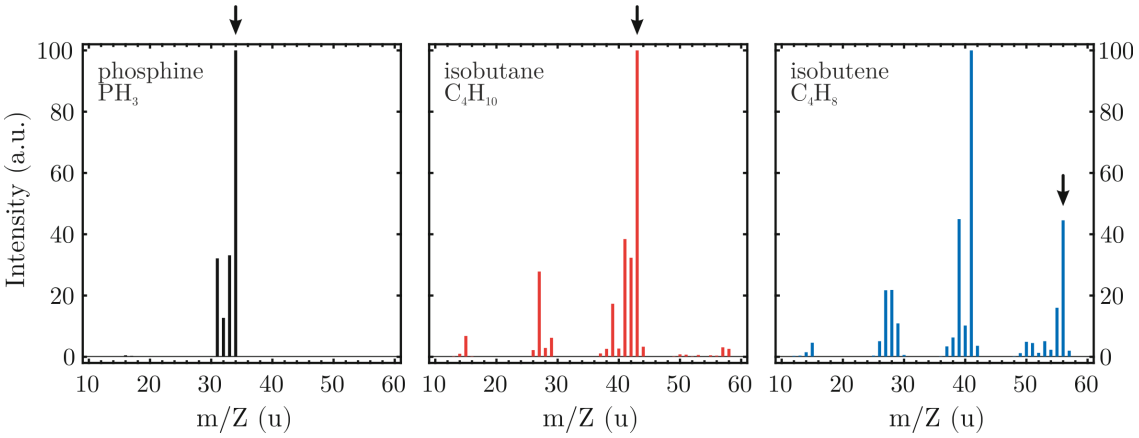

Figure 4.4: Mass spectra of TBP decomposition products phosphine (black), isobutane (red) and isobutane (blue). Independent peaks used to quantify the species are marked with black arrows. Data taken from NIST Chemistry WebBook [63]

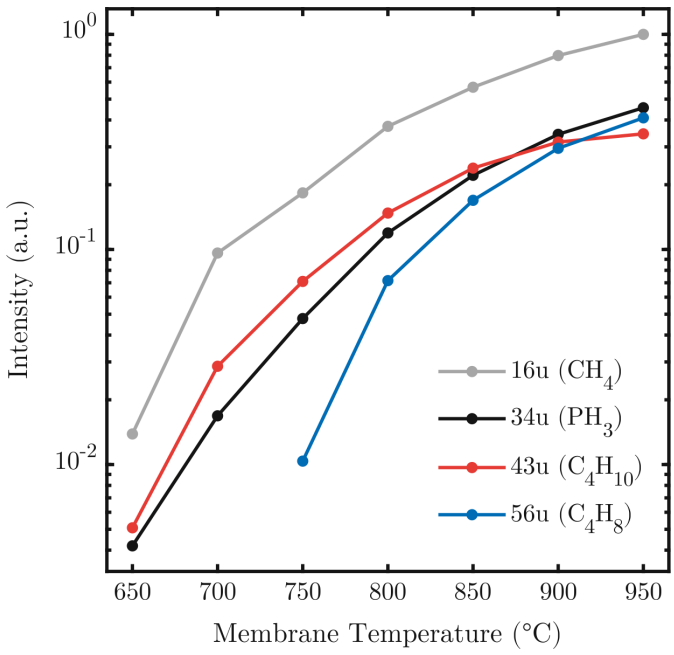

Figure 4.5: Peak intensities correlated to the decomposition products methane (gray), phosphine (black), isobutane (red) and isobutene (blue) plotted against the membrane temperature. All intensities rise with temperature due to an increased heated area.

decomposition curves presented by Maßmeyer et al. [208]. But this behavior is explained by the different setup geometry. Here, only a small area of approximately $0.01\,\mathrm{mm}^2$ is heated to the labeled temperature. The surrounding surface obtains a temperature gradient of approximately $(-6.4 \pm 0.2)\,^\circ\mathrm{C}\,\mu\mathrm{m}^{-1}$ (see section 4.1) so that most of the precursor material is conducted through the reactor without being exposed to elevated temperatures (see figure 4.1 in section 4.1). Increasing the temperature increases the surface that is heated to a sufficient temperature to pyrolyze the precursor, and more and more molecules are decomposed. Due to this, all observed decomposition peak intensities increase with temperature. Nevertheless, conclusions about preferred reaction pathways and relative abundances of decomposition products can be made. As reported by Maßmeyer et al., all suggested decomposition pathways of TBP result in the formation of a phosphine molecule (PH_3) or radical ($PH_{1\text{-}2}$). Each of them would be detected as molecular species since radicals most probably undergo a hydrogen abstraction reaction with TBP or any other alkyl group forming a phosphine molecule. They have sufficient time to react on their way to the spectrometer. Determining the relative change in the formation of a decomposition species to the formation of phosphine reveals the variation in reaction pathways with temperature. Alternatively, the amount of decomposed TBP can be used to this end. The normalized decomposition curves for phosphine and TBP are shown in the left part of figure 4.6 in black and yellow, respectively. TBP pyrolysis is indicated by the decreasing 90 u and rising 34 u peak intensity correlated to TBP and phosphine, respectively. Furthermore, these curves show the effect of the difference in the reactor geometry mentioned above. Once the decomposition temperature is exceeded, the phosphine curve increases approximately quadratic with temperature. This observation is in line with the increase in area, surpassing the required temperature for pyrolysis. Due to the approximately linear temperature gradient in the regime of elevated temperatures (compare figure 4.1), the diameter of the surface at sufficiently high temperature for decomposition grows linearly. This results in a quadratic area increase. Extrapolating the quadratic behavior by a fit to lower temperatures and determining the minimum of the parabola enable a more precise estimation of the pyrolysis membrane temperature of $(641 \pm 20)\,^\circ\mathrm{C}$. This temperature is comparable to the susceptor temperature of 650 °C reported in reference [208], which is assigned to a decomposition gas phase temperature of around 430 °C. By this, it can be concluded that the gas phase temperature scales with the membrane temperature comparably, as it does in epitaxy machines with the susceptor temperature. The complementary trend can be observed in the temperature curves of TBP decomposition products. At a temperature of 950 °C, a fraction of 67 % of the initial TBP remains undecomposed,

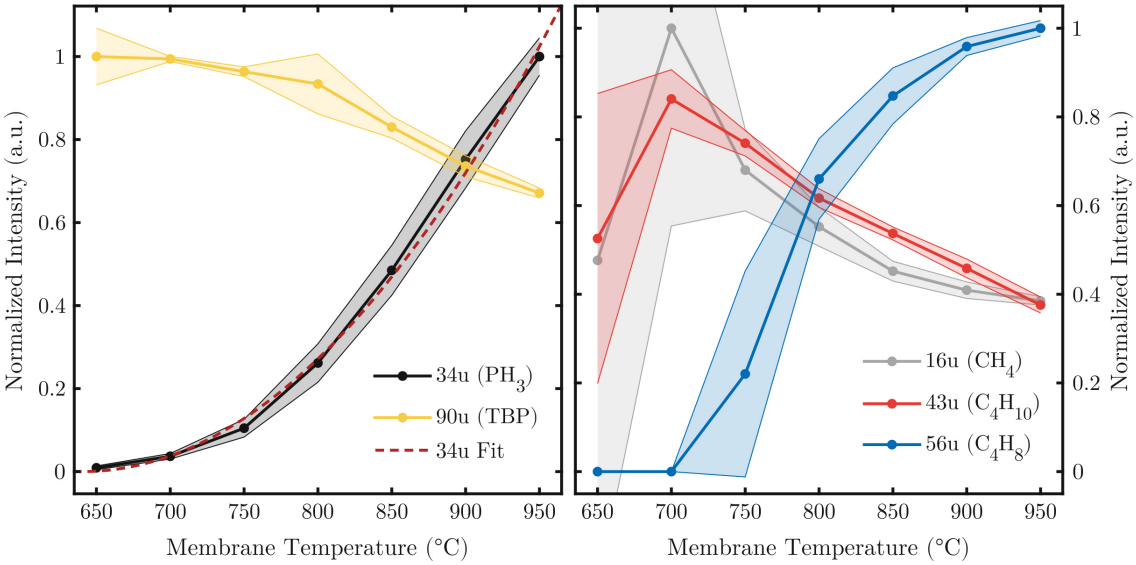

Figure 4.6: Left: Intensities of the peaks corresponding to phosphine (black) and TBP (yellow) plotted versus the membrane temperature. The phosphine intensity shows a parabolic progression (red). Right: Peak intensities of decomposition products normalized to the formed phosphine. These curves represent the relative amount of formed methane (gray), isobutane (red) and isobutene (blue) dependent on the membrane temperature.

allocating a poor decomposition efficiency in the *in-situ* TEM holder. This decomposition efficiency further depends on the time the molecules are exposed to elevated temperatures and by this on the flow velocity. A reduction in flow velocity can increase the fraction of decomposed molecules [214]. In the right-hand plot of figure 4.6, the temperature curves of the decomposition products methane (gray), isobutane (red) and isobutene (blue) are displayed. Their values are calculated as the ratio to formed phosphine, as explained previously, and their maximum value is set equal to one. A qualitative determination of these molecules' partial pressure is impossible in the given setup without calibration for the specific molecular species. Hence, they do not display their relative concentrations but their change in partial pressure relative to the one of phosphine. The significant error in the temperature interval of 650 °C to 700 °C is a consequence of the low phosphine peak intensity utilized to normalize the data. At a low temperature of 650 °C, where the pyrolysis is initiated, isobutane is formed and increases up to a temperature of 700 °C to 750 °C. Isobutene is not detected in this temperature range. The detection of isobutane can be related to the decomposition reactions of intramolecular coupling or homolytic fission illustrated in figure 4.7. In the first case, a bond between the central C atom

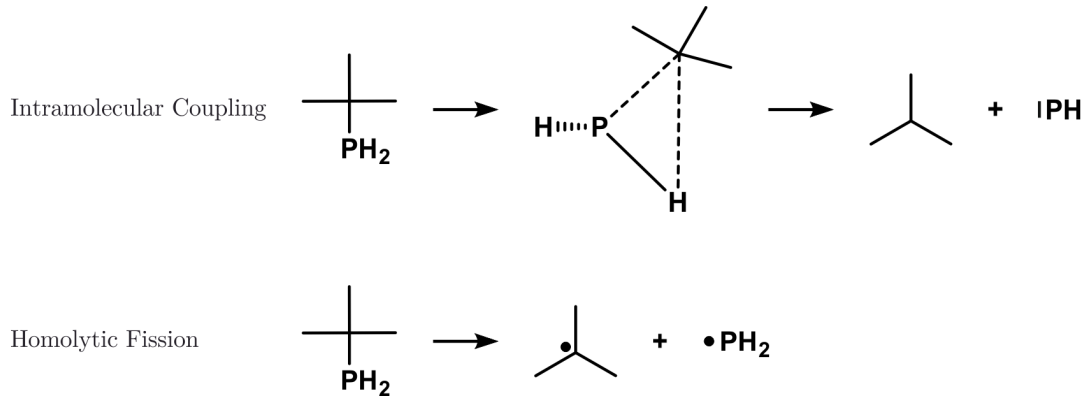

Figure 4.7: Illustration of the decomposition pathways of TBP in the lower temperature regime up to 750 °C. Intramolecular coupling forms isobutane and a PH radical and homolytic fission a tertiary butyl group and a PH_2 radical.

and an H atom bound to the P is formed at the cost of one of the P-H bonds. This results in the formation of isobutane and a phosphine radical (PH), which is detected as a phosphine molecule. In the case of homolytic fission beside isobutane, isobutene could also be detected. A tertiary butyl radical and a phosphine radical (PH_2) are formed there. The former would be detected as isobutane, due to a further hydrogen abstraction reaction with an alkyl or isobutene, due to a radical removal step by releasing an H atom. From a chemical point of view, the radical removal step is assumed to be unfavorable since the tertiary butyl radicals are stable due to hyperconjugation [52, 218]. Hence, isobutene is not expected to be observed for the reaction pathway of homolytic fission. The also-formed phosphine radical is again detected as molecular phosphine. These findings suggest that homolytic fission and intramolecular coupling are the dominant reaction pathways in this temperature range.

A further increase of membrane temperature leads to the detection of isobutene as well, which can be the product of homolytic fission, as already mentioned, and a β-hydrogen elimination depicted in figure 4.8. At the same time, the relative amount of isobutane decreases. This indicates a less dominant role of the intramolecular coupling reaction with increasing temperature. In which of the two possible reactions isobutene is formed can not be concluded from the presented data since it can not be distinguished between the formed PH_2 in homolytic fission or PH_3 in β-hydrogen elimination. Absolute intensities at 950 °C indicate that more isobutene than isobutane is formed. With the assumption that the sensitivity of the spectrometer is approximately the same for both molecules, which is valid since they consist of the same atomic species, possess a similar structure,

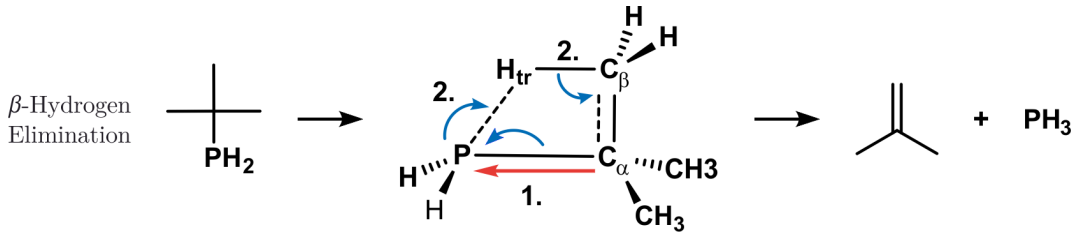

Figure 4.8: Illustration of the decomposition pathways of TBP in the higher temperature regime from 750 °C. β-hydrogen elimination results in the formation of isobutene and phosphine.

and do not differ in mass significantly, more isobutene is formed for temperatures higher than approximately 750 °C to 800 °C. A mass spectrum recorded at 950 °C can be seen in figure 4.9. At this temperature, isobutene is the dominating decomposition product since the 56 u peak intensity (44.5 % of the isobutene base peak) exceeds the 43 u base peak of isobutane. Additionally, the most intense peak is at the isobutene base peak position of 41 u. Methane (plotted in gray) is formed preferentially in the lower temperature range, and its relative abundance decreases together with the one of isobutane. It does not share a peak with the other decomposition products at 16 u. This leads to the conclusion that its formation is coupled with the one of isobutane. It can be formed through a further homolytic or heterolytic fission reaction. These reactions are more probable for isobutane than for isobutene, which is more stable due to the C=C double bond. The relative peak intensities do not match the reference fragmentation pattern, since especially the 15 u is not independent and interferes with the fragmentation patterns of isobutane and isobutene. In the range of 31 u to 34 u, the fragmentation pattern of phosphine is visible. Furthermore, a small fraction of diphosphine (P_2H_4) is detected. This molecule results from a reaction of two formed phosphine radicals during the decomposition of TBP. Its fragmentation pattern appears from 62 u to 66 u. The relative peak intensities are ambiguous in the literature. There are reports for the 62 u peak having the highest abundance [221], as well as for the 66 u peak [222]. Due to this, a comparison of the fragmentation pattern to literature is precarious.

The presented findings are further validated by comparison to the results presented in literature [208, 214], even though there the carrier gas is hydrogen in contrast to nitrogen, which influences the decomposition temperature. There the formation of tertiary butyl groups and isobutane is observed for lower temperatures and related to homolytic fission and intramolecular coupling, whereas these pathways get superseded by β-hydrogen

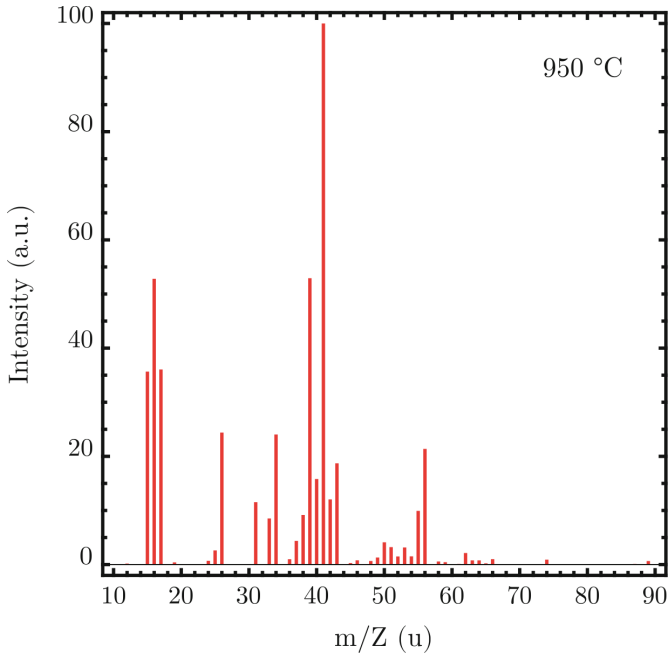

Figure 4.9: Mass spectrum of TBP decomposition products at 950 °C. The fragmentation pattern is dominated by isobutene. The fragmentation pattern of isobutane contributes less to the mass spectrum.

elimination, which forms isobutene, at a susceptor temperature of around 770 °C. This temperature matches with the observed temperature interval of 750 °C to 800 °C. In the here presented investigation, it is expected to be observed presumably for higher temperatures due to the overlap with lower temperature regimes located around the membrane center. Furthermore, the reported decomposition susceptor temperature for TBP of 630 °C matches the observed membrane temperature. This indicates that the susceptor temperature in an epitaxy reactor is comparable to the membrane temperature of the MEMS chip. The presented investigation of the thermal decomposition of TBP in the *in-situ* TEM setup was capable of reproducing the results known from literature in a qualitative and, for some findings, also in a qualitative way.

4.1.3 Thermal Decomposition of TMGa

In this section, the results of the pyrolysis of TMGa, which is an intensively studied precursor molecule also concerning its decomposition [104, 208, 223, 224], is presented. The decomposition study was performed with an analyte mixture of 100 mbar argon and

1 mbar TMGa with a flow of 0.01 sccm. Here argon was chosen as carrier gas instead of nitrogen because ethyl groups are expected decomposition products [104]. Their fragmentation pattern would overlap with the 28 u peak of nitrogen, which has an intensity several orders of magnitude higher than the ones of the decomposition products for the adjusted partial pressures. Additionally, the doubly ionized nitrogen at 14 u interferes with the methane fragmentation pattern. While the TMGa fragmentation pattern is still possible to be separated from nitrogen at 12 u, 15 u and 16 u, the weak intensities of the decomposition products can not be separated. Consequently, no decomposition product is detectable with N_2 carrier gas. Argon shows two peaks in its fragmentation pattern at 20 u and 40 u. Both do not interfere with fragmentation patterns of expected decomposition products. A comparison between the pyrolysis performed in nitrogen and argon is valid since both gas species are inert and possess a similar mass. Nevertheless, small disparities in the decomposition behavior between argon and nitrogen can not be excluded.
The fragmentation pattern of TMGa is tabulated in table 4.3 and can be seen in figure 4.10.

m/Z (u)	h_m (%)	Ionic species	m/Z (u)	h_m (%)	Ionic species
12	(2.2 ± 0.2)	C^+	15	(86.9 ± 1.2)	$CH_3{}^+$
13	(7.2 ± 0.1)	CH^+	16	(100.0 ± 1.3)	$CH_4{}^+$
14	(13.5 ± 0.4)	$CH_2{}^+$	17	–	$CH_3D^+/{}^{13}CH_4{}^+$

Table 4.3: Relative intensities in the mass spectrum of TMGa assigned to the molecular species. Fragmentation is due to 70 eV electron ionization.

Gallium appears in the two stable isotopes ^{69}Ga (60.1 %) and ^{71}Ga (39.9 %) [225]. The TMGa molecule peaks, which would appear therefore at 114 u and 116 u, are not observed. Moreover, the potential fragments dimethyl gallium (GaC_2H_6), methyl gallium ($GaCH_3$) or gallium itself do not arise as well. The mass spectrum solely contains peaks caused by the methyl groups. Methyl groups (CH_3) are the most expected fragment on dissociation. They are detected at 15 u. However, the base peak appears at 16 u caused by methane (CH_4). Furthermore, the fragmentation pattern matches the one of methane, which can be seen in gray in the left mass spectrum of figure 4.11. That the methyl groups undergo a hydrogen abstraction reaction prior to ionization and get detected as methane is unlikely due to the low pressure of 9×10^{-4} Pa present in the ionizer. More probably, the TMGa dissociates through an intramolecular coupling reaction in which the C atom of the cleaved bond interacts with an H atom of another methyl group and forms a C-H bond resulting in CH_4. The methane formed this way gets ionized and dissociates, resulting in the observed

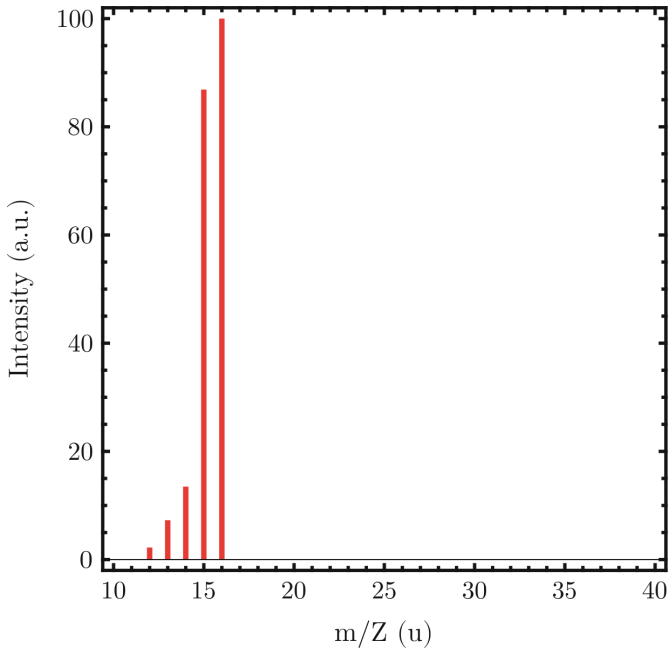

Figure 4.10: Background corrected mass spectrum of TMGa.

fragmentation pattern. Since the GaC_2H_5 counterpart of the TMGa is not detected, it is expected to remain as a neutral particle or to form a further methane ion or molecule analogous to the TMGa.

Pyrolysis is again initiated by a step-wise temperature increase of 50 °C, and each step was sustained for 50 min as it was performed for TBP decomposition. Observed decomposition products are methane and ethane. Their reference spectra are shown in figure 4.11 in gray and black for methane and ethane, respectively. Since TMGa interferes in all peaks with the fragmentation pattern of methane, no independent peak is available to determine the amount of decomposed precursor. To identify the additional methane, the initial fragmentation pattern of TMGa is subtracted from the mass spectra. This may lead to an underestimation of the methane abundance since the TMGa concentration drops with temperature due to decomposition. Neglecting the TMGa influence on the fragmentation pattern, methane exhibits an independent peak at 16 u serving as an abundance measure. The interference-free peak at 27 u with an intensity of 33.2 % of the base peak is chosen to measure the amount of ethane and weighted with the respective base peak intensity. It is preferred over the base peak at 28 u because the residual nitrogen causes a background intensity peak at 28 u. In contrast, the background intensity at 27 u is negligible. Both

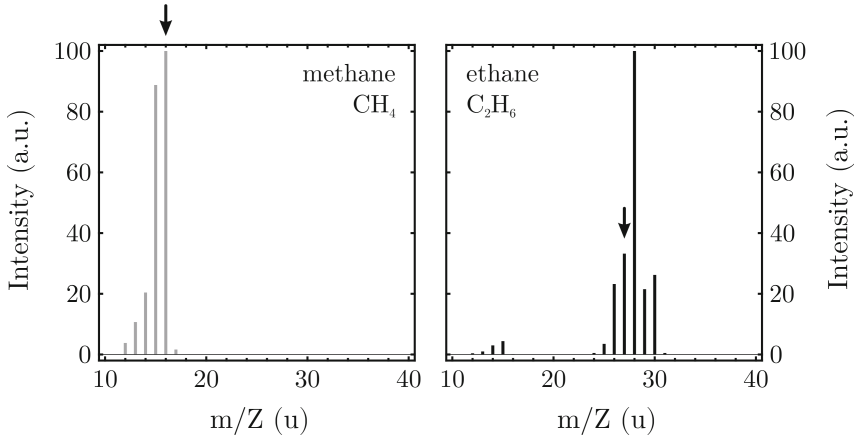

Figure 4.11: Mass spectra of TMGa Decomposition products methane (gray) and ethane (black). The independent peaks are marked by black arrows. Data taken from NIST Chemistry WebBook [63]

peaks are again marked by black arrows in the mass spectra. The temperature-dependent curves for methane and ethane are illustrated in figure 4.12. Decomposition starts at a membrane temperature between 500 °C and 550 °C, as can be concluded from the emerging

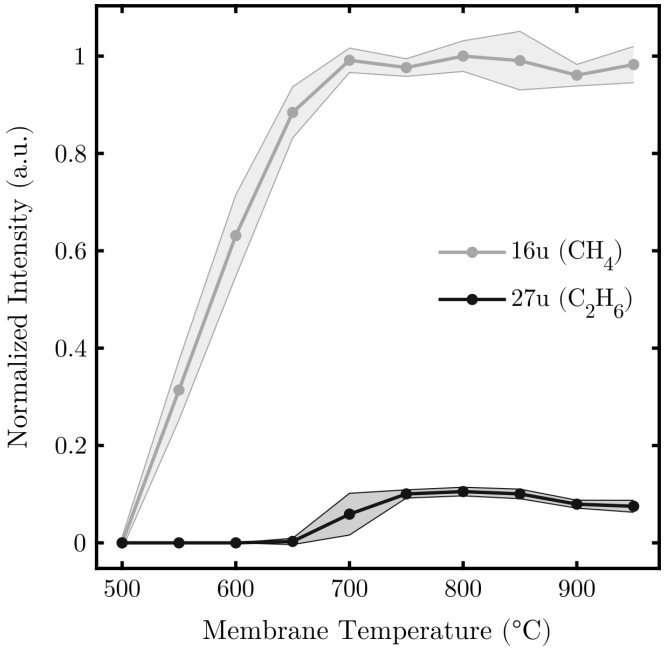

Figure 4.12: Thermal decomposition species of TMGa methane (gray) and ethane (black) versus membrane temperature.

methane intensity in this temperature range. This temperature can be assigned to a lower gas phase temperature than the reported decomposition temperature of 520 °C in nitrogen atmosphere [104]. A lower decomposition temperature of (340 ± 10) °C is reported in the literature as well [208]. However, due to their low partial pressure of 9.5×10^{-4} hPa, this value is not considered as a reference for the here presented investigation. This reduction in decomposition temperature might be observed due to the usage of an argon environment. Due to its slightly higher mass compared to nitrogen, argon may transfer thermal energy more efficiently to TMGa. The methane detection indicates homolytic fission of a methyl group from TMGa, forming a methyl radical. These are expected to further react with TMGa enhancing its decomposition. Beginning from 650 °C, ethane is also detected, and the methane abundance approaches a saturation. Ethane is produced by two previously formed methyl radicals. The corresponding reaction pathways occurring in the unimolecular decomposition of TMGa are illustrated in figure 4.13. The formation

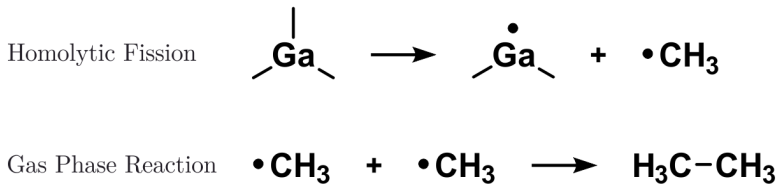

Figure 4.13: Illustration of the reaction pathways of TMGa in thermal decomposition. Methyl radicals and Ethane are formed.

of ethane is expected to occur as soon as methyl radicals are formed. But due to the low fraction of decomposed TMGa at low temperatures, two methane radicals are unlikely to collide in the gas phase. With an increasing fraction of decomposed TMGa, this reaction becomes more probable. Both decomposition curves reach a plateau at a temperature of 750 °C. Complete mass spectra of the decomposition products can be seen in figure 4.14 for 550 °C in blue and 750 °C in red. The fragmentation pattern of methane occurs from 12 u to 16 u. The peak caused by methyl groups at 15 u possesses a higher intensity than the base peak of the reference spectrum. This may result from overestimating the TMGa fragmentation pattern as the decomposed fraction increases. The absolute amount of methane is higher than the one of ethane. Even though the exact ratio can not be determined precisely, this can be concluded from the lack of influence on the methane peak intensities of the ethane side peaks.

In comparison to reports in the literature on the thermal decomposition of TMGa, some observations are in line, while others show discrepancies. Reference [104] reported on the formation of methane and ethane in nitrogen ambient. There, both products arise as

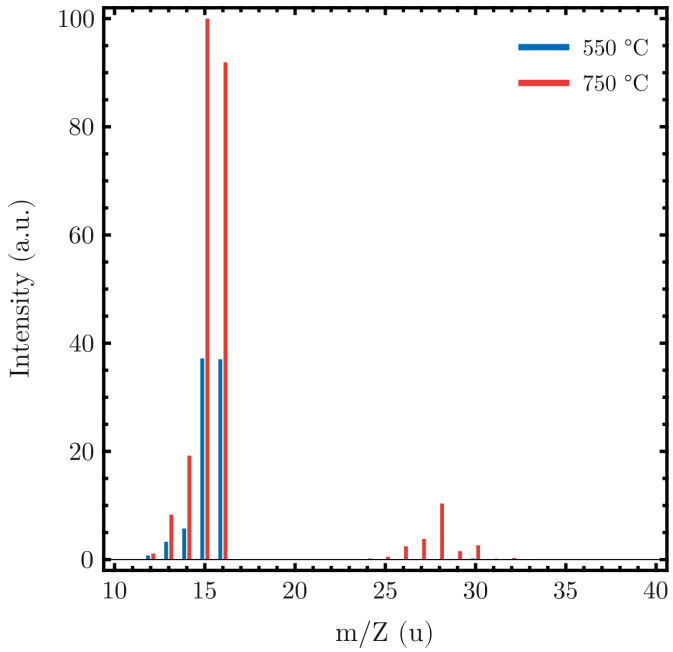

Figure 4.14: Mass spectra of TMGa decomposition products at 550 °C (blue) and 750 °C (red).

TMGa decomposes at 520 °C, with methane being the dominant one. These findings are in line with the here presented results. In reference [208] also dimethyl gallium (GaC_2H_6) is observed as a decomposition product in a hydrogen environment at 98 u and 100 u, which is the expected counterpart to the methyl radicals in TMGa dissociation. Furthermore, they report on the observation of these ions in the TMGa fragmentation pattern. These observations of the larger and heavier gallium containing TMGa fragmentation and dissociation products could not be reproduced in the presented study.

4.1.4 Bimolecular Decomposition of TBP and TMGa

In the last section of this chapter, results on the bimolecular decomposition of TBP and TMGa are presented and compared to MOVPE investigations that utilized this precursor combination. An analyte mixture of 1 mbar TBP and 1 mbar TMGa with nitrogen carrier gas at a total pressure of 100 mbar with a gas flow of 0.01 sccm is investigated. Mass spectra were scanned from mass over charge ratios from 10 u to 130 u.
In the here presented setup, the precursor molecules get mixed prior to the conduction through the TEM holders reaction chamber, in contrast to MOVPE reactors, where they

are conducted separately and meet just before the reactor to avoid pre-reactions. Figure 4.15 presents the fragmentation pattern of the mixture of TBP and TMGa. Intensities overlaying with the nitrogen fragmentation pattern at 14 u and 28 u are not able to be resolved. However, a nitrogen carrier is preferred over argon, which overlaps with the intensities of the isobutane and isobutene around 40 u. In the range from 20 u to 90 u, the fragmentation pattern mirrors the one of TBP. The relative peak intensities are on par with the ones presented in the unimolecular case in section 4.1.2 (compare the left mass spectrum of figure 4.3). Intensity values are presented in table 4.4. Between mass over charge ratios of 10 u and 20 u, the two fragmentation patterns of TBP and TMGa interfere since both precursors possess methyl groups as fragmentation products by electron ionization. Comparing the methyl peaks from 12 u to 16 u with the unimolecular ones of both molecules reveals that TMGa predominantly causes these peaks. The TBP portion of the spectrum is eliminated by subtracting its unimolecular fragmentation pattern, weighted with the basis peak intensity of (37.1 ± 0.6) % at 41 u. The remaining intensities are comparable to the unimolecular fragmentation pattern of TMGa (see table 4.3) and tabulated in table 4.5. In consequence, the bimolecular mass spectrum represents an

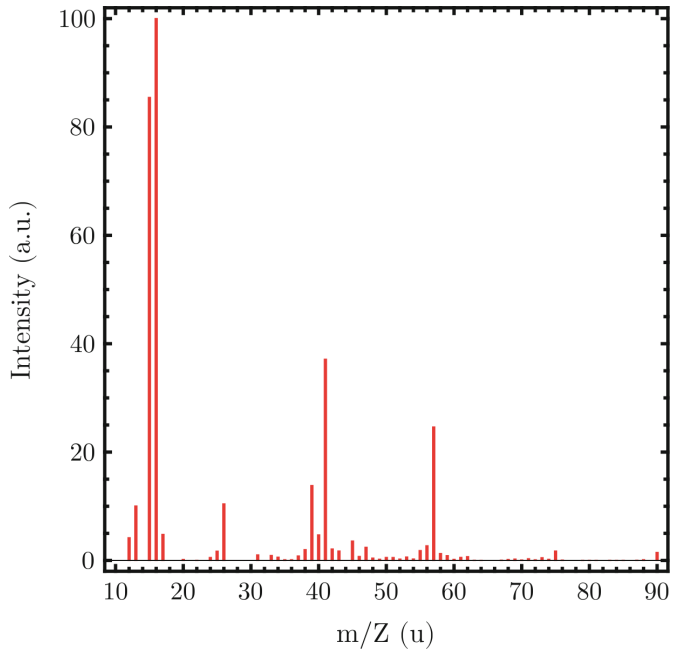

Figure 4.15: Background corrected mass spectrum of a mixture of TBP and TMGa in nitrogen recorded at room temperature.

m/Z (u)	h_m (%)	Ionic species	m/Z (u)	h_m (%)	Ionic species
12	(4.2 ± 0.1)	C^+	41	(37.1 ± 0.6)	$C_3H_5{}^+$
13	(10.0 ± 0.2)	CH^+	42	(2.1 ± 0.1)	$C_3H_6{}^+$
15	(85.4 ± 0.9)	$CH_3{}^+$	43	(1.7 ± 0.1)	$C_3H_7{}^+$
16	(100.0 ± 1.3)	$CH_4{}^+$	45	(3.6 ± 0.1)	$CPH_2{}^+$
17	(4.8 ± 0.3)	$NH_3{}^+$ / OH^+	47	(2.4 ± 0.1)	$CH_2PH_2{}^+$
25	(1.7 ± 0.2)	C_2H^+	55	(1.8 ± 0.1)	$C_4H_7{}^+$
26	(10.4 ± 0.8)	$C_2H_2{}^+$	56	(2.7 ± 0.1)	$C_4H_8{}^+$
31	(1.0 ± 0.1)	P^+	57	(24.6 ± 0.4)	$C_4H_9{}^+$
38	(2.0 ± 0.1)	$C_3H_2{}^+$	58	(1.3 ± 0.1)	$C_4H_{10}{}^+$
39	(13.8 ± 0.3)	$C_3H_3{}^+$	75	(1.7 ± 0.1)	$C_3H_6PH_2{}^+$
40	(4.7 ± 0.1)	$C_3H_4{}^+$	90	(1.5 ± 0.1)	$C_4H_9PH_2{}^+$

Table 4.4: Relative intensities in the mass spectrum of the TBP and TMGa mixture assigned to the molecular species. Fragmentation is due to 70 eV electron ionization.

addition of the unimolecular spectra. The lack of peaks that can not be described by this show that no products formed in a gas phase reaction due to the pre-mixture of precursor gases are observed.

Thermal decomposition is investigated by increasing the membrane temperature starting from 450 °C up to 950 °C in steps of 50 °C every 45 min. The total fraction of decomposed precursor can only be determined for TBP utilizing the independent peak at 90 u. For TMGa, due to the lack of an independent peak, conclusions can only be drawn from the decomposition products. Figure 4.16 illustrates the normalized intensity versus temperature curves of the TBP in yellow and methane in gray, which is the main decomposition product of TMGa, but also emerges to a smaller extent from TBP pyrolysis. The TBP curve exhibits a significantly reduced decrement compared to the unimolecular decomposition. Only a fraction of (4 ± 1) % of the precursor is pyrolyzed at 950 °C. Thus, the presence of TMGa in the gas phase hinders TBP decomposition. Contrarily, the methane decomposition curve indicates more efficient pyrolysis compared to the absence of TBP. It does not approach a plateau at 700 °C but continues to rise linearly with temperature. Furthermore, TMGa

m/Z (u)	h_m (%)	Ionic species	m/Z (u)	h_m (%)	Ionic species
12	(3.1 ± 0.2)	C^+	15	(80.8 ± 1.2)	$CH_3{}^+$
13	(11.9 ± 0.3)	CH^+	16	(100.0 ± 1.8)	$CH_4{}^+$

Table 4.5: Relative intensities assigned to the molecular species in the mass spectrum of TBP and TMGa after subtracting the TBP fragmentation pattern.

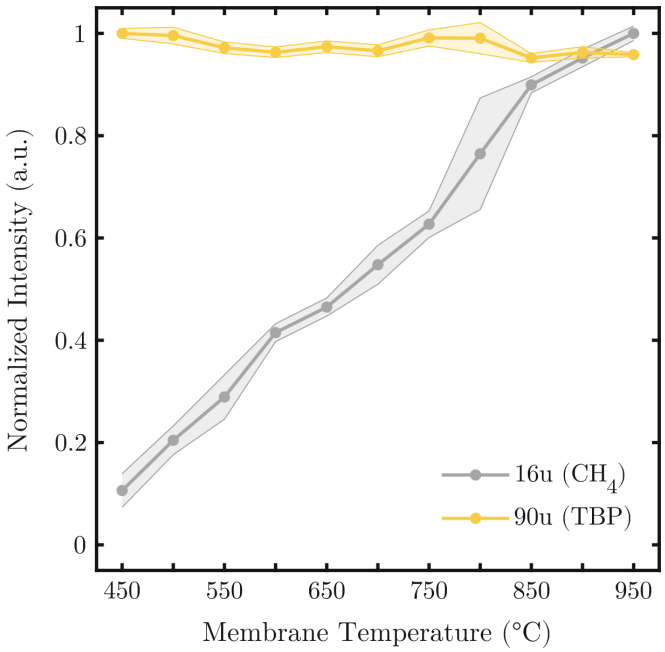

Figure 4.16: Detected amount of methane (gray) and TBP (yellow) in dependence on the membrane temperature of a gas mixture of TBP and TMGa in a nitrogen carrier gas.

starts to decompose already at lower temperatures. Extrapolating the methane intensity indicates a decomposition membrane temperature of $(391 \pm 35)\,°C$. The TBP temperature curve is not capable of resolving its pyrolysis temperature. Instead of this, the appearance of phosphine and isobutane can be utilized. These products occur at a temperature between 450 °C and 500 °C as can be seen in figure 4.17. Phosphine, correlated to the 34 u intensity, and isobutane, correlated to the 43 u intensity, are plotted in black and red, respectively. Both occur at significantly lower temperatures with the presence of TMGa. In the unimolecular decomposition of TBP, this temperature was determined to $(641 \pm 20)\,°C$. The reduction of decomposition temperature of around 150 °C demonstrates a catalytic effect on the TBP pyrolysis of TMGa, even though the decomposition efficiency is reduced.

With increasing temperature, the decomposed fraction of TBP rises, as indicated by the dropping TBP as well as the growing phosphine intensity. However, the increase in phosphine per decomposed TBP is reduced compared to the unimolecular case. This may be the result of different decomposition pathways that do not end up in phosphine, which is, however, unlikely. More probably, gas phase reactions, including the formed phosphine, can reduce the abundance of phosphine. Therefore, it cannot be used as calibration for the

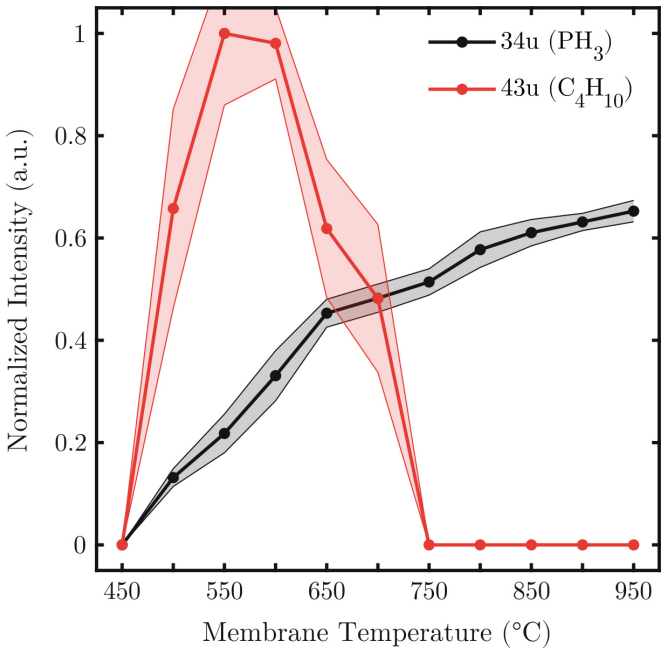

Figure 4.17: Detected amount of phosphine (black) and isobutane (red) in dependence on the membrane temperature of a gas mixture of TBP and TMGa in a nitrogen carrier gas.

relative amount of TBP decomposition products. Another observation is that isobutane is formed only at temperatures below 750 °C. Its formation indicates the decomposition of TBP via homolytic fission or intramolecular coupling, analogous to the unimolecular reaction. The absence of isobutane from temperatures over 750 °C suggests that either it undergoes a further reaction, for example, with dimethyl gallium (GaC_2H_6), which results from homolytic fission of a methyl group from TMGa, or that its formation is prevented. The unimolecular decomposition already demonstrated that its occurrence is reduced with increasing temperature. Isobutene is not observed as a decomposition product for any investigated temperature. Consequently, decomposition via β-hydrogen elimination is not assumed. The facts that the amount of formed phosphine does not drop together with the isobutane and that no further decomposition products of TBP are observed suggest that the remaining decomposition products undergo a further reaction in the gas phase.
Contrary to the unimolecular decomposition of TMGa, the formation of ethane as a result of a gas phase reaction of two methyl radicals is not observed. However, due to the interference of nitrogen in the fragmentation pattern, its formation cannot entirely be excluded. Therefore, the only decomposition product that can be related to a homogeneous TMGa reaction is methane. The observations of products, which are not observed in either

unimolecular decomposition, suggest bimolecular reactions of the precursor molecules and their decomposition products. The observed bimolecular reaction products are methyl phosphine (H_2PCH_3) and a larger gallium-containing molecule. Methyl phosphine is related to the detection of ions at 46 u. The reference mass spectrum plotted in blue in the left part of figure 4.18 reveals that its base peak is expected to be at 46 u marked by the black arrow. A further intense peak is expected at 48 u with 86.7 % of the base

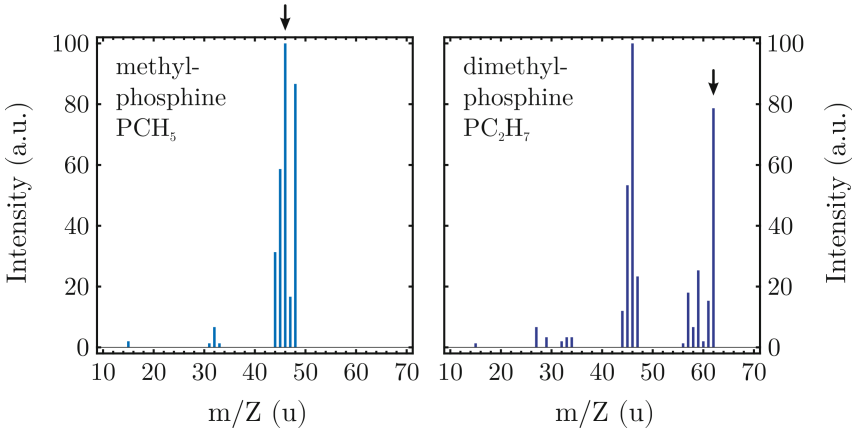

Figure 4.18: Mass spectra of bimolecular reaction products methyl phosphine (clue) and dimethyl phosphine (dark blue). Peaks used for quantification are marked by black arrows. Data taken from NIST Chemistry WebBook [63]

peak intensity. This peak is detected as well, however, it only shows an intensity of (33.8 ± 1.1) % of the detected 46 u intensity. The relative peak intensity might vary due to the interference of the 46 u peak in the fragmentation pattern of TBP as an artifact of the background correction. The occurrence of the 46 u peak could, in principle, also indicate the formation of dimethyl phosphine possessing its basis peak at 46 u as well illustrated in the right part of figure 4.18 in dark blue. But due to the missing dominant side peak at 62 u marked by the black arrow, its formation can be excluded. Additionally, the side peak of methyl phosphine at 48 u, which is observed, is not included in the fragmentation pattern of dimethyl phosphine. Next, the findings are described, which lead to the conclusion that a larger gallium-containing molecule is formed. The fragmentation pattern of this molecule contains the ion species gallium (Ga^+), methyl gallium ($GaCH_3{}^+$) and dimethyl gallium ($Ga(CH_3)_2{}^+$). Gallium has a ratio of 60.1 to 39.9 in the ^{69}Ga and ^{71}Ga isotopes. This ratio is also observed in the 69 u and 71 u, 84 u and 86 u, as well as in the 99 u and 101 u peak intensities that can be assigned to the ions mentioned above. Therefore, these pairs originate from a common gallium-containing ionic species.

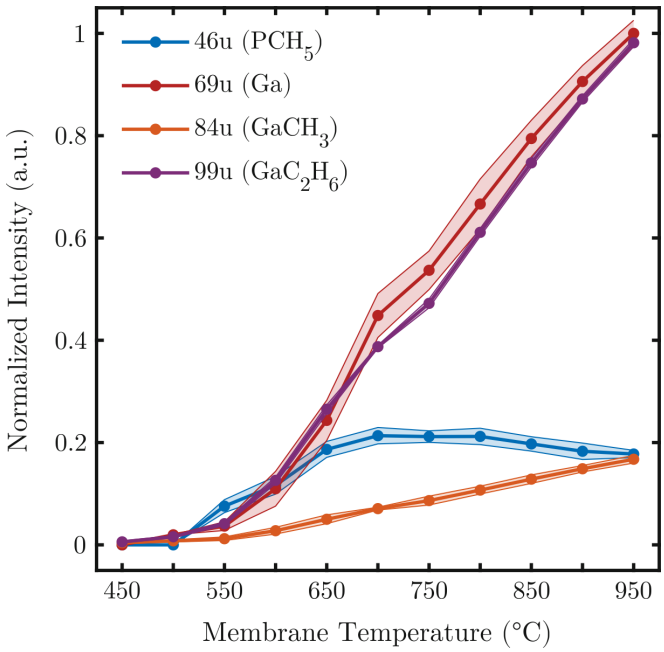

Figure 4.19: Detected amount of the ionic species methyl phosphine (blue), gallium (dark red), methyl gallium (orange) and dimethyl gallium (purple) in dependence on the membrane temperature of a gas mixture of TBP and TMGa in a nitrogen carrier gas.

The temperature curves of the bimolecular reaction products are plotted in figure 4.19. Methyl phosphine related to the 46 u intensity can be seen in blue. The dominant ^{69}Ga isotope containing gallium (69 u), methyl gallium (84 u) and dimethyl gallium (99 u) ions are plotted in red, orange and purple respectively. Throughout the whole temperature range, they possess the same intensity ratio, from which it can be deduced that they belong to the fragmentation pattern of the same parent molecule. The fragments differ in mass over charge ratio by 15 u, which matches the mass of a methyl group and corresponds to the structure of TMGa. However, TMGa can be excluded as a parent molecule since it would appear even without an applied elevated temperature, but the formation is only observed for temperature starting from 500 °C to 550 °C. Furthermore, it was shown in the unimolecular decomposition experiment that the TMGa fragmentation pattern does not contain the observed ions. For that reason, the molecule must consist of gallium bound to two methyl groups and a further unknown constituent. Hence, TMGa needs to undergo a gas phase reaction. An alkyl exchange reaction of TBP and TMGa with the exchange of a tertiary butyl and a methyl group could result in such a molecule, as illustrated in figure 4.20. Due to the elevated precursor partial pressures the two precursor

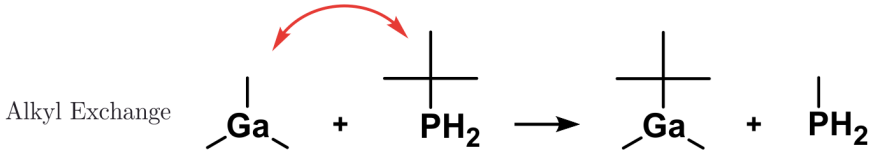

Figure 4.20: Illustration of the suggested alkyl exchange reaction between TMGa and TBP. A methyl group of TMGa is exchanged with the tertiary butyl group of TBP forming tertiary butyl dimethyl gallium and methyl phosphine.

species meet with a reasonable probability in the gas phase. It would form tertiary butyl dimethyl gallium (H_9C_4-$Ga(CH_3)_2$) and methyl phosphine. The latter one is, in fact, detected as a product, as discussed previously. The detection of dimethyl gallium then indicates the dissociation of the exchanged tertiary butyl group. This is in line with the dissociation of the largest alkyl group as the most favorable dissociation of a molecule [56]. Another potential reaction pathway for that molecule is the decomposition of TMGa to dimethyl gallium and a methyl radical via homolytic fission, the expected reaction pathway shown in the unimolecular decomposition of TMGa. This reaction is followed by a gas phase reaction between the dimethyl gallium and one of the TBP decomposition products, which could be either a phosphine or a butyl group. Together with phosphine, this could result in the formation of phosphine dimethyl gallium (H_2P-$Ga(CH_3)_2$), which could give rise to the observed fragmentation pattern. Another possibility is a reaction with a butyl group forming tertiary butyl dimethyl gallium (H_9C_4-$Ga(CH_3)_2$) again. Furthermore, this reaction would be feasible to explain the lack of isobutane and isobutene at higher temperatures as well as the reduced formation of phosphine in comparison to the decomposed TBP. The experiment was repeated and investigated for mass over charge ratios up to 200 u to identify the molecular species giving rise to the gallium-containing ions. Phosphine dimethyl gallium (H_2P-$Ga(CH_3)_2$) would be detected as molecule peak at 132 u and 134 u, whereas tertiary butyl dimethyl gallium (H_9C_4-$Ga(CH_3)_2$) would arise at 156 u and 158 u. None of these peaks were observed in the measurement.

The occurrence of methyl phosphine can be explained by the above-mentioned alkyl exchange reaction of TBP and TMGa, as well as a gas phase reaction of phosphine and a methyl radical originating from the unimolecular decomposition of TBP and TMGa, respectively. Moreover, the gas phase reaction lead to the observed reduction in phosphine formation and the lack of ethane, which is formed by two methyl groups. Thus, methyl groups undergo a different reaction than in the unimolecular case. If tertiary butyl radicals would be available as a reaction partner for methyl groups, they could form neopentane

($C(CH_3)_4$). Since this product is not observed, the formation of tertiary butyl radicals is not suggested. This finding leads additionally to the conclusion that the alkyl exchange reaction between TBP and TMGa is more likely to cause the observed gallium-containing species than the gas phase reaction of the unimolecular decomposition products because it would require butyl radicals.
The following conclusion can sum up these observations. The decomposition temperatures of TBP and TMGa are reduced in the bimolecular decomposition by approximately 150 °C. TBP enhances TMGa decomposition. In contrast, TBP decomposition is hindered by TMGa. Observed unimolecular decomposition products related to TBP are phosphine and isobutane, which are most probably formed as PH radical and isobutane in an intramolecular coupling reaction or as PH_2 radical and tertiary butyl group by homolytic fission. Due to the absence of isobutene, β-hydrogen elimination reactions are not suggested to proceed. This observation deviates from the unimolecular decomposition. The only identified unimolecular reaction product of TMGa is methane, presumably formed by homolytic fission. The dimethyl gallium counterpart is expected to be formed but is not detected in correlation to methane. The unimolecular decomposition products can form new molecular species through gas phase reactions. The observed methyl phosphine can result from a reaction between a phosphine radical and a methyl group. The formed dimethyl gallium may react with phosphine or a butyl group forming phosphine dimethyl gallium (H_2P-$Ga(CH_3)_2$) or tertiary butyl dimethyl gallium (H_9C_4-$Ga(CH_3)_2$), respectively. These larger molecules may give rise to the detected gallium, methyl gallium and dimethyl gallium fragment ions. Furthermore, TBP and TMGa can directly react via an alkyl exchange, forming methyl phosphine and tertiary butyl dimethyl gallium. This represents a suggested reaction since it can explain the detected molecular species.
Reports on the bimolecular decomposition of TBP and TMGa are already presented in the literature. Li et al. [215] investigated the pyrolysis above a GaP surface in a deuterium atmosphere. There, the additional products methyl phosphine and dimethyl phosphine were observed, which is believed to occur by alkyl exchange on the surface or interaction between the unimolecular decomposition products of TBP and TMGa. Furthermore, homogeneous decomposition of TMGa-forming methane was observed. Additionally, TMGa decomposition scales with the V/III ratio, concluding that TBP enhances its decomposition. On the other hand, TBP decomposition is suppressed by TMGa.
The formation of methyl phosphine is confirmed by the presented data. However, it can not be related to a GaP surface reaction due to its absence but a gas phase reaction. The exclusion of a surface reaction as a possible pathway may also explain why dimethyl

phosphine is not observed in this work. A further observation in common is the enhanced decomposition of TMGa, and the suppressed TBP pyrolysis.
In the work of Maßmeyer et al. [208], the bimolecular decomposition was investigated with significantly lower precursor partial pressures in a hydrogen ambient. Methyl phosphines were not observed. Their formation becomes unlikely due to the reduced partial pressure. Furthermore, they show results of a reduced decomposition temperature of TBP due to the presence of TMGa of 50 °C, which is, in fact, a reduced influence than it was observed in this work. This may also be related to the reduced partial pressure and the lower probability of interaction between these molecules. However, they argued with an alkyl exchange between TBP and TMGa, which is concluded from the presented data as well.
Concluding can be said that the results of the unimolecular decomposition of TBP and TMGa, as well as their bimolecular decomposition observed in ordinary MOVPE reactors, were partially able to be reproduced in the used *in-situ* TEM setup, even though it suffers from experimental drawbacks like the significant spatial separation of reaction volume and analyte volume or the immense delay time as discussed at the beginning of this chapter. Taking these into account, the residual gas analysis leads to comparable conclusions about the reaction pathways. That is why it is concluded that the reactions taking place in the utilized setup are capable of initiating MOVPE and that growth observations performed in the *in-situ* holder are capable of delivering meaningful results for the MOVPE growth process.
The next step that needs to be taken is to investigate the impact of the electron beam that impinges the precursor gases during an *in-situ* (S)TEM observation on the decomposition of metal organic precursors. Even though the interaction of the 200 keV primary electrons is low due to their high energy, they induce the emission of, for example, lower energy secondary electrons capable of interacting stronger with the precursor gases. By this, the decomposition behavior could change. For instance, it could result in a reduced decomposition temperature since not only thermal energy is supplied to the molecules but also energy from electron impacts.

4.2 Vapor Liquid Solid Growth of GaP Nanowires

This section addresses the *in-situ* STEM observations on the gold-catalyzed VLS growth of GaP nanowires. It starts with an explanation of the software-based data derivation from recorded STEM videos and introduces relevant quantities. Afterwards, the growth process is analyzed, with particular interest on the growth rate dependencies, its limiting step in the VLS mechanism and the formation of kinks.

4.2.1 Data Evaluation

The key advantage of *in-situ* STEM for VLS growth observation is the ability to live monitoring of the process and not be limited to post-growth interpretation. Especially the liquid catalyst alloy, the most important constituent connecting the participating phases in VLS growth, is expected to be influenced by interrupting the precursor supply and the cool-down after the growth process. The Au-Ga phase diagram (compare figure 3.8) suggests a phase separation of Au and Ga due to the temperature drop. Consequently, the post-growth observation of the catalyst particle at the nanowire tip does not represent the growth process. With live observation comes a multitude of image information. Thousands of image frames contain information about the experiment, which necessitates an automated data evaluation. In the case of VLS nanowire growth, the catalyst droplet geometry gives insights into the growth process. In order to automatically measure its geometry, a MATLAB script was used that is described in the following.
The main processing of a HAADF STEM image taken of a GaP nanowire during growth is summarized in figure 4.21. In a) a nanowire is grown from bottom to top with its brighter liquid catalyst droplet at its tip. The droplet appears bright due to the higher atomic number of gold compared to gallium and phosphorus. The dark background intensity is caused by the SiN e-chip windows. Since the script is based on edge detection and intensity thresholding, a combination of Gaussian, median and Laplace filters are applied in order to improve the robustness against image noise. In an first step, a convolution of the image intensities with a two-dimensional Gaussian smoothes the image [226]. The median filter assigns the median of its neighborhood to each pixel. By this, the image noise is reduced without significant effect on intensity edges [226]. Fast local Laplacian filtering is used to further smooth the image without affecting the image sharpness [227, 228]. In b), the effect of the applied filters can be seen. Intensities are more smooth, while the edges of the nanowire are conserved. In a next step, the image is segmented into background, wire and

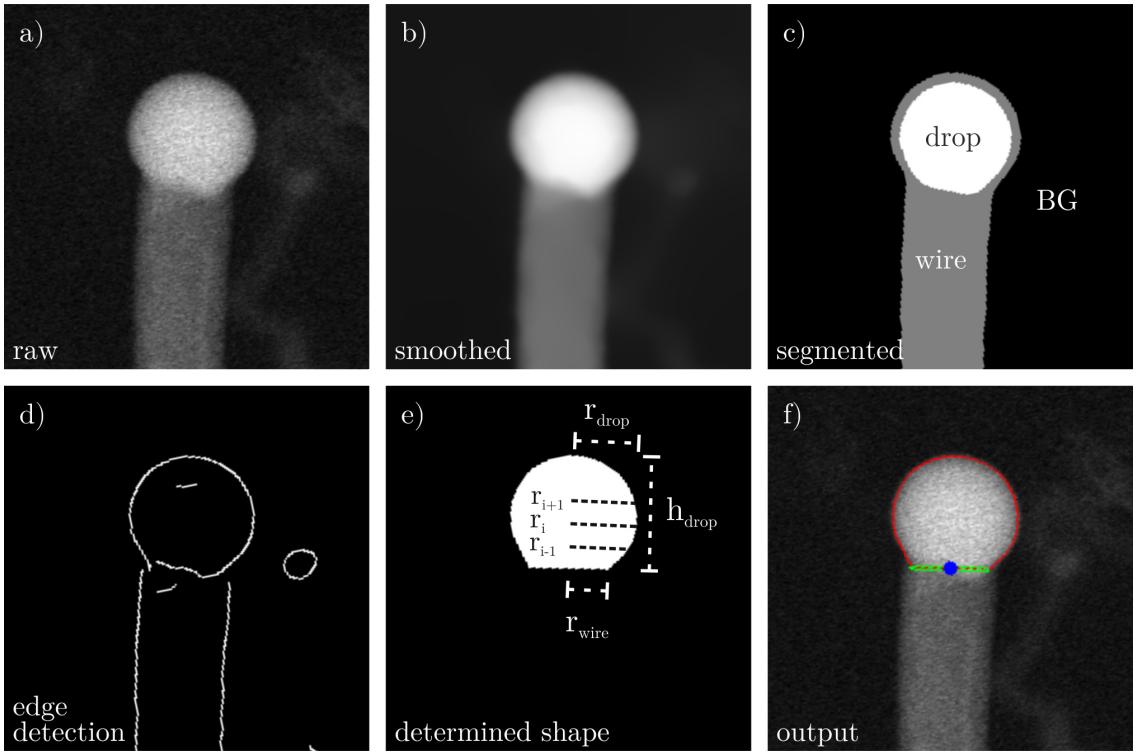

Figure 4.21: a) Initial image of a GaP nanowire with liquid Au droplet. b) Filtered and smoothed image with reduced noise and edge conservation. c) Image segmentation after adaptive thresholding of intensities. d) Edge detection using the Canny method delivers droplet and wire boundaries. e) Detected shape of Au droplet. The quantities wire radius (r_{wire}), droplet radius (r_{drop}) and height (h_{drop}) can be measured. f) Initial image with overlayed droplet boundary (red), growth surface (green) and position tracker (blue).

droplet. This is done by thresholding using the Otsu method, which determines intensity thresholds that separate the image pixels into different classes by minimizing the variance in every class [229]. In figure c), the segmentation of the filtered image in b) can be seen. Image pixels assigned to the background, labeled as BG in the illustration, wire and droplet are displayed in black, gray and white, respectively. As can be seen as a gray halo around the white droplet class, the segmentation fails for the boundary between background and droplet since intensities gradually decrease to the background value, falling below the droplet threshold but exceeding the background threshold. An additional artifact is that multiple image regions can appear, which are assigned to the droplet class if their intensity is higher than the respective threshold. Consequently, the image threshold is ambiguous for the identification of the droplet. Nevertheless, the droplet does not move by much

between two image frames. To overcome the issue of misinterpretations, the centroid position of every object in the droplet class is determined and compared to the centroid of the droplet in the previous frame. The object with the least distance to the previous droplet is therefore identified as the catalyst particle. The class objects are later utilized as image masks for the assigned image objects, for example, to consider the right edges of wire or droplet after edge detection. Edges are identified by the Canny method, which looks for the local maxima of the intensity values gradient by calculating the derivative [230]. A threshold is applied to neglect minor local maxima. The detected edges of the filtered image in b) can be seen in d). The algorithm detects the edges of the droplet and wire, as well as the bright segment of the unfocused wire on the right. Since this segment is disjunct from the droplet mask determined by segmentation, it is neglected. The growth plane is determined by the boundary of the segmentation classes of droplet and wire displayed in c), as well as its conjunction with the detected edges. Similarly, the droplet's shape is determined by the conjunction of the dilated droplet segment with the detected edges. The convex hull of these edges defines the droplet shape. It is shown in figure 4.21 e). This object contains all relevant parameters of the droplet and wire. The diameters and height can be measured as indicated in the figure. In figure f), an overlay of the initial image with the determined droplet boundary (red) and droplet wire interface (green) can be seen. Furthermore, the center of the interface, marked in blue, is utilized to identify the position of the growth front. This process is applied to all image frames of a video. By this, all parameters are achieved in dependence on time. Additionally, every frame is assigned to the corresponding experimental conditions at the point in time.
Quantities of interest that can be derived from the nanowire's and catalyst's shape are the droplet's surface and the growth front. The droplet surface is determined by a solid of revolution of its radii along its height. It can be seen as slicing the droplet from bottom to top in one pixel thin conical frustums. The area of the outer surface of the frustums is summed up as surface area A_{drop} of the catalyst droplet

$$A_{drop} = \sum_i \frac{\pi}{2} (r_i + r_{i+1}) \cdot \sqrt{\Delta x^2 + \frac{1}{4} (r_i + r_{i+1})^2}. \tag{4.8}$$

i represents the pixel position along the droplet height, r_i the respective droplet radius as illustrated in figure 4.21 e) and Δx the pixel size. This derivation of the surface comes along without the approximation of a spherical droplet and is capable of considering

distortions. The first radius r_1 additionally equals the radius of the nanowire at the growth plane and can be used to calculate the growth plane surface

$$A_{wire} = \pi r_1^2. \tag{4.9}$$

The radius of the catalyst droplet is straightforward to determine if the contact angle γ is larger than 90°. A scheme of this geometry is shown in figure 4.22 a). If, in contrast

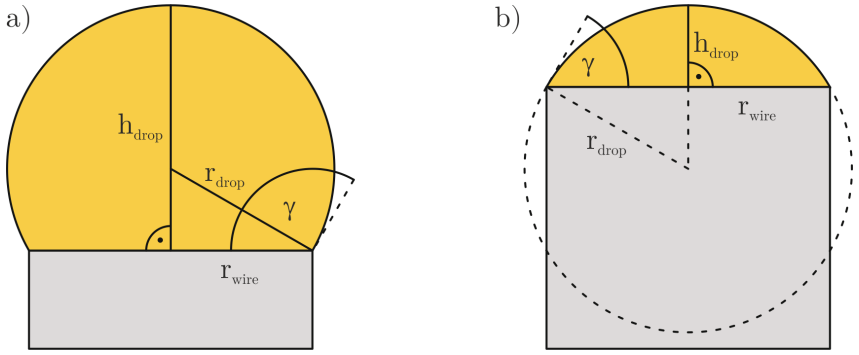

Figure 4.22: a) Illustration of a gold droplet geometry with $\gamma > 90°$ and b) $\gamma < 90°$. In the latter case, the gold droplet radius is not directly measurable.

to this, γ is smaller than 90°, the radius of the droplet cannot be measured directly, as can be seen in b). It can be determined by its surface curvature, its height h_{drop} and wire radius r_{wire}. Under the approximation of a cylindrical wire and a spherical droplet, the geometry at the nanowire tip is completely determined by the contact angle γ. Therefore it determines the ratio of the droplet radius r_{drop} and wire radius r_{drop}, as well as the surface ratio R of the liquid-vapor and liquid-solid interface A_{drop} and A_{wire}.

$$\begin{aligned} R &= \frac{A_{drop}}{A_{wire}} \\ &= \frac{1}{\pi r_{wire}^2} \int_0^{\gamma} 2\pi r_{drop}^2 \sin(\theta)\, d\theta \\ &= \sec^2\left(\frac{\gamma}{2}\right) \end{aligned} \tag{4.10}$$

Since the contact angle is difficult to measure directly from the image in figure 4.21 e), equation (4.10) is applied for determination using the surface ratio R and the surface values determined by equations (4.8) and (4.9).

4.2.2 Nanowire Growth Analysis

Samples for *in-situ* observation of the VLS growth of GaP nanowires are prepared by drop casting a suspension of gold nanoparticles and isopropanol onto the thermal MEMS chip. Hence, the particles are randomly distributed across the SiN surface. Increasing the membrane temperature and supplying the precursor gases creates a eutectic of gold and the growth material, mainly gallium (see section 3.1.4). Nanowire growth is observed at a temperature of 450 °C using tertiary butyl phosphine (TBP), trimethyl gallium (TMGa) and nitrogen as carrier gas with varied partial pressures, respectively. Recorded STEM videos are evaluated to reveal the dynamics of VLS growth. The shape of the tips of the nanowires is determined in every video frame as described in the previous section 4.2.1. Introductorily, the growth of two exemplary nanowires is discussed before the evaluation of the whole volume of data is presented. Both were grown under the same conditions with partial pressures of (4.13 ± 0.17) Pa and (0.86 ± 0.06) Pa of TBP and TMGa, respectively, and a total pressure of (410 ± 2) hPa. This results in a V/III ratio of (4.80 ± 0.39). Figure 4.23 illustrates frames of a STEM video showing the growth process. Images show a GaP

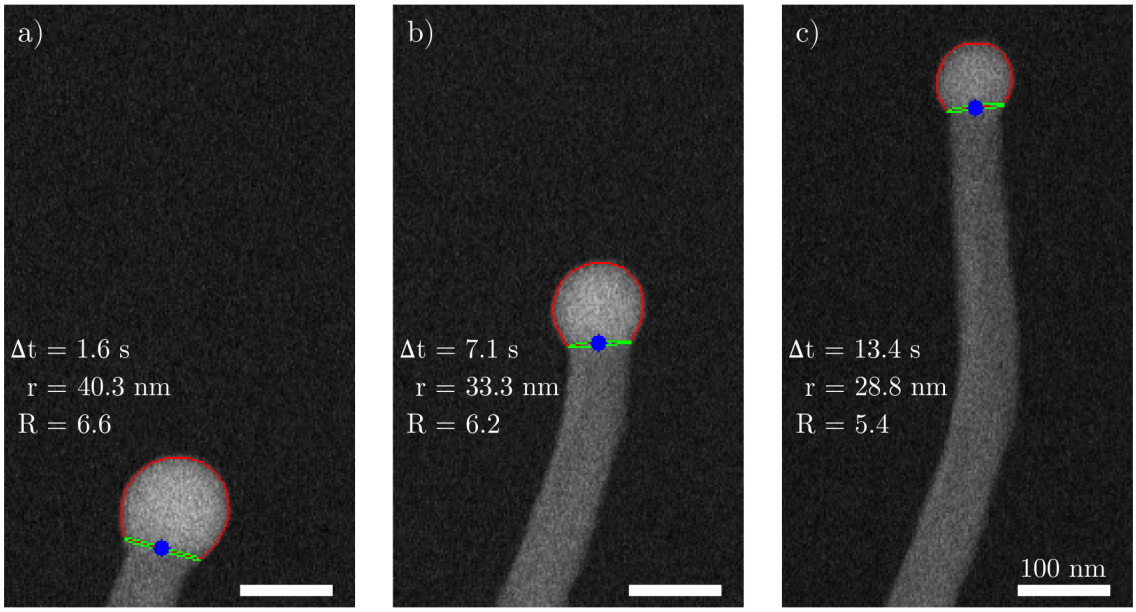

Figure 4.23: Processed STEM video frames of a GaP nanowire during growth. Droplet edges, growth interfaces and positions are highlighted in red, green and blue, respectively. The wire radius reduces from a) to c). The geometry of the nanowire tip represented by R persists nearly unchanged while the wire radius r decreases.

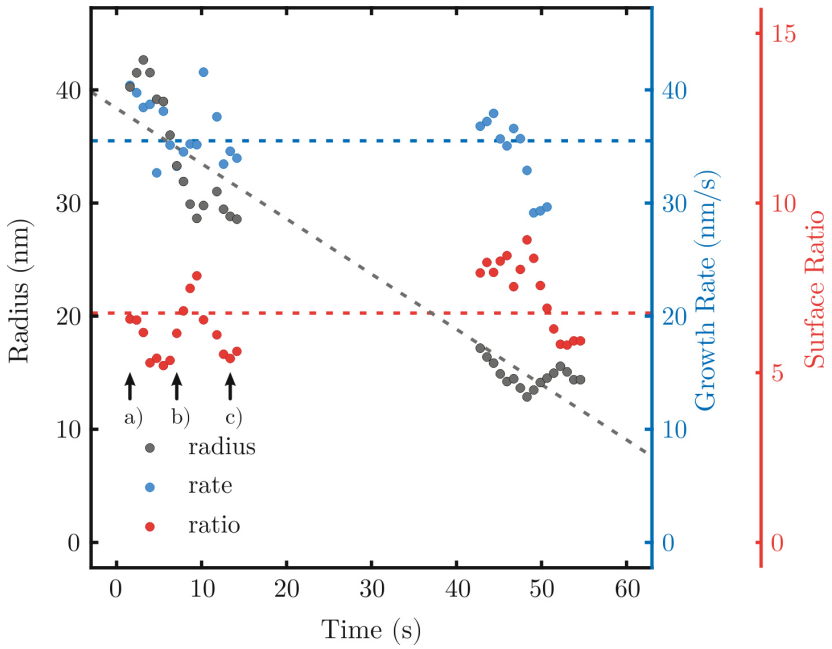

Figure 4.24: Wire radius (gray), growth rate (blue) and surface ratio (red) of a growing GaP nanowire tracked during a STEM video. The surface ratio and growth rate stay constant while the radius reduces its value. Black arrows indicate the frames of figure 4.23. ($T = 450\,°\mathrm{C}$, $p_{TBP} = (4.13 \pm 0.17)\,\mathrm{Pa}$, $p_{TMGa} = (0.86 \pm 0.06)\,\mathrm{Pa}$, $p_{tot} = (410 \pm 2)\,\mathrm{hPa}$)

nanowire with the SiN window in the background. The round catalyst droplet can be seen with bright contrast at the nanowire tip. The shape and position determined by the MATLAB script are indicated colored. The frames cover a time interval of 11.8 s. The video was recorded with a frame rate of $0.84\,\mathrm{s}^{-1}$, but only three frames are illustrated. By comparing the catalyst's shape in frames a) to c), it is conspicuous that the droplet reduces its size during the growth process. The wire radius reduces its length as well in order to minimize the impact of the shrinking droplet on the contact angle γ, which is represented by R in the figure label (see equation (4.10)). Reasons for the droplet shrinkage are discussed later on in this section. Thereby, the catalyst geometry does not follow the trend of the wire radius. The geometrical parameters, as well as the growth rate of the wire, are plotted in figure 4.24 for every video frame. Wire radius, growth rate and surface ratio are plotted against the frame time in gray, blue and red, respectively. The void of data points between the times of 15 s and 40 s is due to a movement of the sample stage to keep the growing nanowire in the field of view. The data show that the wire radius is reduced in size during its growth from around 40 nm to 15 nm within 50 s.

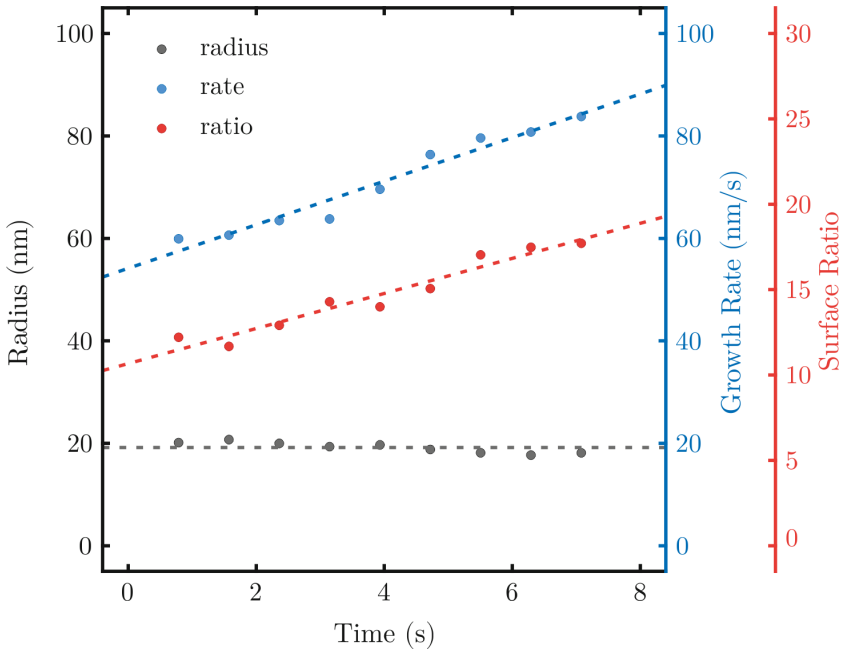

Figure 4.25: Wire radius (gray), growth rate (blue) and surface ratio (red) of a growing GaP nanowire tracked during a STEM video. The surface ratio and growth rate increase in time, while the radius remains unchanged.
($T = 450\,°\mathrm{C}$, $p_{TBP} = (4.13 \pm 0.17)\,\mathrm{Pa}$, $p_{TMGa} = (0.86 \pm 0.06)\,\mathrm{Pa}$, $p_{tot} = (410 \pm 2)\,\mathrm{hPa}$)

The gray line is a linear fit to the data points to visualize the temporal radius gradient. Even though the radius shrinks, the droplet geometry stays constant at a surface ratio of around 7. This implies that the droplet and wire radii ratio is constant, as well as the contact angle. The red dashed line marks the mean value of the surface ratio. Notably, the nanowires growth rate of $35.5\,\mathrm{nm\,s^{-1}}$ is not influenced by the shrinking nanowires radius but sustains similarly to the surface ratio.

An analogous plot is shown for another wire in figure 4.25, growing under the same experimental conditions. The wire possesses a smaller radius of around 20 nm, which remains unchanged, whereas the surface ratio rises from 12.0 to 17.5. Compared to the previously discussed wire, the surface ratio is significantly bigger. Concurrently, the growth rate shows an increase as well from $59.9\,\mathrm{nm\,s^{-1}}$ to $83.8\,\mathrm{nm\,s^{-1}}$ maintaining their ratio. Linear fits of the growth rate and surface ratio are plotted in the figure as a guide to the eye. The observations of the two nanowires suggest a linear relationship between growth rate and surface ratio since both show the same factor of approximately $5\,\mathrm{nm\,s^{-1}}$ between these quantities during the time of observation. This dependency is investigated

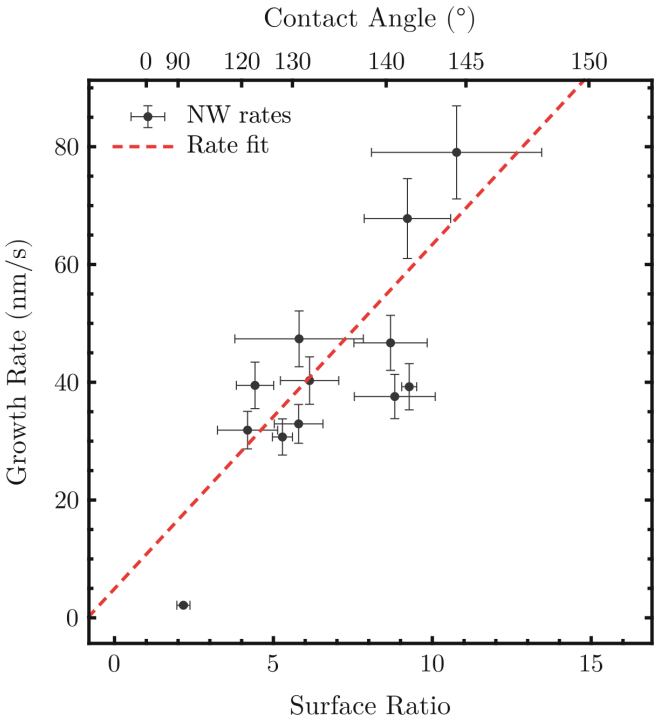

Figure 4.26: Nanowire growth rate plotted against the surface ratio. The red line illustrates a linear fit. Its slope equals the normalized growth rate of $(5.84 \pm 1.50)\,\mathrm{nm\,s^{-1}}$. ($T = 450\,^{\circ}\mathrm{C}$, $p_{TBP} = (4.13 \pm 0.17)\,\mathrm{Pa}$, $p_{TMGa} = (0.86 \pm 0.06)\,\mathrm{Pa}$, $p_{tot} = (410 \pm 2)\,\mathrm{hPa}$)

for several observed wires and different growth conditions. In figure 4.26, the growth rate is plotted in dependence on the surface ratio. Each data point represents the evaluation of a whole video of a single growing nanowire. Additionally, the contact angle is labeled on the second x-axis at the top. Data of twelve nanowires are derived in the experiment with surface ratios between around 4 and 14. Even though the linear dependency is solely vague visible, the data points show an explicit scaling of the growth rate with the surface ratio. In consequence, the growth rate is determined by a geometrical parameter, namely the surface ratio or, equivalently, the contact angle. The red line depicts a linear fit of the data with a slope of $(5.84 \pm 1.50)\,\mathrm{nm\,s^{-1}}$. This slope is hereafter called normalized growth rate. It represents the fraction of the growth rate per surface ratio. To investigate which parameters influence the normalized growth rate, the experiment is repeated with adjusted growth conditions revealing that it is determined by the precursor's partial pressure, as will be discussed in the following. Results on GaP nanowires grown at a temperature of $450\,^{\circ}\mathrm{C}$, a total pressure of $(206 \pm 1)\,\mathrm{hPa}$ and reduced TBP and TMGa partial pressures

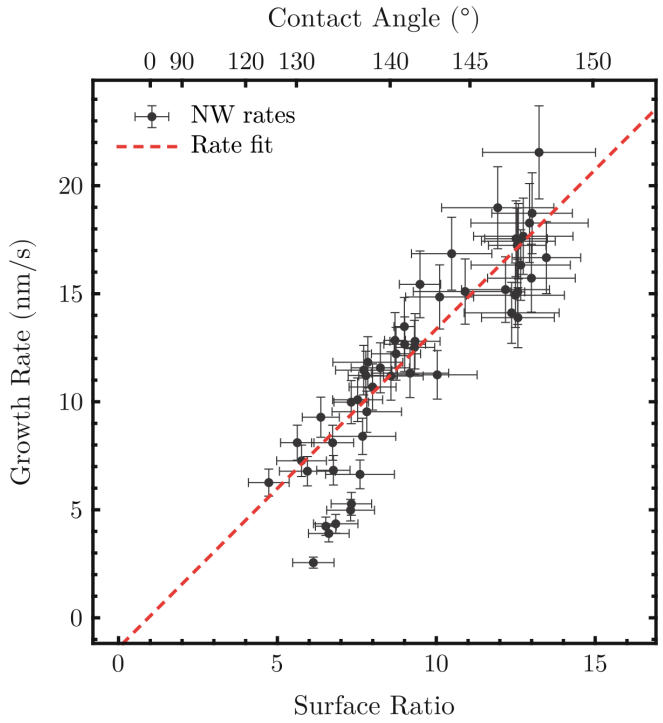

Figure 4.27: Nanowire growth rate plotted against the surface ratio. The red line illustrates a linear fit. Its slope equals the normalized growth rate of $(1.48 \pm 0.11)\,\mathrm{nm\,s^{-1}}$. ($T = 450\,^{\circ}\mathrm{C}$, $p_{TBP} = (0.957 \pm 0.036)\,\mathrm{Pa}$, $p_{TMGa} = (0.185 \pm 0.012)\,\mathrm{Pa}$, $p_{tot} = (206 \pm 1)\,\mathrm{hPa}$)

of $(0.957 \pm 0.036)\,\mathrm{Pa}$ and $(0.185 \pm 0.012)\,\mathrm{Pa}$ respectively, are shown in figure 4.27. The corresponding V/III ratio of (5.2 ± 0.4) is comparable to the previous data set. The growth rate scales according to precursor partial pressure. The slope of the linear fit is determined to a normalized growth rate of $(1.48 \pm 0.11)\,\mathrm{nm\,s^{-1}}$. Growth rate and surface ratio are changed by the factors of (3.95 ± 1.06) and (4.32 ± 0.24), respectively. In the respective error range, these values cannot be distinguished from each other. The reduction in total pressure from $(410 \pm 2)\,\mathrm{hPa}$ to $(206 \pm 1)\,\mathrm{hPa}$ does not influence the growth rate. Surface ratios are again in the range of 4 to 14, demonstrating a comparable nanowire-droplet geometry during growth. The precursor partial pressures were further tweaked in additional experiments, leading to different V/III ratios to reveal the rate-limiting precursor species. Pressures of $(0.184 \pm 0.005)\,\mathrm{Pa}$ for TBP and $(0.097 \pm 0.009)\,\mathrm{Pa}$ for TMGa, as well as $(0.184 \pm 0.005)\,\mathrm{Pa}$ and $(0.097 \pm 0.009)\,\mathrm{Pa}$ for TBP and TMGa, respectively, leading to a V/III ratio of (1.9 ± 0.2) and accordingly (26.6 ± 1.5), were utilized. These data suggest the growth to be first limited by the group V precursor TBP and that a transition to a

TMGa limitation takes place for an increasing V/III ratio. A linear dependency exists between the normalized growth rate and its partial pressure if a species limits the growth rate. Consequently, their quotient is a constant. In contrast, for a precursor that is not growth limiting, the quotient is proportional to the V/III ratio for group III species and inversely proportional for group V species. This quotient is shown in the plot of figure 4.28. The normalized growth rates determined in the *in-situ* VLS growth experiments divided by the respective precursor partial pressures are plotted against the V/III ratio for TMGa in red and TBP in blue. As expected, the data at V/III ratios around 5 do not differ in the range of the error, even though they were derived with different partial pressures. In the range of V/III ratios up to 6, the plot reveals an invariant value of the quotient in the case of TBP illustrated by the horizontal dashed blue line with a mean value of $(1.48 \pm 0.15)\,\mathrm{nm\,s^{-1}\,Pa^{-1}}$. This value determines the normalized growth rate for the group V limited regime for given TBP partial pressures. In contrast, the data of TMGa show a linear increase with the V/III ratio, which is indicated by the red dashed line representing a linear fit. The data points at a V/III ratio of (26.6 ± 1.5) do not continue these trends. The quotient is significantly reduced in the case of TBP, and the one of TMGa is on a comparable value of $(9.3 \pm 1.3)\,\mathrm{nm\,s^{-1}\,Pa^{-1}}$ as for a V/III ratio of around 5. This demonstrates a transition from the group V limited to the group III limited growth regime. The transition value of the V/III ratio can be extracted from these data. It occurs at a V/III ratio of (6.2 ± 0.9) marked by the vertical black line, where the linear increasing regime equals the quotient of the group III limited regime due to the constant value in this interval. For this value, the effective V/III ratio is equal to 1. The TBP quotient scales inversely proportional from this point, as illustrated by the dashed blue line. The group III limitation is furthermore supported by the observation that the surface ratios of growing nanowires are reduced for the high V/III ratio to values between 2.7 and 4.6, compared to values up to 14 in the group V limited regime. Since TMGa is the limiting species, no reservoir of gallium builds up in the gold droplet. The surplus of phosphorus cannot be incorporated into the catalyst due to its low solubility. Therefore, the gold volume is reduced, leading to lower surface ratios. This finding demonstrates that the V/III ratio controls the droplet geometry. Consequently, gold-catalyzed VLS growth of GaP nanowires using TMGa and TBP is group V limited within the presented pressure range and temperature up to a V/III ratio of at least (6.2 ± 0.9). That group V is limiting the growth rate, although a surplus of TBP is present in the vapor phase, is due to the low solubility of phosphorus in gold [151]. The eutectic liquid is saturated with gallium, and just a low amount of phosphorus is incorporated. Further increase of the TBP fraction

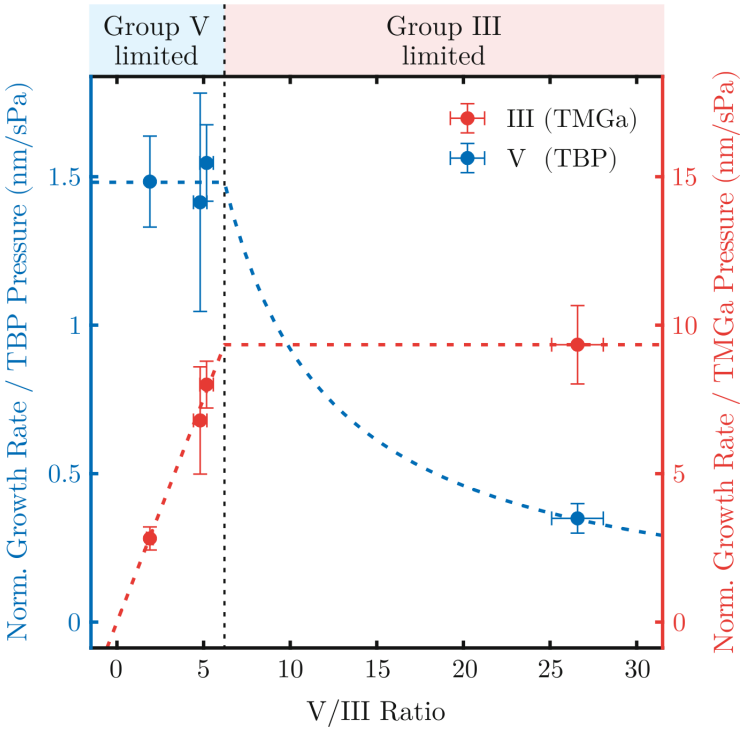

Figure 4.28: Normalized growth rates divided by the precursor partial pressure plotted against the V/III ratio. Blue data points are of the group V species (TBP), and red data points are of the group III species (TMGa). At a V/III ratio of (6.2 ± 0.9) marked by the black line, a transition from the group V (blue shaded) to the group III limited regime (red shaded) occurs. The limiting species is independent of the V/III ratio and remains at a constant value. The surplus species scales proportionally in the case of group III and inversely in the case of group V.

leads to a group III limited growth regime since it becomes the less dominant species. The transition from group V to group III limiting growth appears for significantly different V/III ratios in MOVPE reactors operated at elevated total pressure compared to *in-situ* TEM observations performed in ETEMs in ultra-high vacuum conditions. For example, Liu et al. reported on group III limited GaAs nanowire growth from V/III ratios below 70 using TMGa and arsine in MOVPE and nitrogen ambient [231]. In contrast, Joacobsson et al. observed group V limited growth for V/III ratios up to 1000 using the same precursor gases but in an ultra-high vacuum ETEM [29]. They also commented that these severe differences in experimental conditions are less comparable to MOVPE than MBE and that the effective group V supply is strongly reduced in a vacuum. Here the applied closed gas cell setup bridges the gap towards *in-situ* TEM observations under MOVPE-comparable

conditions. Steidl et al. reported on group III limited VLS growth of GaP nanowires using TMGa and TBP as well with a V/III ratio of 10 and a hydrogen carrier gas at 50 hPa [232]. The here presented results on the group III limitation correspond to this behavior in MOVPE, which the ones reported from ETEM setups cannot. This highlights the unique ability of this setup to operate under MOVPE conditions.
The findings show that growth rates do not depend on the nanowire radius, which became clearly visible in figures 4.24 and 4.25. From this, it can be concluded that the rate-limiting step of the VLS growth under the utilized growth conditions is the incorporation of growth material from the vapor phase into the liquid droplet, as discussed in chapter 3.1.3. Moreover, the proportionality between the growth rate and surface ratio supports this conclusion. Diffusion from the vapor into the liquid phase proceeds on the liquid surface. The larger the surface, the more material diffuses. Suppose the crystallization rate is not limiting the growth rate, and diffusion proceeds fast. In that case, the growth velocity is determined by the ratio of the droplet surface and the growth interface that equals the nanowire cross-section in VLS growth.
It is conspicuous in the plots of figures 4.26 and 4.27 that there are data points deviating from the linear trend towards lower growth rates and higher surface ratios. This is expected to have two reasons. First, nanowires may contain velocity components parallel to the viewing direction. This would decrease the observed growth rate according to the cosine of the angle between the growth direction and projection plane. Hence, growth rates can be shifted to lower values. Unfortunately, this effect cannot be quantified in the videos. Second, for some nanowires, it can be the case that they grow on the SiN surface. In a simple geometric model, this would reduce the effective surface ratio for contact angles bigger than 90° as illustrated in figure 4.29, since an additional liquid-solid interface between the droplet and the SiN is formed. By this, the vapor-liquid interface across which diffusion takes place is reduced. The missing surface fraction is marked in red. The effective droplet surface still depends on the contact angle γ:

$$A_{drop,eff} = \int_0^{\gamma} 2\pi r_{drop}^2 \sin(\theta)\, d\theta - \int_0^{\gamma-\frac{\pi}{2}} 2\pi r_{drop}^2 \sin(\theta)\, d\theta \tag{4.11}$$

With the second integral term describing the missing free droplet surface follows an effective surface ratio R_{eff} with the expression

$$R_{eff} = R - 2\left(\csc^2(\gamma) - \csc(\gamma)\right). \tag{4.12}$$

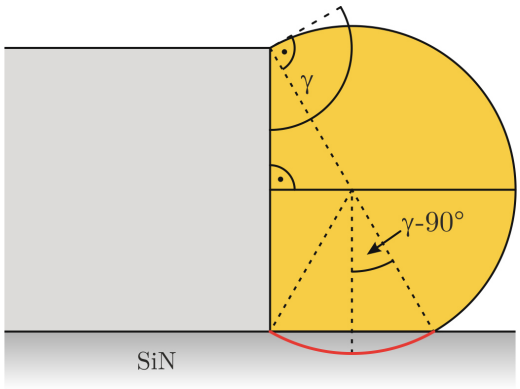

Figure 4.29: Illustration of a geometric model of a wire growing on the SiN surface. Contact angles above 90° lead to an additional liquid-solid interface between the droplet and the SiN, reducing the vapor-liquid interface.

It represents only a rough estimation of the impact of this effect. Especially at the triple phase line of vapor-liquid and SiN, the droplet is expected to be distorted due to the droplet surface tension, which is not considered by equation (4.12). According to this simple model, the surface ratio would be slightly overestimated, causing the data point to shift to the right. From the videos, it is generally hard to judge whether a nanowire is growing in contact with the SiN surface, and it is unclear whether nanowires follow the same growth mechanism for all growth conditions if they do so. Especially at higher temperatures where the precursors get decomposed efficiently on the SiN, surface diffusion is expected to impact the growth process significantly. Nevertheless, the growth rate still scales with the surface ratio, or rather an effective surface ratio, indicating that the transport of growth material again proceeds via the vapor through the liquid to the solid phase, with the incorporation step being limiting. It indicates further that surface diffusion is negligible. Growth on the surface can explain why the droplets shrink with time. While the wire is moving forward, some liquid gold is smeared at the liquid-solid interface between the droplet and SiN and gets lost. Simultaneously, the wire radius decreases to sustain the contact angle with reduced droplet volume.

A further significant aspect that is mandatory to investigate is how the observation by the electron beam influences the nanowire growth. To this end, the electron beam dose rate exposed to a growing nanowire was changed during the observation. It was performed by changing the field of view by controlling the imaging magnification. Higher magnifications condense the electron beam current onto a reduced area, increasing the dose rate and vice versa. In figure 4.30, the normalized growth rate of a nanowire is plotted over the electron

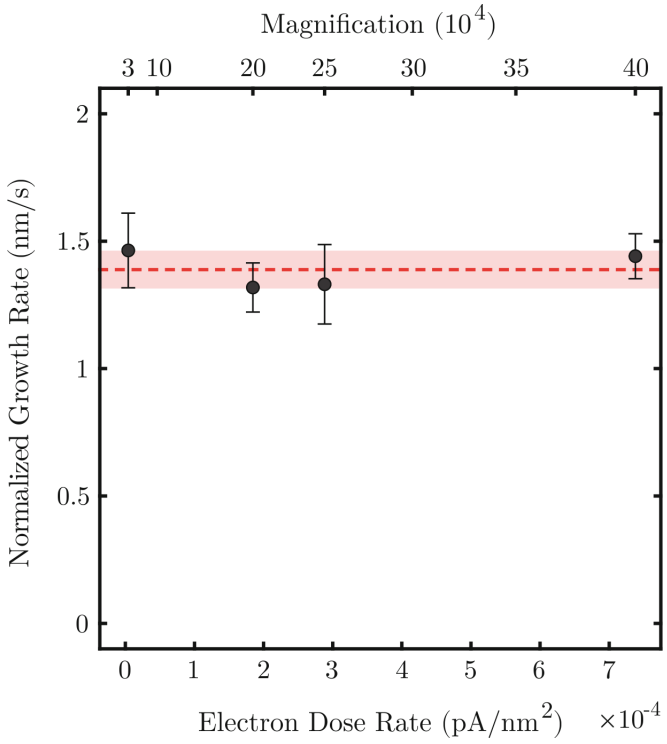

Figure 4.30: Normalized growth rate of a nanowire versus electron dose rate of the impinging beam. The dose was controlled by changing the field of view due to different magnifications. The red line and the shaded area show the mean value and its error respectively. ($T = 450\,°\mathrm{C}$, $p_{TBP} = (0.957 \pm 0.036)\,\mathrm{Pa}$, $p_{TMGa} = (0.185 \pm 0.012)\,\mathrm{Pa}$, $p_{tot} = (206 \pm 1)\,\mathrm{hPa}$)

dose rate according to magnifications between 30 k and 400 k. The corresponding electron doses ranges from $4.2 \times 10^{-6}\,\mathrm{pA\,nm^{-2}}$ to $7.4 \times 10^{-4}\,\mathrm{pA\,nm^{-2}}$. The plot reveals that for all electron doses, the normalized growth rate remains unchanged within the error. The mean of $(1.39 \pm 0.08)\,\mathrm{nm\,s^{-1}}$, which is in line with the determined value of $(1.48 \pm 0.11)\,\mathrm{nm\,s^{-1}}$ of the corresponding experiment displayed in figure 4.27, is marked by the red dashed line. From this can be concluded that the nanowire growth rates are unaffected by the dose rate of the primary electron beam. Further growth experiments were performed while keeping the sample holder outside the TEM but in a vacuum pumping station to exclude any effects induced by the TEM itself. Post-growth observations of these samples showed nanowires with identical morphology and structure. Obviously, no statement about dynamics, such as growth rate or surface ratios can be made without observation. But the comparison to *in-situ* investigated samples demonstrate that growth with and without TEM observation deliver qualitatively the same results. In future investigations, the effect

on the total electron dose should also be carried out by directly varying the beam current during live observation that remained constant in the presented results.
In summary, it was found that the growth rate depends linearly on the surface ratio of the vapor-liquid and the liquid-solid interfaces and that a transition from group V to group III limitation takes place at a V/III ratio of (6.2 ± 0.9). Growth rates scale with the partial pressure of the respective limiting species. Consequently, the rate-limiting step of VLS growth in the presented regimes of growth conditions is the incorporation of growth material from the gas phase into the liquid phase of the catalyst particle. The incorporation step proceeds on the liquid surface and thus possesses a proportionality of its rate on the surface of the vapor-liquid interface. Since the other steps of the VLS mechanism consequently are not limiting and proceed fast enough, the growth rate is furthermore inversely proportional to the growth plane surface. Contributions of surface diffusion are found to be negligible. A dependence of the growth rate on the electron beam dose rate or nanowire radius is not observed. These findings and conclusions are in line with and complement the ones Kodambaka et al. have reported for the VLS growth kinetics [233].

4.2.3 Nanowire Kink Formation

The growth of nanowires via the VLS mechanism predicts the development of straight wires. However, besides their generally straight proceeding growth, nanowires also show kink formation, separating the wires into straight, angle-inclining segments. In section 4.3, these kinks are investigated in post-growth studies via SEM, HRTEM and SPED, showing their structural properties. In this section, the formation of such kinks is presented based on *in-situ* STEM observation, demonstrating the dynamics of the kink formation. Figure 4.31 shows a slide show of the evolution of a kink. Each image is a frame from a STEM video with a frame time of 1.95 s. The experiment was performed at a temperature of 450 °C, a total pressure of (206 ± 1) hPa and TBP and TMGa partial pressures of (0.957 ± 0.036) Pa and (0.185 ± 0.012) Pa, respectively. In each frame, the bright catalyst particle can be seen on top of a nanowire of 25 nm radius growing from bottom to top. The darker background consists of a SiN window. The growth interfaces are highlighted in yellow for each frame and maintained to the following ones. The coordinate system is chosen according to an initial (111) growth front viewed along $[\bar{1}10]$. In the beginning, the catalyst droplet is arranged symmetrically on the tip of the straight-growing nanowire. In frame a), a distortion emerges to the right of the droplet. Such distortions can be

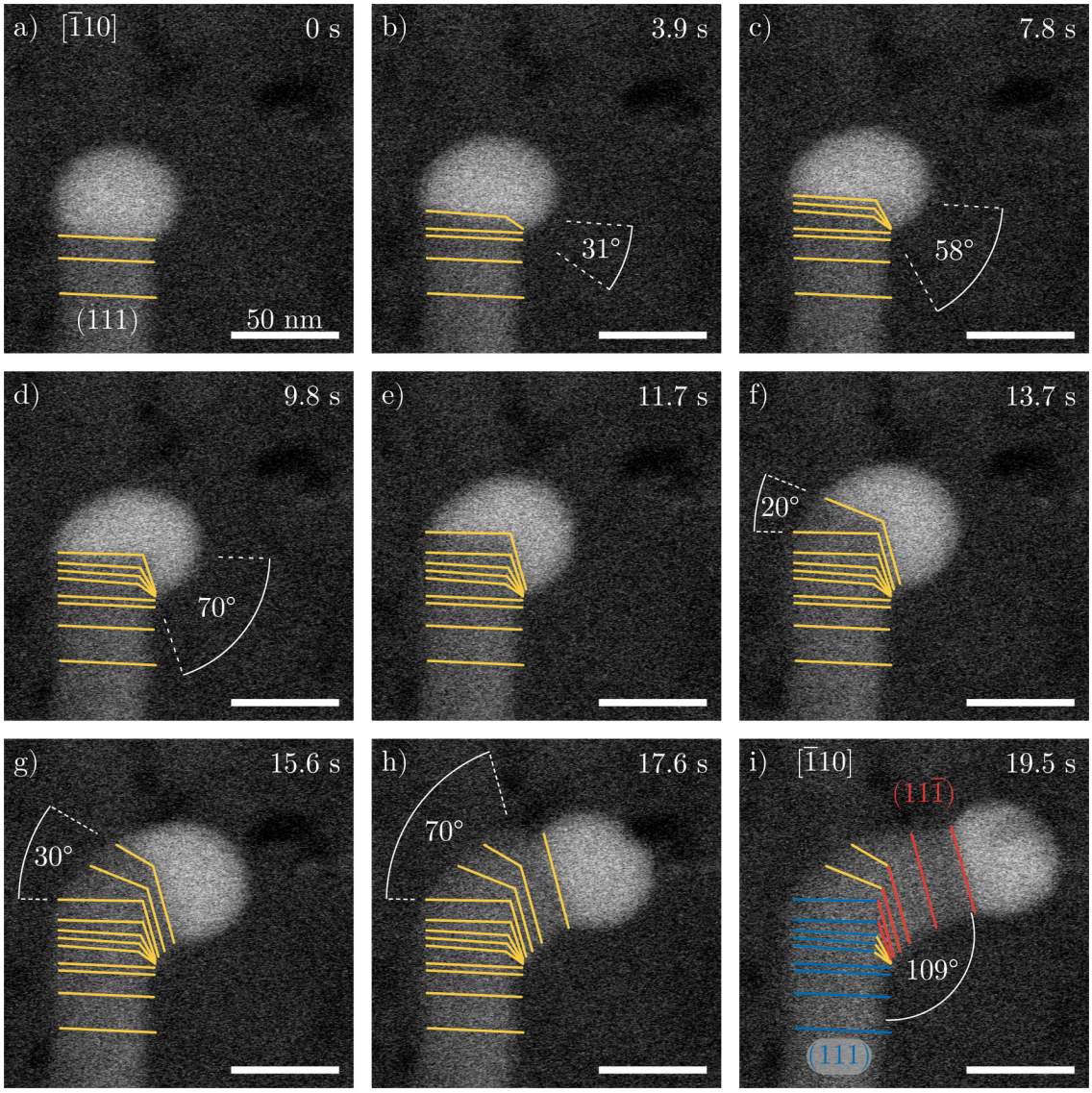

Figure 4.31: Frames of a STEM video showing the evolution of a 109.5° kink. Colored lines highlight growth interfaces. Zone axis is close to $[\bar{1}10]$.
($T = 450\,^{\circ}\mathrm{C}$, $p_{TBP} = (0.957 \pm 0.036)\,\mathrm{Pa}$, $p_{TMGa} = (0.185 \pm 0.012)\,\mathrm{Pa}$, $p_{tot} = (206 \pm 1)\,\mathrm{hPa}$)

explained by the stacked octahedron shape of the wire. During growth, the wire can form triangular growth planes rather than perfect hexagons [234]. The droplet's surface tension leads to an asymmetric distortion in ⟨110⟩ projections, with a higher contact angle at the triangle edges than at its corners [235]. According to the model, the left side of the growth front consists of a triangle corner and the right of an edge. In the next video frame, which is not illustrated in the figure, the growth slows down and a truncation on the right side possessing the higher contact angle becomes visible in the succeeding image b). The truncation creates a tilted growth front on the side of the wire as the (111) plane continues growing. It is tilted by an angle of around 31°. Measured angles may deviate by a few degrees from the real value since the images are most likely not recorded in the exact $[\bar{1}10]$ zone axis. In the next two successive frames, the angle increases to 58°, as can be seen in frame c). This further tilt of the truncation is driven by the continuing growth of the initial (111) plane on the left side of the wire. The yellow marked growth interface's reduced spacing reveals a reduced growth velocity of the (111) plane while the truncating plane is getting tilted. In table 4.6, planes of different orientations parallel to $[\bar{1}10]$ are listed with their respective tilt angle to (111). The tilted interface changes its orientation gradually and probably consists of combinations of planes according to its tilt. Some are listed in the table possessing small Miller indices. Planes with higher Miller

Plane	(332)	(221)	(331)	(110)	$(33\bar{1})$	$(22\bar{1})$	$(33\bar{2})$	$(11\bar{1})$
Angle (°)	10.9	15.8	22.0	35.3	48.5	54.7	60.5	70.5

Table 4.6: Angles of planes to (111) plane in $[\bar{1}10]$ projection. All planes are parallel to $[\bar{1}10]$.

indices commonly possess higher surface energies due to an increased amount of dangling bonds [36]. Furthermore, the area of the growth interface is enlarged compared to a plain growth front. Consequently, these planes are unfavorable to be formed by the crystal and cause the chemical potential of the nanowire to rise. Additionally, the distortion of the catalyst droplet increases its surface fraction, leading to an increased chemical potential of the liquid. In contrast, the gas phase's chemical potential remains unchanged, reducing the difference in chemical potentials between the vapor and liquid phases. Corresponding to section 4.2.2, where the growth rate-limiting step was identified to be the incorporation from vapor to liquid phase, the growth rate reduces. In the next frame, which is shown in d), the truncating plane is tilted to 70°. This orientation matches the one of the $(11\bar{1})$ plane and is maintained as a new growth front, determining the growth direction. As this plane is built up, the surface energy of the growth plane reduces compared to the tilted

intermediate planes, and the growth on the (111) accelerates again, as can be seen by the transition to frame e). Furthermore, growth on the newly formed $(11\bar{1})$ plane is initiated. In a next step the initial (111) plane becomes tilted towards $(11\bar{1})$. This becomes visible in image f), where the intermediate plane forms an angle of 20° to (111). In the next frame g), this angle is increased to 30° as the plane is truncated further. Simultaneously, the growth rate on $(11\bar{1})$ further increases as the higher energetic intermediate plane shrinks. In frame h), the kink is completed and the $(11\bar{1})$ growth interface has built up in a 70° angle to the initial one. After the completion of the kink, the growth rate returned to a comparable velocity to before. This becomes visible by the increased spacing of the last two yellow growth fronts. A straight segment and a symmetric droplet at the tip continue the wire growth. In the last frame i), which is shown in figure 4.31, the (111) and $(11\bar{1})$ planes are marked in blue and red, respectively. Intermediate planes are displayed in yellow. The growth rates of the (111) and $(11\bar{1})$ planes are plotted in figure 4.32 in the same color code. The gray-shaded intervals highlight the time in which the intermediate planes were formed for the transition from (111) to $(11\bar{1})$. The blue curve illustrates the slowing down of the (111) prior to the kink. The growth rate is reduced while the intermediate planes are present. As the transition to the $(11\bar{1})$ plane is completed, the growth rate accelerates again until the plane undergoes the transition to $(11\bar{1})$ as well. Since no (111) exists anymore, its growth rate vanishes. As mentioned above, the growth on $(11\bar{1})$ represented by the red curve starts slowly once the plane is built up. It keeps on being slow, while the residual (111) plane undergo the transition to $(11\bar{1})$ by creating intermediate planes. The second shaded interval highlights this period. The kink formation is completed at its end, and the growth direction has changed to $[11\bar{1}]$. The growth rate is accelerated again.

By comparing the geometrical parameters of the wire before and after forming the kink, it becomes visible that the geometry of the wire has changed. The radius of the wire reduces from (24.8 ± 2.5) nm to (21.6 ± 2.2) nm. In consequence, the height of the catalyst particle increases from (44.2 ± 4.4) nm to (49.3 ± 4.9) nm, as the amount of the catalyst eutectic stays roughly the same. Accordingly, the surface ratio rises from (4.7 ± 0.6) to (5.6 ± 0.5), which leads to an increasing growth velocity from $(6.25 \pm 0.63)\,\mathrm{nm\,s^{-1}}$ to $(8.10 \pm 0.81)\,\mathrm{nm\,s^{-1}}$.

Additionally, the formation of the kink is likely connected to the formation of a twin boundary either on the (111) or $(11\bar{1})$ plane. It is known that the triangular distortion of the catalyst is accompanied by twin formation [235]. Here, the *in-situ* STEM study does not deliver quantitative information on the crystal orientation or defects, due to the lack of atomic resolution imaging, as a consequence of the single tilt capability of the sample

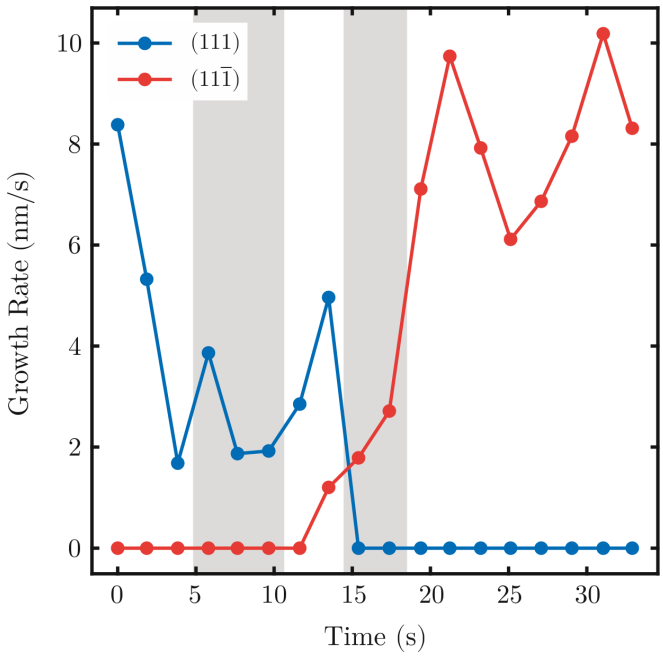

Figure 4.32: Growth rates on the (111) plane (blue) and $(11\bar{1})$ plane (red) during the formation of the kink illustrated in figure 4.31. The gray-shaded intervals mark the formation of intermediate planes.

holder. A more detailed investigation of the twinning in connection to kink formation is presented in the following chapter 4.3. It will be shown that a 109.5° kink, like the one observed in this section, is connected to an inversion of termination of the {111}, from $\{111\}_A$ to $\{111\}_B$ occupied by gallium and phosphorus respectively or vice versa. Before forming the kink, the wire shows a normalized growth rate of $(1.32 \pm 0.18)\,\mathrm{nm\,s^{-1}}$. After the kink, the termination has changed and the normalized growth rate is determined to $(1.45 \pm 0.14)\,\mathrm{nm\,s^{-1}}$. In the scope of the errors, these growth rates do not differ from each other. Rates on $\{111\}_A$ or $\{111\}_B$ are not expected to be different since the termination only affects the chemical potential of the solid phase. The chemical potential difference between the vapor and liquid phase, which limits the growth rate, is not affected.

4.3 Post Growth Investigations

In this section, the structure of nanowires grown in the *in-situ* TEM holder is analyzed with respect to their macroscopic shape as well as their crystal structure. Nanowire growth performed at 450 °C results in straight-growing nanowire segments with a length of several micrometers following the VLS mechanism. In between these segments, the nanowires form kinks. SEM images reveal the appearance of nanowires at a micrometer scale. Insights into the atomic structure are obtained by HRTEM and four-dimensional SPED data sets, with precession angles of 0.25° to 0.50°. First, the nanostructure of nanowires is described since it is found to be the reason for their shape and kink formation.

GaP nanowires grow in zinc blende structure along ⟨111⟩ direction, as can be seen in the HRTEM image in figure 4.33 a). The image shows a section of a nanowire with amorphous SiN background. Nanowire sidewalls show a saw tooth faceting, marked by the dashed line exemplarily, rather than straight surfaces parallel to the growth direction, such as {112} or {110} planes. For cubic GaP, no stable surfaces parallel to ⟨111⟩ are available due to their high surface energies [37]. Sidewalls consist of {111} surfaces with an inclination angle of 141°. This angle results from the tetrahedron geometry of {111} planes as the doubled opposite tetrahedral angle ($2 \cdot (180° - 109.5°) = 141°$). The surface energy of GaP {111} planes is $\sigma_{(111)} = 1.69\,\mathrm{J\,m^{-2}}$, whereas the surface energies of {110} and {111} are $\sigma_{(110)} = 2.06\,\mathrm{J\,m^{-2}}$ and $\sigma_{(112)} = 2.36\,\mathrm{J\,m^{-2}}$, respectively [36]. Even though the surface area increases due to the formation of {111} surfaces, the total surface energy is reduced by 13 % in comparison to {110} facets and by 24 % in comparison to {112} sidewalls. The surface faceting comes with twin boundaries on the (111) growth plane. Each side of a saw tooth consists of a {111} plane of twinned domains. By this, the ⟨111⟩ growth direction is maintained, and the surface energy is minimized with the formation of twin boundaries [236]. In the HRTEM image in figure 4.33 a), four twin boundaries (TBs) between twinned domains can be seen, indicated by the white arrows. Domains with brighter or darker contrast share the same crystal orientation. Twinning on a (111) plane can be described by a 60° rotation of the crystal around the [111] direction and leads to a misorientation between the twinned domains of 60°. Accordingly the zone axis of the left domain changes from $[1\bar{1}0]$ to $[0\bar{1}1]$ in the twinned domains. In 4.33 b), the orientation map of the segment obtained by SPED can be seen. It is weighted with the index and reliability map to visualize only the nanowire, neglecting the amorphous background surrounding the wire. The color code describes the orientation of the crystal according to the colored inverse pole figure obtained via stereographic projection. The reference

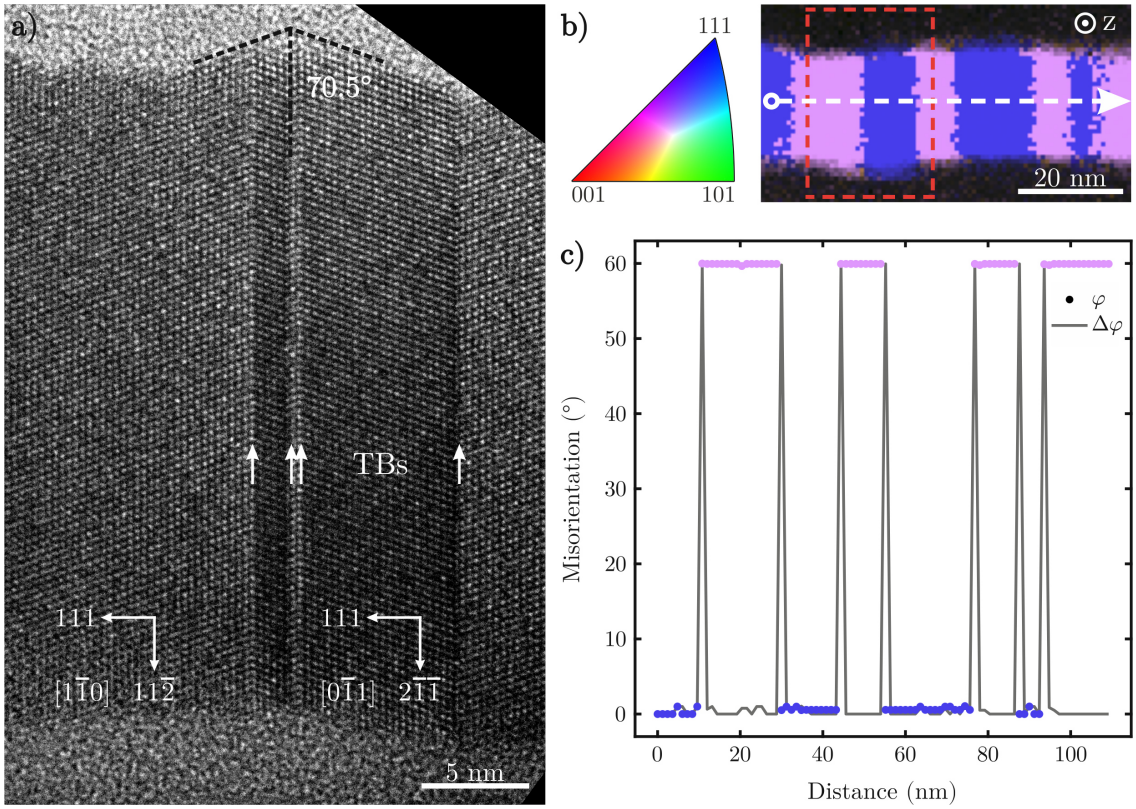

Figure 4.33: a) HRTEM image of twinned domains. b) Misorientation across twin domains. c) Orientation map weighted with index and reliability map. The red box marks the area of the HRTEM image. The white arrow is the scanned line for misorientations in b)

direction is in the viewing direction labeled as z. The misorientation plot in figure 4.33 c) is generated from the data along the linescan depicted by the white arrow. A white circle on the left marks the reference point. It shows the misorientation φ along the wire segment across seven parallel twin boundaries with respect to the leftmost domain plotted with colored dots and the misorientation with respect to the previous point $\Delta\varphi$ represented by the gray line. Following the linescan shows a misorientation of 0° in φ and $\Delta\varphi$ in the misorientation plot within the first twin domain color-coded in blue. Transitioning across the twin boundary at a scanned distance of 10 nm to the twinned domain color-coded in pink shows a misorientation φ of 60° along the whole domain. $\Delta\varphi$, on the other hand, only reveals the twin boundary between the jump in φ with a misorientation of 60°. Across the pink domain from 10 nm to 30 nm the orientation does not change, accordingly $\Delta\varphi$ is approximately equal to 0°. Further following the linescan show consecutive twinning on

(111) planes. Twin boundaries appear as 60° misorientation peaks in $\Delta\varphi$. The repeating color of the domains demonstrates the switching back and forth between the crystal orientations and, accordingly, misorientations φ of 0° and 60°. This is due to 120° rotation symmetry around ⟨111⟩ of zinc blende structure, which makes a total rotation of 120° indistinguishable from a counterclockwise and clockwise rotation of $60° - 60° = 0°$. The field of view of the HRTEM image in a) is marked by the red rectangle. Comparing the HRTEM image with the orientation map reveals that SPED cannot resolve the central twin domain, which only consists of two atomic layers with a thickness of 0.63 nm, which is approximately a tenth of the precessing electron beam probe size. The SPED resolution is limited to ≈ 7 nm in the used microscope.
The misorientation changes for domains separated by twin boundaries on different ⟨111⟩ planes. Possible misorientations of twin domains up to the 5th order are determined. For this reason, all possible combinations of twin planes are considered. Due to symmetrization, only a single rotation angle of 60° needs to be considered. There exist four possible twin planes, which are (111), $(\bar{1}11)$, $(1\bar{1}1)$ and $(11\bar{1})$, leading to 4^n possible combinations of n consecutive twin boundaries. The unique misorientations of twin domains are tabulated in table 4.7. Twins of first order solely cause misorientations of 60° corresponding to the

Order	Misorientation			
1	60.0°			
2	38.9°			
3	35.4°	31.6°		
4	60.4°	54.5°	38.4°	
5	49.8°	43.1°	12.2°	7.4°

Table 4.7: Calculated values for misorientations of consecutive {111} twinned domains up to a order of five.

rotation on the {111} plane. The only misorientation for twins of second order is 38.9°. In principle, they are capable of canceling the 60° misorientation of the first-order twin to 0° again. But this case is assigned to a not twinned domain. In the same way, twin domains of higher orders that reduce the misorientation to the lower order value are again assigned to the lower order twin. Further increase of the twin order leads to an increased number of possible misorientations. Figure 4.34 a) shows a kinked wire segment's index and reliability-weighted orientation map. The color code represents the orientation with respect to the x-direction pointing from left to right according to the colored inverse pole figure sown in b). The misorientation scan along the white arrow in a) is plotted in c). The

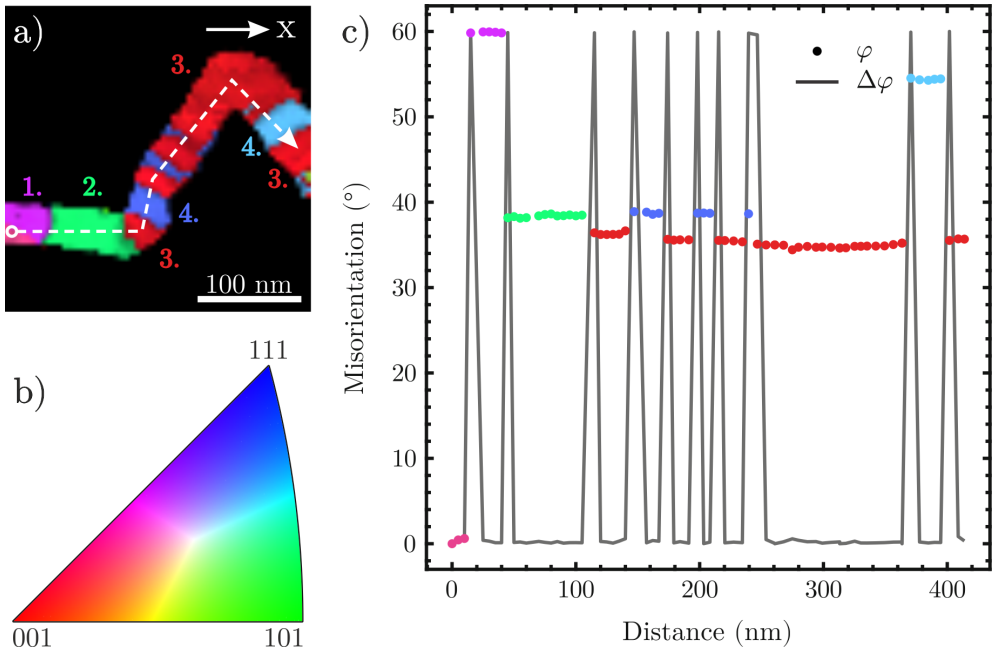

Figure 4.34: a) Orientation map of a kinked GaP nanowire segment showing twinned domains up to an order of 4. Kinks are formed at twin boundaries. b) Color code of symmetrized orientations in the stereographic projection of the Euler's space. c) Misorientation along the white arrow. The white circle in a) indicates the reference point for φ.

reference point for the misorientation φ is the first scan point marked by the white circle. It is clear that not all {111} twin boundaries in this wire segment are parallel. Hence, indicating that twins of higher order appear that do not show a misorientation of 60°. Each boundary between the domains shows a 60° misorientation in $\Delta\varphi$. So, neighbored domains are still twins of the first order. A crystal domain is visible at the bottom left corner of the wire segment, colored in pink, acting as reference orientation for φ. It has a {111} twin boundary tilted by 70° with respect to the growth direction. The following purple domain shows a misorientation of 60° as a twin of the first order. Its twin boundary with the green domain is now perpendicular to the growth direction and consequently not parallel to the previous twin boundary. The misorientation with respect to the first domain is $(38.4 \pm 1.0)°$, which can be designated as a twin of the second order. The next twin boundary is again tilted, leading to the red domain with a misorientation of $(36.4 \pm 1.0)°$ followed by a twin boundary with the same orientation resulting in the blue domain with misorientation of $(38.7 \pm 1.0)°$. These misorientations match one of the expected third and fourth-order twins, respectively. The measured value of $(38.7 \pm 1.0)°$ of the fourth-order

twin can not be separated from the misorientation of second-order twins. Nevertheless, it can be concluded from the consecutive boundary orientations that it is a fourth-order twin with respect to the first domain. Additionally, the misorientation between the green and blue domain is $(39.0 \pm 1.0)^\circ$, indicating that these are twins of second order. Furthermore, the misorientation of $(36.0 \pm 1.0)^\circ$ between the purple and blue domains demonstrates a third-order twin. The consecutive parallel twin boundaries between red and blue domains switch back and forth between the same crystal orientations and end up again with a red third-order twin. Its boundary with the light blue domain possesses a different orientation than the previous ones. As a result, the measured misorientation is $(54.4 \pm 1.0)^\circ$, which is a further expected value for a fourth-order twin.

These examples showed that with SPED, a determination of the nanostructure by means of the crystal orientation is possible without the necessity of atomic resolution HRTEM imaging. It further provides the advantage of crystal phase and orientation determination out of zone axis tilt conditions. This is especially beneficial for investigating samples containing domains with different orientations.

In the orientation map of a nanowire in figure 4.34 a), it is conspicuous that at every kink, the nanowire shows a twin boundary. In the case that twinning is connected to the formation of kinks, the angles of kinks are not arbitrary. Possibilities for kink angles are calculated under the two following assumptions. First is that growth proceeds only in the $\langle 111 \rangle$ direction, and second, the twinning plane is perpendicular to the new growth direction, which is the commonly observed case. Depending on the order of twinning table 4.8 summarizes the kink angles that are expected to be observable. Depending on the final growth direction, the termination of the growth plane may change. Growth proceeding in opposite directions occurs on oppositional terminated planes. In consequence, kink angles with inverted termination are the opposite angles of the ones that conserve the termination. The table additionally distinguishes between angles with the respective termination behavior. The tetrahedral angle and its opposite are possible kinks for twins of the first order since they are inclined by $\{111\}$ directions. For higher orders, the situation becomes more and more complex due to the repetition of these angles in various directions depending on the twinning plane orientation. To form kinks of higher-order nanowires, they need to change their growth directions multiple times due to twin formation. Hence high-order twins are more a mathematical consideration than a prediction. Nevertheless, they could be utilized to further understand nanowire growth directions in segments separated by multiple kinks. In general, zinc blende III/V nanowires tend to grow along $\{111\}_B$ terminated surfaces, occupied by group V atoms [237]. Consequently, angles that

Order	Kink angle									
	Termination conserved					Termination inverted				
1	70.5°					109.5°				
2	38.9°	123.7°				56.3°	141.1°			
3	22.2°	87.9°	114.0°	148.4°		31.6°	66.0°	92.1°	157.8°	
4	34.2°	57.9°	67.5°	76.4°		18.1°	36.6°	49.1°	77.9°	
	93.5°	102.1°	130.9°	143.4°	161.9°	86.5°	103.6°	112.5°	122.1°	145.8°

Table 4.8: Calculated values for angles between ⟨111⟩ growth directions due to consecutive {111} twinned domains up to a order of four. Possible angles of lower orders also apply for the higher orders.

invert the termination are expected to occur with a lower probability. Furthermore, if they are formed, a further kink that inverts the A termination again to B is expected. In general, the angles of nanowire kinks cannot be measured in a single TEM or SEM image since they represent a projection onto the viewing plane of a three-dimensional structure. To overcome this issue, a series of SEM images are recorded, each with a different viewing angle ranging from $-8°$ to $55°$, which is the SEM stage tilt range. They represent projections of the nanowire from various directions and can be utilized to reconstruct the arms of the kink in three dimensions. The rotation axis is defined as the x-axis in the images. The components x and y of a vector $\vec{r} = (x,y,z)$, that is assigned to an arm, are measured in the image with a tilt of α. From an image with a stage tilt of $\alpha' \neq \alpha$ the components x' and y' of the respective vector $\vec{r}' = (x',y',z')$ in the by $\beta = \alpha' - \alpha$ rotated coordinate system are derived. $\vec{r}'$ can be transferred in the initial coordinate system by

$$\vec{r} = R_x^{-1}(\beta)\,\vec{r}' \tag{4.13}$$

with $R_x(\beta)$ describing a rotation of the coordinate system by β around $\vec{r}_x$. Equation (4.13) can be solved for the unknown component z of $\vec{r}$ by

$$z = y' \csc(\beta) - y \cot(\beta)\,. \tag{4.14}$$

By this, the corresponding arms of vectors can be determined and used to calculate the inclined angle. In figure 4.35, SEM images of a GaP nanowire from different viewing directions over an angular range of 58.1° can be seen. Nanowires with bright contrast are visible in front of the SiC membrane, which appears as a dark background. The respective tilt condition is denoted in the upper right image corners. Projections of the

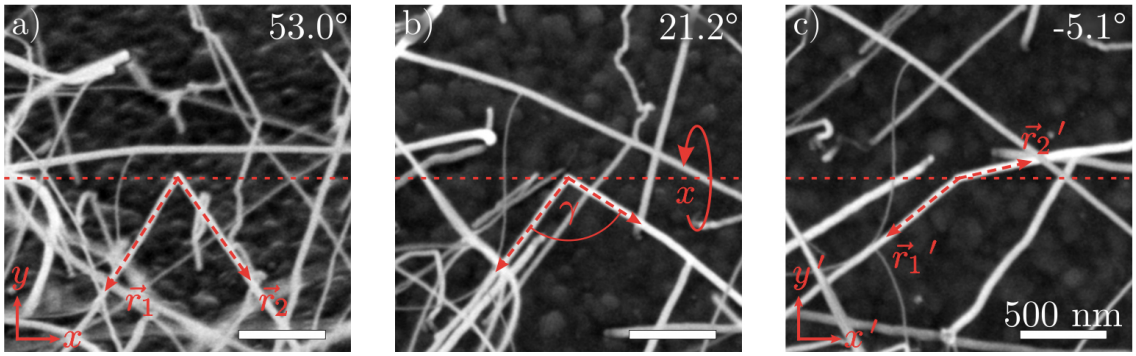

Figure 4.35: SEM images from a tilt series for nanowire kink determination with a viewing angle of 53.0° (a)) 21.2° (b)) and −5.1° (c)), rotated around the x axis marked by the red dashed line. Red arrows highlight measured projected directions of nanowire arms in the rotated coordinate systems. The determined inclined angle is $\gamma = (72.0 \pm 1.7)°$.

vectors $\vec{r}_i$ and $\vec{r}_i\,'$ in the initial ($\alpha = 53°$) and tilted ($\alpha' = -5.1°$) coordinate system are highlighted with red arrows. The dashed line indicates the rotation axis (x). The determined angle γ inclined by the nanowires arms is $(72.0 \pm 1.7)°$. A histogram of 65 determined kink angles is shown in figure 4.36. The red curve represents the probability

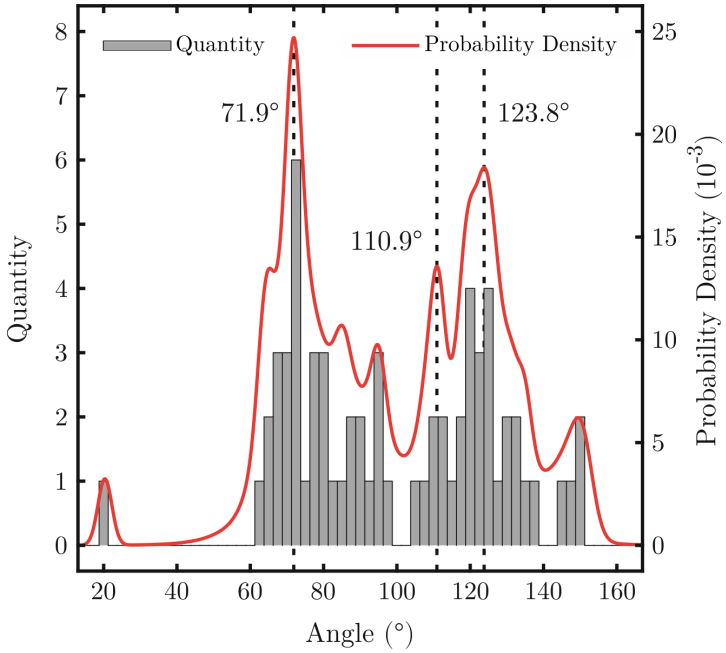

Figure 4.36: Histogram of nanowire kink angles (gray). The red curves represent a kink angle probability density determined by a kernel density estimation. An angular accumulation at approximately 70° and 120° is visible.

density of the angle distribution. It is calculated by kernel density estimation using a Gaussian kernel and the measurement error as standard deviation [238]. The histogram of angular distribution shows clusters at angles around 70° and 120°. The probability density smoothes the discrete histogram data to a continuous distribution. It contains three distinctive maxima at 71.9°, 110.9° and 123.8° marked by the dashed lines. In the following, the origin of these angles is investigated by SPED. Figure 4.37 a) shows an index and reliability weighted orientation map of a GaP nanowire that inclines an angle of $(110.2 \pm 6.1)°$, determined by the above-mentioned three-dimensional reconstruction via SEM tilt series. The relatively large error is a consequence of the short straight segment, which reduces the direction determination accuracy of the left nanowire arm. The color code is the same as in the previous figures. Orientations are determined with respect to the y-axis. Misorientaions plotted in b) are determined along the white arrow. The turquoise domain on the right acts as a reference for φ marked by the white circle. Again misorientations between turquoise and red $\{111\}$ twinned domains of 60° can be seen. The growth direction of the wire is from right to left and proceeds in all domains along a $\langle 111 \rangle$ direction. The nanowire kink appears directly at the twin boundary. To prove, the results obtained by SPED figure 4.37 c) additionally shows an HRTEM image of the kink with FFTs of the twinned domains labeled with A and B. Twin boundaries are marked with dashed white lines. The FFTs reveal the defect at the twin boundary. In the transition from B to A, the 111 spot is invariant since the defect is a rotation on the (111) plane. The other spots are rotated by the tetrahedral angle of 109.5°. Domain A changes its growth direction from [111] to $[\bar{1}11]$. By this, the inclined angle is 109.5°. The HRTEM enables direct measuring of the kink in the image since the plane spanned by the angles arms lies within the image plane. The growth direction of $[\bar{1}11]$ implies a change in growth plane termination, as the kinks angle also predicts it. The blue domain on the left side of the orientation map is a second-order twin compared to the turquoise one. Its twin boundary induces a change in growth direction again, that inverts the growth plane termination merely 50 nm after the previous change. As discussed previously, nanowires tend to maintain the $\langle 111 \rangle_B$ growth plane, and changes in termination are not favorable. The initial growth direction and the one after the second kink incline a 123.7° angle that shows conservation in termination.

An orientation map of a nanowire that formed an angle of $(70.2 \pm 2.0)°$ can be seen in figure 4.38 a). Again, it is weighted with the index and reliability map, and its color code corresponds to the previous direction. Directions are determined in z direction. In b), a TEM image of the wire is presented. Due to the single tilt capabilities of the TEM

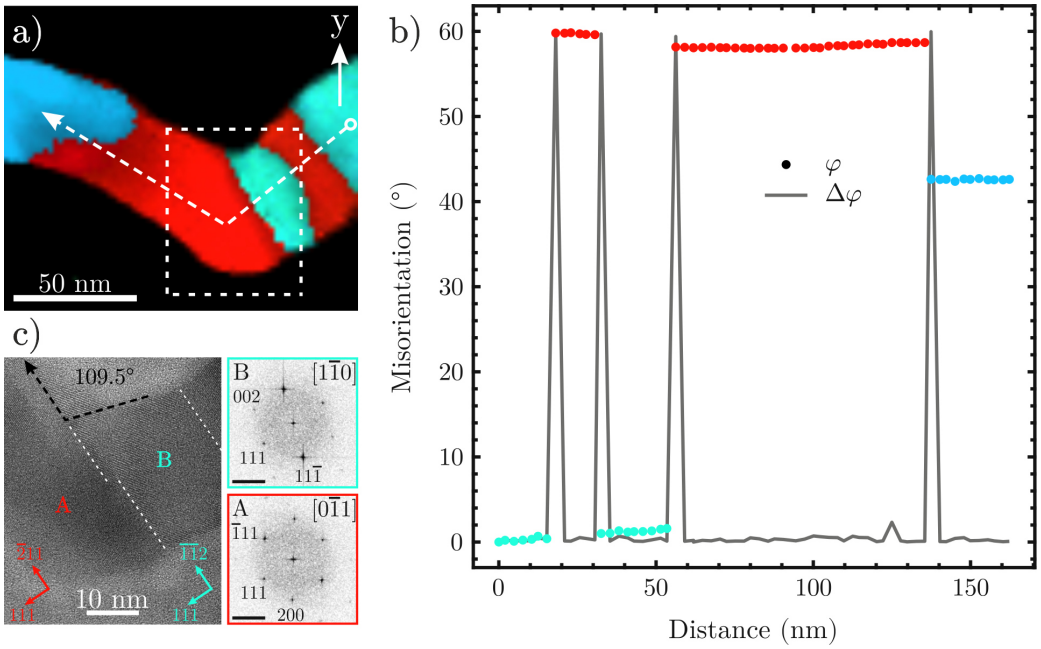

Figure 4.37: a) Orientation map of a nanowire that kinks at an angle of 109.5°. The white box indicates the field of view of the HRTEM image. b) misorientation along the white arrow in the orientation map. The white circle in a) denotes the reference point for φ. c) HRTEM image of the kink segment. FFT of the red (A) and turquoise (B) domains reveal {110} zone axes twinned on the (111) plane. FFT scale bar equals $3\,\mathrm{nm}^{-1}$.

holder, it cannot be tilted to a proper zone axis in order to resolve the atomic structure. Nevertheless, SPED can reveal the atomic structure without the necessity of atomically resolved imaging, as shown in the previous example. The white box in the image marks the field of view in figure a). The purple and yellow domains are again {111} twinned domains, possessing a misorientation of 60°, as can be seen in the misorientation scan in c) along the white arrow in a). The change in growth direction emerges anew directly at the twin boundary. The change in growth direction from [111] to [$\bar{1}\bar{1}$1] does not change the termination of the growth plane.

The last frequently observed angle is around 123°. Like the 70.5° kink, 123.7° kinks conserve the termination of the growth plane but emerge as a result of second-order twinning. The weighted orientation map in figure 4.39 a) depicts the orientation of domains around a kink, whose inclined angle is determined to $(121.1 \pm 1.0)°$. Orientations are given corresponding to the y-axis of the image. Figure 4.39 b) states the misorientation along the white arrow in a). The reference point for φ is the green domain marked by

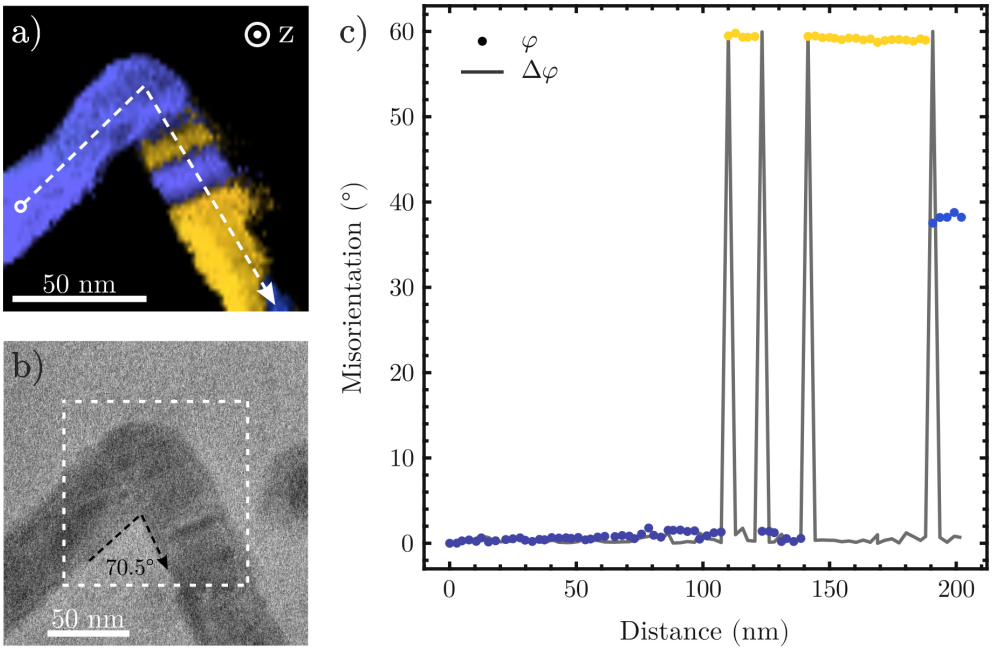

Figure 4.38: a) Orientation map and b) TEM image of a GaP nanowire forming an angle of 70.5°. The white circle marks the reference point for φ. The white box indicates the region scanned by SPED. c) Misorientation determined along the white arrow in a).

the white circle. Starting at the bottom, twin domains in yellow and green are visible that share twin boundaries perpendicular to the growth direction. In the center of the kink, the yellow domain has two non-parallel twin boundaries. The neighboring purple domain is also a twin of the first order but a second-order twin with respect to the green one. Both twin boundaries changed the growth direction of the wire. The purple domain grew out of the plane, but the caused kink is not visible in the orientation map due to projection. The inclined angle of the {111} growth directions is accordingly to table 4.8 123.7° of a termination conserving kink, caused by a twin of second order. At the top of the orientation map, a light blue domain with a tilted twin boundary compared to the purple domain with respect to the growth direction can be seen. Even though the boundary is tilted, it does not cause a further change in the growth direction. The domain increases the order of twinning to three, with respect to the green domain, possessing a misorientation of $(33.1 \pm 0.4)°$. This value can be assigned to the expected one of 31.6°. Deviations in the misorientations from previous domains can arise due to the bending of the wires. The purple domain illustrates this effect by a steady misorientation increase from $(40.6 \pm 0.5)°$ to $(41.9 \pm 0.4)°$ without the formation of defects along the domain.

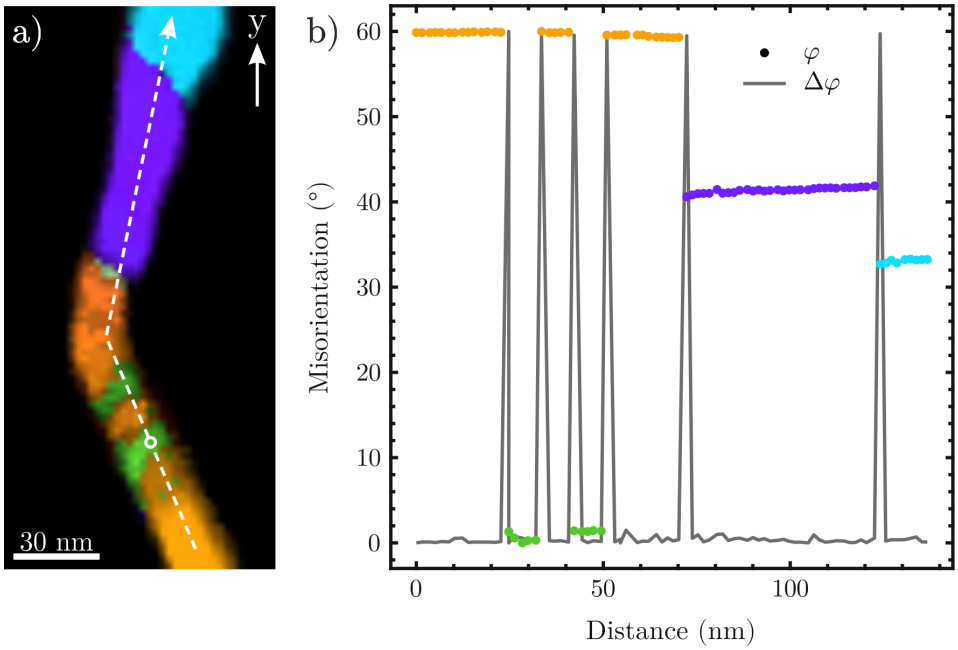

Figure 4.39: a) Orientation map weighted by the index and reliability map of a kinked GaP nanowire with an angle of $(121.1 \pm 1.0)°$. b) Misorientation along the white arrow in a). The white circle indicates the reference point for φ. All boundaries represent {111} twin defects. The angle is caused by a second-order twin of the green and purple domain around the kink.

Table 4.8 further suggests kink angles of 38.9° to preserve the termination. These angles are not observed since they are unlikely to be formed due to geometrical reasons.
It is shown that kinking of nanowires growing in {111} direction can be related to the formation of twin boundaries. The resulting angles are determined by the crystallographic orientation of the twinned domains. Abundances of observed angles show predominantly angles capable of maintaining the termination of the growth plane. These findings differ from those observed in VLS-grown InP nanowires in ⟨111⟩ [239]. Their investigation of the kink angles showed the predominant formation of 109.5° angles over 70.5° angles that were caused by twin boundaries. On the other hand, accumulations of angles around 123.7° were not observed. The different behavior can result from the absence of a preferred termination in InP. Then, the 109.5° angle is more frequently observed since it is geometrically easier to form. In contrast, 123.7° angles are not observed because a changed termination by a 109.5° kink is not needed to be inverted again.

4.4 Substrate for Epitaxial Growth

The experimental results presented in section 4.2 are based on Au nanoparticle samples prepared by drop casting a suspension of gold nanoparticles and isopropanol onto the amorphous SiN layer of the MEMS chip. While this technique is straightforward and fast, it leads to some experimental drawbacks since the amorphous substrate does not predetermine the crystallographic orientation of the growing nanowires. First, atomic resolution imaging is generally not achievable as a consequence of the single tilt restriction of the sample holder that prevents a proper zone axis adjustment. Second, nanowires grow in random directions and often move out of focus. To overcome these issues, a crystalline substrate with controlled orientation can be utilized. In this chapter, two attempts at substrate preparation are presented and discussed. Additionally, results of *in-situ* STEM observations of GaP nanowire VLS growth on a crystalline substrate are shown.
Group IV or III/V semiconductor materials are suitable candidates for a substrate for GaP nanowire growth due to their similar crystal structure. Silicon is chosen as substrate material since GaP can be grown nearly lattice-matched because of the minor lattice mismatch of 0.36 % [34, 240]. Furthermore, the growth of GaP nanowires on silicon is particularly interesting for III/V material integration on silicon and for many applications. A silicon wafer with a (111) surface is used to prepare substrates for VLS growth. The required geometry of such a substrate is illustrated in figure 4.40. A crystalline silicon block that can be seen in gray is located next to a SiN window of the MEMS chip in

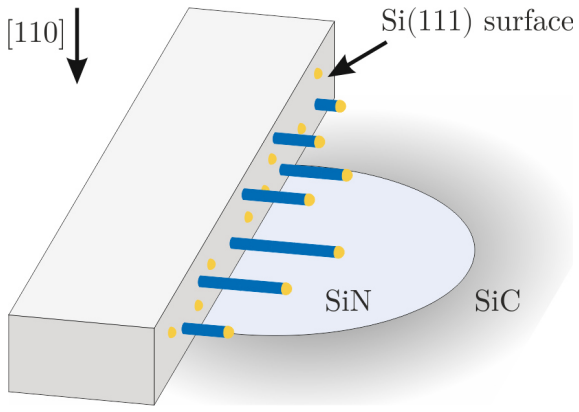

Figure 4.40: Illustration of a substrate for epitaxial growth on MEMS chip. A silicon lamella (gray block) is facing with a (111) surface to the SiN window next to it. The Si(111) surface carries gold particles to catalyze nanowire growth. Nanowires growing in [111] direction grow parallel to the window and can be observed in [110] zone axis.

[110] zone axis orientation. Gold particles are deposited on the (111) surface to catalyze VLS growth. Its surface normal is facing parallel to the SiN. GaP nanowires illustrated in blue can adopt the surface orientation and grow perpendicular in the [111] direction. Thereby, the disadvantages of vertical growth velocity components and growth on the SiN surface discussed in chapter 4.2.2 would be eliminated. However, some challenges need to be overcome to transfer such a substrate in the desired orientation. The prepared substrate needs to have a thickness below the gas cell height of the *in-situ* holder of 5 µm. Furthermore, growing with an epitaxial relationship to the substrate requires a crystalline surface. Silicon forms an amorphous native oxide layer with a thickness of around 1 nm in contact with air [241] capable of preventing epitaxial growth. It was shown that GaP nanowires grow in random directions on a Si(111) surface due to the oxide layer [242]. Nevertheless, this oxide layer can be removed by wet etching using 40 % hydrofluoric acid. Moreover, the dangling bonds of the silicon surface remain saturated with hydrogen for over 100 min after etching, preventing the oxide layer from forming anew [243]. During this time the surface is passivated by a gold layer with a thickness equivalent of a few nanometer. It is sputtered in a high vacuum onto the silicon surface. In the experiment, the gold layer will act as a catalyst particle as the gold nanoparticles did in experiments presented in previous sections. The continuous layer of gold will form droplets in contact with the precursor gases during heating in the investigation. Compared to the drop-casting of nanoparticles, preparing a sputtered gold layer offers the following advantages. On the one hand, surface contamination on the MEMS chip is strongly reduced. After evaporation of the solvent of the nanoparticle solution, organic residues remain on the surface. In contrast, a sputtered gold layer is free of contamination. On the other hand, the amount of deposited gold can be controlled precisely. The thickness of the sputtered layer can be determined with sub-nanometer precision by the natural frequency of a quartz crystal that gets modulated in dependence on the deposited layer thickness. The drop casted gold amount depends on the droplet size, which is poorly controllable by hand. Consequently, preparation by sputter coating is easier to control and reproducible than drop-casting of nanoparticles. The sputtered gold layer possesses a rough surface structure, evocative of a cauliflower surface. The layer is liquefied for VLS growth by heating, forming droplets on the surface. To prove the passivation of the silicon surface, a cross-section lamella is prepared and investigated by STEM. Figure 4.41 shows an atomic resolution HAADF image of the lamella at the silicon (111) surface. The image is recorded in $[1\bar{1}0]$ direction. At the bottom, the projected dumbbell pattern of silicon can be seen. The deposited gold is visible with bright contrast on top of the silicon. The black layer at the top consists of a

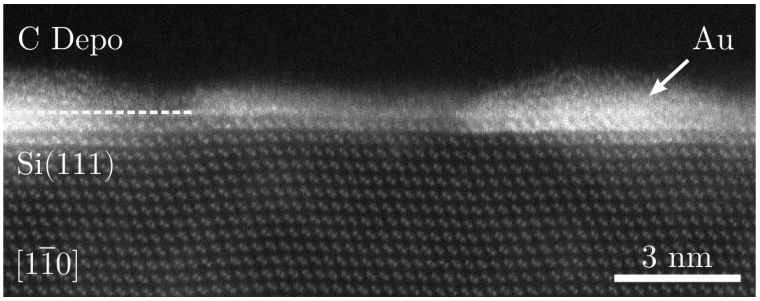

Figure 4.41: STEM image of Au on Si(111) surface

carbon layer that protects the surface during lamella preparation. It can be seen that the silicon's crystallinity underneath the deposited gold is conserved up to the topmost layer, and no amorphous oxide has formed underneath the gold. Furthermore, a high contrast underneath the silicon surface marked by the white dashed line can be seen. It can be caused by the FIB beam that smeared the deposited gold over the lamella surface during preparation. Alternatively, it can be the result of the gold diffusing into the first layers of silicon. Due to the rough gold layer surface, small regions exist between gold flakes where the silicon surface is not completely covered. In these regions, the native oxide can form locally. The amorphous oxide causes a diffuse image intensity, which in projection overlaps with the atomic columns of the crystalline silicon. These effects cause the topmost silicon layers to have lower contrast visible in the HAADF image.
In the subsequent sections, preparation methods for a silicon substrate on the MEMS chip are presented. The first approach describes a direct FIB cutout of the surface, whereas the second one is based on mechanical grinding.

4.4.1 Focused Ion Beam Preparation

FIB preparation techniques ensure control over the specimen's thickness, orientation and shape. Precise samples can be prepared in a desired zone axis orientation for investigations at atomic resolution [244]. In addition, these can be transferred to MEMS-based sample holders, enabling zone axis orientation even in holder designs without double tilt capability [245]. Conventionally these preparation techniques use deposition layers protecting the region of interest, which usually is directly at the sample surface. In contrast, preparing a substrate requires an uncovered surface, prohibiting the use of protective deposition layers. An alternative way to protect the surface is a preparation geometry in which the surface is averted from the ion beam. Nevertheless, a chunk of silicon needs to be cut out. Even

though the direct impingement of ions onto the desired surface region can be avoided in FIB, redeposition, ion implantation and beam damage occur in the surrounding area of milling [246]. The impact of these is investigated in the following.
A roughly 50 µm long silicon lamella with a thickness of 6 µm is trenched from a silicon (111) wafer sputtered with a thickness equivalent of 3 nm gold by a 30 kV gallium beam. Figure 4.42 illustrates the gold coverage on the surrounding silicon surface after milling. In a), the gold coverage is plotted versus the distance from the lamella center. The edge

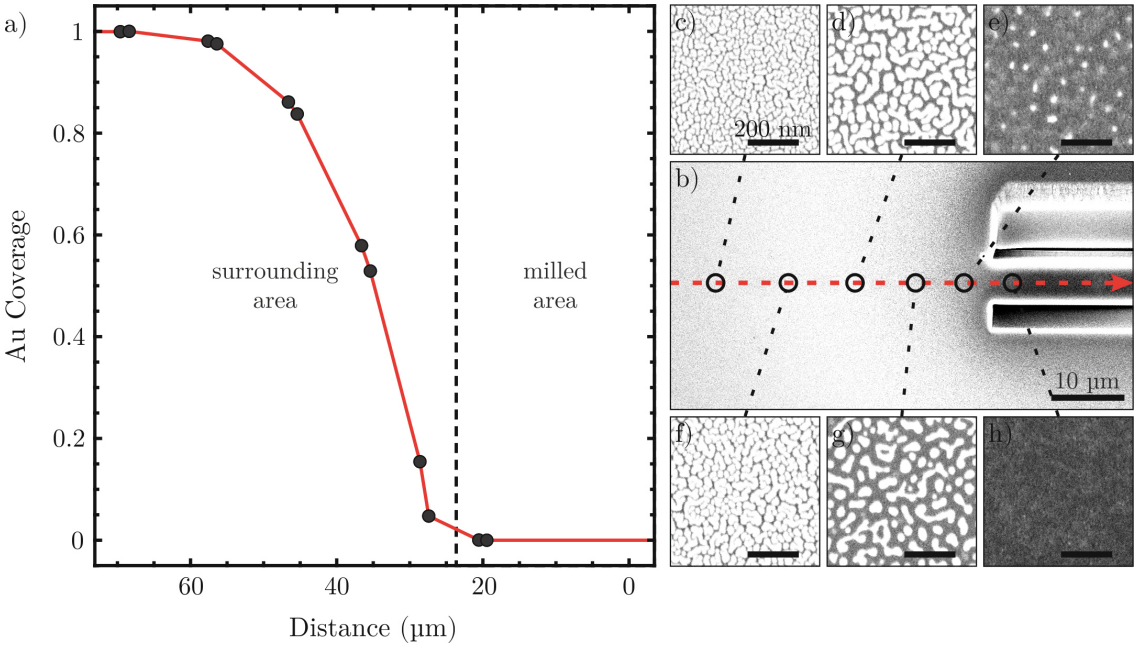

Figure 4.42: a) Gold coverage in the surrounding FIB milling area after lamella trenching. The plotted distance is relative to the lamella center. The dashed line marks the border to the milled sector. b) SEM overview image of the trench's surroundings. The red arrow marks the x-axis in a). c)-h) SEM images of the surface regions marked in b) with higher magnification reveal the gold coverage. Gold can be seen with bright contrast on top of the silicon.

of the milled surface is at 23 µm. The coverage percentage is determined by SEM images recorded using electron energy of 5 kV and intensity threshold-based segmentation. Figures 4.42 c) - h) show the central sections of the images used for the determination. The left and right half of each image were evaluated independently. The recorded image positions are marked in the SEM overview image in figure 4.42 b) by black circles. Figure 4.42 c) shows the pristine gold layer possessing a porous cauliflower-like surface. Its coverage of the silicon surface is defined as 100 % since it represents a pristine gold layer coverage. The

image was recorded nearly 70 µm away from the lamella center. Approaching the milled area around the lamella, the gold coverage drops rapidly. On the lamella surface, no gold could be observed by SEM. It is either covered or sputtered away by redepositing atoms. The same region is investigated by EDX using an electron accelerating voltage of 5 kV. In figure 4.43 the $Au_{M_{\alpha\beta}}$ and Ga_{L_α} peak intensity at 2.123 keV and 1.098 keV are plotted along the red arrow in figure 4.42 e) in red and blue respectively. The $Au_{M_{\alpha\beta}}$ intensity

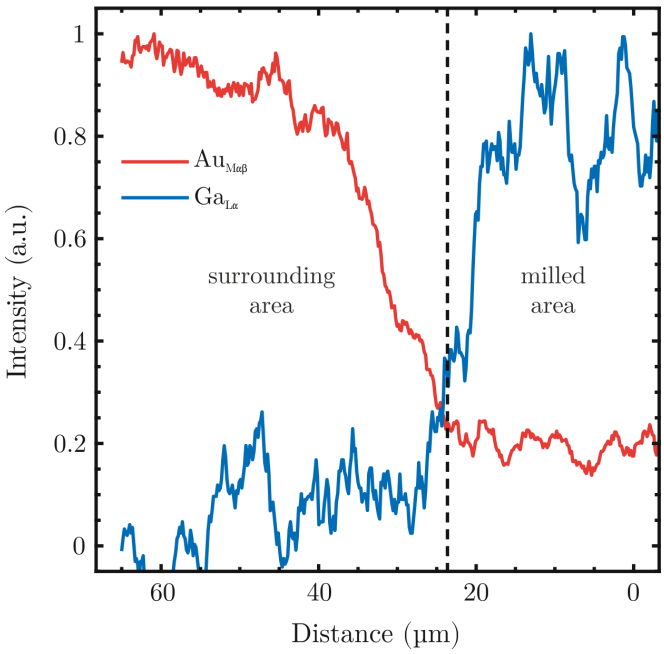

Figure 4.43: EDX intensity of $Au_{M_{\alpha\beta}}$ and Ga_{L_α} peaks along the red arrow in figure 4.42 e). The distance is relative to the lamella center.

supports the finding derived by SEM. A pristine gold layer remains at a distance of 60 µm from the lamella center. Closer to the milled area, the gold signal drops on one the hand, indicating that the gold layer got sputtered away. This suggests damage to the silicon surface as well. On the other hand, the Ga_{L_α} signal rises, indicating gallium implantation and redeposition. The gold intensity reaches a plateau at around 20 % of the pristine layer intensity on the lamella next to the milled area. This value is an overestimation of the actual gold signal. Electrons emitted due to the impinging of primary electrons can induce the emission of characteristic X-rays in the surrounding area, detected as X-rays emerging from the lamella surface. Accordingly, the regions with the lowest gold signal also show the highest Ga signal.

The investigations show that the surface layer is damaged up to a distance of around

40 µm from the milled area. To prepare a substrate in this way, with a 10 µm wide pristine gold surface at the center, would require a lamella at least 100 µm wide. However, these dimensions are impracticable for FIB since a cut of this size would imply a depth of around 100 µm, causing a more significant amount of redeposition, exacerbating the damage and redeposition coverage of the gold surface. Furthermore, it obstructs the milled gap reducing the milling rate, with increasing cut depth. In the end, the presented FIB-based surface preparation is not feasible. The amount of damage the surface suffers during milling is too high.

4.4.2 MultiPrep Preparation

Substrate preparation by FIB is shown to be an unsuitable technique due to its inherently damaging of the surface layer. A combination of mechanical and FIB preparation is feasible to overcome this issue. In a first step, a thin slice of silicon is prepared by mechanical grinding, conserving the pristine gold surface layer. This slice is cut by FIB and transferred to a MEMS chip in a second step.
In order to predetermine the orientation of growing nanowires, the substrate's orientation needs to be controlled during preparation. Growth proceeds in the [111] direction, which is orthogonal to the Au-sputtered silicon surface. In the experiment, this surface is therefore desired to be parallel to the electron beam for observation. In this case, growing wires stay in the focal plane of the imaging system. Accordingly, the resulting zone axis is restricted to be orthogonal to the [111] direction. The orientation is determined either by the wafer's flat or its cleaving edges. In figure 4.44 a) a (111) silicon wafer is sketched with a (110) flat. The cleaving edge orientations resulting from cleaving along (111) are marked by dashed lines. From a wafer fragment with known orientation, a cuboid 1.5 mm x 3 mm in size, as illustrated in figure 4.44 b), is cut using a diamond wire saw. The orientation of the 3 mm edge determines the resulting zone axis orientation and is chosen to be $[1\bar{1}0]$. The cuboid is polished on one of the $(1\bar{1}0)$ surfaces prepared with the diamond wire saw. It is glued onto a milling support on its sidewall with resin. The support is clamped in a MultiPrep milling device that uses rotating abrasive papers rinsed with ultrapure water to mill down the sample with micrometer precision. The polishing of the sidewall marked by the black arrow in figure 4.44 c) is done to flatten the surface and remove sidewall damage caused by the diamond wire saw. During milling, the Au-containing surface is oriented away from the direction of rotation to keep it free of abraded material. The grain size of the abrasive paper is reduced gradually from 15 µm to 1 µm according to the

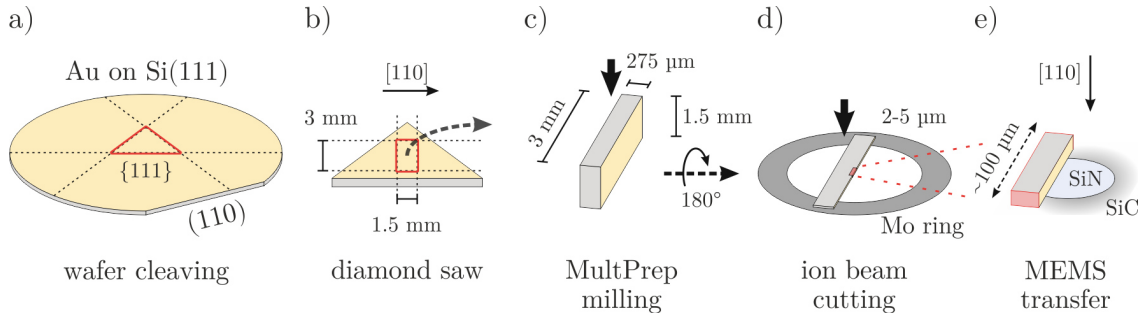

Figure 4.44: Steps of MultiPrep based preparation. a) A wafer piece is cleaved out of an HF etched and Au-sputtered wafer. b) A small silicon cuboid is cut with a diamond wire saw from the cleaved piece. c) The first sidewall cut is polished by the MultiPrep. d) The cuboid is mounted on a Mo ring with the polished side. The opposite sidewall is milled down to prepare a thin slice. e) A lamella is cut from the s slice using FIB and transferred onto a MEMS chip. FIB-induced damages are restricted to the Au-averted sidewalls marked in red.

first column of table 4.9. In each step, at least three times the thickness of the previous abrasive paper grain size needs to be milled in order to remove the surface damage caused during the last step. The second column of the table shows the thickness reduction in each polishing step. In total, the thickness of the cuboid is reduced by approximately 180 µm. Next, the sample is detached from the milling support and cleaned with acetone, isopropanol and ethanol. Subsequently, the cuboid is rotated by 180° and mounted with the polished side onto a 3 mm diameter molybdenum ring, acting as support, using an epoxy resin. The ring is then again mounted onto the milling support. To end up with a thickness below 5 µm, the opposite sidewall is thinned down to the thicknesses listed in the last column of table 4.9 with the respective grain sizes. This step is illustrated in figure 4.44 d). The sample is again detached and cleaned using acetone, isopropanol and ethanol. The result is a thin slice of silicon mounted on a ring support with length and width of approximately 3 mm and 0.3 mm, respectively. Next, this sample is transferred

Grain size	1. Polishing	2. Thinning
15 µm	−100 µm	≈ 80 µm
6 µm	−50 µm	≈ 35 µm
3 µm	−20 µm	≈ 15 µm
1 µm	−10 µm	< 5 µm

Table 4.9: Polishing and thinning steps by MultiPrep. The second column give a reduction in thickness of the cuboid, whereas the third column specify final thicknesses.

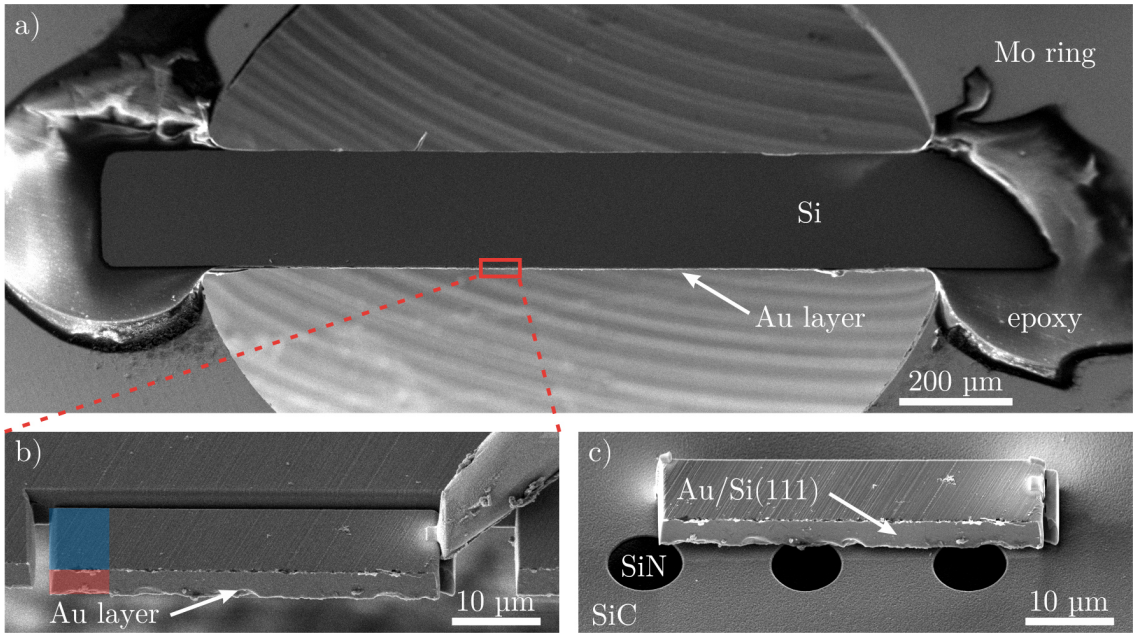

Figure 4.45: FIB transfer of Si lamella. a) SEM image showing the silicon slice mounted on the Mo ring. The Au-covered surface is located at the lower edge of the silicon. b) prepared silicon lamella after FIB cut. The manipulator needle is attached to the right to lift it and transfer it to a MEMS chip. The red rectangle in a) illustrates the imaged section of the silicon slice. The red and blue shaded areas are example regions for recording the EDX spectra of figure 4.46. c) transferred silicon lamella attached to the MEMS chip by tungsten depositions over the SiC heating membrane. The Au-covered surface faces towards the SiN windows.

to the SEM/FIB dual beam system, where a silicon lamella substrate is prepared and transferred to a MEMS chip as indicated in 4.44 e). An SEM image of a prepared silicon slice with a thickness of 5 µm can be seen in figure 4.45 a). The slice can be seen in the image center mounted on its side on the molybdenum ring by the epoxy resin. The lower side of the silicon consists of the Au-sputtered (111) surface indicated by the white arrow. From this slice, multiple silicon substrates can be prepared and transferred to a MEMS chip. To this end, smaller lamella each 50 µm to 100 µm x 15 µm to 20 µm in size are cut from the Au-sputtered edge by FIB. An enlarged SEM image of the Au-sputtered edge can be seen in figure 4.45 b). There, a prepared lamella is shown as it is lifted out. The lift-out is performed by attaching the lamella to a micromanipulator needle using a tungsten deposition. Ion beam-induced damage and gallium implantation are limited to the cut sidewalls, and gallium ions do not impinge the gold surface, which is averted from the ion beam. The milled trenches are much smaller than the ones needed in pure FIB

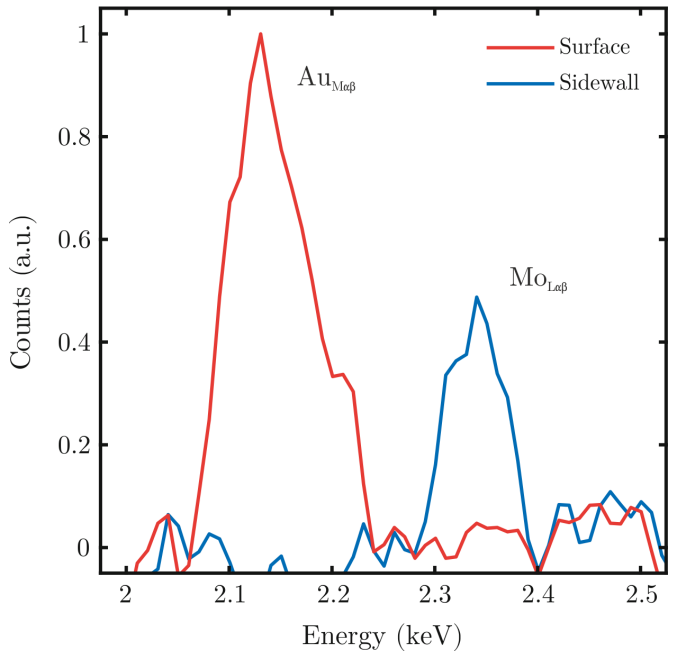

Figure 4.46: EDX spectra of silicon lamella acquired with 15 kV accelerating voltage. The spectrum recorded on the gold-covered substrate surface is plotted in red. The one recorded on the polished sidewall is plotted in blue. Peaks are caused by the gold M_α and M_β transition energies of 2.123 keV and 2.203 keV and molybdenum L_α and L_β transition energies of 2.293 keV and 2.404 keV respectively.

preparation, which tremendously reduces the amount of redeposition. Furthermore, the gold layer is shadowed and not exposed to the redepositing atoms. The lamella is finally attached to the MEMS chip surface by tungsten depositions. The gold surface is placed at the side of the SiN windows to enable observation of the substrate surface in the electron microscope. Figure 4.45 c) shows an SEM image of the lamella mounted on a MEMS chip. The dark circles are the SiN windows surrounded by the SiC heating membrane. To prove that the gold is preserved at the silicon (111) surface, the lamella was investigated by SEM EDX. X-ray spectra of the Au/Si(111) surface and the polished sidewall are shown in figure 4.46 in red and blue, respectively. Example areas for acquiring these spectra are highlighted by the red and blue shaded areas in figure 4.45 b). The plotted energy range contains the gold M_α and M_β transition energies at 2.123 keV and 2.203 keV respectively, as well as the molybdenum L_α transition energy at 2.293 keV and L_β transition energy at 2.404 keV. The spectrum originating from the gold surface (red) shows a peak at the gold transition energies, which in contrast, cannot be observed in the spectrum originating

from the sidewall (blue). Consequently, gold is still present on the silicon (111) surface. The EDX spectrum of the polished sidewall reveals a peak at the molybdenum transition energies, which is missing in the gold-containing surface spectrum. The molybdenum arises due to abrasion of the support ring during milling. The observation that it is not detected on the gold surface implies that abrasions do not contaminate it during the milling process. Characteristic X-rays assigned to gallium could not be detected in either spectrum.
The developed preparation method allows transferring a crystalline substrate passivated by gold with a defined orientation onto a MEMS chip. By this, the observation of epitaxial growth of nanowires in the TEM comes into the scope of experiments that can be performed. Furthermore, such experiments offer the advantage of a predefined zone axis orientation of the wires, which is required for atomic resolution imaging.

4.4.3 GaP Nanowire Growth on Si(111)

Nanowire growth via the VLS mechanism requires catalyst particles to initiate the process. Experiments presented in section 4.2 utilized drop-cast gold nanoparticles in an isopropanol suspension. The preparation of silicon substrates shown in section 4.4.2 does not end up in spherical particles but a granular gold film. Prior to the growth, the gold layer is expected to become liquefied by heating in contact with the precursor gases and to form droplets that change their size with time due to coalescence and Ostwald ripening. This behavior is mandatory to initiate VLS growth. To prove the formation of such droplets, the size distribution of the gold particles has been determined before and after heating. A silicon lamella sputtered with 3 nm of gold and placed on a SiC heating membrane of a MEMS chip was heated to 730 °C with a temperature rate of 5 °C min^{-1} in the TEM vacuum. Melting starts at a temperature of around 650 °C in the observed area, and gold droplets became mobile, moving on the silicon surface. The elevated temperature is due to the absence of precursor gases that would reduce the melting temperature of gold. Melting starts earlier in the area observed with the electron beam, which leads to the conclusion that the beam locally increases the temperature of the sample. From SEM images, the size distribution of the pristine and annealed gold layer is determined by intensity threshold-based segmentation. The particle area is calculated and converted to a size-equivalent particle diameter, which equals the diameter of a circle of the same area. Particle size determination of the annealed gold was performed utilizing a not observed area to eliminate the heating effect of the electron beam. Figure 4.47 depicts a histogram of the determined particle diameters. The red curve represents a kernel density estimation

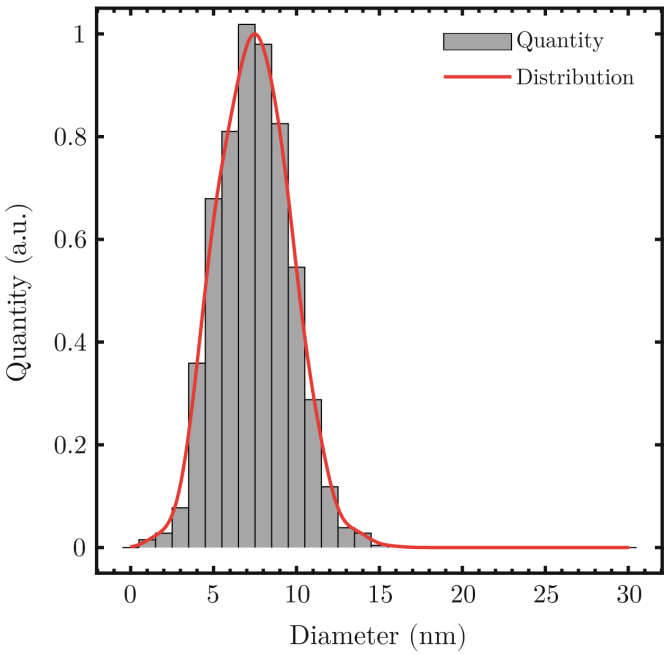

Figure 4.47: Histogram of area equivalent gold particle diameters of the pristine sample. The red curve represents a smoothed size distribution obtained via a Gaussian kernel density estimation. The distribution is Gaussian shaped with a mean of 7.5 nm and a standard deviation of 2.2 nm.

using a Gaussian kernel to smooth the distribution. All particles possess a diameter smaller than 16 nm. The histogram shows a Gaussian shape with a mean value of 7.4 nm and a standard deviation of 2.2 nm. Diameters down to 1.2 nm are observed, which is at the edge of the resolution limit of the SEM.

The size distribution after the heating experiment can be seen in figure 4.48. The red curve again shows the Gaussian kernel density estimation. For comparison, the previous distribution is plotted as well, and the distributions are normalized to each other. On the one hand, it shows that the highest accumulation of particle diameters is at a diameter of around 8 nm, which is comparable to the previous one of 7.4 nm. On the other hand, the distribution is asymmetrically shifted to higher diameters. Diameters up to 30 nm are observed and the mean value has increased to 11.8 nm. The mean values of the two distributions are marked by the dashed black lines in figure 4.48. All observed particles show diameters larger than 4 nm. Smaller particles down to diameters of 1.2 nm are consumed completely. Due to the formation of particles with a larger diameter at the cost of smaller ones, the surface coverage of gold is reduced. Only 53 % of the previous surface

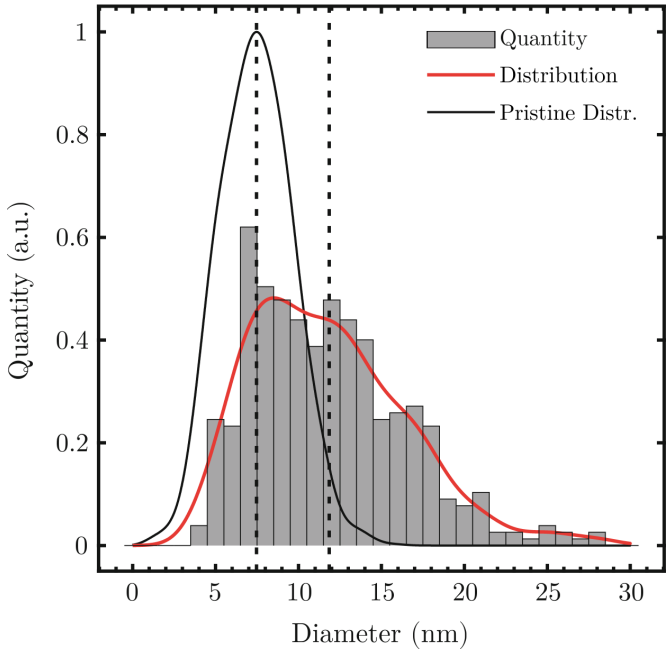

Figure 4.48: Histogram of area equivalent gold particle diameters of the heated sample. The red curve represents a smoothed size distribution obtained via a Gaussian kernel density estimation. The distribution of the pristine sample is plotted for comparison. The black lines mark the pristine and heated samples size distribution mean values of 7.5 nm and 11.8 nm, respectively.

coverage is left after the temperature treatment. These observations reveal the formation of larger gold particles capable of VLS growth initiation.

During a growth experiment, precursors need to be supplied to the gold-covered surface. Elevated temperatures cause the gold to form droplets in contact with the gaseous species. Nucleation occurs on the interface of the droplet and silicon (111) surface. The crystallographic orientation of the substrate can be adapted by the nucleation site, leading to epitaxial VLS growth of nanowires. An *in-situ* STEM experiment using precursor partial pressures of TBP and TMGa of (0.1066 ± 0.0033) Pa and (0.0108 ± 0.0010) Pa, respectively with a nitrogen carrier gas pressure of (210 ± 1) hPa was performed. The corresponding V/III ratio is (9.85 ± 0.99). A temperature of 450 °C was applied to the sample. The growth of GaP nanowires started after a nucleation time of (15 ± 1) min. During this time, droplets are formed on the silicon surface and saturated by the growth material until nucleation sites initiate the growth process. GaP nanowires growing from the silicon (111) surface can be seen in figure 4.49. The silicon substrate is visible at the top with the

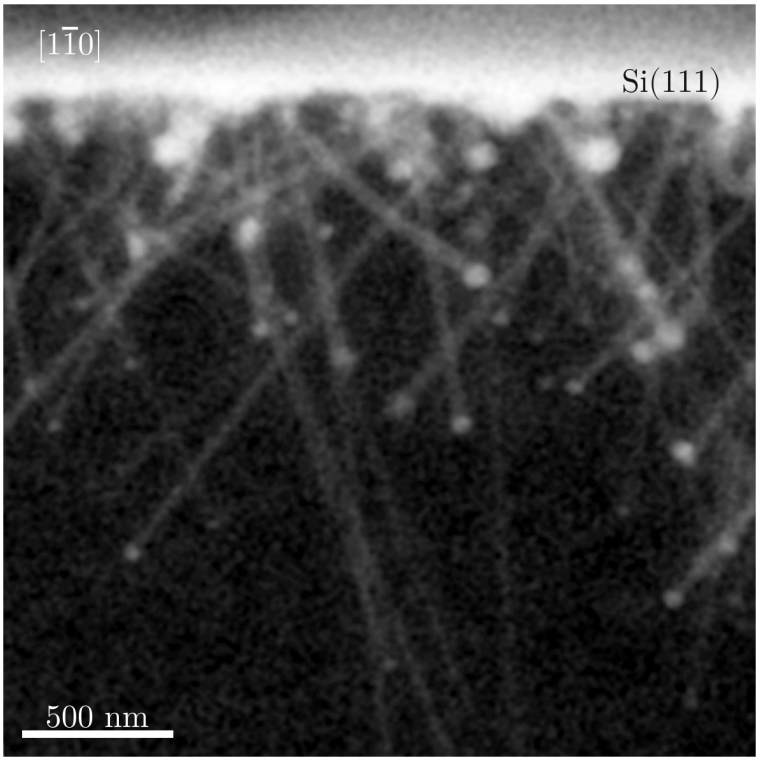

Figure 4.49: GaP nanowires growing by VLS mechanism on a Si(111) substrate view along $[1\bar{1}0]$. Growth conditions are a temperature of 450 °C, precursor partial pressures of TBP and TMGa of (0.1066 ± 0.0033) Pa and (0.0108 ± 0.0010) Pa respectively and a nitrogen carries gas pressure of (210 ± 1) hPa.

gold-covered (111) surface facing down. The silicon is oriented close to the $[1\bar{1}0]$ zone axis orientation. GaP nanowires can be seen growing out of the silicon. The dark background consists of SiN. Nanowires do not share a common focal height due to the lamella thickness of around 5 µm, which is larger than the focal depth of below 100 nm. Over the whole depth of the lamella, nanowires can nucleate, possessing different focal heights. Hence, most of them appear blurred and have reduced contrast. Growth rates follow the findings derived in section 4.2.2 with a normalized growth rate of $(0.40 \pm 0.15)\,\mathrm{nm\,s^{-1}}$. To investigate the crystallographic relationship between the nanowires and the substrate, their growth direction relative to the substrate was determined. Many nanowires can be observed growing parallel to each other, but multiple directions of growth exist. A set of wires is growing downwards, approximately perpendicular to the substrate, whereas others grow to the right or to the left, resulting in a hatch-like growth pattern. A polar histogram of the angles of growth directions in $[1\bar{1}0]$ projection to the surface normal is illustrated in

figure 4.50. A Gaussian kernel density estimation is plotted in red. The histogram reveals three major growth directions of $(-38.5 \pm 3.6)°$, $(7.7 \pm 3.7)°$ and $(58.6 \pm 4.0)°$, which are indicated by the gray shaded intervals. Values are derived from STEM images recorded approximately 7 min after nucleation. Growth directions derived from images recorded later pass over to a more homogeneous distribution. Video recordings of the growth reveal that this is caused by the wires tangling and bending due to the high wire density or by hitting the SiN surface. The presented data are already affected by this, which gives rise to the less dominant accumulations of growth directions close to the dominant ones. The highest abundance of growth directions is at $(7.7 \pm 3.7)°$, which is closest to the surface normal and is interpreted as [111] direction. This direction is the desired and expected one. Beside this, two other favored growth directions are observed. Nevertheless, all wires are expected to grow along a ⟨111⟩ direction. The additional directions can be explained by other {111} planes of the zinc blende structure. There are already reports of gold-catalyzed InAs and InP nanowires grown on Si(111) showing this morphology [247]. Deposited gold on silicon forms a eutectic at elevated temperatures that consumes some of the silicon and sinks into the surface, forming four {111} interfaces [247]. Nucleation

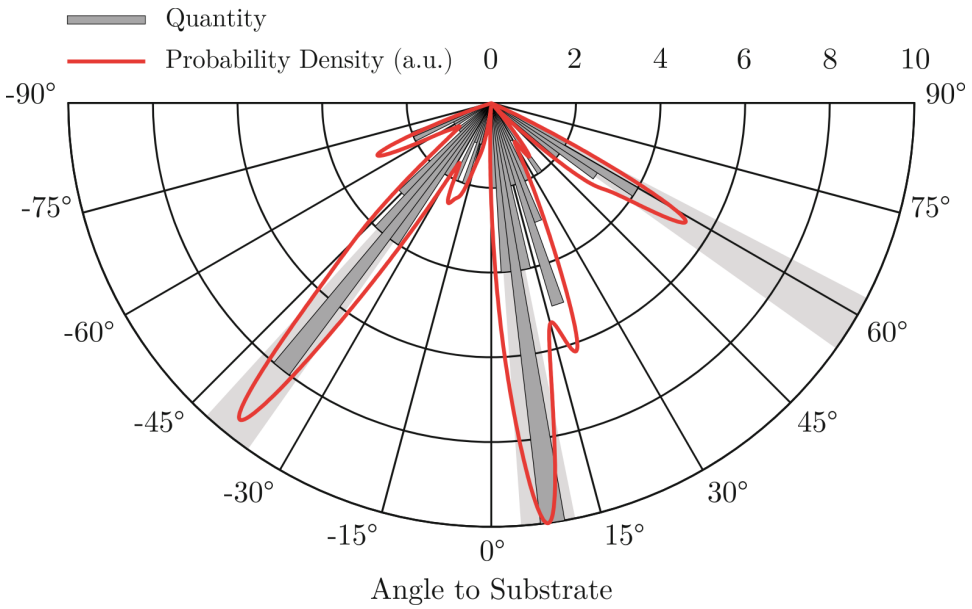

Figure 4.50: Polar histogram of GaP NW growth directions relative to the Si(111) surface normal. The red curve represents a Gaussian kernel density estimation. Three dominant directions can be seen in the distribution at $(7.7 \pm 3.7)°$, $(-38.5 \pm 3.6)°$ and $(58.6 \pm 4.0)°$, which are shaded in gray.

seeds can form on any of these planes. They are sketched in figure 4.51 a), forming an octahedron in [111] projection. The outer octahedron facets are seen under an angle and appear more narrow. The surface normal of either one of the four planes is pointing out of the (111) surface and is available as a possible growth direction. Growth is observed in $[1\bar{1}0]$ zone axis, which is indicated by the arrow in the figure. The corresponding projection of nanowires growing in the four directions is sketched in figure 4.51 b). It can be seen, that the $[\bar{1}11]$ and $[1\bar{1}1]$ directions, possessing a component opposite and along $[1\bar{1}0]$, are indistinguishable in this projection. Both, in theory, show a projected angle of 54.7° to the [111] direction. The remaining $[11\bar{1}]$ growth direction lies in the $(1\bar{1}0)$ projection plane and has an angle of 70.5° to the [111] direction. The three additional $\langle 111 \rangle$ directions are equivalent from a crystallographic point of view. Hence, they should appear with the same probability. 65 % of the observed wires, showing one of the dominant angles with respect to [111], belong to the −38.5° accumulation and 35 % to the accumulation at 58.6°, which is approximately a ratio of 2 to 1. This is explained by the two possibilities resulting in an angle to the left and only one direction resulting in an angle to the right. However, these projected growth directions have angles of $(46.2 \pm 5.2)°$ and $(50.9 \pm 5.4)°$ to the [111] direction, which does not match the expected angles of 54.7° and 70.5°. Reasons for this deviation include a slight substrate misorientation due to inadequate preparation. However, this cannot explain a deviation of this magnitude on its own. Further reasons might be an unexpected assembling of the nucleation site on the silicon substrate. To clarify this question, a TEM sample of a nanowire-substrate interface could be prepared to investigate the crystal orientation and atomic ordering. Furthermore, a slight distortion

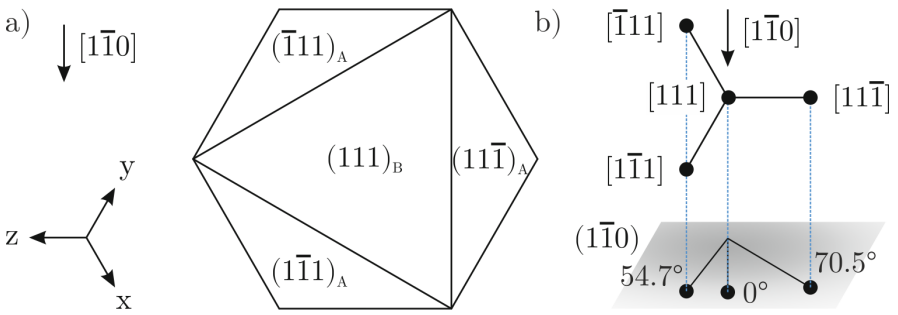

Figure 4.51: a) {111} planes of an octahedron in [111] projection. The central plane has different termination (B) than the neighboring ones. $[1\bar{1}0]$ direction of the STEM image in figure 4.49 is from top to bottom. b) Sketch of the four {111} surface normals in [111] projection. The lines on the gray surface illustrate the direction of surface normals in $[1\bar{1}0]$ projection.

of the STEM image caused by the scan generator could cause these deviations. Image post-processing was applied to compensate for this effect, but the possibility of remaining image distortion cannot be dismissed. Therefore, the exact angular values are arguable and must be treated cautiously. The fraction of 49 % and 51 % of wires growing in [111] or in another ⟨111⟩ direction, respectively is close to 1 to 1. This finding suggests that the growth proceeding perpendicular or skewed to the substrate is connected to the termination of the nucleation site. The silicon substrate has a diamond structure that does not possess different terminations on the {111} planes, as in contrast to the zinc blende structure of GaP does. With the assumption that the sum of interface energies of both termination configurations is the same, it cannot determine the termination of the nucleus at the liquid-solid interface during nucleation. The configuration would be arbitrarily chosen as A or B in this case. As sketched in figure 4.51 a), the central (111) plane differs from the neighboring ones in termination. GaP nanowires tend to grow on B terminated surfaces [237]. If the nucleation takes place so that a $(111)_B$ plane is formed, the wire tends to grow perpendicular to the substrate. In a $(111)_A$ nucleation, the wire tends to grow along a slanted direction with a B termination. These considerations are capable of explaining the ratio of 3 to 2 to 1 in the dominant projected growth directions of 7.7°, −38.5° and 58.6° respectively.

To prove this interpretation, a way to prepare a TEM sample of the interface of GaP nanowire and silicon substrate needs to be developed. By this, the termination of nanowires could be determined, as well as the crystal structure around the interface. This could investigate the epitaxial relationship and show whether the substrate's orientation is adopted in all dominant growth directions. If the nanowire tends to a different orientation, this might be an alternative explanation for different growth directions, as well as the deviation of observed projected angles to the expected ones.

However, the observation that distinct growth directions are preferred when using a silicon substrate implies that an epitaxial relationship to the nanowires exists and that their growth direction and orientation can be controlled. By this, the main hurdle towards atomic resolution imaging of the VLS growth process in a closed gas cell holder has been overcome.

CHAPTER 5

Summary

The presented work introduces *in-situ* (S)TEM using a closed gas cell and heating TEM holder as a new experimental approach to investigate crystal growth on an atomic scale under MOVPE-comparable conditions. This bridges the gap from *in-situ* investigations performed in ETEMs comparable to MBE towards the industrially relevant MOVPE processes. The setup enables the safe handling of toxic and pyrophoric gases, such as metal organic precursors utilized in the growth of semiconductor materials. A proof of concept is given by thermal decomposition studies of the precursor molecules TBP and TMGa, and a comparison of these findings to those obtained in industrial reactor designs. Moreover, live observations of the growth of GaP nanowires in zinc blende structure by gold-catalyzed VLS growth using TBP and TMGa were performed, demonstrating the versatile capabilities of the technique and setup. Thereby, its dynamic was investigated, revealing unique insights into the growth process.

Thermal precursor decomposition was investigated by mass spectrometry utilizing an inline quadrupole mass spectrometer. Even though this setup is not optimal for this exact purpose due to temporal delay and spatial separation that impede data interpretation, the reaction pathways could still be revealed through methodical data analysis. Unimolecular decomposition of TBP in a nitrogen environment was found to proceed by intramolecular coupling and homolytic fission in the lower temperature regime from 650 °C to 750 °C forming isobutane and a phosphine radical, as well as isobutene and a phosphine molecule, respectively. In the higher regime starting from around 800 °C, the predominant reaction pathway was found to be β-hydrogen elimination resulting in isobutene and phosphine molecules. The observed TBP decomposition temperature of (641 ± 20) °C on the MEMS

chip indicates that gas phase temperature shows a similar dependency on the membrane temperature as it does on the susceptor temperature in an MOVPE reactor. The unimolecular decomposition of TMGa in argon revealed the homolytic fission of methyl groups as its reaction pathway. Some of these form ethane in a further gas phase reaction. The decomposition temperature is determined to be in the range of 500 °C to 550 °C. The methyl gallium and dimethyl gallium counterparts of the homolytic fission reaction were not observed in the mass spectra, even though their formation is suggested.
The bimolecular decomposition was investigated with a mixture of TBP and TMGa with nitrogen as carrier gas. Reaction products that would hint at pre-reactions between the two precursors were not observed. It was found that by combining them, the respective decomposition temperatures for TBP and TMGa are reduced by approximately 150 °C to (475 ± 25) °C and (391 ± 35) °C. Furthermore, TMGa decomposition yield is enhanced by the addition of TBP, while TMGa diminishes TBP decomposition. Results suggest an alkyl exchange reaction between TBP and TMGa that results in the formation of methyl phosphine and tertiary butyl dimethyl gallium. These conclusions are compatible with results obtained in conventional reactor designs. Due to experimental limitations, such as the availability of different carrier gases or the absence of a large reactive surface, some observations from the literature could not be replicated in this setup. But overall, the setup has been shown to be an appropriate model for an MOVPE reactor on a micrometer scale.

In-situ STEM observations of gold-catalyzed VLS growth of GaP nanowires were performed under MOVPE-comparable conditions. Precursor partial pressures of TBP and TMGa were varied in the range of 10^{-2} Pa to 10^{1} Pa and total pressures between 200 hPa and 400 hPa with nitrogen as carrier gas at a temperature of 450 °C. In order to handle vast amounts of image data gathered during the STEM video recordings in a reasonable time, an automated MATLAB-based data evaluation was created. Important geometric properties of the nanowires, such as diameter, areas of the phase boundaries, as well as growth rate are determined and synchronized with the experimental parameters, such as growth and imaging conditions.
It was shown that the utilized growth conditions lead to diameter-independent growth kinetics. The precursor partial pressure and the ratio of the vapor-liquid and liquid-solid interfaces solely determined growth rates. The growth is limited by the group V species for V/III ratios up to (6.2 ± 0.9). At this point, a transition to the group III limited regime occurs that aligns with the growth kinetics observed in MOVPE. The confirma-

tion of this transition at V/III ratios also observed in MOVPE represents an essential difference to other *in-situ* studies performed in ETEMs under high vacuum conditions more comparable to MBE and highlights the importance of a setup capable of operating at MOVPE conditions. Furthermore, it was shown that the V/III ratio can control the droplet geometry. Moreover, the rate-limiting step of VLS growth is identified as the incorporation of growth material from the vapor into the liquid phase under the conditions mentioned above. Surface diffusion effects play a negligible role if any. The dependence of the growth rate on the surface ratio has not been reported in the literature so far. Revealing this dependency was enabled through live monitoring of the growth process and the availability of many different wire geometries simultaneously under the same conditions. In dealing with nanowire growth rates, the introduced normalized growth rate as a fraction of growth velocity and surface ratio should be considered in the diffusion-limited regime. In addition, nanowire kink formation could be observed as it was happening. This revealed that kinking conserves the ⟨111⟩ growth direction and proceeds via transition growth surfaces possessing higher surface energies. First, a truncation of the initial growth plane appears until the truncating surface matches the new growth direction. Subsequently, the initial growth plane tilts towards the new growth surface via intermediate surfaces. These energetically unfavorable surfaces lower the difference in the chemical potential of the liquid and solid phases, which results in a reduction of growth rate during the kink formation.

In agreement with the *in-situ* observations, post-growth investigations confirmed that most angles of nanowire kinks correspond to changes between ⟨111⟩ growth directions. Furthermore, the formation of kinks could be related to twin formation by SPED measurements. SPED is capable of crystal phase and orientation determination without the necessity of proper zone axis orientation. It is found that nanowires prefer to create 70.5° kinks that maintain the growth plane termination under the formation of a twin boundary. On the other hand, if a 109.5° kink is formed, the termination is inverted, and the wire tends to revert to the original termination again by forming a further inverting kink. With the obtained knowledge about the formation of twin boundaries within the kinks, additional occurring angles could be related to transitions of ⟨111⟩ growth directions accompanied by the formation of twins of higher order and confirmed by SPED. By this, the significant abundance of 123.7° kinks could be linked to second-order twin formation caused by consecutive termination changes.

To further improve the *in-situ* VLS growth observation, a substrate preparation method was developed that facilitates epitaxial growth in zone axis imaging conditions. The method is based on mechanical abrading the substrate, conserving the nanometer-thin gold layer deposited on its crystalline surface, and FIB transfer onto a MEMS chip. Additionally, the gold layer passivates the silicon surface preventing the native oxide formation.
GaP nanowires grown by the VLS mechanism on a silicon (111) substrate prepared in this manner exhibit three discrete growth directions in [110] projection. These are believed to result from the available equivalent $\langle 111 \rangle$ directions of the silicon substrate. The nucleation layer of the GaP nanowires seems to have an arbitrary termination on the nonpolar silicon. Subsequently, growth will proceed on one of the preferred phosphorus terminated $\{111\}_B$ surfaces, which is non-orthogonal to the substrate in 50 % of cases corresponding to the nucleus termination. While a microscopic investigation of the nucleation on the GaP/Si interface is still required for definitive proof, the discrete growth directions are a strong indication of an epitaxial relationship between the nanowires and the silicon substrate.
With the advantages of this technique, investigations with a predetermined zone axis orientation of growing nanowires become possible, opening the door to live imaging of crystal growth at atomic resolution. While the experimental proof is still pending, the advantages of this technique promise deeper insights into growth kinetics by examining, for example, the nucleation of crystalline layers or the formation of crystal defects.

Thereby lays the foundation for crystal growth observations under MOVPE-comparable conditions in a TEM. Besides successfully demonstrating functionality and delivering new insights into the VLS growth process, this method promises a wide variety of possible avenues of investigation.
The results of this study suggest some possible directions for further investigations. For instance, the effects of the electron beam on the thermal precursor decomposition should be investigated. To this end, the presented mass spectrometry experiments could be repeated under electron beam exposure. By this, the impact of various electron beam doses and dose rates could be quantified.
Additionally, *in-situ* observations of the VLS growth of GaP nanowires deliver plenty of promising experimental possibilities. An objective of interest could be to examine under which growth conditions the transition between different rate-limiting steps of VLS growth takes place and how to control the crystal phase of nanowires.
Beyond the scope of this thesis, the axial growth on the nanowire sidewall could be investigated, which occurs at higher temperatures. Insights gained from GaP nanowires

could be expanded to other III/V compounds and group IV materials by using different precursor sources. Doing so would provide the means for the investigation of axial as well as radial nanowire heterostructures.
Another future challenge to take on is to bridge the gap from nanowire growth towards layered growth in MOVPE. This is especially challenging with respect to enabling imaging with the TEM in sample geometries thin enough to allow for electron transparency. One approach could be to image the growing layers on the edge of a thin lamella. In another geometry, it might be possible to observe the growth process in plane view using a two-dimensional (2D) substrate. Here the amorphous SiN windows of the MEMS chips may prohibit the imaging of atomic layer formation. One possible solution could be to construct the windows of the closed gas cell by the used two-dimensional substrate. Candidates could be common 2D materials such as graphene or tungsten disulfide. On the whole, the groundwork on closed gas cell *in-situ* TEM laid in this work is expected to lead to many new insights into the VLS growth process, as well as deepen the understanding of the MOVPE process in general.

Zusammenfassung (Summary in German)

Der moderne Alltag und das gesellschaftliche Miteinander sind abhängig von Technologien, die auf Halbleitermaterialien basieren. Ein Leben ohne Smartphones, das Internet oder Computer ist heutzutage kaum noch vorstellbar. Auch wenn diese Errungenschaften der letzten Jahrzehnte eine technische Revolution bedeuteten, ist diese noch längst nicht abgeschlossen. Wissenschaft und Forschung sind weiterhin mit technischen sowie gesellschaftlichen Herausforderungen konfrontiert. Beispielsweise stellt der Klimawandel alle Gesellschaften gleichermaßen vor die gemeinsame Aufgabe, verantwortungsvoll und nachhaltig Energie zu produzieren, zu speichern und zu konsumieren, um die Emission von Treibhausgasen zu reduzieren. Halbleitertechnologien können dazu einen Beitrag zu leisten. Beispielsweise konnte bereits mit der Entwicklung von Lichtquellen durch Licht emittierende Dioden (LEDs) eine energiesparende Alternative für Beleuchtungen im privaten und öffentlichen Sektor geschaffen werden [1]. Auch in anderen Anwendungsbereichen wird bereits an effizienteren Alternativen geforscht. So etwa in der optischen Signalübertragung, die, getrieben durch das Internet und dessen stetig wachsenden Datenvolumen, zu einem der größten Energieverbraucher geworden ist [2], allerdings auf Lasern mit geringer Effizienz basiert. Effizientere Laser, die Wellenlängen von 1.3 µm mit geringer Dispersion oder 1.55 µm im Absorptionsminimum von Glasfaserkabeln emittieren, ohne dabei zusätzliche Energie für deren Kühlung zu verbrauchen, haben das Potential, den globalen Energieverbrauch drastisch zu senken [3–8]. Ein weiteres Anwendungsbeispiel sind Solarzellen. Obwohl diese bereits großflächig zum Einsatz kommen, bieten sie weiter Potential zur Verbesserung. Neben einem höheren Wirkungsgrad der Stromgewinnung, sollen Solarzellen zur Erzeugung von grünem Wasserstoff entwickelt werden [9]. So könnte Sonnenenergie zusätzlich in chemische Form umgewandelt und gespeichert werden. Wasserstoff als Energieträger bietet den Vorteil portabel zu sein und kann darüber hinaus direkt als Treibstoff für energieintensive Industrien wie die Stahlindustrie genutzt werden.
In dieser Arbeit wurde das Halbleitermaterialsystem GaP in Gestalt von Nanodrähten

untersucht. Solche Nanodrahtstrukturen sind vielversprechende Materialien für die zuvor genannten Entwicklungen. Es wurde bereits gezeigt, dass mit InP/InAs Nanodrahtheterostrukturen Laserdioden realisierbar sind, die bei Raumtemperatur Licht im Telekommunikationsband zwischen 1.2 µm und 1.6 µm emittieren [10]. Da Nanodrähte eine ausgeprägte Fähigkeit besitzen, Verspannungen im Material defektfrei zu relaxieren [11], können sie auf Substraten mit hoher Gitterfehlanpassung von bis zu 10 % hergestellt werden [12]. Damit bieten III/V Halbleiternanodrähte die Möglichkeit, auf Silizium integriert zu werden. Dies könnte in auf Silizium basierten Solarzellen zum Einsatz kommen [13]. GaP-Nanodrähte in der Wurtzitstruktur besitzen eine direkte Bandlücke von 2.1 eV, welche zur elektrochemischen Erzeugung von Wasserstoff aus Wasser geeignet ist [14–16].
Vorwiegend werden solche Halbleitermaterialien mittels metallorganischer Gasphasenepitaxie (MOVPE) hergestellt. Diese ist auf industriellen Maßstab skalierbar und ist in der Lage, vielfältige Materialien, unter anderem auch Nanodrahtstrukturen, zu produzieren [17]. Die Erforschung dieses Wachstumsprozesses, der häufig auch als "black box" bezeichnet wird, ist bis heute nicht abgeschlossen. Viele offene Fragen müssen noch beantwortet werden.
Diese Arbeit soll eine neue experimentelle Methode zur Untersuchung des MOVPE-Prozesses demonstrieren, mit dessen Hilfe das Verständnis dieser "black box" vertieft werden soll. Die Methode verbindet das Wachstum der Halbleitermaterialien und dessen Beobachtung auf atomarer Skala mittels *in-situ* Transmissionselektronenmikroskopie (TEM). Zu diesem Zweck wird ein geschlossener Gaszellenprobenhalter verwendet, der es ermöglicht, Gase mit bis zu Atmosphärendruck über eine Probe im Transmissionselektronenmikroskop (TEM) zu leiten und mittels einer Membran zu heizen. Der Aufbau ermöglicht durch einige Modifikationen den sicheren Einsatz von giftigen und entflammbaren Gasen, wie metallorganische Präkursoren [18]. Dadurch ist es möglich, den Halter als MOVPE-Reaktor im Miniaturmaßstab innerhalb eines TEMs zu verwenden. Die Echtzeitbeobachtung auf einer vergleichbaren Längenskala innerhalb eines konventionellen Reaktors ist bisher nicht realisierbar. Es stehen lediglich *in-situ* Analysemethoden wie beispielsweise Reflektionsanisotropiespektroskopie (RAS), die zur Untersuchung von Oberflächenstrukturen genutzt wird [19], optische Reflektometrie zur Bestimmung von Wachstumsraten [20–22] oder Massenspektrometrie, die Informationen über chemische und thermodynamische Prozesse liefert [23], zur Verfügung. In anderen *in-situ* TEM Aufbauten, die auf environmental TEM (ETEM) basieren [24], wurde bereits eindrucksvoll gezeigt, dass die Beobachtung von Kristallwachstum mit atomarer Auflösung möglich ist [25]. Allerdings haben sie den Nachteil, dass sie nur mit einem limitierten Gasdruck verwendet werden können [26–28]

und die erzielten Ergebnisse eher vergleichbar zur Molekularstrahlepitaxie (MBE) statt MOVPE sind [29]. Diese Lücke füllt die hier vorgestellte experimentelle Methode, die es ermöglicht, Bedingungen der MOVPE im TEM zu realisieren.
Allerdings muss der Beweis der Funktionsfähigkeit der Methode und des Aufbaus erbracht werden. Darüber hinaus stellt sich die Frage der Vergleichbarkeit der Resultate, die in einem Miniaturreaktor erzielt werden, mit denen in industriellen Reaktoren. Um dieser Frage nachzugehen, ist die thermische Zerlegung der metallorganischen Präkursoren, die einen essenziellen Schritt im MOVPE-Prozess darstellt, im *in-situ* Probenhalter untersucht und mit der in konventionellen Reaktoren verglichen worden. Außerdem wurde gezeigt, dass Nanodrähte mittels des "vapor-liquid-solid" (VLS) Wachstumsmechanismus, der auch in der MOVPE zum Einsatz kommt, hergestellt werden können. Die *in-situ* Beobachtung hat neue Erkenntnisse über die Grundlagen dieses Prozesses geliefert. Diese stehen im Zusammenhang mit der Struktur und Geometrie der wachsenden Nanodrähte, die nicht in nachträglichen Untersuchungen oder durch andre *in-situ* Methoden, sondern nur durch die Echtzeitbeobachtung, erhalten werden können. Gleichwohl sind auch mit nachträglichen Untersuchungen der gewachsenen Strukturen wertvolle komplementäre Ergebnisse zu erzielen. So wurden mittels hochauflösender TEM und Rasterpräzessionselektronenbeugung (SPED) wichtige strukturelle Ergebnisse, beispielsweise über Ebenendefekte, generiert, welche neue Schlüsse über den Wachstumsprozess ermöglicht haben.

Die thermische Zerlegung der metallorganischen Präkursormoleküle Trimethylgallium (TMGa) und Tertiärbutylphosphin (TBP) wurde mittels Quadrupolmassenspektrometrie untersucht. Obwohl die Interpretation der Daten durch experimentelle Nachteile, wie eine zeitliche Verzögerung und abreagierte Analytgase, die in der speziellen Versuchsanordnung in Kauf genommen werden müssen, erschwert wird, konnten die einzelnen Zerlegungsmechanismen identifiziert werden. Die unimolekulare Pyrolyse von TBP in Stickstoff findet bei Temperaturen zwischen 650 °C und 750 °C bevorzugt durch intramolekulare Kopplung und homolytische Spaltung statt, wodurch Isobutan und ein Phosphinradikal, beziehungsweise Isobuten und Phosphinmolekül entstehen. Bei höheren Temperaturen ab circa 800 °C findet die Zerlegung vorwiegend durch β-Wasserstoffeliminierung statt. Dabei entstehen die beiden Moleküle Isobuten und Phosphin. Die Pyrolyse von TBP beginnt ab einer Membrantemperatur von (641 ± 20) °C. Diese ist vergleichbar mit der Zerlegungstemperatur in MOVPE-Reaktoren, weshalb vermutet werden kann, dass sich die Gasphasentemperatur im Probenhalter zur Membrantemperatur verhält wie zur Suszeptortemperatur in der MOVPE. Die unimolekulare Zerlegung von TMGa wurde, wegen starker Über-

lagerung im Massenspektrum mit Stickstoff, in einem Argonträgergas untersucht. Die Zerlegungstemperatur wurde zwischen 500 °C und 550 °C eingegrenzt. Als Mechanismus der Zerlegung konnte dabei die homolytische Abspaltung von Methylgruppen identifiziert werden. Diese reagieren zum Teil miteinander zu Ethan in einer Gasphasenreaktion. Die schweren überbleibenden Molekülfragmente Dimethylgallium und Methylgallium konnten im Massenspektrometer nicht beobachtet werden.
Weiterhin wurde die bimolekulare Zerlegung von TBP und TMGa in Stickstoff beobachtet. Reaktionsprodukte, die auf eine Vorreaktion der beiden Präkursoren deuten würden, konnten nicht gefunden werden. Allerdings wurden geringe Zerlegungstemperaturen der beiden Moleküle beobachtet. Sie reduzieren sich jeweils um etwa 150 °C auf (475 ± 25) °C im Fall von TBP und auf (391 ± 35) °C für TMGa. Darüber hinaus wurde die Pyrolyse von TMGa durch die Anwesenheit von TBP begünstigt. Umgekehrt hemmt TMGa allerdings die Zerlegung von TBP. Zerlegungsprodukte lassen auf einen Alkylaustausch zwischen TBP und TMGa schließen, wodurch Methylphosphin und Tertiärbutyldimethylgallium entstehen. Diese Ergebnisse sind weitgehend kompatibel mit gewonnenen Erkenntnissen aus Zerlegungsuntersuchungen in MOVPE-Reaktoren. Es kann geschlussfolgert werden, dass für den MOVPE-Prozess aussagekräftige Resultate im geschlossenen Gaszellen *in-situ* Probenhalter gewonnen werden können, da dieser als Miniaturreaktor innerhalb eines TEMs agiert.

In-situ STEM-Untersuchungen des mit Gold katalysierten VLS-Wachstums von GaP-Nanodrähten wurden unter MOVPE vergleichbaren Bedingungen durchgeführt. Präkursorpartialdrucke von TBP und TMGa zwischen 10^{-2} Pa und 10^{1} Pa wurden bei einem Gesamtdruck zwischen 200 hPa und 400 hPa mit einem Stickstoffträgergas realisiert. Das Kristallwachstum wurde bei einer Temperatur von 450 °C beobachtet. Um die Menge an einzelnen Bildern der aufgenommenen Videos des Wachstumsprozesses in angemessener Zeit auswerten zu können, wurde eine automatisierte auf MATLAB basierte Datenauswertung geschaffen. So können relevante Größen, wie Nanodrahtdurchmesser, Goldtropfengröße und Wachstumsgeschwindigkeit bestimmt und mit experimentellen Parametern, wie Wachstumsbedingungen und Abbildungsbedingungen des Mikroskops, synchronisiert werden.
Es wurde gezeigt, dass die verwendeten Wachstumsbedingungen zu einer vom Radius der Nanodrähte unabhängigen Wachstumsrate führen, welche jedoch durch die Präkursorpartialdrücke und das Flächenverhaltnis der Grenzflächen zwischen Gas- und Flüssigphase, sowie Flüssigkeit und Feststoff bestimmt ist. Das Wachstum ist bis zu einem V/III-Verhältnis von (6.2 ± 0.9) durch das Gruppe V Material TBP limitiert. Bei diesem Wert

findet ein Übergang vom Gruppe V zum Gruppe III limitierten Wachstumsregime statt und die Wachstumsrate skaliert mit dem TMGa Partialdruck. Außerdem zeigte sich, dass das V/III Verhältnis die Geometrie des Goldtropfens bestimmt. Ist Gallium das limitierende Material ist, kann sich kein Reservoir im Tropfen aufbauen, wodurch dessen Volumen reduziert ist und zu geringeren Kontaktwinkeln führt. Aus Wachstumsexperimenten der MOVPE war zu erwarten, dass der Übergang zwischen den Limitierungen vor einem III/V-Verhältnis von 10 stattfindet. Dessen experimentelle Bestätigung im *in-situ* Probehalter demonstriert seine Vergleichbarkeit zur MOVPE, die für andere *in-situ* Aufbauten bisher nicht gegeben war. In ETEM Experimenten unter Vakuumbedingungen findet dieser Übergang erst bei sehr viel größeren V/III-Verhältnissen statt. Darüber hinaus zeigen die Ergebnisse, dass der wachstumslimitierende Schritt des VLS-Mechanismus der Einbau des Wachstumsmaterials aus der Gas- in die Flüssigphase darstellt. Oberflächendiffusion spielte bei den oben genannten Wachstumsbedingungen, wenn überhaupt, eine vernachlässigbare Rolle. Die Abhängigkeit der Wachstumsrate von dem Grenzflächenverhältnis wurde zuvor noch nicht entdeckt. Ohne die Möglichkeit der Echtzeitbeobachtung hätte dieses Resultat nicht gewonnen werden können. Um Wachstumsraten bei gegebenen Bedingungen miteinander zu vergleichen, wurde die normalisierte Wachstumsrate, die dieses Flächenverhältnis berücksichtigt, eingeführt.
Zusätzlich konnte die Entstehung eines Knicks während des VLS-Wachstums beobachtet werden. Das Knicken der Nanodrähte erhält die ⟨111⟩-Wachstumsrichtung und geschieht über die Bildung von energetisch ungünstigen Zwischenebenen, die die eigentliche Wachstumsfront verkürzen. Diese reduzieren die Differenz der chemischen Potentiale der Flüssigkeit und des Kristalls und verlangsamen dadurch das Kristallwachstum. Sobald der Übergang zwischen den Wachstumsebenen vollzogen ist, stellt sich wieder die vorherige Wachstumsrate ein.

Durch strukturelle Analyse der gewachsenen GaP-Nanodrähte konnte gezeigt werden, dass das Knicken mit der Bildung von Zwillingsebenen im Zusammenhang steht. Mittels SPED kann die Kristallstruktur und ihre Orientierung bestimmt werden, ohne die Probe dafür in eine geeignete Zonenachsenorientierung zu bringen. Die entstehenden Winkel der Knicke ergeben sich dabei aus den entsprechenden ⟨111⟩-Wachstumsrichtungen, wie es auch während des Wachstums beobachtet wurde. Dadurch entstehen bevorzugt 70.5°-Winkel, welche die Terminierung der polaren (111)-Ebene erhalten. Ein 109.5°-Winkel invertiert dahingegen die Terminierung. Wird ein solcher Winkel gebildet strebt, der Kristall eine erneute Invertierung unter Änderung der Wachstumsrichtung an, um die

bevorzugte Polarität wieder herzustellen. Dies resultiert unter anderem in 123.7°-Winkeln, durch die Bildung von Zwillingsdomänen zweiter Ordnung.

Zur Optimierung der *in-situ* TEM-Beobachtung des VLS-Wachstums wurde eine Methode zur Substratpräparation entwickelt. Die Präparation basiert auf mechanischem Schleifen, das eine einige Nanometer dicke Goldschicht, die auf der gewünschten Oberfläche eines Siliziumwafers deponiert wird, erhält, und dem Transfer mittels Fokussiertem Ionenstrahl (FIB) auf den Probenhalter. Darüber hinaus passiviert das Gold die Siliziumoberfläche und verhindert die Entstehung einer nativen Oxidschicht. Dieses Substrat bietet die Möglichkeit, die Kristallorientierung und damit die Wachstumsrichtung der Nanodrähte vorzubestimmen. Experimentell gehen damit zwei bedeutende Vorteile einher. Erstens können die wachsenden Nanodrähte in einer geeigneten Zonenachse untersucht werden, wodurch die Abbildung des Kristallgitters mit atomarer Auflösung ermöglicht wird. Zweitens kann die Wachstumsrichtung parallel zur Bildebene definiert werden und die Drähte bewegen sich nicht während des Wachstums aus der Fokusebene des Mikroskops.
Das VLS-Wachstum von GaP-Nanodrähten auf einem so präparierten (111)-Siliziumsubstrat zeigt in [110]-Projektion drei diskrete Wachstumsrichtungen, welche den verfügbaren $\langle 111 \rangle$-Richtungen, die aus der (111)-Oberfläche zeigen, zugeordnet werden. Die Nukleationsschicht des GaP-Kristalls besitzt eine zufällige Terminierung, da das unpolare Siliziumsubtrat diese nicht vorgeben kann. Das Wachstum findet anschließend auf der bevorzugten mit Phosphor terminierten $\{111\}_B$-Oberfläche statt. Dieses ist, entsprechend der Nukleation, nur in 50 % der Fälle orthogonal zum Substrat. Daneben ergeben sich gleichermaßen die anderen Wachstumsrichtungen. Die diskreten Wachstumsrichtungen deuten auf eine epitaktische Beziehung der Nanodrähte zum Substrat hin. Für den experimentellen Beweis benötigt es eine Präparationsmethode, die es erlaubt, die Grenzfläche zwischen Silizium und GaP zu analysieren.
Die Präparation eines Substrates innerhalb des Gaszellenhalters schafft die Möglichkeit zur Beobachtung des Kristallwachstums mit atomarer Auflösung. Dies verspricht einen tieferen Einblick in dessen dynamische Prozesse, wie beispielsweise die Bildung von Nukleationslagen oder Kristalldefekten. Die experimentelle Umsetzung ist in dieser Arbeit zwar noch nicht gelungen, ist aber in nachfolgenden Experimenten zu erwarten.

Diese Arbeit hat die Grundlage für die Beobachtung des Kristallwachstums in einem TEM unter zur MOVPE vergleichbaren Bedingungen gelegt. Neben der erfolgreichen Demonstration der Funktionsfähigkeit des Aufbaus und der experimentellen Methode konnten

neue Einblicke in das VLS Wachstum von Nanodrähten gewonnen werden. Außerdem ist damit die Möglichkeit für eine Vielzahl von weiteren Untersuchungen gegeben. Damit verbunden stellen sich aber auch weitere Herausforderungen.
Die präsentierten Ergebnisse legen einige weitere Untersuchengen nahe. Beispielsweise kann der Einfluss des Elektronenstrahls im TEM auf die Präkursormoleküle untersucht werden. Zu diesem Zweck können die hier durchgeführten Experimente unter Einfluss des Elektronenstrahls reproduziert und verglichen werden.
Die *in-situ* Beobachtung des VLS-Wachstums bietet viele weitere experimentelle Möglichkeiten. Es könnte systematisch untersucht werden, unter welchen Bedingungen der Übergang zwischen den wachstumslimitierenden Schritten des VLS-Wachstums stattfindet, oder wie die Kristallstruktur der Nanodrähte kontrolliert werden kann.
Die gewonnenen Erkenntnisse könnten weiterhin auf neue Materialsysteme angewandt werden, indem andere Präkursormoleküle zum Wachstum weiterer III/V oder Gruppe IV Materialien, sowie Heterostrukturen verwendet werden. Axiales Wachstum, welches bei höheren Temperaturen stattfindet, bietet die Möglichkeit zur Synthese von Core-Shell Nanodrähten. Zukünftige Unteruchungen versprechen daher neue Einblicke in den VLS Mechanismus.
Eine verbeleibende Herausforderung ist der Übergang vom Wachstum eindimensionaler Strukturen wie Nanodrähten zum Wachstum zweidimensionaler (2D) Schichten, wie es beispielsweise auf Wafern in der MOVPE stattfindet. Die große Herausforderung besteht dabei in der Notwendigkeit einer elektronentransparenten Probe, was besondere Anforderungen an deren Geometrie stellt. Ein Ansatz wäre, auf der Kante einer kristallinen Lamelle das Schichtwachstum im Querschnitt zu beobachten. Eine weitere Möglichkeit könnte die Beobachtung in Aufsicht mittels eines 2D Substrates sein. Dabei könnten die amorphen SiN-Fenster des Probenhalters die Abbildung des Wachstumsprozesses verhindern. Eine Lösung könnte sich dadurch ergeben, die Sichtfenster in die Gaszelle aus dem 2D Substrat herzustellen. Mögliche Materialien dafür könnten Materialien wie Graphen oder Wolframdisulfid sein. Daher sind zukünftig weitere bedeutende Ergebnisse durch *in-situ* TEM mittels eines geschlossenen Gaszellenhalters zu erwarten, welche das Verständnis der "black box" MOVPE vertiefen.

Bibliography

[1] N. Khan and N. Abas. 'Comparative study of energy saving light sources.' *Renewable and Sustainable Energy Reviews* **15, 1**: 296 (2011)

[2] N. Jones. 'How to stop data centres from gobbling up the world's electricity.' *Nature* **561, 7722**: 163 (2018)

[3] G. P. Agrawal. *Fiber-optic communication systems*, Volume 222 of *Wiley series in microwave and optical engineering*. Wiley and IEEE Xplore, New York and Piscataqay, New Jersey, 4th Edition (2011)

[4] E. Murphy. 'Enabling optical communication.' *Nature Photonics* **4, 5**: 287 (2010)

[5] T. R. Chen et al.. 'Carrier leakage and temperature dependence of InGaAsP lasers.' *Applied Physics Letters* **43, 3**: 217 (1983)

[6] T. P. Pearsall et al.. 'Photoluminescence and impurity concentration in $Ga_xIn_{1-x}As_yP_{1-y}$ alloys lattice-matched to InP.' *Journal of Applied Physics* **54, 2**: 1037 (1983)

[7] S. Sweeney et al.. 'The effect of temperature dependent processes on the performance of 1.5-μm compressively strained InGaAs(P) MQW semiconductor diode lasers.' *IEEE Photonics Technology Letters* **10, 8**: 1076 (1998)

[8] T. Eales et al.. 'The Nature of Auger Recombination in Type-I Quantum Well Lasers Operating in the Near- and Mid-Infrared.' In '2018 IEEE International Semiconductor Laser Conference (ISLC),' 1–2. IEEE (2018)

[9] M. G. Walter et al.. 'Solar water splitting cells.' *Chemical reviews* **110, 11**: 6446 (2010)

[10] G. Zhang et al.. 'Telecom-band lasing in single InP/InAs heterostructure nanowires at room temperature.' *Science Advances* **5, 2**: eaat8896 (2019)

[11] M. W. Larsson et al.. 'Strain mapping in free-standing heterostructured wurtzite InAs/InP nanowires.' *Nanotechnology* **18, 1**: 015504 (2007)

[12] T. Mårtensson et al.. 'Epitaxial Growth of Indium Arsenide Nanowires on Silicon Using Nucleation Templates Formed by Self-Assembled Organic Coatings.' *Advanced Materials* **19, 14**: 1801 (2007)

[13] M. T. Borgstrom et al.. 'Towards Nanowire Tandem Junction Solar Cells on Silicon.' *IEEE Journal of Photovoltaics* **8, 3**: 733 (2018)

[14] A. Standing et al.. 'Efficient water reduction with gallium phosphide nanowires.' *Nature communications* **6**: 7824 (2015)

[15] J. Sun et al.. 'Surfactant-free, large-scale, solution-liquid-solid growth of gallium phosphide nanowires and their use for visible-light-driven hydrogen production from water reduction.' *Journal of the American Chemical Society* **133, 48**: 19306 (2011)

[16] K. Tateno et al.. 'Wurtzite GaP nanowire grown by using tertiarybutylchloride and used to fabricate solar cell.' *Japanese Journal of Applied Physics* **58, 1**: 015004 (2019)

[17] G. B. Stringfellow. 'Development and current status of organometallic vapor phase epitaxy.' *Journal of Crystal Growth* **264, 4**: 620 (2004)

[18] R. Straubinger et al.. 'In Situ Thermal Annealing Transmission Electron Microscopy (TEM) Investigation of III/V Semiconductor Heterostructures Using a Setup for Safe Usage of Toxic and Pyrophoric Gases.' *Microscopy and Microanalysis* **23, 4**: 751 (2017)

[19] W. Richter and J.-T. Zettler. 'Real-time analysis of III–V-semiconductor epitaxial growth.' *Applied Surface Science* **100-101**: 465 (1996)

[20] K. P. Killeen and W. G. Breiland. 'In situ spectral reflectance monitoring of III-V epitaxy.' *Journal of Electronic Materials* **23, 2**: 179 (1994)

[21] W. G. Breiland and K. P. Killeen. 'A virtual interface method for extracting growth rates and high temperature optical constants from thin semiconductor films using insitu normal incidence reflectance.' *Journal of Applied Physics* **78, 11**: 6726 (1995)

[22] M. Heurlin et al.. 'In situ characterization of nanowire dimensions and growth dynamics by optical reflectance.' *Nano letters* **15, 5**: 3597 (2015)

[23] L. Nattermann et al.. 'An experimental approach for real time mass spectrometric CVD gas phase investigations.' *Scientific reports* **8, 1**: 319 (2018)

[24] J. B. Wagner et al.. 'Exploring the environmental transmission electron microscope.' *Micron* **43, 11**: 1169 (2012)

[25] J.-C. Harmand et al.. 'Atomic Step Flow on a Nanofacet.' *Physical review letters* **121, 16**: 166101 (2018)

[26] L. F. Allard et al.. 'Novel MEMS-based gas-cell/heating specimen holder provides advanced imaging capabilities for in situ reaction studies.' *Microscopy and Microanalysis* **18, 4**: 656 (2012)

[27] T. W. Hansen and J. B. Wagner. 'Environmental transmission electron microscopy in an aberration-corrected environment.' *Microscopy and microanalysis : the official journal of Microscopy Society of America, Microbeam Analysis Society, Microscopical Society of Canada* **18, 4**: 684 (2012)

[28] C. Hetherington et al.. 'In situ metal-organic chemical vapour deposition growth of III–V semiconductor nanowires in the Lund environmental transmission electron microscope.' *Semiconductor Science and Technology* **35, 3**: 034004 (2020)

[29] D. Jacobsson et al.. 'Interface dynamics and crystal phase switching in GaAs nanowires.' *Nature* **531, 7594**: 317 (2016)

[30] N. W. Ashcroft and D. N. Mermin. *Festkörperphysik*. Oldenbourg, München, 3rd Edition (2007)

[31] B. Souvignier. 'A general introduction to groups: Chapter 1.1.' In C. P. Brock et al. (Editors), 'International Tables for Crystallography,' 2–11. International Union of Crystallography, Chester, England (2016)

[32] T. Hahn et al.. 'Guide to the use of the space-group tables: Chapter 2.1.' In C. P. Brock et al. (Editors), 'International Tables for Crystallography,' 142–174. International Union of Crystallography, Chester, England (2016)

[33] C. P. Brock et al. (Editors). *International Tables for Crystallography: Space-group symmetry*, Volume A. International Union of Crystallography, Chester, England (2016)

[34] Y. A. Goldberg. 'Gallium Phosphide (GaP).' In M. Levinshtein et al. (Editors), 'Handbook Series on Semiconductor Parameters,' Volume 1, 104–124. World Scientific, London (1996)

[35] C. Y. Yeh et al.. 'Zinc-blende-wurtzite polytypism in semiconductors.' *Physical Review B* **46, 16**: 10086 (1992)

[36] N. V. Sibirev et al.. 'Surface energy and crystal structure of nanowhiskers of III–V semiconductor compounds.' *Physics of the Solid State* **52, 7**: 1531 (2010)

[37] V. G. Dubrovskii et al.. 'Growth kinetics and crystal structure of semiconductor nanowires.' *Physical Review B* **78, 23** (2008)

[38] V. G. Dubrovskii and N. V. Sibirev. 'Growth thermodynamics of nanowires and its application to polytypism of zinc blende III-V nanowires.' *Physical Review B* **77, 3** (2008)

[39] C. Kittel. *Einführung in die Festkörperphysik*. Oldenbourg, München, 14th Edition (2006)

[40] S. Hunklinger. *Festkörperphysik*. Oldenbourg, München, 5th Edition (2018)

[41] M. Perez. 'Gibbs-Thomson effects in phase transformations.' *Scripta Materialia* **52, 8**: 709 (2005)

[42] P. Caroff et al.. 'High-quality InAs/InSb nanowire heterostructures grown by metal-organic vapor-phase epitaxy.' *Small* **4, 7**: 878 (2008)

[43] P. Caroff et al.. 'InSb heterostructure nanowires: MOVPE growth under extreme lattice mismatch.' *Nanotechnology* **20, 49**: 495606 (2009)

[44] S. Assali et al.. 'Direct band gap wurtzite gallium phosphide nanowires.' *Nano letters* **13, 4**: 1559 (2013)

[45] S. Assali et al.. 'Optical study of the band structure of wurtzite GaP nanowires.' *Journal of Applied Physics* **120, 4**: 044304 (2016)

[46] C. Y. Yeh et al.. 'Relationships between the band gaps of the zinc-blende and wurtzite modifications of semiconductors.' *Physical Review B* **50, 4**: 2715 (1994)

[47] G. B. Stringfellow. *Organometallic vapor-phase epitaxy: Theory and practice*. Academic Press, San Diego, California, 2nd Edition (1999)

[48] O. Maßmeyer. 'Investigation of the Surface Reconstruction and Gas Phase Composition during Growth by MOVPE.' PhD thesis, Philipps-Universität Marburg (2021)

[49] G. B. Stringfellow. 'Fundamental Aspects of MOVPE.' In S. Irvine and P. Capper (Editors), 'Metalorganic Vapor Phase Epitaxy (MOVPE),' 19–69. Wiley (2019)

[50] P. Muller. 'Glossary of terms used in physical organic chemistry (IUPAC Recommendations 1994).' *Pure and Applied Chemistry* **66, 5**: 1077 (1994)

[51] A. Stegmüller and R. Tonner. 'β-Hydrogen elimination mechanism in the absence of low-lying acceptor orbitals in EH_2(t-C_4H_9)(E = N–Bi).' *Inorganic chemistry* **54, 13**: 6363 (2015)

[52] G. B. Stringfellow. 'Fundamental aspects of vapor growth and epitaxy.' *Journal of Crystal Growth* **115, 1-4**: 1 (1991)

[53] L. K. Nattermann. 'MOVPE Growth Studies on Dilute Bismide Containing III / Vs and Development of an MOVPE in-situ Gas Phase Analysis Setup.' PhD thesis, Philipps-Universität Marburg (2017)

[54] D. K. Russell. 'Gas-Phase Pyrolysis Mechanisms in Organometallic CVD.' *Chemical Vapor Deposition* **2, 6**: 223 (1996)

[55] Wetzel et al.. 'Absolute cross sections for electron-impact ionization of the rare-gas atoms by the fast-neutral-beam method.' *Physical Review. A* **35, 2**: 559 (1987)

[56] J. H. Gross. *Mass spectrometry: A textbook*. Springer International Publishing, Cham, Switzerland (2017)

[57] M. Born and R. Oppenheimer. 'Zur Quantentheorie der Molekeln.' *Annalen der Physik* **389, 20**: 457 (1927)

[58] J. Franck and E. G. Dymond. 'Elementary processes of photochemical reactions.' *Transactions of the Faraday Society* **21**: 536 (1926)

[59] E. Condon. 'A Theory of Intensity Distribution in Band Systems.' *Physical Review* **28, 6**: 1182 (1926)

[60] D. Rapp and P. Englander-Golden. 'Total Cross Sections for Ionization and Attachment in Gases by Electron Impact: I. Positive Ionization.' *The Journal of Chemical Physics* **43, 5**: 1464 (1965)

[61] S. J. King and S. D. Price. 'Electron ionization of H_2O.' *International Journal of Mass Spectrometry* **277, 1-3**: 84 (2008)

[62] S. J. King and S. D. Price. 'Electron ionization of CO_2.' *International Journal of Mass Spectrometry* **272, 2-3**: 154 (2008)

[63] P. Linstrom. 'NIST Chemistry WebBook: NIST Standard Reference Database 69.'

[64] M. M. Wolff and W. E. Stephens. 'A Pulsed Mass Spectrometer with Time Dispersion.' *Review of Scientific Instruments* **24, 8**: 616 (1953)

[65] H. Y. Chung et al.. 'Very sensitive real-time inline process mass spectrometer based on FFT Ion Trap technique.' In '2016 27th Annual SEMI Advanced Semiconductor Manufacturing Conference (ASMC),' 263–266. IEEE (2016)

[66] W. Paul and H. Steinwedel. 'Ein neues Massenspektrometer ohne Magnetfeld.' *Zeitschrift für Naturforschung A* **8, 7**: 448 (1953)

[67] R. Post and L. Heinrich. 'University of California Radiation Laboratory Report (S. Shewchuck), in UCRL 2209.' *Berkeley, CA* (1953)

[68] E. D. Courant et al.. 'The Strong-Focusing Synchroton - A New High Energy Accelerator.' *Physical Review* **88, 5**: 1190 (1952)

[69] J. P. Blewett. 'Radial Focusing in the Linear Accelerator.' *Physical Review* **88, 5**: 1197 (1952)

[70] J. E. Campana. 'Elementary theory of the quadrupole mass filter.' *International Journal of Mass Spectrometry and Ion Physics* **33, 2**: 101 (1980)

[71] P. H. Dawson. *Quadrupole mass spectrometry and its applications*. Elsevier, Amsterdam (1976)

[72] É. Mathieu. 'Mémoire sur le mouvement vibratoire d'une membrane de forme elliptique.' *Journal de Mathématiques Pures et Appliquées* **13, E**: 137 (1868)

[73] D. R. Herschbach. 'Tables of Mathieu Integrals for the Internal Rotation Problem.' *The Journal of Chemical Physics* **27, 4**: 975 (1957)

[74] N. W. McLachlan. *Theory and Application of Mathieu Functions*. Oxford Univerity Press, London (1947)

[75] M. Strutt. 'Mathieu'sche Differentialgleichung.' In 'Lamésche-Mathieusche-und Verwandte Funktionen in Physik und Technik,' 23–51. Springer, Berlin (1932)

[76] D. B. Williams and C. B. Carter. *Transmission electron microscopy: A textbook for materials science*. Springer, New York and London, 2nd Edition (2009)

[77] A. Rosenauer. *Transmission Electron Microscopy of Semiconductor Nanostructures: An Analysis of Composition and Strain State*. Springer, Berlin, Heidelberg (2003)

[78] P. A. Doyle and P. S. Turner. 'Relativistic Hartree-Fock X-ray and electron scattering factors.' *Acta Crystallographica Section A* **24, 3**: 390 (1968)

[79] A. Weickenmeier and H. Kohl. 'Computation of absorptive form factors for high-energy electron diffraction.' *Acta Crystallographica Section A* **47, 5**: 590 (1991)

[80] E. J. Kirkland. *Advanced Computing in Electron Microscopy*. Springer Nature Switzerland, Cham (2020)

[81] H. Alexander. *Physikalische Grundlagen der Elektronenmikroskopie*. Vieweg und Teubner Verlag, Wiesbaden (1997)

[82] P. P. Ewald. 'Introduction to the dynamical theory of X-ray diffraction.' *Acta Crystallographica Section A* **25, 1**: 103 (1969)

[83] A. Howie. 'Image contrast and localized signal selection techniques.' *Journal of Microscopy* **117, 1**: 11 (1979)

[84] E. Rutherford. 'LXXIX. The scattering of α and β particles by matter and the structure of the atom.' *Philosophical Magazine and Journal of Science* **21, 125**: 669 (1911)

[85] W. Demtröder. *Experimentalphysik 3: Atome, Moleküle und Festkörper*. Springer-Lehrbuch. Springer, Berlin, Heidelberg, 5th Edition (2016)

[86] A. Amali and P. Rez. 'Theory of Lattice Resolution in High-angle Annular Dark-field Images.' *Microscopy and microanalysis : the official journal of Microscopy Society of America, Microbeam Analysis Society, Microscopical Society of Canada* **3, 1**: 28 (1997)

[87] S. J. Pennycook et al.. 'Elemental mapping with elastically scattered electrons.' *Journal of Microscopy* **144, 3**: 229 (1986)

[88] W. T. Scott. 'The Theory of Small-Angle Multiple Scattering of Fast Charged Particles.' *Reviews of Modern Physics* **35, 2**: 231 (1963)

[89] J. C. Slater. 'Atomic Shielding Constants.' *Physical Review* **36, 1**: 57 (1930)

[90] E. Clementi and D. L. Raimondi. 'Atomic Screening Constants from SCF Functions.' *The Journal of Chemical Physics* **38, 11**: 2686 (1963)

[91] E. Clementi et al.. 'Atomic Screening Constants from SCF Functions. II. Atoms with 37 to 86 Electrons.' *The Journal of Chemical Physics* **47, 4**: 1300 (1967)

[92] H. M. Manasevit. 'Single-Crystal Gallium Arsenide on Insulating Substrates.' *Applied Physics Letters* **12, 4**: 156 (1968)

[93] E. Bauer. 'Phänomenologische Theorie der Kristallabscheidung an Oberflächen. I.' *Zeitschrift für Kristallographie - Crystalline Materials* **110, 1-6** (1958)

[94] F. C. Frank and J. H. van der Merwe. 'One-dimensional dislocations. I. Static theory.' *Proc. R. Soc. Lond. A* **198, 1053**: 205 (1949)

[95] F. C. Frank and J. H. van der Merwe. 'One-dimensional dislocations. II. Misfitting monolayers and oriented overgrowth.' *Proc. R. Soc. Lond. A* **198, 1053**: 216 (1949)

[96] F. C. Frank and J. H. van der Merwe. 'One-dimensional dislocations - III. Influence of the second harmonic term in the potential representation, on the properties of the model.' *Proc. R. Soc. Lond. A* **200, 1060**: 125 (1949)

[97] M. Volmer and A. Weber. 'Keimbildung in übersättigten Gebilden.' *Zeitschrift für Physikalische Chemie* **119, 1**: 277 (1926)

[98] U. W. Pohl. *Epitaxy of Semiconductors: Introduction to Physical Principles*. Springer, Berlin, Heidelberg (2013)

[99] I. N. Stranski and L. Krastanow. 'Zur Theorie der orientierten Ausscheidung von Ionenkristallen aufeinander.' *Monatshefte für Chemie* **71, 1**: 351 (1937)

[100] D. H. Reep and S. K. Ghandhi. 'Deposition of GaAs Epitaxial Layers by Organometallic CVD: Temperature and Orientation Dependence.' *Journal of The Electrochemical Society* **130, 3**: 675 (1983)

[101] S. Irvine and P. Capper (Editors). *Metalorganic Vapor Phase Epitaxy (MOVPE)*. Wiley, 1st Edition (2019)

[102] C. Plass et al.. 'A comparative study of $Ga(CH_3)_3$, $Ga(C_2H_5)_3$ and $Ga(C_4H_9)_3$ in the low pressure MOCVD of GaAs.' *Journal of Crystal Growth* **88, 4**: 455 (1988)

[103] P. W. Lee et al.. 'In situ mass spectroscopy and thermogravimetric studies of GaAs MOCVD gas phase and surface reactions.' *Journal of Crystal Growth* **85, 1-2**: 165 (1987)

[104] C. A. Larsen et al.. 'Decomposition mechanisms of trimethylgallium.' *Journal of Crystal Growth* **102, 1-2**: 103 (1990)

[105] C. A. Larsen and G. B. Stringfellow. 'Decomposition kinetics of OMVPE precursors.' *Journal of Crystal Growth* **75, 2**: 247 (1986)

[106] C. H. Chen et al.. 'MOVPE growth of InP using isobutylphosphine and tert-butylphosphine.' *Journal of Crystal Growth* **77, 1-3**: 11 (1986)

[107] W. Seifert et al.. 'Growth of one-dimensional nanostructures in MOVPE.' *Journal of Crystal Growth* **272, 1-4**: 211 (2004)

[108] R. S. Wagner and W. C. Ellis. 'Vapor–Liquid–Solid Mechanism of Single Crystal Growth.' *Applied Physics Letters* **4, 5**: 89 (1964)

[109] K. Hiruma et al.. 'Growth and optical properties of nanometer–scale GaAs and InAs whiskers.' *Journal of Applied Physics* **77, 2**: 447 (1995)

[110] N. Wang et al.. 'Growth of nanowires.' *Materials Science and Engineering: R: Reports* **60, 1-6**: 1 (2008)

[111] M. S. Gudiksen et al.. 'Growth of nanowire superlattice structures for nanoscale photonics and electronics.' *Nature* **415, 6872**: 617 (2002)

[112] H. J. Joyce et al.. 'High Purity GaAs Nanowires Free of Planar Defects: Growth and Characterization.' *Advanced Functional Materials* **18, 23**: 3794 (2008)

[113] N. Guan et al.. 'Nitride Nanowires for Light Emitting Diodes.' In J. Li and G. Q. Zhang (Editors), 'Light-Emitting Diodes,' Volume 4 of *Solid State Lighting Technology and Application Series*, 425–484. Springer International Publishing, Cham (2019)

[114] X. Zhu et al.. 'Enhancing Performance of a GaAs/AlGaAs/GaAs Nanowire Photodetector Based on the Two-Dimensional Electron-Hole Tube Structure.' *Nano letters* **20, 4**: 2654 (2020)

[115] F. M. Ross. 'Controlling nanowire structures through real time growth studies.' *Reports on Progress in Physics* **73, 11**: 114501 (2010)

[116] M. Law et al.. 'Semiconductor Nanowires and Nanotubes.' *Annual Review of Materials Research* **34, 1**: 83 (2004)

[117] V. G. Dubrovskii et al.. 'Gibbs-Thomson and diffusion-induced contributions to the growth rate of Si, InP, and GaAs nanowires.' *Physical Review B* **79, 20** (2009)

[118] V. Schmidt et al.. 'Growth, thermodynamics, and electrical properties of silicon nanowires.' *Chemical reviews* **110, 1**: 361 (2010)

[119] G. A. Bootsma and H. J. Gassen. 'A quantitative study on the growth of silicon whiskers from silane and germanium whiskers from germane.' *Journal of Crystal Growth* **10, 3**: 223 (1971)

[120] X. Duan and C. M. Lieber. 'General Synthesis of Compound Semiconductor Nanowires.' *Advanced Materials* **12, 4**: 298 (2000)

[121] V. G. Dubrovskii. 'Understanding the vapor–liquid–solid growth and composition of ternary III–V nanowires and nanowire heterostructures.' *Journal of Physics D: Applied Physics* **50, 45**: 453001 (2017)

[122] M. S. Gudiksen and C. M. Lieber. 'Diameter-Selective Synthesis of Semiconductor Nanowires.' *Journal of the American Chemical Society* **122, 36**: 8801 (2000)

[123] V. A. Nebol'sin and A. A. Shchetinin. 'Role of Surface Energy in the Vapor-Liquid-Solid Growth of Silicon.' *Inorganic Materials* **39, 9**: 899 (2003)

[124] V. G. Dubrovskii. 'Development of Growth Theory for Vapor–Liquid–Solid Nanowires: Contact Angle, Truncated Facets, and Crystal Phase.' *Crystal Growth & Design* **17, 5**: 2544 (2017)

[125] V. Schmidt et al.. 'Diameter dependence of the growth velocity of silicon nanowires synthesized via the vapor-liquid-solid mechanism.' *Physical Review B* **75, 4**: 045335 (2007)

[126] E. I. Givargizov. 'Fundamental aspects of VLS growth.' *Journal of Crystal Growth* **31**: 20 (1975)

[127] W. Nolting. *Grundkurs Theoretische Physik 4/2: Thermodynamik*. Springer, Berlin, Heidelberg, 9th Edition (2016)

[128] V. G. Dubrovskii and N. V. Sibirev. 'General form of the dependences of nanowire growth rate on the nanowire radius.' *Journal of Crystal Growth* **304, 2**: 504 (2007)

[129] J. M. Blakely and K. A. Jackson. 'Growth of Crystal Whiskers.' *The Journal of Chemical Physics* **37, 2**: 428 (1962)

[130] V. Ruth and J. P. Hirth. 'Kinetics of Diffusion–Controlled Whisker Growth.' *The Journal of Chemical Physics* **41, 10**: 3139 (1964)

[131] M. T. Borgström et al.. 'Synergetic nanowire growth.' *Nature nanotechnology* **2, 9**: 541 (2007)

[132] E. I. Givargizov and A. A. Chernov. 'Growth-rate of whiskers grown by vapor-liquid-solid mechanism, and role of surface-energy.' *Kristallografiya* **18, 1**: 147 (1973)

[133] E. I. Givargizov. 'Periodic instability in whisker growth.' *Journal of Crystal Growth* **20, 3**: 217 (1973)

[134] V. G. Dubrovskii et al.. 'Semiconductor nanowhiskers: Synthesis, properties, and applications.' *Semiconductors* **43, 12**: 1539 (2009)

[135] L. E. Fröberg et al.. 'Diameter-dependent growth rate of InAs nanowires.' *Physical Review B* **76, 15** (2007)

[136] T. Y. Tan et al.. 'Is there a thermodynamic size limit of nanowires grown by the vapor-liquid-solid process?' *Applied Physics Letters* **83, 6**: 1199 (2003)

[137] V. G. Dubrovskii and Y. Hervieu. 'Diffusion-induced growth of nanowires: Generalized boundary conditions and self-consistent kinetic equation.' *Journal of Crystal Growth* **401**: 431 (2014)

[138] D. Shakthivel et al.. 'Kinetic Analysis of the VLS Growth of Semiconducting Nanowires.' In '2020 IEEE International Conference on Flexible and Printable Sensors and Systems (FLEPS),' 1–4. IEEE (2020)

[139] J. Johansson and M. H. Magnusson. 'From diffusion limited to incorporation limited growth of nanowires.' *Journal of Crystal Growth* **525**: 125192 (2019)

[140] Morales and C. M. Lieber. 'A laser ablation method for the synthesis of crystalline semiconductor nanowires.' *Science* **279, 5348**: 208 (1998)

[141] C.-Y. Wen et al.. 'Structure, growth kinetics, and ledge flow during vapor-solid-solid growth of copper-catalyzed silicon nanowires.' *Nano letters* **10, 2**: 514 (2010)

[142] C. B. Maliakkal et al.. 'Vapor-solid-solid growth dynamics in GaAs nanowires.' *Nanoscale advances* **3, 20**: 5928 (2021)

[143] T. Hanrath and B. A. Korgel. 'Nucleation and growth of germanium nanowires seeded by organic monolayer-coated gold nanocrystals.' *Journal of the American Chemical Society* **124, 7**: 1424 (2002)

[144] T. Hanrath and B. A. Korgel. 'Supercritical Fluid–Liquid–Solid (SFLS) Synthesis of Si and Ge Nanowires Seeded by Colloidal Metal Nanocrystals.' *Advanced Materials* **15, 5**: 437 (2003)

[145] F. Wang et al.. 'Solution-liquid-solid growth of semiconductor nanowires.' *Inorganic chemistry* **45, 19**: 7511 (2006)

[146] J. Wang et al.. 'Solution-solid-solid mechanism: superionic conductors catalyze nanowire growth.' *Nano letters* **13, 9**: 3996 (2013)

[147] P. Wagener et al.. 'Fabrication of nanoparticles and nanomaterials using laser ablation in liquids.' *Photonic international* 20–23 (2011)

[148] R. P. Elliott and F. A. Shunk. 'The Au-Ga (Gold-Gallium) system.' *Bulletin of Alloy Phase Diagrams* **2, 3**: 356 (1981)

[149] C. J. Cooke and W. Hume-Rothery. 'The equilibrium diagram of the system gold-gallium.' *Journal of the Less Common Metals* **10, 1**: 42 (1966)

[150] H. Okamoto. 'Au-Ga (Gold-Gallium).' *Journal of Phase Equilibria and Diffusion* **34, 2**: 174 (2013)

[151] H. Okamoto and T. B. Massalski. 'The Au-P (Gold-phosphorus) system.' *Bulletin of Alloy Phase Diagrams* **5, 5**: 490 (1984)

[152] P. Buffat and J.-P. Borel. 'Size effect on the melting temperature of gold particles.' *Physical review. A, General physics* **13, 6**: 2287 (1976)

[153] J.-P. Borel. 'Thermodynamical size effect and the structure of metallic clusters.' *Surface Science* **106, 1-3**: 1 (1981)

[154] F. Font and T. G. Myers. 'Spherically symmetric nanoparticle melting with a variable phase change temperature.' *Journal of Nanoparticle Research* **15, 12** (2013)

[155] R. Straubinger et al.. 'Thermally Introduced Bismuth Clustering in Ga(P,Bi) Layers under Group V Stabilised Conditions Investigated by Atomic Resolution In Situ (S)TEM.' *Scientific reports* **8, 1**: 9048 (2018)

[156] E. Abbe. 'Beiträge zur Theorie des Mikroskops und der mikroskopischen Wahrnehmung.' *Archiv für Mikroskopische Anatomie* **9, 1**: 413 (1873)

[157] L. de Broglie. 'Research on the theory of quanta.' *Annales de Physique* **10, 3**: 22 (1925)

[158] M. Knoll and E. Ruska. 'Beitrag zur geometrischen Elektronenoptik. I.' *Annalen der Physik und Chemie* **404, 5**: 607 (1932)

[159] M. Knoll and E. Ruska. 'Beitrag zur geometrischen Elektronenoptik. II.' *Annalen der Physik und Chemie* **404, 6**: 641 (1932)

[160] M. Knoll and E. Ruska. 'Das Elektronenmikroskop.' *Zeitschrift für Physik* **78, 5-6**: 318 (1932)

[161] E. Ruska. 'Über Fortschritte im Bau und in der Leistung des magnetischen Elektronenmikroskops.' *Zeitschrift für Physik* **87, 9-10**: 580 (1934)

[162] J. M. Cowley and S. Iijima. 'Electron Microscope Image Contrast for Thin Crystal.' *Zeitschrift für Naturforschung A* **27, 3**: 445 (1972)

[163] L. Reimer. *Transmission Electron Microscopy: Physics of Image Formation and Microanalysis*, Volume 36 of *Optical Sciences*. Springer-Verlag, Berlin, Heidelberg, 4 Edition (1997)

[164] A. I. Kirkland et al.. 'Atomic Resolution Transmission Electron Microscopy.' In P. W. Hawkes and J. C. H. Spence (Editors), 'Science of Microscopy,' 3–64. Springer New York, NY (2007)

[165] P. W. Hawkes and E. Kasper. *Principles of electron optics: Wave Optics*, Volume 3. Academic press (1996)

[166] O. Scherzer. 'The Theoretical Resolution Limit of the Electron Microscope.' *Journal of Applied Physics* **20, 1**: 20 (1949)

[167] A. V. Crewe et al.. 'A High–Resolution Scanning Transmission Electron Microscope.' *Journal of Applied Physics* **39, 13**: 5861 (1968)

[168] A. V. Crewe et al.. 'Visibility of single atoms.' *Science* **168, 3937**: 1338 (1970)

[169] A. V. Crewe and J. Wall. 'A scanning microscope with 5 Å resolution.' *Journal of Molecular Biology* **48, 3**: 375 (1970)

[170] P. D. Nellist. 'Scanning Transmission Electron Microscopy.' In P. W. Hawkes and J. C. H. Spence (Editors), 'Science of Microscopy,' 65–132. Springer New York, NY (2007)

[171] E. J. Kirkland and M. G. Thomas. 'A high efficiency annular dark field detector for STEM.' *Ultramicroscopy* **62, 1-2**: 79 (1996)

[172] P. Hartel et al.. 'Conditions and reasons for incoherent imaging in STEM.' *Ultramicroscopy* **63, 2**: 93 (1996)

[173] S. J. Pennycook. 'Z-contrast stem for materials science.' *Ultramicroscopy* **30, 1-2**: 58 (1989)

[174] S. J. Pennycook and D. E. Jesson. 'High-resolution Z-contrast imaging of crystals.' *Ultramicroscopy* **37, 1-4**: 14 (1991)

[175] E. Gatti and P. Rehak. 'Semiconductor drift chamber - An application of a novel charge transport scheme.' *Nuclear Instruments and Methods in Physics Research* **225, 3**: 608 (1984)

[176] R. F. Egerton. *Electron Energy-Loss Spectroscopy in the Electron Microscope*. Springer US, Boston, MA, 3rd Edition (2011)

[177] P. Oleynikov et al.. 'Precession electron diffraction: observed and calculated intensities.' *Ultramicroscopy* **107, 6-7**: 523 (2007)

[178] E. F. Rauch et al.. 'Automated nanocrystal orientation and phase mapping in the transmission electron microscope on the basis of precession electron diffraction.' *Zeitschrift für Kristallographie* **225, 2-3**: 103 (2010)

[179] D. Viladot et al.. 'Orientation and phase mapping in the transmission electron microscope using precession-assisted diffraction spot recognition: state-of-the-art results.' *Journal of Microscopy* **252, 1**: 23 (2013)

[180] E. F. Rauch et al.. 'Automatic Crystal Orientation and Phase Mapping in TEM by Precession Diffraction.' *Microscopy and Analysis* **128**: 5 (2008)

[181] I. Ghamarian et al.. 'Development and application of a novel precession electron diffraction technique to quantify and map deformation structures in highly deformed materials—as applied to ultrafine-grained titanium.' *Acta Materialia* **79**: 203 (2014)

[182] R. Vincent and P. A. Midgley. 'Double conical beam-rocking system for measurement of integrated electron diffraction intensities.' *Ultramicroscopy* **53, 3**: 271 (1994)

[183] J. Portillo et al.. 'Precession Electron Diffraction Assisted Orientation Mapping in the Transmission Electron Microscope.' *Materials Science Forum* **644**: 1 (2010)

[184] E. F. Rauch and M. Veron. 'Coupled microstructural observations and local texture measurements with an automated crystallographic orientation mapping tool attached to a tem.' *Materialwissenschaft und Werkstofftechnik* **36, 10**: 552 (2005)

[185] T. E. Everhart and R. F. M. Thornley. 'Wide-band detector for micro-microampere low-energy electron currents.' *Journal of Scientific Instruments* **37, 7**: 246 (1960)

[186] J. Belz et al.. 'Direct investigation of (sub-) surface preparation artifacts in GaAs based materials by FIB sectioning.' *Ultramicroscopy* **163**: 19 (2016)

[187] F. M. Ross. 'In Situ Transmission Electron Microscopy.' In P. W. Hawkes and J. C. H. Spence (Editors), 'Science of Microscopy,' 445–534. Springer New York, NY (2007)

[188] E. D. Boyes and P. L. Gai. 'Environmental high resolution electron microscopy and applications to chemical science.' *Ultramicroscopy* **67, 1-4**: 219 (1997)

[189] K. Kishita et al.. 'Development of an analytical environmental TEM system and its application.' *Journal of electron microscopy* **58, 6**: 331 (2009)

[190] J. R. Jinschek. 'Advances in the environmental transmission electron microscope (ETEM) for nanoscale in situ studies of gas-solid interactions.' *Chemical communications* **50, 21**: 2696 (2014)

[191] P. L. Gai and E. D. Boyes. 'Advances in atomic resolution in situ environmental transmission electron microscopy and 1Å aberration corrected in situ electron microscopy.' *Microscopy research and technique* **72, 3**: 153 (2009)

[192] J. F. Creemer et al.. 'Atomic-scale electron microscopy at ambient pressure.' *Ultramicroscopy* **108, 9**: 993 (2008)

[193] N. de Jonge et al.. 'Atmospheric pressure scanning transmission electron microscopy.' *Nano letters* **10, 3**: 1028 (2010)

[194] T. Yaguchi et al.. 'Development of a high temperature-atmospheric pressure environmental cell for high-resolution TEM.' *Journal of electron microscopy* **60, 3**: 217 (2011)

[195] F. M. Ross. 'In-Situ TEM Studies of Vapor- and Liquid-Phase Crystal Growth.' In G. Dehm et al. (Editors), 'In-situ electron microscopy,' 171–189. Wiley-VCH, Weinheim (2012)

[196] E. L. Lawrence et al.. 'Approaches to Exploring Spatio-Temporal Surface Dynamics in Nanoparticles with In Situ Transmission Electron Microscopy.' *Microscopy and Microanalysis* **26, 1**: 86 (2020)

[197] Protochips, Inc. 'Atmosphere User Manual.' (2015)

[198] R. Straubinger. '*In-situ* Thermal Annealing and Growth Investigations on III/V Semiconductor Materials.' PhD thesis, Philipps-Universität Marburg (2018)

[199] J. A. Becker et al.. 'Properties and Uses of Thermistors - Thermally Sensitive Resistors.' *Bell System Technical Journal* **26, 1**: 170 (1947)

[200] J. S. Steinhart and S. R. Hart. 'Calibration curves for thermistors.' *Deep Sea Research and Oceanographic Abstracts* **15, 4**: 497 (1968)

[201] S. Dai et al.. 'Transmission electron microscopy with atomic resolution under atmospheric pressures.' *MRS Communications* **7, 4**: 798 (2017)

[202] Stanford Research Systems. 'Operating Manual and Programming Reference: Models RGA100, RGA200, and RGA300 Residual Gas Analyzer.' (2009)

[203] I. E. Dayton et al.. 'The Measurement of Two–Dimensional Fields. Part II: Study of a Quadrupole Magnet.' *Review of Scientific Instruments* **25, 5**: 485 (1954)

[204] P. H. Dawson. 'Quadrupole mass analyzers: Performance, design and some recent applications.' *Mass Spectrometry Reviews* **5, 1**: 1 (1986)

[205] R. D. Craig and E. H. Harden. 'The interpretation of mass spectra in vacuum measurement.' *Vacuum* **16, 2**: 67 (1966)

[206] Stanford Research Systems. 'SRS Tech Note: Residual Gas Analysis Basics.' (2020)

[207] T. C. Isabell et al.. 'Plasma Cleaning and Its Applications for Electron Microscopy.' *Microscopy and Microanalysis* **5, 2**: 126 (1999)

[208] O. Maßmeyer et al.. 'Revealing the Significance of Catalytic and Alkyl Exchange Reactions during GaAs and GaP Growth by Metal Organic Vapor Phase Epitaxy.' *ACS omega* **6, 42**: 28229 (2021)

[209] MATLAB. *9.12.0.1927505 (R2022a).* The MathWorks Inc., Natick, Massachusetts (2022)

[210] W. H. Richardson. 'Bayesian-Based Iterative Method of Image Restoration.' *Journal of the Optical Society of America* **62, 1**: 55 (1972)

[211] L. B. Lucy. 'An iterative technique for the rectification of observed distributions.' *The Astronomical Journal* **79**: 745 (1974)

[212] P. H. Dawson. 'A detailed study of the quadrupole mass filter.' *International Journal of Mass Spectrometry and Ion Physics* **14, 4**: 317 (1974)

[213] K. Blaum et al.. 'Peak shape for a quadrupole mass spectrometer: comparison of computer simulation and experiment.' *International Journal of Mass Spectrometry* **202, 1-3**: 81 (2000)

[214] S. H. Li et al.. 'OMVPE growth mechanism for GaP using tertiarybutylphosphine and trimethylgallium.' *Journal of Crystal Growth* **96, 4**: 906 (1989)

[215] S. H. Li et al.. 'Study of tertiarybutylphosphine pyrolysis using a deuterated source.' *Journal of Applied Physics* **65, 12**: 5161 (1989)

[216] S. H. Li et al.. 'Pyrolysis of tertiarybutylphosphine.' *Journal of Electronic Materials* **18, 3**: 457 (1989)

[217] A. Stegmüller et al.. 'A quantum chemical study on gas phase decomposition pathways of triethylgallane (TEG, $Ga(C_2H_5)_3$) and tert-butylphosphine (TBP, $PH_2(t\text{-}C_4H_9)$) under MOVPE conditions.' *Physical Chemistry Chemical Physics* **16, 32**: 17018 (2014)

[218] I. V. Alabugin et al.. 'Hyperconjugation.' *WIREs Computational Molecular Science* **1, 1**: 109 (2011)

[219] T.-L. Chang and W.-J. Li. 'A calibrated measurement of the atomic weight of carbon.' *Chinese Science Bulletin* **35, 4**: 290 (1990)

[220] R. Hagemann et al.. 'Absolute isotopic scale for deuterium analysis of natural waters. Absolute D/H ratio for SMOW.' *Tellus* **22, 6**: 712 (1970)

[221] F. E. Saalfeld and H. J. Svec. 'The Mass Spectra of Volatile Hydrides. I. The Monoelemental Hydrides of the Group IVB and VB Elements.' *Inorganic chemistry* **2, 1**: 46 (1963)

[222] Y. Wada and R. W. Kiser. 'Mass Spectrometric Study of Phosphine and Diphosphine.' *Inorganic chemistry* **3, 2**: 174 (1964)

[223] M. G. Jacko and S. J. W. Price. 'The Pyrolysis of Trimethyl Gallium.' *Canadian Journal of Chemistry* **41, 6**: 1560 (1963)

[224] M. Yoshida et al.. 'Mass Spectrometric Study of $Ga(CH_3)_3$ and $Ga(C_2H_5)_3$ Decomposition Reaction in H_2 and N_2.' *Journal of The Electrochemical Society* **132, 3**: 677 (1985)

[225] L. A. Machlan et al.. 'Absolute Isotopic Abundance Ratio And Atomic Weight Of a Reference Sample of Gallium.' *Journal of research of the National Bureau of Standards* **91, 6**: 323 (1986)

[226] J. C. Russ. *The image processing handbook*. CRC Press, Boca Raton, Fla, 6. ed. Edition (2011)

[227] M. Aubry et al.. 'Fast Local Laplacian Filters.' *ACM Transactions on Graphics* **33, 5**: 1 (2014)

[228] S. Paris et al.. 'Local Laplacian filters.' *Communications of the ACM* **58, 3**: 81 (2015)

[229] N. Otsu. 'A Threshold Selection Method from Gray-Level Histograms.' *IEEE Transactions on Systems, Man, and Cybernetics* **SMC-9, 1**: 62 (1979)

[230] J. Canny. 'A Computational Approach to Edge Detection.' *IEEE Transactions on Pattern Analysis and Machine Intelligence* **PAMI-8, 6**: 679 (1986)

[231] Y. Liu et al.. 'The effect of V/III ratio on the morphology and structure of GaAs nanowires by MOCVD.' *AIP Advances* **8, 5**: 055108 (2018)

[232] M. Steidl et al.. 'Impact of N Incorporation on VLS Growth of GaP(N) Nanowires Utilizing UDMH.' *Nanoscale research letters* **13, 1**: 417 (2018)

[233] S. Kodambaka et al.. 'Diameter-independent kinetics in the vapor-liquid-solid growth of Si nanowires.' *Physical review letters* **96, 9**: 096105 (2006)

[234] R. E. Algra et al.. 'Twinning superlattices in indium phosphide nanowires.' *Nature* **456, 7220**: 369 (2008)

[235] R. E. Algra et al.. 'Paired Twins and $\{11\bar{2}\}$ Morphology in GaP Nanowires.' *Nano letters* **10, 7**: 2349 (2010)

[236] F. M. Davidson et al.. 'Lamellar Twinning in Semiconductor Nanowires.' *The Journal of Physical Chemistry C* **111, 7**: 2929 (2007)

[237] J. Johansson et al.. 'Growth related aspects of epitaxial nanowires.' *Nanotechnology* **17, 11**: S355 (2006)

[238] G. R. Terrell and D. W. Scott. 'Variable Kernel Density Estimation.' *The Annals of Statistics* **20, 3**: 1236 (1992)

[239] M. Zhang et al.. 'Formation mechanisms for the dominant kinks with different angles in InP nanowires.' *Nanoscale research letters* **9, 1**: 211 (2014)

[240] M. Levinshtein et al. (Editors). *Handbook Series on Semiconductor Parameters*, Volume 1. World Scientific, London (1996)

[241] M. Morita et al.. 'Growth of native oxide on a silicon surface.' *Journal of Applied Physics* **68, 3**: 1272 (1990)

[242] C. B. Maliakkal et al.. 'Growth, structural and optical characterization of wurtzite GaP nanowires.' *Nanotechnology* **30, 25**: 254002 (2019)

[243] H. Angermann et al.. 'Wet-chemical passivation of Si(111)- and Si(100)-substrates.' *Materials Science and Engineering: B* **73, 1-3**: 178 (2000)

[244] M. Schaffer et al.. 'Sample preparation for atomic-resolution STEM at low voltages by FIB.' *Ultramicroscopy* **114**: 62 (2012)

[245] R. Straubinger et al.. 'Preparation and Loading Process of Single Crystalline Samples into a Gas Environmental Cell Holder for In Situ Atomic Resolution Scanning Transmission Electron Microscopic Observation.' *Microscopy and Microanalysis* **22, 3**: 515 (2016)

[246] S. Rubanov and P. R. Munroe. 'FIB-induced damage in silicon.' *Journal of Microscopy* **214, 3**: 213 (2004)

[247] A. L. Roest et al.. 'Position-controlled epitaxial III–V nanowires on silicon.' *Nanotechnology* **17, 11**: 271 (2006)

Danksagung

Zum Schluss möchte ich mich bei Allen bedanken, die mich im Vorfeld und im Rahmen dieser Arbeit unterstützt haben. Viele Personen haben durch wissenschaftlichen Austausch, Diskussionen und Kritik, sowie Unterstützung im Privaten zum Gelingen beigetragen. Mein besonderer Dank gilt dabei:

Prof. Dr. Kerstin Volz für die Betreuung und Unterstützung während meiner Promotion, die Möglichkeit meine Arbeit in der Arbeitsgruppe zu schreiben, die hilfreichen Diskussionen und Anregungen und für die Geduld mit dem Projekt, auch wenn es oft nicht nach Plan lief.

Prof. Dr. Marina Gerhard für die Teilnahme an der Prüfungskommission und damit verbunden die Übernahme des Zweitgutachtens meiner Arbeit.

Prof. Dr. Stefan Wippermann für die Bereitschaft zum Beitritt der Prüfungskommission.

Der Deutschen Forschungsgemeinschaft für die Finanzierung meiner Forschung im Rahmen des Graduiertenkollegs 1782 "Functionalization of Semiconductors".

Den Korrekturlesern Shamail, Jürgen, Felix, Thilo, David und Oli, die mir, durch ihre Kommentare und Kritik am Manuskript, sehr geholfen haben.

Meinen *in-situ* Kollegen David und Felix für die gute Zusammenarbeit und das Durchhaltevermögen.

Der gesamten Arbeitsgruppe für die tolle freundschaftliche Atmosphäre und offenen Bürotüren. Die Lockdowns haben sehr deutlich gemacht, wie viel das wert ist! Außerdem für die zahlreichen Gespräche zwischendurch und das Feedback in den Seminaren, die mich

immer wieder auf neue Ideen gebracht und zu neuen Ansätzen geführt haben. Hier darf sich jeder von euch angesprochen fühlen!

Den Technikern Celina, Michael, Thomas und Stefan, die die Geräte am laufen halten, bei Softwareproblemen parat sind, Ventile, Pumpen oder Quellen gewechselt haben.

Dem Sekretariat, Isabelle und Marieke, für viel Organisation und die administrative Unterstützung.

Meiner Familie, insbesondere meinen Eltern, für die vielfältige Unterstützung in allen Lebenslagen.

Außerdem der Boulder-Gang und dem Squashteam, die für den nötigen sportlichen Ausgleich gesorgt haben.

Wissenschaftlicher Werdegang